Springer Series in Optical Sciences 199

Oleksiy Shulika
Igor Sukhoivanov *Editors*

Contemporary Optoelectronics

Materials, Metamaterials and Device Applications

Springer

Springer Series in Optical Sciences

Volume 199

Springer Series in Optical Sciences

The Springer Series in Optical Sciences, under the leadership of Editor-in-Chief William T. Rhodes, Georgia Institute of Technology, USA, provides an expanding selection of research monographs in all major areas of optics: lasers and quantum optics, ultrafast phenomena, optical spectroscopy techniques, optoelectronics, quantum information, information optics, applied laser technology, industrial applications, and other topics of contemporary interest.

With this broad coverage of topics, the series is of use to all research scientists and engineers who need up-to-date reference books.

The editors encourage prospective authors to correspond with them in advance of submitting a manuscript. Submission of manuscripts should be made to the Editor-in-Chief or one of the Editors. See also www.springer.com/series/624

Oleksiy Shulika · Igor Sukhoivanov
Editors

Contemporary Optoelectronics

Materials, Metamaterials and Device Applications

Springer

Editors
Oleksiy Shulika
Departamento de Ingeniería Electrónica, Campus Irapuato-Salamanca
Universidad de Guanajuato
Salamanca
México

Igor Sukhoivanov
Departamento de Ingeniería Electrónica, Campus Irapuato-Salamanca
Universidad de Guanajuato
Salamanca
México

ISSN 0342-4111 ISSN 1556-1534 (electronic)
Springer Series in Optical Sciences
ISBN 978-94-017-7314-0 ISBN 978-94-017-7315-7 (eBook)
DOI 10.1007/978-94-017-7315-7

Library of Congress Control Number: 2015945602

Springer Dordrecht Heidelberg New York London

Printed on acid-free paper

Springer Science+Business Media B.V. Dordrecht is part of Springer Science+Business Media (www.springer.com)

Contents

Editors and Contributors

About the Editors

Oleksiy Shulika had received the Ph.D. degree in optics and laser physics from V.N. Karazin National University, Ukraine, in 2008 and academic title of Associate Professor in 2012. He is a member of "Sistema Nacional de Investigadores" with distinction level II. His research interests are ultrafast and nonlinear photonics, THz photonics, semiconductor optics, semiconductor nanostructures, and optoelectronic devices. He is the coeditor of three books "Terahertz and Mid Infrared Radiation: Basic Research and Practical Applications" Springer©2011, "Terahertz and Mid Infrared Radiation: Detection of Explosives and CBRN (Using Terahertz)" Springer©2014, and "Advanced Lasers: Laser Physics and Technology for Applied and Fundamental Science" Springer©2015.

Dr. Shulika is a member of IEEE Photonics Society, Optical Society of America, and SPIE. He is a member of the organizing committee of the Conference Series "International Conference on Advanced Optoelectronics and Lasers (CAOL)," NATO Advanced Research Workshop "Terahertz and Mid Infrared Radiation: Basic Research and Applications (TERA-MIR)," and "International Conference on Laser and Fiber-Optical Networks Modeling (LFNM)."

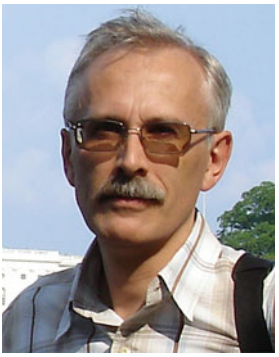

Igor Sukhoivanov had received the Ph.D. degree in 1985, the D.Sc. degree in optics and laser physics from V.N. Karazin National University, Kharkiv, Ukraine, in 2002, and academic title of Full Professor in 2004. Currently, he is with the Guanajuato University, Department of Electronics, DICIS, Salamanca, Mexico, Professor Titular B., member of "Sistema Nacional de Investigadores" with distinction level II.

He is the author/coauthor of nine book chapters and more than 130 journal papers. He is the coauthor/coeditor of two books "Photonic Crystals: Physics and Practical Modeling" Springer©2009 and "Advanced Lasers: Laser Physics and Technology for Applied and Fundamental Science" Springer©2015.

His research interests include photonic devices, semiconductor lasers and theory of quantum confinement structures, photonic crystal elements, and ultrashort pulse propagation in fibers.

Professor Sukhoivanov is a senior member of the IEEE Photonics Society (IPS) and of the Optical Society of America (OSA) and a member of the American Physical Society (APS) and the Society of Photo-Optical Instrumentation Engineers (SPIE). He is the organizer and chairman of International Conference on Advanced Optoelectronics and Lasers (CAOL), International Conference on Laser and Fiber-Optical Networks Modeling (LFNM), etc. He is also a co-organizer of separate topics in LEOS Summer Topicals'2008 and PHO Summer Topicals'2010 in Mexico.

Contributors

Alejandro B. Aceves Department of Mathematics, Southern Methodist University, Dallas, TX, USA

José Amparo Andrade Lucio Departamento de Ingeniería Electrónica, DICIS, Universidad de Guanajuato, Salamanca, México

Miguel V. Andrés University of Valencia, Burjassot, Valencia, Spain

Laura Aparicio-Ixta Centro de Investigaciones en Óptica A.C., León, Guanajuato, Mexico

N.N. Beletski O. Ya Usikov Institute for Radiophysics and Electronics of NAS of Ukraine, Kharkiv, Ukraine

Krzysztof Borzycki National Institute of Telecommunications (NIT), Warsaw, Poland

Volodymyr O. Byelobrov Institute of Radiophysics and Electronics NASU, Kharkiv, Ukraine

Jiří Čtyroký Institute of Photonics and Electronics AS CR, v.v.i., Prague 8, Czech Republic

Antonio Diez University of Valencia, Burjassot, Valencia, Spain

Igor V. Dzedolik Taurida National V.I. Vernadsky University, Simferopol, Ukraine

Volodymyr I. Fesenko Institute of Radio Astronomy of NASU, Kharkiv, Ukraine; Lab. "Photonics", Kharkiv National University of Radio Electronics, Kharkiv, Ukraine

Igor V. Guryev Departamento de Estudios Multidisciplinarios, DICIS, Universidad de Guanajuato, Salamanca, México

Sergii O. Iakushev Kharkiv National University of Radio Electronics, Kharkiv, Ukraine

Oscar G. Ibarra Manzano Division of Engineering Campus Irapuato Salamanca, University of Guanajuato, León, Mexico

E.V. Kazantseva Department of Physics and Technology of Nanostructures, Moscow Institute of Physics and Technology, Moscow, Russia; Joint Institute for High Temperatures, Russian Academy of Sciences, Moscow, Russia

V. Khardikov Institute of Radio Astronomy of National Academy of Sciences of Ukraine, Kharkiv, Ukraine; School of Radio Physics, V.N. Karazin National University, Kharkiv, Ukraine

Yuri S. Kivshar Nonlinear Physics Center, Research School of Physics and Engineering, The Australian National University, Canberra, ACT, Australia

Mykhailo V. Klymenko Department of Chemistry, B6c, University of Liege, Liege, Belgium

Tsampikos Kottos Department of Physics, Wesleyan University, Middletown, CT, USA

A.I. Maimistov Department of Solid State Physics and Nanosystems, National Research Nuclear University Moscow Engineering Physics Institute, Moscow, Russia; Department of Physics and Technology of Nanostructures, Moscow Institute of Physics and Technology, Moscow, Russia

Marian Marciniak National Institute of Telecommunications, Warsaw, Poland; Kielce University of Technology, Kielce, Poland

P. Mladyonov Institute of Radio Astronomy of National Academy of Sciences of Ukraine, Kharkiv, Ukraine

Alexander I. Nosich Institute of Radiophysics and Electronics NASU, Kharkiv, Ukraine

S. Yu Polevoy O. Ya Usikov Institute for Radiophysics and Electronics of NAS of Ukraine, Kharkiv, Ukraine

S. Prosvirnin Institute of Radio Astronomy of National Academy of Sciences of Ukraine, Kharkiv, Ukraine; School of Radio Physics, V.N. Karazin Kharkiv National University, Kharkiv, Ukraine

Gabriel Ramos-Ortiz Centro de Investigaciones en Óptica A.C., León, Guanajuato, Mexico

Mario Rodriguez Centro de Investigaciones en Óptica A.C., León, Guanajuato, Mexico

José Ramón Salgueiro Departamento de Física Aplicada, Universidade de Vigo, Ourense, Spain

Kay Schuster Leibniz Institute of Photonic Technology Jena (IPHT), Jena, Germany

Oleksiy V. Shulika Departamento de Ingeniería Electrónica, DICIS, Universidad de Guanajuato, Salamanca, México

Marat Soskin Institute of Physics, NAS of Ukraine, Kiev, Ukraine

Igor A. Sukhoivanov Departamento de Ingeniería Electrónica, DICIS, Universidad de Guanajuato, Salamanca, México

S.I. Tarapov O. Ya Usikov Institute for Radiophysics and Electronics of NAS of Ukraine, Kharkiv, Ukraine

Vladimir R. Tuz Institute of Radio Astronomy of National Academy of Sciences of Ukraine, Kharkiv, Ukraine; School of Radio Physics, V.N. Karazin Kharkiv National University, Kharkiv, Ukraine

Vasyl Vasil'ev Institute of Physics, NAS of Ukraine, Kiev, Ukraine

Tatiana L. Zinenko Institute of Radiophysics and Electronics NASU, Kharkiv, Ukraine

Part I
Materials for Contemporary Optoelectronics

Chapter 1
Phonon-Polaritons in Nonlinear Dielectric Medium

Igor V. Dzedolik

Abstract We discuss the properties of polaritons and obtain theoretically the phonon-polariton spectrum in nonlinear dielectric medium with the third order Kerr-type nonlinearity. We investigate the dependence of number of the polariton spectrum branches on the intensity of electromagnetic field and demonstrate that the appearance of new branches located in the polariton spectrum gap is caused by the dispersion of the third order dielectric susceptibility at the intensive electromagnetic field in the medium. The modulation instability of new spectrum branch waves leads to the appearance of the spatial solitons or cnoidal waves. Also we theoretically investigate the properties of scalar and vector phonon-polariton spatial solitons and cnoidal waves propagating in boundless dielectric medium. These new nonlinear waves one can use for designing the optical devices such as the optical converter, controllable filter, all-optical logic gates, etc.

1.1 Introduction

The spectra of polaritons in the dielectric media were obtained firstly by Tolpygo using the quantum approach [1] and by Huang using the classical approach [2] in an ionic crystal. The polaritons are the collective dipole excitations (quasiparticles) in different media. The phonon-polaritons [1–11] correspond to the bound states of photons and optical phonons in a dielectric medium. The magnon-polaritons [7, 11–13] are the bound states of magnons, photons and optical phonons in magnetic. The exciton-polaritons [4–6, 11] are the bound states of photons and excitons in a semiconductor. The polaritons are divided into the volume quasiparticles and the surface quasiparticles. In the 60–70th years many theoretical and experimental works were done researching the volume polaritons [1–10], in the 80th years the

I.V. Dzedolik (✉)
Taurida National V.I. Vernadsky University, 4, Vernadsky Avenue,
95007 Simferopol, Ukraine
e-mail: dzedolik@crimea.edu

O. Shulika and I. Sukhoivanov (eds.), *Contemporary Optoelectronics*,
Springer Series in Optical Sciences 199, DOI 10.1007/978-94-017-7315-7_1

surface polaritons [14, 15], and the nonlinear polaritons [8, 9, 16–18] were also researched.

The polariton properties still attract attention of the researchers because the interaction of electromagnetic field with different media can be more adequately explained by polariton conception, for example, at a nonlinear pulse propagation [19, 20], in the periodical structures [21], or at the nonlinear wave interaction [22]. It is caused by the clear understanding of the generation, propagation, transformation and instability of the electromagnetic and polarization waves in the active and passive media.

The phonon-polariton properties in the dielectric medium are important in designing of the controllable filters [23], all-optical logic gates [24], time-delayed beamsplitters [25], delay-lines [26], and other devices of the microwave and optical circuits [27–29]. The polariton conception is applied to explain the generation of continuous and solitary waves in the Bose-Einstein exciton condensate [30, 31]. Now the surface plasmon-polaritons [32–36] are actively investigated with the purpose to apply them in the devices of transmission lines and processing information. The above mentioned papers are devoted to the analysis of polariton properties in the different media and illustrate the common interest of researchers in this area of physics.

The polaritons in the media can be described by means of the microscopic multiparticle quantum approach and the macroscopic classical approach with the practically same results. The polaritons are efficiently generated when the frequency of electromagnetic wave is close to the crystal lattice resonance frequency lying in the terahertz range $\sim 10^{12}$ s^{-1}, or to the electron resonance frequency lying near the infrared or optical ranges $\sim 10^{14}$ s^{-1}. It leads to enhancement of the vibration amplitude, i.e. to the nonlinear oscillations of the ions and electrons. The nonlinear effects also appear in the generation of polaritons out of these ranges, if the nonlinear electron response of the medium arises due to the intensive electromagnetic wave or pulse scattering. In these cases some new branches of the phonon-polariton spectrum appear.

The dispersion relation of the frequency $\omega(k)$ on the wave vector k in the nonlinear medium, $D(\omega, k, E_a) = 0$, is modified by the electromagnetic field amplitude E_a. The polariton spectrum has a gap, where the polariton wave damps. The input electromagnetic wave with the frequency in the spectral gap does not propagate through dielectric medium. The enhancement of electromagnetic field intensity leads to the increasing of the nonlinear response of the dielectric medium, and it results in appearance of the additional branches in the polariton spectrum gap. In order to demonstrate this effect we have obtained the phonon-polariton spectra in the nonlinear medium considering the dispersion of the third order nonlinear susceptibility for the first harmonic of the wave frequency.

We show how the intensity of electromagnetic field influences the number of polariton spectrum branches. We also theoretically investigate the properties of phonon-polariton waves propagating as the cnoidal waves and longitudinal or transverse spatial solitons in the Kerr-type solid medium. We research the instability

of the wave in nonlinear media, and analyze the conditions of the wave transformations. We show that polariton wave representing as polariton flow can decompose into several flows. The envelope of the polariton wave in the transverse plane can transform to the cnoidal wave or spatial soliton depending on the field density and medium parameters in the self-focusing and self-defocusing medium.

1.2 Polaritons in Ionic Crystal

We investigate theoretically the properties of phonon-polariton spectrum in the nonlinear dielectric medium using the macroscopic classical approach. An electromagnetic wave falling onto the crystal produces the moving of the electron shells and ions, i.e. it excites the dipole excitations of the electron shells and ions in crystal lattice.

1.2.1 Theoretical Model

We consider the simple theoretical model of the classical electromagnetic field interaction with the ions forming a crystal lattice [37]. If the electromagnetic wave propagates in the dielectric crystal we can describe this process using the following: (1) the equation of ion motion in a unit cell of the crystal lattice

$$m_{eff}\frac{d^2\mathbf{R}}{dt^2}+m_{eff}\Gamma\frac{d\mathbf{R}}{dt}+\nabla_R U_R=e_{eff}\left(\mathbf{E}+\frac{1}{c}\frac{d\mathbf{R}}{dt}\times\mathbf{B}\right), \tag{1.1}$$

where e_{eff}, m_{eff} are the effective ion charge and mass in the lattice cell, $\mathbf{R}=\mathbf{r}_+-\mathbf{r}_-$ is the displacement vector of the positive and negative layers of the ions, $U_R=(q_{1R}/2)R^2+(q_{2R}/3)R^3-(q_{3R}/4)R^4+\cdots$ is the potential energy of the ions, Γ is the damping factor; (2) the equation of outer shell electron motion of the ion

$$m\frac{d^2\mathbf{r}}{dt^2}+m\Gamma\frac{d\mathbf{r}}{dt}+\nabla_r U_r=-e\left(\mathbf{E}+\frac{1}{c}\frac{d\mathbf{r}}{dt}\times\mathbf{B}\right), \tag{1.2}$$

where $U_r=(q_{1r}/2)\,r^2+(q_{2r}/3)\,r^3-(q_{3r}/4)\,r^4+\cdots$ is the potential energy of the electron; (3) the electromagnetic field equations

$$\nabla\times\mathbf{B}=c^{-1}\left(\dot{\mathbf{E}}+4\pi\dot{\mathbf{P}}\right),\quad \nabla\times\mathbf{E}=-c^{-1}\dot{\mathbf{B}}, \tag{1.3}$$

where $\mathbf{P}=e_{eff}N_C\mathbf{R}-eN_e\mathbf{r}$ is the polarization vector of medium, N_C is the number of cells in the unit of volume, N_e is the number of electrons in the unit of volume, q_{jr}, q_{jR} are the phenomenological elastic parameters of the medium; the overdot denotes partial time derivative. In the system of (1.1)–(1.3) we take into account the bound of charges by the electromagnetic field.

We can neglect the response of the magnetic component of the high-frequency electromagnetic field $|\mathbf{E}| \gg \left|c^{-1}(d\mathbf{R}/dt) \times \mathbf{B}\right|$, $|\mathbf{E}| \gg \left|c^{-1}(d\,\mathbf{r}/dt) \times \mathbf{B}\right|$ in the medium. Then we represent solutions of the motion (1.1) and (1.2) as the series where lower index of the terms is the order of an infinitesimal $\mathbf{r} = \mathbf{r}_0 + \mathbf{r}_1 + \mathbf{r}_2 + \mathbf{r}_3$, $\mathbf{R} = \mathbf{R}_0 + \mathbf{R}_1 + \mathbf{R}_2 + \mathbf{R}_3$. If the electromagnetic field is harmonic $E \sim \exp(-i\omega t)$, it is easy to obtain the polarization vector of medium by the method of the successive approximations. Generally by this method we can obtain the polarization vector including the first, the second and the third harmonics

$$\begin{aligned}\mathbf{P} = {} & \chi_1 \mathbf{E}_a \exp(-i\omega t) + \chi_{20} E_a \mathbf{E}_a + \chi_{22} E_a \mathbf{E}_a \exp(-i2\omega t) \\ & + \chi_{31} E_a^2 \mathbf{E}_a \exp(-i\omega t) + \chi_{33} E_a^2 \mathbf{E}_a \exp(-i3\omega t),\end{aligned} \tag{1.4}$$

where $\chi_1 = \frac{1}{4\pi}\left(\frac{\omega_e^2}{\tilde{\omega}_1^2} + \frac{\omega_I^2}{\tilde{\Omega}_1^2}\right)$,

$$\chi_{20} = \frac{1}{4\pi}\left(\frac{e\alpha_{2r}\omega_e^2}{m\omega_0^2\left(\left(\omega_0^2 - \omega^2\right)^2 + \omega^2\Gamma^2\right)} - \frac{e_{eff}\alpha_{2R}\omega_I^2}{m_{eff}\Omega_\perp^2\left(\left(\Omega_\perp^2 - \omega^2\right)^2 + \omega^2\Gamma^2\right)}\right),$$

$$\chi_{22} = \frac{1}{4\pi}\left(\frac{e\alpha_{2r}\omega_e^2}{m\left(\tilde{\omega}_1^2\right)^2\tilde{\omega}_2^2} - \frac{e_{eff}\alpha_{2R}\omega_I^2}{m_{eff}\left(\tilde{\Omega}_1^2\right)^2\tilde{\Omega}_2^2}\right),$$

$$\chi_{31} = -\frac{1}{4\pi}\left(\frac{e^2\alpha_{3r}\omega_e^2}{m^2\left(\tilde{\omega}_1^2\right)^3\left(\tilde{\omega}_1^2\right)^*} + \frac{e_{eff}^2\alpha_{3R}\omega_I^2}{m_{eff}^2\left(\tilde{\Omega}_1^2\right)^3\left(\tilde{\Omega}_1^2\right)^*}\right),$$

$\chi_{33} = -\frac{1}{4\pi}\left(\frac{e^2\alpha_{3r}\omega_e^2}{m^2\left(\tilde{\omega}_1^2\right)^3\tilde{\omega}_3^2} + \frac{e_{eff}^2\alpha_{3R}\omega_I^2}{m_{eff}^2\left(\tilde{\Omega}_1^2\right)^3\tilde{\Omega}_3^2}\right)$ are the linear and nonlinear susceptibilities of medium, $\tilde{\omega}_1^2 = \omega_0^2 - \omega^2 - i\Gamma\omega$, $\tilde{\omega}_2^2 = \omega_0^2 - (2\omega)^2 - i2\Gamma\omega$, $\tilde{\omega}_3^2 = \omega_0^2 - (3\omega)^2 - i3\Gamma\omega$, $\tilde{\Omega}_1^2 = \Omega_\perp^2 - \omega^2 - i\Gamma\omega$, $\tilde{\Omega}_2^2 = \Omega_\perp^2 - (2\omega)^2 - i2\Gamma\omega$, $\tilde{\Omega}_3^2 = \Omega_\perp^2 - (3\omega)^2 - i3\Gamma\omega$; $\omega_e^2 = 4\pi e^2 N_e m^{-1}$, $\omega_I^2 = 4\pi e_{eff}^2 N_C m_{eff}^{-1}$ are the electron and ion plasma frequencies; $\omega_0^2 = q_{1r}m^{-1}$ is the electron resonance frequency, $\Omega_\perp^2 = q_{1R}m_{eff}^{-1}$ is the resonance frequency of lattice; $\alpha_{2r} = q_{2r}m^{-1}$, $\alpha_{3r} = q_{3r}m^{-1}$, $\alpha_{2R} = q_{2R}m_{eff}^{-1}$, $\alpha_{3R} = q_{3R}m_{eff}^{-1}$; Γ, q_{jr}, q_{jR} are the phenomenological parameters depending on the linear and nonlinear properties of the medium. The susceptibility of the third order is more than zero $\chi_{31} > 0$, because the coefficients $\alpha_{3R} = -q_{3R}m_{eff}^{-1} < 0$ and $\alpha_{3r} = -q_{3r}m^{-1} < 0$ are negative. The influence of optical phonon to the susceptibilities χ_{ij} is taken into account by the terms with ω_I^2.

Some crystals with centrums of inversion at lattices and glasses with isotropic structure are suitable media with necessary properties for arising of examined nonlinear polaritons. The linear and nonlinear properties of various materials are measured and described at the present time [38, 39]. For example, the high-usage crystal that is the zinc selenide ZnSe has the parameters: the real part of refractive

index $n_1 = n_1{}' + in_1{}''$ is $n_1' , = 2.67$, and the imaginary part is $n_1{}'' \approx 10^{-5}$ at the wavelength $\lambda = 0.532\,\mu\text{m}$ [39]. We have used in our model the phenomenological parameters $\alpha_{1R,1r}$, $\alpha_{3R,3r}$, ω_e, ω_I, Γ_e, Γ_I connected with the susceptibilities χ_1 and χ_{31} that are expressed after (1.4). The susceptibilities χ_1 and χ_{31} are used in the expression for permittivity $\varepsilon = \varepsilon_1 + 4\pi\chi_{31}|E|^2$, where $\varepsilon_1 = 1 + 4\pi(\chi_1{}' + i\chi_1{}'')$, $\chi_{31} = \chi_{31}{}' + i\chi_{31}{}''$. The real and imaginary parts of the refractive index and the permittivity are connected as $\varepsilon_1{}' = n_1{}'^2 - n_1{}''^2$ and $\varepsilon_1{}'' = 2n_1{}'n_1{}''$. The real and imaginary parts of the linear susceptibilities of ZnSe we can calculate as $\chi_1{}' = (\varepsilon_1{}' - 1)/4\pi = 0.49$ and $\chi_1{}'' = \varepsilon_1{}''/4\pi \approx 0.4 \times 10^{-5}$; the real part of the third order susceptibility is $\chi_{31}{}' = 2n'^2\varepsilon_0 c\gamma$, the imaginary part of the third order susceptibility is $\chi_{31}{}'' = n'^2\varepsilon_0\omega^{-1}c^2\beta$, where the measured values of the parameters are $\beta = 5.8 \times 10^{-9}$ cm/W and $\gamma = 6.7 \times 10^{-14}$ cm^2/W.

1.2.2 Nonlinear Medium with the Local Inversion Centers

We consider the application of our theory only in the medium with the local centers of inversion in the medium with the third order susceptibility χ_{31}, where the second-order susceptibility vanishes due to the symmetry, i.e. the Kerr-type medium. We represent the electromagnetic field as the set of plane waves and consider the interaction degenerates involving only at the first harmonic $\mathbf{E} = \mathbf{E}_a \exp(-i\omega t + i\mathbf{kr})$. In this case the polarization vector (1.4) of the medium has the form $\mathbf{P} = \left(\chi_1 + \chi_{31}E_a^2\right)\mathbf{E}$.

One can eliminate the magnetic inductance vector $\mathbf{B}$ from the Maxwell's equation (1.3), $\nabla \times \nabla \times \mathbf{E} + c^{-2}\,\ddot{\mathbf{E}} = -4\pi c^{-2}\,\ddot{\mathbf{P}}$, and get the algebraic vector equation

$$\left(k^2 - c^{-2}\varepsilon\omega^2\right)\mathbf{E}_a = \mathbf{k}(\mathbf{k}\mathbf{E}_a). \tag{1.5}$$

The permittivity of medium is defined by the expression $\varepsilon = 1 + 4\pi\chi_1 + 4\pi\chi_{31}E_a^2$. In the expression for permittivity ε both the electron and ion responses of the medium at the electromagnetic field are considered.

We resolve the electric field vector at the transverse and longitudinal components $\mathbf{E} = \mathbf{E}_\perp + \mathbf{E}_{||}$ relating to the wave vector $\mathbf{k}$. Having assumed that the interaction of the electromagnetic waves and charges in the medium occurs as affected transverse field component $\mathbf{E}_\perp$, that is $\mathbf{k}\mathbf{E}_\perp = 0$, we obtain from the (1.5) the dispersion equation for the nonlinear polaritons in the Kerr-type medium

$$k^2 - c^{-2}\omega^2\left[1 + 4\pi\chi_1(\omega) + 4\pi\chi_{31}(\omega)E_a^2\right] = 0. \tag{1.6}$$

Equation (1.6) allows obtaining the nonlinear phonon-polariton spectrum $\omega = \omega\left(k, E_a^2\right)$ in this medium, where the frequency ω (or energy $\hbar\omega$) of polariton depends on the field density $\sim E_a^2$ of the polariton wave.

1.2.3 Polariton Spectrum in the Nonlinear Medium

The polariton spectrum depends on the density of electromagnetic field $\sim E_a^2$ in the Kerr-type nonlinear medium. In the linear medium at $4\pi\chi_{31}E_a^2 \to 0$ the spectrum of polaritons has only three branches 1, 2, 3 (two low frequency and one high frequency branches, Fig. 1.1a), and this result agrees with the deduction in [16]. In the nonlinear medium, for example at $4\pi\chi_{31}E_a^2 = 10^{-5}$, the polariton spectrum has nine branches (Fig. 1.1b). In this case the spectrum still has the branches 1, 2, 3, but six new branches with the numbers 4, 5, 6 and 7, 8, 9 appear. New branches 4 and 5 coincide with themselves and smoothly go up, but the branch 6 has a weak declination down. The branches 7, 8, 9 have the same behavior: the branch 7 has the weak declination down, and the branches 8, 9 smoothly go up and completely coincide. The appearance of new branches in the polariton spectrum is caused by the dispersion of the third order dielectric susceptibility of the medium $\chi_{31}(\omega)$ at increasing of the electromagnetic field density $\sim E_a^2$ [see (1.4)].

The polariton spectrum in the linear medium has only two gaps, but as the electromagnetic field density increases, the third gap appears: the first gap (between the branch 2 and the branches 4, 5, 6), the second gap (between the branch 2 and the branches 7, 8, 9) and the third gap (between the branch 3 and the branches 7, 8, 9). In the linear medium the dispersion (1.6) has the sixth degree of the frequency ω.

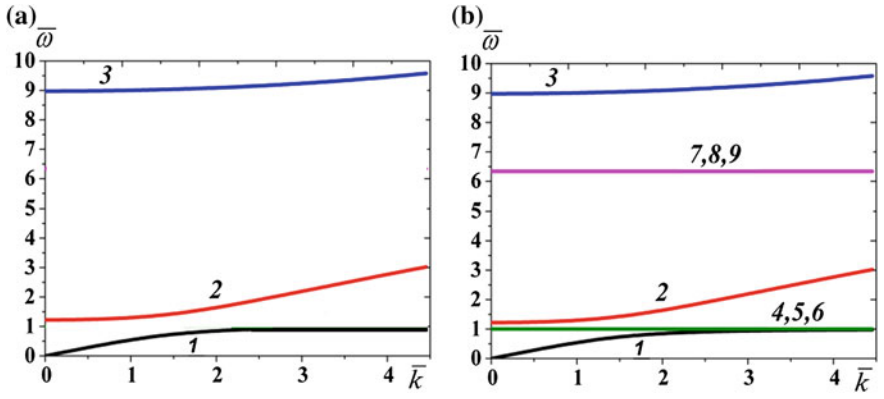

Fig. 1.1 The polariton spectra in the nonlinear medium with the dispersion of the third order susceptibility χ_3: **a** at $4\pi\chi_{31}E_a^2 \to 0$; **b** $4\pi\chi_{31}E_a^2 = 10^{-5}$; $\Gamma = 0$. Here $\bar{\omega} = \omega/\Omega_\perp$ and $\bar{k} = ck/\Omega_\perp$ are dimensionless

In the nonlinear medium the dispersion (1.6) has the eighteenth degree of the frequency because the susceptibility of the third order $\chi_{31}(\omega)$ possesses the dispersion. In other words the more high frequency polaritons of the branches 3 (and 2) decay to three low frequency polaritons of the branches 7, 8, 9 (and 4, 5, 6), therefore the new spectrum branches appear. The spectrum curves have been obtained numerically by solving the dispersion (1.6) at the medium and the wave parameters $\Omega_\perp \sim 10^{13}$ s^{-1}, $k = 3 \times 10^2 \ldots 3 \times 10^3$ cm^{-1}.

Each polariton can decay to a new photon with the same frequency or two phonons with the frequencies amount a sum equal to the initial frequency.

1.2.4 The Longitudinal Instability of Polariton Wave

We can investigate the instability of new spectrum branch waves by the equation obtained from the electromagnetic field (1.3) for transverse electric field in the Kerr-type transparent medium at $\Gamma = 0$,

$$\frac{\partial^2 E}{\partial z^2} - \frac{\varepsilon_1}{c^2}\frac{\partial^2 E}{\partial t^2} - \frac{4\pi\chi_{31}}{c^2}\frac{\partial^2 |E|^2 E}{\partial t^2} = 0, \tag{1.7}$$

where $\varepsilon_1 = 1 + 4\pi\chi_1$. The factor $|E|^2$ depends on the wave amplitude only, and doesn't on the wave phase. Consider the perturbed polariton wave as $E = [E_a + u(t,z)]\exp[-i\omega t + ikz + iw(t,z)]$, where ω and k are the frequency and wave vector of a spectrum branch wave, $u(t,z)$ and $w(t,z)$ are the slowly varying amplitude and phase [40] of the perturbing wave propagating along the axis z. We linearize (1.7), separate the real and the imaginary parts, and taking into account the dispersion (1.6) for unperturbed polariton waves we obtain the set of equations for $u(t,z)$ and $w(t,z)$,

$$\begin{gathered}\left(\frac{\partial^2}{\partial z^2} - \frac{\tilde{\varepsilon}}{c^2}\frac{\partial^2}{\partial t^2} + \frac{\omega^2\tilde{\varepsilon}}{c^2} - k^2\right)u - 2E_a\left(k\frac{\partial}{\partial z} + \frac{\omega\varepsilon}{c^2}\frac{\partial}{\partial t}\right)w = 0, \\ 2\left(k\frac{\partial}{\partial z} + \frac{\omega\tilde{\varepsilon}}{c^2}\frac{\partial}{\partial t}\right)u + E_a\left(\frac{\partial^2}{\partial z^2} - \frac{\varepsilon}{c^2}\frac{\partial^2}{\partial t^2}\right)w = 0,\end{gathered} \tag{1.8}$$

where $\varepsilon = 1 + 4\pi\chi_1 + \bar{I}$, $\tilde{\varepsilon} = 1 + 4\pi\chi_1 + 3\bar{I}$, $\bar{I} = 4\pi\chi_{31}E_a^2$.

One can represent the solutions of the set of (1.8) as $u = u_0\cos(Kz - \Omega t)$, $w = w_0\sin(Kz - \Omega t)$, where Ω and K are the complex frequency and wave vector of the perturbing wave. We obtain the dispersion relation for the frequency Ω and the wave vector K of perturbing waves from the determinant of the equation set (1.8),

$$\Omega^4 - a_1\Omega^2 + a_2\Omega + a_3 = 0, \tag{1.9}$$

where $a_1 = c^2(\tilde{\varepsilon}^{-1} + \varepsilon^{-1})K^2 + 3\omega^2 + c^2\tilde{\varepsilon}^{-1}k^2$, $a_2 = 4c^2k\omega(\tilde{\varepsilon} + \varepsilon)\tilde{\varepsilon}^{-1}\varepsilon^{-1}K$, $a_3 = c^4\tilde{\varepsilon}^{-1}\varepsilon^{-1}K^4 - (3c^4\tilde{\varepsilon}^{-1}\varepsilon^{-1}k^2 + c^2\omega^2\varepsilon^{-1})K^2$.

In general case the solutions $\Omega_{1,2,3,4}$ of (1.9) have the complex values for the perturbing wave frequency. Four values of the frequency Ω_j represent eight perturbing modes $u_{\pm j} = u_0 \exp(\pm i\Omega_j t)/2$, where $j = 1, 2, 3, 4$. The instability of polariton wave with the frequency ω and wave vector k takes place when the solutions Ω_j of (1.9) have the complex values, and the amplitude $u_j \sim \exp[\mathrm{Im}\,(\Omega_j)\,t]$ of the perturbing mode exponentially increases. The convective instability [40] takes place when the imaginary part of perturbing wave frequency greater than zero $i\,\mathrm{Im}\,\Omega > 0$ and the real part of the wave vector greater than zero too $\mathrm{Re}\,K > 0$ at the wave propagation along the axis z.

We may normalize (1.9) for the perturbing wave frequency as $\bar{\Omega}_j = \Omega_j/\Omega_\perp$. The normalized perturbing frequency satisfy the equation $\bar{\Omega}^4 - \bar{a}_1\bar{\Omega}^2 + \bar{a}_2\bar{\Omega} + \bar{a}_3 = 0$, where $\bar{a}_1 = a_1\Omega_\perp^{-2}$, $\bar{a}_2 = a_2\Omega_\perp^{-3}$, $\bar{a}_3 = a_3\Omega_\perp^{-4}$. The analysis of the dependence of perturbing frequency $\bar{\Omega}_j$ on the normalized perturbing wave vector $\bar{K} = cK/\Omega_\perp$ allows predict the instability of polariton wave of a spectrum branch (Fig. 1.1). The dependence of $\bar{\Omega}_j$ on $\bar{K}$ is presented in Fig. 1.2 for the polariton wave of new spectrum branch with the normalized frequency $\bar{\omega} \cong 6.4$ and the wave vector $\bar{k} = 4$, when $\Gamma = 0$, $\bar{I} = 4\pi\chi_{31}E_a^2 = 0.1$.

The polariton waves are stable at the perturbations represented by the roots with the real parts $\mathrm{Re}\,\Omega_1$ and $\mathrm{Re}\,\Omega_3$ (Fig. 1.2a), and with the imaginary parts $\mathrm{Im}\,\Omega_1 = 0$ and $\mathrm{Im}\,\Omega_3 = 0$ (Fig. 1.2b), when $\bar{K}$ increases. The waves are unstable at the small perturbations $\mathrm{Re}\,\Omega_2$ and $\mathrm{Re}\,\Omega_4$ (Fig. 1.2a) with the imaginary parts $\mathrm{Im}\,\Omega_2$ and $\mathrm{Im}\,\Omega_4$ (Fig. 1.2b), when the perturbing waves become shorter. The coefficients $a_{1,2,3}$ in (1.9) depend on the electromagnetic field density $\sim E_a^2$ because of the permittivity.

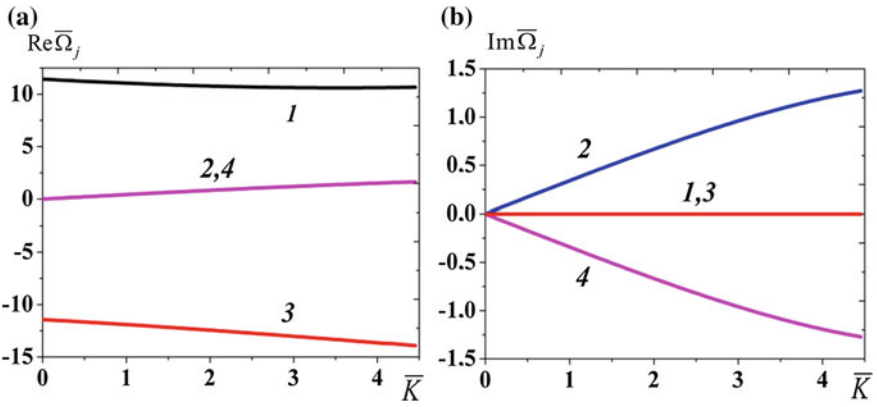

Fig. 1.2 The dependence of the normalized perturbing frequency $\bar{\Omega}_j = \Omega_j/\Omega_\perp$ on the real part of normalized perturbing wave vector $\bar{K} = c\mathrm{Re}\,(K)/\Omega_\perp$

The imaginary parts of the frequency roots Im Ω_j define the longitudinal instability of the polariton wave. The perturbations excite the transverse and longitudinal modulation instability of the nonlinear wave leading to the appearance of the cnoidal waves and solitons [40–42]. We can represent the electric field vector of the polariton wave of a new spectrum branch as $E = e(t,z)\exp(-i\omega t)$, then obtain from (1.7) the equation for slowly varying amplitude $e(t,z)$,

$$\frac{\partial^2 e}{\partial z^2} + \frac{\varepsilon_1 \omega^2}{c^2} e + \frac{4\pi\chi_{31}\omega^2}{c^2}|e|^2 e - \frac{\varepsilon_1}{c^2}\left(\frac{\partial^2 e}{\partial t^2} - i2\omega\frac{\partial e}{\partial t}\right) - \frac{4\pi\chi_{31}}{c^2}\left(e\frac{\partial^2|e|^2}{\partial t^2} + 2\frac{\partial|e|^2}{\partial t}\frac{\partial e}{\partial t} + |e|^2\frac{\partial^2 e}{\partial t^2} - i2\omega\, e\frac{\partial|e|^2}{\partial t} - i2\omega|e|^2\frac{\partial e}{\partial t}\right) = 0. \tag{1.10}$$

We can suppose that $e(t,z)$ is the "adiabatically" varying at time amplitude at stationary process of the polariton wave propagation. In this case we reduce (1.10)

$$\frac{\partial^2 e}{\partial z^2} + \bar{\varepsilon} e + \bar{\chi}|e|^2 e = 0, \tag{1.11}$$

where $\bar{\varepsilon} = c^{-2}\omega^2\varepsilon_1$, $\bar{\chi} = 4\pi c^{-2}\omega^2\chi_{31}$. For the wave of new spectrum branch the boundary conditions at $z = 0$ are zero value of amplitude $e_0 = 0$ and nonzero value of the derivative of amplitude, then the integration constant is $C = (de/dz)_0^2$. We obtain the solution in the form of elliptic cosine

$$e = B\,cn\left\{K(\tilde{k}) - \left[\bar{\chi}\left(\alpha^2/4 + C'\right)^{1/2}\right]^{1/2} z, \tilde{k}\right\}, \tag{1.12}$$

where $K(\tilde{k})$ is the complete elliptic integral, $\tilde{k} = B/(A^2 + B^2)^{1/2}$ is the modulus of elliptic integral, $A^2 = \alpha/2 + (\alpha^2/4 + C')^{1/2}$, $B^2 = -\alpha/2 + (\alpha^2/4 + C')^{1/2}$, $C' = 2C/\bar{\chi}$, $C = (de/dz)_0^2 + \bar{\varepsilon}e_0^2 + \bar{\chi}e_0^4/2$, $\alpha = 2\bar{\varepsilon}/\bar{\chi}$. In case when the modulus tend to unit $\tilde{k} \to 1$ (if $\alpha < 0$ and $C' \to 0$), (1.12) transforms to the hyperbolic secant that describes a longitudinal spatial soliton

$$e = \sqrt{|\alpha|}\, sch\left(\sqrt{\bar{\varepsilon}}z\right). \tag{1.13}$$

1.2.5 The Nonlinear Optical Filter-Converter

The weak intensity waves with the frequency in a spectrum gap don't propagate through the medium. On the contrary the power waves with the frequency of new spectrum branches (Fig. 1.1b) appearing in the spectrum gaps as the nonlinear

periodic cnoidal waves [see (1.12)] or longitudinal spatial solitons [see (1.13)] depending on the sign of the nonlinear susceptibility χ_{31} and the value of the wave perturbation $(de/dz)_0^2$. Thus, the transparency of medium depends on the input wave intensity and the imaginary parts Im Ω_j of perturbation frequency [see (1.9)]. The given effects are similar to the nonlinear self-induced transparency for the power wave or power pulse with the carrier frequency close to the resonance transition of the medium atoms [9], but we examine the non-resonance case. The appearance of new spectrum branch waves can be used for design and creation of the nonlinear filter-converter that transforms the power harmonic wave to the nonlinear cnoidal wave or spatial soliton. This transformation takes place in case when the input harmonic wave has the carrier frequency in the polariton spectrum gap. The values of perturbation parameters Ω and K determine the length of the filter-converter along the axis of the wave propagation. Thus, the matching of the medium and input wave parameters allows creating the concerned nonlinear filter-converter [37].

1.3 Vector Polariton Wave in Nonlinear Dielectric Medium

It is well known that the plane harmonic wave is unstable in nonlinear medium [40, 41]. Instability of the plane wave depends on the field and medium parameters, and it leads to transversal or longitudinal modulation and further transformation of the plane wave to the spatial soliton, or to several polariton fluids due to the polariton wave filamentation [41–45], i.e. to the appearance of nonlinear periodic cnoidal wave at transverse plane. We consider the forming process of the transverse cnoidal wave and spatial soliton from the harmonic plane polariton wave with the frequency ω in the nonlinear infinite dielectric medium with the third order susceptibility [42].

1.3.1 Theoretical Model of Nonlinear Polariton Wave

We consider a medium with local centers of inversion, i.e. the medium with response of the third order susceptibility χ_3. We represent the medium polarization vector (1.4) for harmonic electromagnetic field $E \sim \exp(-i\omega t)$ as

$$\mathbf{P} = \chi_1 \mathbf{E}_a \exp(-i\omega t) + \chi_{31} E_a^2 \mathbf{E}_a \exp(-i\omega t), \tag{1.14}$$

and obtain the equation for vector polariton wave

$$-\nabla^2 \mathbf{E} + \nabla(\nabla \mathbf{E}) + c^{-2}\, \ddot{\mathbf{E}} = -c^{-2} 4\pi\, \ddot{\mathbf{P}}. \tag{1.15}$$

The polaritons are generated as the bound states of transverse electromagnetic field and optical phonons. Assuming that the electric field $\mathbf{E} = \mathbf{1}_x E_x(x,y,z) + \mathbf{1}_y E_y(x,y,z)$ is polarized in plane (x,y) we obtain from (1.15) the following set of nonlinear equations

$$\begin{aligned}
&\frac{\partial^2 E_x}{\partial y^2} + \frac{\partial^2 E_x}{\partial z^2} - \frac{\partial^2 E_y}{\partial x \partial y} + \frac{\omega^2}{c^2}(1 + 4\pi\chi_1)E_x + \frac{4\pi\omega^2\chi_{31}}{c^2}\left(|E_x|^2 + |E_y|^2\right)E_x = 0,\\
&\frac{\partial^2 E_y}{\partial x^2} + \frac{\partial^2 E_y}{\partial z^2} - \frac{\partial^2 E_x}{\partial x \partial y} + \frac{\omega^2}{c^2}(1 + 4\pi\chi_1)E_y + \frac{4\pi\omega^2\chi_{31}}{c^2}\left(|E_x|^2 + |E_y|^2\right)E_y = 0,
\end{aligned} \tag{1.16}$$

where expressions for χ_1 and χ_{31} are given after (1.4). In general case we can't neglect the mixed derivatives in (1.16) due to the permittivity of medium ε depends on coordinates. As it follows from the Maxwell equation $\nabla(\varepsilon\mathbf{E}) = 0$, the gradient of the divergence of the electric field $\nabla(\nabla\mathbf{E}) \neq 0$ doesn't equal zero in (1.15), because $\nabla\mathbf{E} = -\varepsilon^{-1}(\mathbf{E}\nabla\varepsilon) \neq 0$ in this case.

1.3.2 The Equation for Envelopes of Vector Polariton Wave

The carrier harmonic may be described as $E_{x,y} = \tilde{E}_{x,y}(x,y,z)\exp(ikz)$, where $\tilde{E}_{x,y}(x,y,z)$ are the slowly varying amplitudes of two transverse electric field components, k is the wave vector along the axis z. If we neglect the second derivatives on z from the slowly varying amplitudes $\tilde{E}_{x,y}(x,y,z)$, we obtain from the equation set (1.16) the combined equations with mixed derivatives

$$\begin{aligned}
&i2k\frac{\partial \tilde{E}_x}{\partial z} + \frac{\partial^2 \tilde{E}_x}{\partial y^2} - \frac{\partial^2 \tilde{E}_y}{\partial x \partial y} + \alpha_3\left(|\tilde{E}_x|^2 + |\tilde{E}_y|^2\right)\tilde{E}_x = 0,\\
&i2k\frac{\partial \tilde{E}_y}{\partial z} + \frac{\partial^2 \tilde{E}_y}{\partial x^2} - \frac{\partial^2 \tilde{E}_x}{\partial x \partial y} + \alpha_3\left(|\tilde{E}_x|^2 + |\tilde{E}_y|^2\right)\tilde{E}_y = 0,
\end{aligned} \tag{1.17}$$

where $\alpha_3 = 4\pi c^{-2}\omega^2\chi_{31}$; the coefficient $\alpha_3 > 0$ at $\chi_{31} > 0$ in the self-focusing medium, and $\alpha_3 < 0$ at $\chi_{31} < 0$ in the self-defocusing medium. The set of (1.17) looks like the combined nonlinear Schrödinger-type equations describing the nonlinear periodic and solitary polariton waves in nonlinear medium with the third order susceptibility. But the mixed derivatives are absent in the set of Schrödinger equations for wave function. In the special case of the absence of the mixed derivatives of cross members, the equation set (1.17) describes the vector spatial solitons in infinite dielectric nonlinear medium having researched in [41].

In the case when the vector polariton wave does not change the amplitude $\tilde{E}_{x,y}(x,y,z)$ along the axis z, we can define the dependence of field on longitudinal coordinate by the constant phase shift q as $\tilde{E}_j = e_j(x,y)\exp(iqz)$, $j = x,y$. In this

case we obtain from the set (1.17) the equation set for complex transverse envelopes of vector polariton wave

$$\begin{aligned}\frac{\partial^2 e_x}{\partial y^2}-\frac{\partial^2 e_y}{\partial x\partial y}+\alpha_1 e_x+\alpha_3\left(e_x^2+e_y^2\right)e_x=0,\\ \frac{\partial^2 e_y}{\partial x^2}-\frac{\partial^2 e_x}{\partial x\partial y}+\alpha_1 e_y+\alpha_3\left(e_x^2+e_y^2\right)e_y=0,\end{aligned} \tag{1.18}$$

where $\alpha_1=c^{-2}\omega^2(1+4\pi\chi_1)-k^2-2kq$. The equation set (1.18) may be represented as two uncoupled equations by introducing of turning coordinate axes (see Appendix A). But we leave the combined (1.18) in order to analyze two components of polariton wave describing the circular polarization.

1.3.3 Linearly Polarized Polariton Wave

1.3.3.1 Equation for Scalar Polariton Wave

If the polariton wave has the linear polarization, the set of (1.18) can be simplified. The scalar equation of linear wave polarization, for example at the axis x assuming $e_y=0$, is

$$\frac{d^2 e_x}{dy^2}-\bar{\alpha}_1 e_x+\alpha_3 e_x^3=0, \tag{1.19}$$

where the coefficient $\bar{\alpha}_1=2kq+k^2-c^{-2}\omega^2(1+4\pi\chi_1)>0$ is greater than zero because of the term $2kq$. The physical meaning of the parameter $\alpha_1=-\bar{\alpha}_1$ is the dispersion relation of the carrier frequency and wave vector in the medium. Generally the parameter α_1 can be greater, equal or less than zero depending on the value of phase shift q.

The sign "plus" before the nonlinear term $\alpha_3>0$ in (1.19) characterizes the self-focusing medium. The linearly polarized polariton wave looks like the transverse spatial bright soliton (see Appendix B) with polarization along the axis x,

$$\tilde{E}_x(y,z)=\left|\sqrt{\frac{2\bar{\alpha}_{1x}}{\alpha_3}}\right| sch\left(sch^{-1}\left|e(0)\sqrt{\frac{\alpha_3}{2\bar{\alpha}_{1x}}}\right|-\sqrt{|\bar{\alpha}_{1x}|}y\right)\exp(iq_x z),\ \tilde{E}_y=0, \tag{1.20}$$

where $q_x=\left[\alpha_3 e_x^2(0)/2+c^{-2}\omega^2(1+4\pi\chi_1)-k^2\right]/2k$. Besides the spatial solitons, there is the cnoidal wave as the solution of (1.19) in the self-focusing medium. The envelopes of cnoidal polariton waves (see Appendix B) with polarization along the axis x has the form of elliptic cosine

$$\tilde{E}_x(y,z) = \tilde{e}_{0x}\, cn\Big(\left(\alpha_x'^2/4 + C_x'\right)^{1/4} \sqrt{\alpha_3} y - K\left(\tilde{k}_x\right),\ \tilde{k}_x \Big)\, \exp(iq_x z), \tilde{E}_y = 0, \quad (1.21)$$

where $\tilde{e}_{0x} = \left[\alpha_x'/2 + \left(\alpha_x'^2/4 + C_x'\right)^{1/2}\right]^{1/2}$, $\alpha_x' = 2\bar{\alpha}_{1x}|\alpha_3|^{-1}$, $C_x' = 2C_x\alpha_3^{-1}$, $C_x = \alpha_3 e_{x(\infty)}^4/2 - \bar{\alpha}_{1x} e_{x(\infty)}^2$, $q_x = \left[\alpha_3 e_x^2(0)/2 + c^{-2}\omega^2(1 + 4\pi\chi_1) - k^2 - C_x e^{-2}(0)\right]/2k$, $K\left(\tilde{k}_x\right)$ is the complete elliptic integral, $\tilde{k}_x = \left[2 + \alpha_x'\left(\alpha_x'^2/4 + C_x'\right)^{-1/2}\right]^{1/2}/2$ is the modulus of elliptic integral. The polariton wave decomposes at the several flows in the line of axis x, which are propagated along the axis z (Fig. 1.3).

The cnoidal wave, that described by (1.21) may be transformed to the spatial soliton $cn(y, 1) \to 1/\cosh(y)$ at $\tilde{k}_j \to 1$, when the polariton wave envelope is rapidly damped function $e_\infty \to 0$, i.e. $C_x \to 0$ at $y \to \infty$.

In the self-defocusing medium at the sign "minus" before the nonlinear term ($\alpha_3 < 0$) we obtain the solutions of (1.19) in the form of elliptic sine divided by elliptic cosine

$$\tilde{E}_x(y,z) = \tilde{\tilde{e}}_{0x} \frac{sn\left\{\left[\alpha_x'/2 + \left(\alpha_x'^2/4 + C_x'\right)^{1/2}\right]^{1/2} \sqrt{|\alpha_3|/2}\, y,\ \tilde{\tilde{k}}_x\right\}}{cn\left\{\left[\alpha_x'/2 + \left(\alpha_x'^2/4 + C_x'\right)^{1/2}\right]^{1/2} \sqrt{|\alpha_3|/2}\, y,\ \tilde{\tilde{k}}_x\right\}} \exp(iq_x z),\ \tilde{E}_y = 0, \quad (1.22)$$

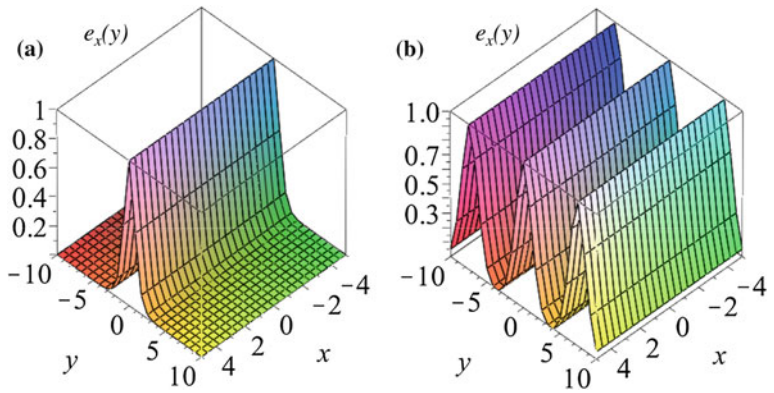

Fig. 1.3 The polariton wave with the envelope $e_x(y)$: **a** one flat flow, **b** several flat flows; (dimensionless units)

where $\tilde{\tilde{e}}_{0x} = \left[\alpha'_x/2 - \left(\alpha'^2_x/4 + C'_x\right)^{1/2}\right]^{1/2}$, $\tilde{\tilde{k}}_x = \left[2\left(\alpha'^2_x/4 + C'_x\right)^{1/2}\right]^{1/2}\left[\alpha'_x/2 + \left(\alpha'^2_x/4 + C'_x\right)^{1/2}\right]^{-1/2}$. The constant C'_x determines the type of polariton wave. The plane polariton wave splits to the narrow flows in the line of axis x, because the function in (1.22) tends to infinity $\tilde{E}(y) \to \infty$, when $cn\{y\} \to 0$. The wave becomes instable close to the points, where $cn\{y\} \to 0$. The envelope represented by (1.22) transforms to the hyperbolic sine $sn(y,1)/cn(y,1) \to \sinh(y)$ at $\tilde{\tilde{k}}_x \to 1$, when $C'_x \to 0$, and gets zero value $\tilde{E}(y) = 0$ at $y = 0$.

1.3.3.2 Stability of the Scalar Polariton Wave

The transverse instability of the linearly polarized polariton wave can be examined by small perturbation of envelope $\tilde{E}_x = [e(y) + u(y,z)]\exp[iqz + iw(y,z)]$, where u and w are the small perturbations. We obtain from (1.19) the linearized set of equations by separated the real and imaginary parts

$$\begin{aligned}\left(\frac{\partial^2}{\partial y^2} + \alpha\prime\right)u - \left(e''\frac{\partial^2}{\partial y^2} + 2\frac{\partial e''}{\partial y}\frac{\partial}{\partial y}\right)w = 2ke'\frac{\partial w}{\partial z},\\ \left(e'\frac{\partial^2}{\partial y^2} + 2\frac{\partial e'}{\partial y}\frac{\partial}{\partial y}\right)w = 2ke''\frac{\partial w}{\partial z} - \left(2k\frac{\partial}{\partial z} + \alpha''\right)u,\end{aligned} \tag{1.23}$$

where $\alpha = \alpha' + i\alpha'' = 3\alpha_3 e^2 - \bar{\alpha}_1$, the envelope $e = e' + ie''$ represented by (1.20), (1.21) or (1.22).

Consider the simple case. The field density e^2 of spatial soliton or cnoidal wave close to the longitudinal axis z at $y \to 0$ is the constant $e(0)^2$ and $e'' \to 0$, then the set of (1.23) looks like

$$\left(\frac{\partial^2}{\partial y^2} + \alpha'\right)u = 2ke'\frac{\partial w}{\partial z}, \quad \left(e'\frac{\partial^2}{\partial y^2}\right)w = -\left(2k\frac{\partial}{\partial z} + \alpha''\right)u. \tag{1.24}$$

We can represent the transverse perturbations as $u = u_0\exp(ik_\perp y + \kappa z)$ and $w = w_0\exp(ik_\perp y + \kappa z)$. In this case from the equation set (24) we obtain the equation for κ,

$$\kappa^2 + (\alpha''/2k)\kappa + k_\perp^2\left(k_\perp^2 - \alpha'\right)/4k^2 = 0. \tag{1.25}$$

One can obtain from (1.25) the expression $\kappa = -\left[\alpha''/2 \pm \left(\alpha''^2/4 + \alpha' k_\perp^2 - k_\perp^4\right)^{1/2}\right]/2k$ for decrement $-\kappa$ or increment $+\kappa$ of the polariton wave. The value κ depends on the wave vector $k_\perp$ of transverse perturbation, field density $e^2(0)$, and medium parameters. The polariton wave damps at the negative value $-\kappa$, and the wave is unstable at the positive value $+\kappa$ describing the wave instability along the

axis z due to the transverse perturbation; the phase modulation appears at $k_\perp^4 > \alpha' k_\perp^2 + \alpha''^2/4$.

The wave envelope $e \sim \exp\left\{-\left[\alpha''/2 \pm \left(\alpha''^2/4 + \alpha' k_\perp^2 - k_\perp^4\right)^{1/2}\right] L/2k\right\}$ is proportional to the coefficients $\bar{\alpha}_1$, α_3 and the wave density $e^2(0)$, that's why the "life length" L of nonlinear polaritons is determined by the relation of real and imaginary parts of α. The life length of nonlinear polariton wave is defined by the inverse value $L = 1/\kappa'$ of the real part of decrement. The stability of polariton wave can be achieved by the matching of the input wave and medium parameters.

1.3.4 Circularly Polarized Polariton Wave

The equation set (1.18) in Cartesian coordinates we can transform to the set of equations for the polariton waves of circular polarization.

1.3.4.1 Equations for Vector Polariton Wave

We introduce the vector envelope for wave with the right spirality $\mathbf{e}_+ = \mathbf{e}_x + i\mathbf{e}_y = e\left(\mathbf{1}_x + i\mathbf{1}_y\right)/\sqrt{2} = e\mathbf{1}_+$ (counterclockwise circular polarization), and with the left spirality $\mathbf{e}_- = \mathbf{e}_x - i\mathbf{e}_y = e\left(\mathbf{1}_x - i\mathbf{1}_y\right)/\sqrt{2} = e\mathbf{1}_-$ (clockwise circular polarization); also two dimensional rotating coordinates $\bar{\xi} = x + iy$, and $\bar{\eta} = x - iy$. Than we compound the equations obtained from the set (1.18) and get the set of complex equations for envelopes of polariton waves with right $\mathbf{e}_+$ and left $\mathbf{e}_-$ spiralities in the rotating coordinates $\left(\bar{\xi}, \bar{\eta}\right)$,

$$\begin{aligned}
&\frac{\partial^2 \mathbf{e}_+}{\partial \bar{\xi}^2} + \frac{\partial^2 \mathbf{e}_+}{\partial \bar{\eta}^2} + i\frac{\partial^2 \mathbf{e}_-}{\partial \bar{\xi}^2} - i\frac{\partial^2 \mathbf{e}_-}{\partial \bar{\eta}^2} - 2\frac{\partial^2 \mathbf{e}_-}{\partial \bar{\xi}\partial \bar{\eta}} - \left(\alpha_1 + \alpha_3 e^2\right)\mathbf{e}_- = 0, \\
&\frac{\partial^2 \mathbf{e}_-}{\partial \bar{\xi}^2} + \frac{\partial^2 \mathbf{e}_-}{\partial \bar{\eta}^2} + i\frac{\partial^2 \mathbf{e}_+}{\partial \bar{\xi}^2} - i\frac{\partial^2 \mathbf{e}_+}{\partial \bar{\eta}^2} - 2\frac{\partial^2 \mathbf{e}_+}{\partial \bar{\xi}\partial \bar{\eta}} - \left(\alpha_1 + \alpha_3 e^2\right)\mathbf{e}_+ = 0.
\end{aligned} \tag{1.26}$$

The set of (1.26) describes the bound nonlinear polariton waves with right $\mathbf{e}_+$ and left $\mathbf{e}_-$ spiralities. One can restore the Cartesian coordinates (x, y) after obtaining the solutions of equation set (1.26) in the rotating coordinates $\left(\bar{\xi}, \bar{\eta}\right)$.

We put the determinant $Det\,(\mathbf{e}_+,\ \mathbf{e}_-)$ of the vector equation set (1.26) equal to zero, and obtain the equation for envelope $e\left(\bar{\xi}, \bar{\eta}\right)$ of polariton wave,

$$(1-i)\frac{\partial^2 e}{\partial \bar{\xi}^2} + (1+i)\frac{\partial^2 e}{\partial \bar{\eta}^2} + 2\frac{\partial^2 e}{\partial \bar{\xi}\partial \bar{\eta}} + \left(\alpha_1 + \alpha_3 e^2\right) e = 0. \tag{1.27}$$

Equation (1.27) in the rotating coordinates $\left(\bar{\xi},\bar{\eta}\right)$ describes the polariton flow composed of the polaritons with both the right and left spiralities. From (1.27) we can obtain the equation for envelope of the "scalar" polariton flow, for example with the right spirality $e_+ = e\left(\bar{\xi}\right)$, depending only on the right spirality coordinate $\bar{\xi}$,

$$\frac{d^2 e_+}{d\bar{\xi}^2} + \alpha_1^{(+)} e_+ + \alpha_3^{(+)} e_+^3 = 0, \tag{1.28}$$

where $\alpha_1^{(+)} = (1+i)\,\alpha_1/2$, $\alpha_3^{(+)} = (1+i)\,\alpha_3/2$. We obtain the solution of (1.28) for the right spirality polaritons in the self-focusing medium at $\alpha_1 = -\bar{\alpha}_1$, $\alpha_3 > 0$ similar to the solutions of (1.19) in the form of (1.20) or (1.21), and in the self-defocusing medium at $\alpha_1 = -\bar{\alpha}_1$, $\alpha_3 < 0$ such as (1.22) for the boundary conditions $e_\infty = const$, $de/d\bar{\xi} = 0$ at $\left|\bar{\xi}\right| \to \infty$ or $|\bar{\eta}| \to \infty$. The elliptic sine and cosine are the functions of the complex argument with double period [46]. The envelopes of the scalar polariton wave with the right or left spirality decompose to the square grid of polariton flows in the transverse plane (x, y) (Fig. 1.4).

In general case we obtain the solution of normalized by $\sqrt{|\alpha_1|}$ (1.27) for the "vector" polariton wave $e\left(\bar{\xi},\bar{\eta}\right)$ depending on the right and left spirality coordinates. We obtain the solution at $\alpha_1 > 0$, $\alpha_3 > 0$,

$$e\left(\bar{\bar{\xi}},\bar{\bar{\eta}}\right) = i\sqrt{\frac{|\alpha_1|}{|\alpha_3|}}\tanh\left\{C_1 + C_2\,\bar{\bar{\xi}} + \frac{i}{2}\left[C_2(i+1) - \left(i - 1 - i2C_2^2\right)^{1/2}\right]\bar{\bar{\eta}}\right\}, \tag{1.29}$$

where $\bar{\bar{\xi}} = \sqrt{|\alpha_1|}\bar{\xi}$, $\bar{\bar{\eta}} = \sqrt{|\alpha_1|}\bar{\eta}$. The constants C_1 and C_2 are determined by the boundary conditions at $\bar{\xi} = 0$ and $\bar{\eta} = 0$ for the polariton wave. For example, if the

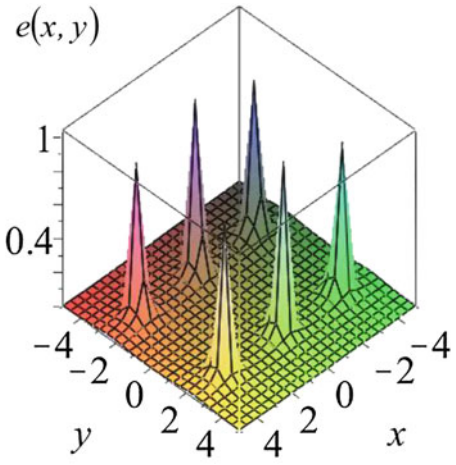

Fig. 1.4 The square grid of polariton flows at the scalar polariton wave with the envelope $\mathrm{Re}\,e\left(\bar{\xi}\right)$, where $\bar{\xi} = x + iy$; (dimensionless units)

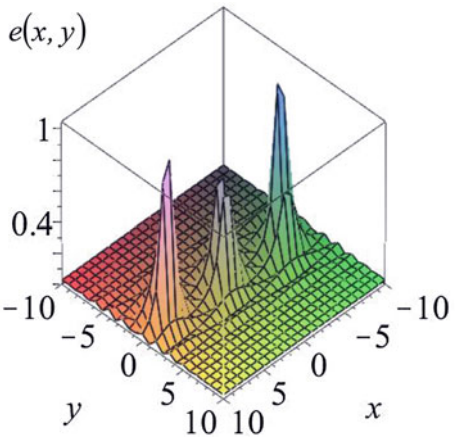

Fig. 1.5 The row of polariton flows at the vector polariton wave with the envelope $\mathrm{Re}\, e\left(\bar{\bar{\xi}}, \bar{\bar{\eta}}\right)$, where $\bar{\bar{\xi}} = \sqrt{|\alpha_1|}(x + iy)$, $\bar{\bar{\eta}} = \sqrt{|\alpha_1|}(x - iy)$; (dimensionless units)

value of envelope at longitudinal axis z is $e(0,0) = \mathrm{Re}\left[i\sqrt{|\alpha_1|/|\alpha_3|}\tanh(C_1)\right] = 0$, it allows to determine the constant as $C_1 = 0$, and $C_2 = 1$. We obtain from (1.29)

$$e\left(\bar{\bar{\xi}}, \bar{\bar{\eta}}\right) = i\sqrt{\frac{|\alpha_1|}{|\alpha_3|}}\tanh\left\{ \bar{\bar{\xi}} + \frac{1}{2}\left[i - 1 + \sqrt{i+1}\right] \bar{\bar{\eta}} \right\}. \tag{1.30}$$

Equation (1.27) has the solutions at $\alpha_1 = -\bar{\alpha}_1$, $\alpha_3 > 0$ in self-focusing medium as

$$e\left(\bar{\bar{\xi}}, \bar{\bar{\eta}}\right) = \sqrt{\frac{\bar{\alpha}_1}{|\alpha_3|}}\tanh\left\{ \bar{\bar{\xi}} + \frac{1}{2}\left[i - 1 - i\sqrt{1 - 3i}\right] \bar{\bar{\eta}} \right\}, \tag{1.31}$$

and at $\alpha_1 = -\bar{\alpha}_1$, $\alpha_3 < 0$ in self-defocusing medium as

$$e\left(\bar{\bar{\xi}}, \bar{\bar{\eta}}\right) = i\sqrt{\frac{\bar{\alpha}_1}{|\alpha_3|}}\tanh\left\{ \bar{\bar{\xi}} + \frac{1}{2}\left[i - 1 - i\sqrt{1 - 3i}\right] \bar{\bar{\eta}} \right\}. \tag{1.32}$$

The envelopes described by (1.30)–(1.32) have the form of row of polariton flows in the transverse plane (Fig. 1.5).

1.4 Conclusion

We have shown theoretically that the dispersion of the third order susceptibility leads to the appearance of new branches in the polariton spectrum in nonlinear dielectric medium. The new branches appear in the polariton spectrum gap, when the electromagnetic field density increases. In other words one high frequency

polariton decays to three low frequency polaritons under the influence of the third order susceptibility of the dielectric medium. The polariton waves of new spectrum branches damp more rapidly, because they depend on the nonlinear medium properties and the wave intensity. The instability of polariton wave depends on the field density. The perturbations excite the longitudinal modulation wave instability leading to the appearance of cnoidal waves and solitons. We've examined the generation of the polariton continuous waves in the spectrum gap of the nonlinear medium and their perturbations at the propagation in the non-resonance case.

The model of nonlinear polariton waves allows predicting the new effects of nonlinear wave and their applications in bulk dielectric media. The plane polariton wave is unstable in nonlinear medium, its transverse envelope can transform to the cnoidal wave or spatial soliton in the self-focusing medium. The forms of transverse envelopes of linearly polarized polariton waves may be represented by the hyperbolic secant (the soliton) or elliptic cosine (the cnoidal wave) in the self-focusing medium. In the first case the polaritons propagate as the single flow, in the second case the polariton wave decomposes into the several flat flows. In the self-defocusing medium the plane polariton wave splits to the narrow flows in transverse plane. We obtain the analytical cnoidal and soliton solutions for transverse envelope in the forms of square grid for the nonlinear scalar waves consisting of polaritons with the right or the left spirality only. We also obtain the analytical solution for transverse envelope of the nonlinear vector polariton wave consisting of polaritons with both the right and left spiralities in the form of row of the polariton flows. The stability of the polariton wave can be achieved by the matching of input wave and medium parameters.

Thus, the form of transverse envelope of polariton wave depends on the wave intensity and parameters of medium, and it can be modified by changing the intensity of input wave or the medium parameters at the wave propagation. These properties of the polariton wave in nonlinear dielectric medium may be used for designing new optical devices such as the optical converter, controllable filter, all-optical logic gates, etc.

Acknowledgements The author is grateful to Anton S. Desyatnikov for fruitful discussions of the work, and Tatiana Nurieva for the help of paper preparing, and Olga Karakchieva for the help of plotting.

Appendix A

The set of (1.18) can be simplified for linearly polarized wave by turning of the coordinate axes at the angle $\pi/4$,

$$-\frac{\partial}{\partial y}\left(\frac{\partial e}{\partial x}-\frac{\partial e}{\partial y}\right)+\left(\alpha_1+\alpha_3|e|^2\right)e=0,\quad \frac{\partial}{\partial x}\left(\frac{\partial e}{\partial x}-\frac{\partial e}{\partial y}\right)+\left(\alpha_1+\alpha_3|e|^2\right)e=0,$$

where $e = \sqrt{2}e_x = \sqrt{2}e_y$. Introducing the "light-cone" coordinates $\xi = (x + y)/2$ and $\eta = (x - y)/2$ we obtain two uncoupled scalar equations

$$\frac{\partial^2 e}{\partial \eta^2} + 2\left(\alpha_1 + \alpha_3 |e|^2\right) e = 0, \qquad \frac{\partial^2 e}{\partial \xi \eta} = 0.$$

The first equation of equations has the cnoidal or soliton solutions $e(\eta)$, the second equation has the solution $e(\eta) = e(x, y)$ describing a one-dimensional wave varying in a single direction η.

Appendix B

The first integral of the equation $d^2e/dx^2 - \bar{\alpha}_1 e + \alpha_3 e^3 = 0$ looks like $(de/dx)^2 = \bar{\alpha}_1 e^2 - \alpha_3 e^4/2 + C$, where C is an integration constant.

The boundary conditions for soliton $e \to 0$, $de/dx \to 0$ at $|x| \to \infty$ allow to define the integration constant as $C = 0$ [41]. The boundary conditions $e(0) = const$ and $de(0)/dx = 0$ for soliton centre $x = 0$ allow to define the phase shift as $q = [\alpha_3 e^2(0)/2 + c^{-2}\omega^2(1 + 4\pi\chi_1) - k^2]/2k$ in case without perturbation. The second integral of the equations for bright soliton looks like $\sqrt{\alpha_3/2}x = \int e^{-1}(\alpha' - e^2)^{-1/2} de$, where $\alpha' = 2\bar{\alpha}_1 \alpha_3^{-1}$, and after its integration we obtain $e(x) = \left|\sqrt{\alpha'}\right| sch\left(sch^{-1}\left|e(0)/\sqrt{\alpha'}\right| - \sqrt{\bar{\alpha}_1}x\right)$.

If we choose the boundary conditions as $e = const$, $de/dx = 0$ at $|x| \to \infty$, i.e. the integration constant is not equal zero $C = \alpha_3 e_\infty^4/2 - \bar{\alpha}_1 e_\infty^2$, we obtain the cnoidal wave. In this case the phase shift at the boundary conditions $e(0) = const$ and $de(0)/dx = 0$ is equal $q = [\alpha_3 e^2(0)/2 + c^{-2}\omega^2(1 + 4\pi\chi_1) - k^2 - Ce^{-2}(0)]/2k$. Then the second integral of the equations for cnoidal wave looks like $\sqrt{\alpha_3/2}x = \int_0^e (C' + \alpha' e^2 - e^4)^{-1/2} de$, where $C' = 2C\alpha_3^{-1}$.

References

1. K.B. Tolpygo, Physical properties of the salt lattice constructed from deforming ions. J. Exp. Theor. Phys. (USSR) **20**(6), 497–509 (1950). (in Russian)
2. Huang K., On the interaction between the radiation field and ionic crystals. Proc. Roy. Soc. A, **208**, 352–365 (1951)
3. S.I. Pekar, Theory of electromagnetic wave in crystal, in which exitons appear. J. Exp. Theor. Phys. (USSR) **33**(4), 1022–1036 (1957). (in Russian)
4. J.J. Hopfield, Theory of the contribution of excitons to the complex dielectric constant of crystals. Phys. Rev. **112**(5), 1555–1567 (1958)
5. V.M. Agranovich, V.L. Ginzburg, Crystal optics with allowance for spatial dispersion and exciton theory. Sov. Phys. Uspekhi **5**, 323–346 (1962)

6. V.M. Agranovich, V.L. Ginzburg, *Crystal Optics with Spatial Dispersion and Excitons* (Springer, Berlin, 1984)
7. C. Kittel, *Quantum Theory of Solids* (Wiley, New York, 1963)
8. N. Bloembergen, *Nonlinear Optics* (Benjamin, New York, 1965)
9. R.H. Pantell, H.E. Puthoff, *Fundamentals of Quantum Electronics* (Wiley, New York, 1969)
10. V.V. Obukhovsky, V.L. Strizhevsky, Raman scattering of light by polaritons. Ukr. Phys. J. **14** (9), 1463–1469 (1969). (in Russian)
11. A.S. Davydov, *Solid State Physics* (Nauka, Moscow, 1976). (in Russian)
12. S.B. Borisov, I.L. Lyubchanskii, V.L. Sobolev, Polaritons in magnetoelectric crystals. Phys. Sol. (USSR) **31**(5), 58–63 (1989)
13. M.I. Kaganov, N.B. Pustyl'nik, T. I. Shalaeva, Magnons, Magnetic polaritons, and magnetostatic waves, *Uspekhi Fizicheskikh Nauk*, **167**(2), 191–237 (1997). (in Russian)
14. V.M. Agranovich, D.L. Mills (eds.), *Surface Polaritons* (North-Holland, Amsterdam, 1982)
15. A.D. Boardman (ed.), *Electromagnetic Surface Modes* (Wiley, New York, 1982)
16. D.N. Klyshko, *Quantum and Nonlinear Optics* (Nauka, Moscow, 1980). (in Russian)
17. Y.R. Shen, *The Principles of Nonlinear Optics* (Wiley, New York, 1984)
18. A.P. Sukhorukov, *Nonlinear Wave Interaction in Optics and Radiophysics* (Nauka, Moscow, 1988). (in Russian)
19. S.A. Darmanyan, A.M. Kamchatnov, M. Neviere, Polariton Effect in Nonlinear Pulse Propagation. J. Exp. Theor. Phys. **96**(5), 876–884 (2003)
20. I.V. Dzedolik, *Polaritons in Optical Fibers and Dielectric Resonators* (Simferopol, DIP, 2007). (in Russian)
21. E.L. Albuquerque, M.G. Cottam, *Polaritons in Periodic and Quasiperiodic Structures* (Elsevier, Amsterdam, 2004)
22. V.K. Miloslavsky, Nonlinear Optics, (Kharkov, V.N. Karazin Kharkov Nat. Univ., 2008). (in Russian)
23. I.V. Dzedolik, One-dimensional controllable photonic crystal. J. Opt. Soc. Am. B **24**(10), 2741–2745 (2007)
24. I.V. Dzedolik, S.N. Lapayeva, A.F. Rubass, All-optical logic gates based on nonlinear dielectric film. Ukr. J. Phys. Opt. **9**(3), 187–196 (2007)
25. G. Campbell, M. Hosseini, B.M. Sparkes, P.K. Lam, B.C. Buchler, Time- and frequency-domain polariton interference. New J. Phys. **14**, 033022 (2012)
26. I.V. Dzedolik, O. Karakchieva, Control of polariton spectrum in bigyrotropic medium. Appl. Opt. **52**(25), 6112–6118 (2013)
27. H. Inoue, K. Katayma, Q. Shen, T. Toyoda, K. Nelson, Terahertz reflection response measurement using a phonon polariton wave. J. Appl. Phys. **105**, 054902 (2009)
28. Z. Qi, Z.-Q. Shen, C.-P. Huang, S.-N. Zhu, Y.-Y. Zhu, Phonon polaritons in a nonaxial aligned piezoelectric superlattice. J. Appl. Phys. **105**, 074102 (2009)
29. I.V. Dzedolik, Period variation of polariton waves in optical fiber. J. Opt. A: Pure Appl. Opt. **11**, 094012 (2009)
30. M. Richard, J. Kasprzak, A. Baas, K. Lagoudakis, M. Wouters, I. Carusotto, R. Andre, B. Deveaud-Pledran, Dang L-S (2010) Exciton-polariton Bose-Einstein condensation: advances and issues. Int. J. Nanotechnology **7**((4/5/6/7/8)), 668–685 (2010)
31. E.A. Ostrovskaya, J. Abdullaev, A.S. Desyatnikov, M.D. Fraser, YuS Kivshar, Dissipative solitons and vortices in polariton Bose-Einstein condensates. Phys. Rev. A **86**, 013636 (2012)
32. I.V. Shadrivov, A.A. Sukhorukov, YuS Kivshar, A.A. Zharov, A.D. Boardman, P. Egan, Nonlinear surface waves in left-handed materials. Phys. Rev. E **69**, 016617 (2004)
33. K.L. Tsakmakidis, A.D. Boardman, O. Hess, Trapped rainbow storage of light in metamaterials. Nature **450**(15), 06285 (2007). (397–401)
34. J.M. Pitarke, V.M. Silkin, E.V. Chulkov, P.M. Echenique, Theory of surface plasmons and surface-plasmon polaritons. Rep. Prog. Phys. **70**, 1–87 (2007)
35. H. Fan, R. Buckley, P. Berini, Passive long-range surface plasmon-polariton devices in Cytop. Appl. Opt. **51**(10), 1459–1467 (2012)

36. M.S. Vasconcelos, E.L. Albuquerque, U.L. Fulco, C.A.A. Araujo, Phonon polaritons in metamaterial photonic crystals at terahertz frequency range. Proc. SPIE **8423**, 84232H (2012)
37. I.V. Dzedolik, O. Karakchieva, Polariton spectrum in nonlinear dielectric medium. Appl. Opt. **52**(13), 3073–3078 (2013)
38. S. Santran, L. Cathoni, T. Cardinal, E. Farginc, G. Le Flem, C. Rouyera, L. Sarger, Precise and absolute measurements of the complex third-order optical susceptibility. Proc. SPIE **4106**, 349 (2000)
39. M. Sheik-Bahae, A.A. Said, T.H. Wei, D.J. Hagan, E.W. Van Stryland, Special 30th anniversary feature: sensitive measurement of optical nonlinearities using a single beam. IEEE LEOS Newsletter **21**, 17–26 (2007)
40. A. Scott, *Active and nonlinear wave propagation in electronics* (Wiley, New York, 1970)
41. YuS Kivshar, G.P. Agrawal, *Optical Solitons: from Fibers to Photonic Crystals* (Academic Press, San Diego, 2003)
42. I.V. Dzedolik, O. Karakchieva, Nonlinear vector and scalar polariton waves in dielectric medium. J. Opt. Soc. Am. B **30**(4), 843–850 (2013)
43. V.I. Bespalov, V.I. Talanov, Filamentary structure of light beams in nonlinear liquids. J. Exp. Theor. Phys. Let. (USSR) **3**(11), 471–476 (1966)
44. A. Sukhinin, A.B. Aceves, Optical UV filament and vortex dynamics. J. Opt. **15**(4), 044010 (2013)
45. S.V. Chekalin, V.P. Kandidov, From self-focusing light beams to femtosecond laser pulse filamentation. Phys. Uspekhi **56**(2), 133–152 (2013)
46. G.A. Korn, T.M. Korn, *Mathematical Handbook* (McGraw-Hill Book Company, New York, 1968)

Chapter 2
Organic Nanomaterials with Two-Photon Absorption Properties for Biomedical Applications

Laura Aparicio-Ixta, Mario Rodriguez and Gabriel Ramos-Ortiz

Abstract During recent years there have been notorious advances in the development of organic molecules and π-conjugated polymers with two-photon activity, i.e., emission of fluorescence promoted by the molecular absorption of two photons. Novel organic materials have reached very large two-photon activity, and many of them have been processed successfully into nanostructured platforms. In contrast to their inorganic counterpart, organic nanoparticles with photonic properties is a topic that so far has not been well explored, although deserves big potential in biomedical applications. This chapter presents recent advances in this field, particularly, in the use of organic nanoparticles as contrast agents to obtain bioimages.

2.1 Introduction

In the last two decades organic molecules have emerged as interesting active materials for diverse applications. When these molecules comprise π-conjugated systems their optical and electric properties can be enhanced. One of the most useful optical properties exhibited by these molecules is the two-photon absorption (TPA) process.

The number of organic compounds that exhibit TPA have increased rapidly in recent years, with a variety of photonic and biological applications such as two-photon laser scanning microscopy [1], frequency upconversion lasing [2, 3], optical power limiting [4], 3-D microfabrication [5], high density optical storage [6], sensors [7] and photodynamic therapy [8, 9]. Among these applications, two-photon laser scanning microscopy, or simply two-photon microscopy (TPM) has gained great acceptance in biomedical community as a tool able to provide direct observation of cells or subcellular structures, tissue and biological processes. This technique is based in the use of molecules that exhibit strong luminescence induced by

L. Aparicio-Ixta · M. Rodriguez · G. Ramos-Ortiz (✉)
Centro de Investigaciones en Óptica A.C., A.P. 1-948, 37000 León, Guanajuato, Mexico
e-mail: garamoso@cio.mx

O. Shulika and I. Sukhoivanov (eds.), *Contemporary Optoelectronics*,
Springer Series in Optical Sciences 199, DOI 10.1007/978-94-017-7315-7_2

TPA and offers several advantages such as high resolution, high penetration depth in tissue, weak photobleaching and weak autofluorescence, minimal phototoxicity and excitation confinement exclusively to the focal plane.

This chapter will cover recent advances in organic materials with TPA and fluorescent properties and how they can be processed into different platforms, i.e., nanostructures, in order to confer them utility in biomedical applications. Figure 2.1 presents schematically the approach followed in this field, which consists in the development of novel organic molecular systems, the subsequent characterization of their nonlinear optical properties, and the methodologies to process them and confer them enough biocompatibility to be inserted on biological media. This chapter presents information on organic nanoparticles with luminescent and nonlinear absorption properties intended to obtain bio-images by using TPM. This type of microscopy technique was reported nearly twenty five year ago and it utilizes the localized luminescence induced by nonlinear absorption [1]. So far, TPM utilizes commercially available contrast agents or markers, but these are dyes with rather weak TPA activity. This open the opportunity to develop novel contrast agents or markers based nanostructured organic materials, with enhanced optical characteristics and multifunctionality.

It should be noted that organic nanoparticles is a topic which has not been explored so extensively as their inorganic counterpart (metallic, semiconductor and metallic oxide nanoparticles). The good luminescent and nonlinear properties, combined with low cost, less toxicity that inorganics and relatively easy synthesis, makes that of organic nanoparticles deserve enormous potential in biomedical applications such as TPM. To further exemplify the use of TPA activity in organics, this chapter will also cover partially photodynamic therapy (PDT) which is utilized for the treatment of cancer.

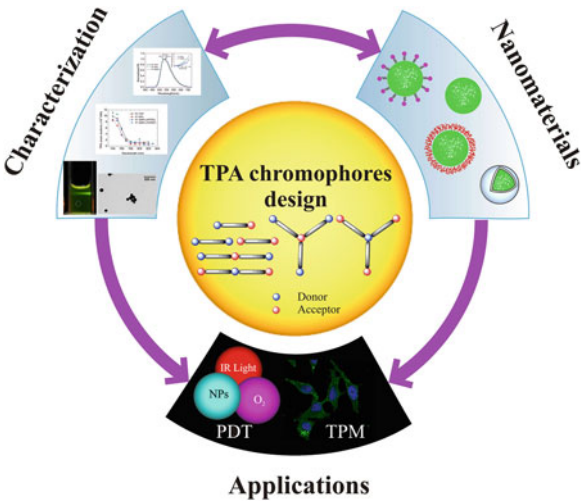

Fig. 2.1 Scheme followed in the development of organic nanomaterial with TPA properties and their application in two-photon microscopy (TPM) and two-photon photodynamic therapy (PDT)

2.2 Two-Photon Absorption Process

The molecular TPA property is defined as the electronic excitation that is induced by a simultaneous absorption of a pair of photons with the same or different energy (Fig. 2.2). This phenomenon was first predicted in 1931 by Göppert-Mayer [10] who calculated the transition probability for the absorption of two quantums of energy. In this process a photon first interacts with the molecule and promotes a transition from ground state to a temporary virtual state of higher energy. This is not a real state of the molecule and it exists only for a short time interval ($\sim 10^{-15}$–10^{-16} s for photon energies in the visible and near-IR ranges) [11]. If during this interval of time other photon interacts with the molecule, the excited state can be achieved. The adjective "simultaneous" for TPA is used to indicate that the two photons interact with the molecule within the interval of time above mentioned and that no real states act as intermediate states in this process.

The TPA is a third-order non-linear optical process whose magnitude is proportional to the square of the light intensity. The magnitude of TPA can be quantified by introducing the parameter called TPA *cross section* (σ_{TPA}). This parameter is usually expressed in Goppert-Mayer units: 1 GM = 10^{-50} cm^4 s/photon. Several techniques have been used to measure the two-photon excitation cross sections of various materials for more than two decades. The two main techniques for measuring σ_{TPA} are Z-scan [12–14] and two-photon excited fluorescence (TPEF) [15], although exist others methods as thermal lensing [16, 17] and photoacoustic measurements [18].

Z-scan is a direct method to determine the non-linear absorption in bulk materials [12–14]; this technique consists in monitoring the transmittance of the sample under test as a function of the incident intensity of a laser beam. In the practice this can be achieved by varying the position Z of the sample in the vicinity of a focused Gaussian beam, hence the term "Z-scan". See Fig. 2.3. The Z-scan curve obtained is

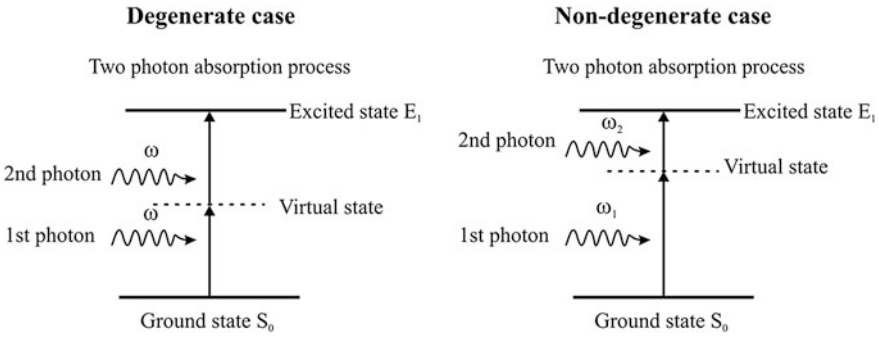

Fig. 2.2 Schematic energy level diagram showing the excitation process of a molecule from the ground state, S_0, to an excited state, E_1. The photons can have the same energy (*degenerate case*), or different energies (*non-degenerate case*)

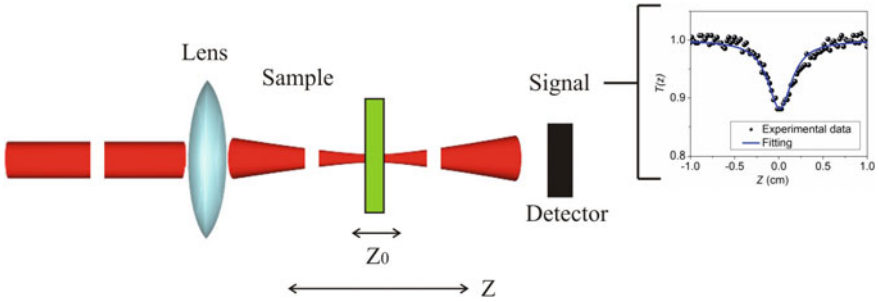

Fig. 2.3 Z-scan technique. The energy of a train of pulses is kept constant, but changes in intensity are achieved by moving the sample along the direction Z. The transmittance is measures at each z position of the sample

symmetrical with respect to the focus (z = 0), with a minimum in the transmittance (multiphoton absorption). The normalized transmittance is given by:

$$T(z) = 1 - \frac{1}{2^{3/2}}\sigma_{TPA}\frac{CN_A}{\hbar\omega}\frac{I_0 L_{eff}}{1+\left(\frac{z}{z_0}\right)^2},$$

where C is the concentration of the material (usually organic materials are characterized in solution), N_A is Avogadro's number, ω is the optical frequency of the laser, z_0 the Rayleigh range of the beam, I_0 the peak intensity at z = 0 and L_{eff} the effective thickness of sample. With this technique σ_{TPA} is determined straightforwardly when short laser pulses (femtosecond or picosecond) are employed by just fitting experimental data to the expression given above. The use of nanosecond pulses can lead to an overestimation for the σ_{TPA} since other effect different than simultaneous TPA can also be present.

The TPEF technique is another procedure for determining σ_{TPA} and consists in measuring the fluorescence signal generated from a solution of the material under tests after it is excited by TPA. From the two-photon fluorescence signal a TPE (two-photon fluorescence excitation) cross section σ_{TPE} can be determined. A representative experimental setup is showed in Fig. 2.4. The σ_{TPE} is linearly proportional to σ_{TPA} with the constant of proportionality being the fluorescence quantum yield (η) of the sample $\sigma_{TPE} = \eta\ \sigma_{TPA}$.

Some variants of this experiment have been developed since it was first reported by the Group of Webb [15, 19]. However, if a standard calibration sample of known σ_{TPE} and spectra is available, then the simplest approach is to compare the two-photon excited fluorescence spectra of the sample with the reference sample tested under identical conditions. With this method is possible to cancel automatically a large number of variables. For instance, it is not necessary to know parameters related to the excitation (pulse energy, pulse duration, and temporal intensity distribution) [20]. The equation to calculate the TPA cross section is given by:

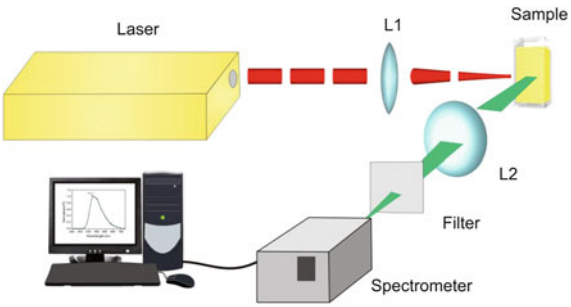

Fig. 2.4 Typical TPEF experimental setup to measure the σ_{TPA} in organic materials. The photoluminescence promoted by the absorption of two photons in a solution of the material under test is detected and compared with that from a standard tested under the same experimental conditions

$$\sigma_{TPA}(\lambda) = \sigma_{TPA(ref)}(\lambda)\frac{\eta_{ref}(\lambda)C_{ref}}{\eta(\lambda)C}\frac{\langle F(t)\rangle}{\langle F(t)\rangle_{ref}}\frac{n_{ref}}{n},$$

where C denotes the concentration of solution, $\langle F(t)\rangle$ is the time averaged fluorescence emission, n is the refractive index of the sample, and λ is the excitation wavelength. The subindex *ref* denotes the parameters for the dye used as reference or standard.

The principal drawback of the TPEF method is that it cannot be used for non-fluorescing or weakly fluorescing materials. TPEF is also difficult to implement in compounds that exhibit wavelength-dependent emission (in either band shape or efficiency) or dual emission, as well as in solid-state samples. In those cases the use of Z-scan is more convenient.

A wide range of organic molecules with large TPA activity have been studied experimentally employing Z-scan and TPEF techniques. In the following section we present some representative samples.

2.3 Design Strategies and Structure–Property Relationships for Organic Molecules

Many organic molecules and polymers having electronic π-conjugated systems in their structure have showed large nonlinear optical properties. So far, the largest values of σ_{TPA} reported in the literature are in the range of 10^2–10^4 GM. The number of examples within this range of nonlinearities has increased notably during the last three lustrums, and scientists have designed different family of molecules to achieve these values. A large number of scientific articles that report new TPA organic fluorescent materials are oriented toward the in vivo or in vitro imaging of bio specimens, as well as the diagnosis of diseases. For these applications it is

necessary to have organic molecules with high quantum yield and large TPA cross section values, in addition to low cell-toxicity and compatibility with aqueous media. In particular, the architecture of organic molecules that have been investigated for their two-photon absorption and fluorescent properties could be classified in two principal groups: (a) linear and (b) two-dimensional architectures. For both structures there are some requirements for maximizing the TPA cross-section response: a long conjugated π-backbone system with a planar conformation; the presence of electron-donor (D) and electron-acceptor (A) groups able to promote an intense displacement of charge during the transition from the donor-centered HOMO (highest occupied molecular orbital) to the acceptor-centered LUMO (lowest unoccupied molecular orbital) [20]. The energy difference between the HOMO and LUMO is the optical gap corresponding to the excitation transition promoted by TPA. Depending on symmetry of the organic molecule, this gap can be the same or different than that promoted by one photon transition (linear absorption). For instance, in centrosymmetric molecules the maximum TPA usually appears at higher energies than the peak corresponding to the one-photon absorption transition. This is because one-photon and two-photon transitions are regulated by different dipole selection rules.

In the case of organic chromophores with linear architecture, including polymers and small molecules, effective molecular architectures have been used to enhance the two-photon absorption. Arrangement such as donor–bridge–acceptor (D–π–A) dipolar structures (Fig. 2.5a), donor–bridge–donor (D–π–D), acceptor–bridge–acceptor (A–π–A), donor–acceptor–donor (D–π–A–π–D) and acceptor–donor–acceptor (A–π–D–π–A), the latter four corresponding to quadrupolar structures (Fig. 2.5b, c), have been designed and synthesized [21–23]. In this context the term bridge refers to a π-backbone system. The appropriate donor-acceptor architecture in organic π-systems can enhance the TPA activity through an increase in the transition dipole moment or the dipole moment difference between the ground state and excited state. Experiments indicate that quadrupolar architectures in some cases are more efficient that dipolar ones. For quadrupolar systems the best results have been obtained for architectures containing D groups in the periphery and A in the core. For molecules that possess two dimensional structures the best results correspond to architectures containing an A group in the core and D groups in a multi-branched configuration (Fig. 2.5d). These type of structures have octupolar response A–$(\pi\text{–D})_3$. Typical D groups are amino moieties as diphenylamino

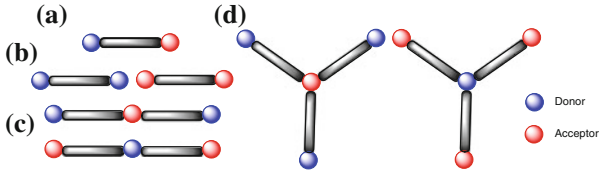

Fig. 2.5 Molecular architectures for the optimization of TPA responses in organic compounds: **a** dipolar, **b**, **c** quadrupolar, **d** octupolar

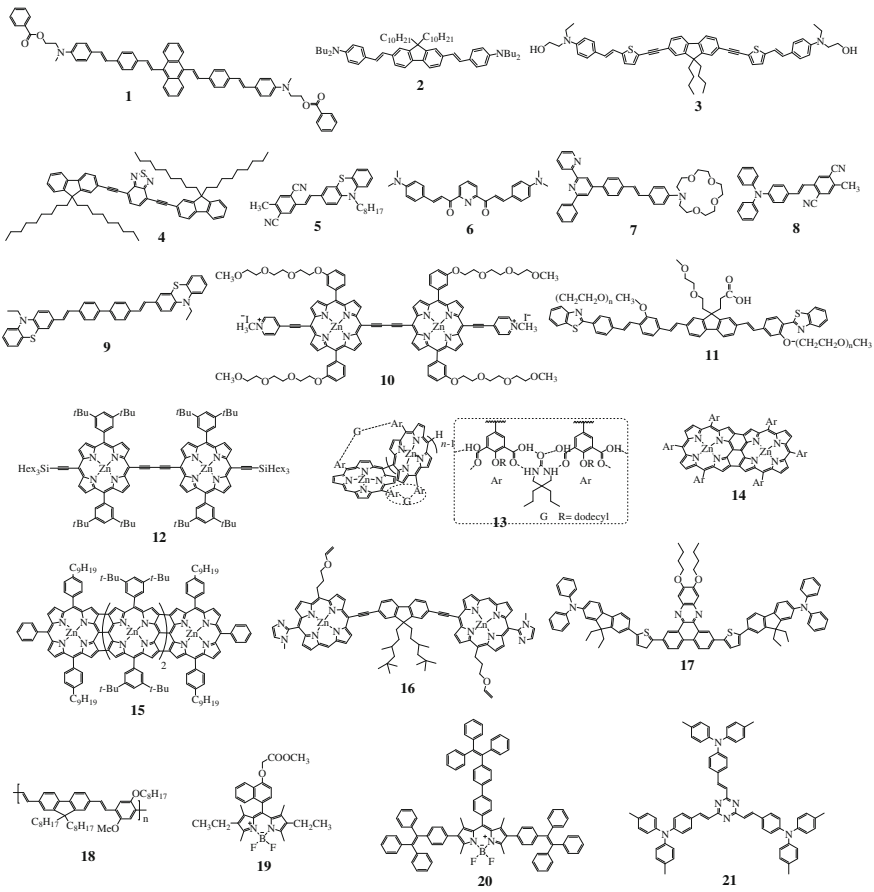

Fig. 2.6 Linear structures of organic molecules with high TPA properties

(NPh_2), dimethylamino (NMe_2) or diethylamino (NEt_2) which are the most employed, while some of the fragments used as A are antracene, fluorine, benzothiadiazole, triazyne, porphyrine or bodipys derivatives. For the π-bridge between D and A is common to utilize aromatic (phenyl or fluorene) or heteroaromatic rings (thiophene) to favor the planar structure. However, some reports indicate that carbon triple bond is also an excellent π-bridge. Figures 2.6 and 2.7 presents examples of organic molecular systems with dipolar, quadrupolar and octupolar character. These organic systems include fluorene based molecules and polymers, porphyrines, bodipy's, dendrimers, etc. and have large TPA activity with linear (Fig. 2.6) and two-dimensional (Fig. 2.7) designs.

Upon excitation, molecules with TPA properties undergo substantial intramolecular charge transfer (ICT) over the π-backbone. Enhancement of the σ_{TPA} is achieved with a correct design of the molecular structure able to modify properly the ICT. The environment is a factor that can affect the ICT process and in turn the

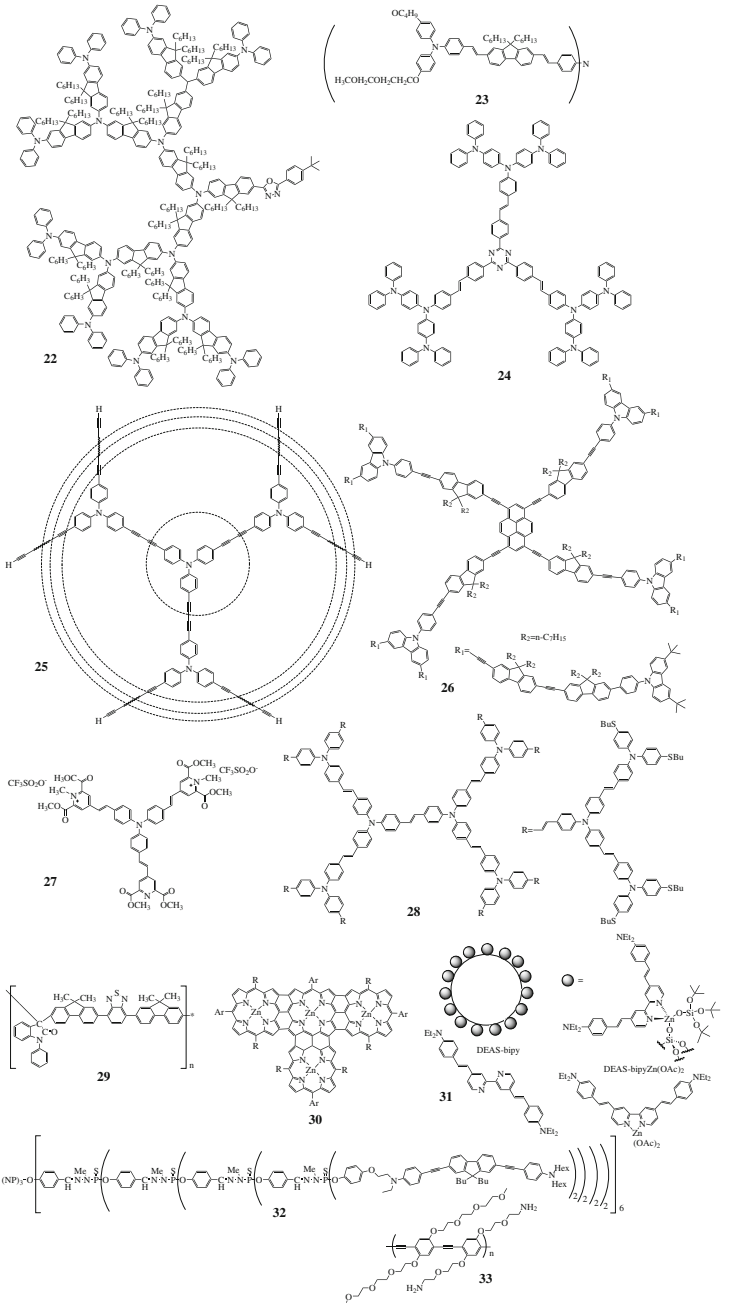

Fig. 2.7 Two-dimensional structures of organic molecules with TPA properties

nonlinear optical response. For instance, the linear TPA dye **8** having dipolar architecture showed intense solvatochromic effect such that in cyclohexane (non-polar solvent) solution exhibits a large σ_{TPA} value of 6670 GM which is reduced in DMF (high polar solvent) to 1450 GM. In low polar solvents, such as toluene, the linear quadrupolar structure **17** showed σ_{TPA} of 7080 GM while the two-dimensional molecule **23** has an acceptable σ_{TPA} of 5300 GM. Other two-dimensional structures show much higher optical nonlinearities than linear structures. Examples of the latter are polymers with quadrupolar architectures (**29**) and dendrimers (**32**) which in different solvents exhibit interesting values of 9860 and 56,000 GM, respectively.

It must be observed that in general the organic molecules are hydrophobic and soluble only in highly toxic solvents. To emphasize this fact, Table 2.1 summarizes the main optical properties of the molecules shown in Figs. 2.6 and 2.7 and the cases in which the molecules can be processed into nanoparticles (NPs) susceptible to be suspended in biocompatible media, i.e., aqueous solutions. Also, as a reference, the Table 2.1 includes the nonlinear optical properties of representative inorganic nanomaterials, i.e., quantum dots (QD) and gold nanorods which are also being studied extensively in the literature for biomedical applications.

Usually organic molecules and polymers, as those shown in Figs. 2.6 and 2.7, exhibit one-photon excitation (linear absorption) in the UV-Vis of the spectrum. Accordingly, their maximum two-photon excitation (assuming that the peak of the two-photon absorption spectrum is located at twice the wavelength of the one-photon absorption) occurs in the Vis-IR range. For biomedical applications, the interest is focused in molecules with TPA in the red and near-infrared region (650–1000 nm). Effective two-photon excitation at this range of wavelengths is observed with organics with relative small optical band gap. Further, the effectiveness in nonlinear absorption must be accompanied by a second molecular functionality. For instance, when a molecule or polymer is intended as a fluorescent label or contrast agent in multiphoton microscopy, it needs to exhibit a large value of quantum yield, η. This is not always achieved, as it can be observed in Table 2.1. Sometimes, large σ_{TPA} values are obtained in detriment of η. In these cases, or in other cases where the needed functionality is other than fluorescence, the energy transfer concept can work satisfactorily. For instance, an effective fluorescent dye (energy acceptor) with poor two-photon activity is indirectly excited through resonant energy transfer from an effective TPA dye unit (energy donor). This concept will be further exemplified in the last section of this chapter for the application of photodynamic therapy.

2.4 Methods Used to Incorporate TPA Materials in Aqueous Suspensions

As mentioned in the previous section, intense studies have been focused on developing efficient TPA organic molecules that can be excited in the 650–1000 nm region, since they deserve potential application in two-photon microscopy

Table 2.1 TPA properties of organic materials shown in Figs. 2.6 and 2.7

Organic Material	Quantum yield (η)	σ_{TPA} (solution) GM/technique	σ_{TPA} (NPs) GM	Reference
Linear structures				
1	0.025 (in solution) 0.13 (NPs)	172/Nonlinear transmission	217	[39]
2	1 (solution) 0.49 (SNPs)	~400/TPEF	–	[59]
3	0.65 (solution) 0.28 (SNPs)	1200/TPEF	1000	[37]
4	0.87 (solution) 0.83 (NPs)	1000/TPEF	514	[30]
5	0.03 (solution)	2800/TPEF	–	[76]
6	0.082 (solution)	5250/TPEF	–	[77]
7	0.027 (solution)	5956/TPEF		[78]
8	0.805 (solution)	6670/TPEF	–	[79]
9	0.61 (solution)	10,870/Z-scan	–	[80]
10	–	17,000/TPEF	–	[81]
11	~0.5 (aqueous solution) 1.0 (ACN solution)	3000 ACN/TPEF ~6000 Water/TPEF		[82]
12	–	9100/Z-scan	–	[83]
13	–	13,200/Z-scan	–	[83]
14	–	41,200/Z-scan	–	[83]
15	–	93,600/Z-scan	–	[84]
16	0.017 (solution)	1.0×10^6/TPEF (5.3×10^4/dimer)	–	[85]
17	~0.25 (in toluene) 0.08 (SNPs)	~7080/TPEF	6800	[86]
18	–	TPEF	200,000/particle[a]	[87]
19	0.99 (solution)	128	–	[88]
20	0.05 (solution) 0.16 (NPs)	264/TPEF	–	[40]
Two-dimensional materials				
21	–	1100/Z-scan	–	[89]
22	0.43	2990/TPEF	–	[90]
23	0.86 (solution) 0.56 (NPs)	5300/TPEF	2790	[31]
24	0.25 (NPs)	TPEF	2015 (covered with DSPE-PEG) 2241 (without DSPE-PEG)	[51]
	0.009 (solution) 0.4 (NPs)	8629/Z-scan	–	[91]

(continued)

Table 2.1 (continued)

Organic Material	Quantum yield (η)	σ_{TPA} (solution) GM/technique	σ_{TPA} (NPs) GM	Reference
25	0.57	9068/TPEF	–	[92]
26	0.49 (solution) 0.22 (NPs)	25,000/TPEF	9750	[93]
27	–	25,318/Z-scan	–	[94]
28	0.55	11,000/TPEF	–	[95]
29	1 (solution) 0.95 (NPs) 0.75 (SNPs)	9860/TPEF	8481 (NPs) 8686 (SNPs)	[41]
30	–	43,000	–	[83]
31	0.36 (solution)	435/TPEF	87,000	[96]
32	0.48–0.75	~56,000 GM/TPEF	–	[97]
33	0.09 (CPNs)	–	11,000/TPEF[a]	[52]
Inorganic materials				
Au (nanorods)	–	–	2320/TPEF[a]	[98]
CdSe-ZnS (QD)	–	–	47,000/TPEF[a]	[99]

These properties correspond to materiales in molecular solution and in the form of nanoparticles
[a]In these cases it is reported the two-photon fluorescence excitation cross section σ_{TPE}, namely the product between σ_{TPA} and η

(TPM) and photodynamic therapy [24]. For these kind of applications is mandatory that the molecules can show excellent TPA activity in aqueous medium, however, most of them are hydrophobic and those that are soluble in water commonly exhibit low values of σ_{TPA} and η [15, 25, 26]. For instance, water-soluble TPA dyes with $\sigma_{TPA} \sim 300$ GM have been used as fluorescent markers in biological media [27]. It is important to notate that water not only has a high dielectric constant, which influences the ICT, but it is also capable of producing effective hydrogen bonding and can therefore interact with donor groups in the ground and the excited state [26]. The hydrophobic nature for most of the TPA organic molecules means that organic polar solvents as tetrahydrofuran (THF), dimethylsulfoxide (DMSO), dichloromethane (DCM) or dimethylformamide (DMF) are required to prepare molecular solutions. These and other solvents imply high cytotoxicity. For this reason, a strategy based in the concept of water-dispersible fluorescent organic nanoparticles which are purely composed of hydrophobic molecular aggregates has been studied [28]. This approach works fine, although sometimes promotes aggregation-induced quenching (AIQ) and severe reduction of fluorescence intensity is detected (see Table 2.1). Recently, a new category of TPA fluorescent dyes with exactly the opposite characteristic to the AIQ, aggregation-induced emission (AIE), has been developed [29]. In this context an excellent option is to develop

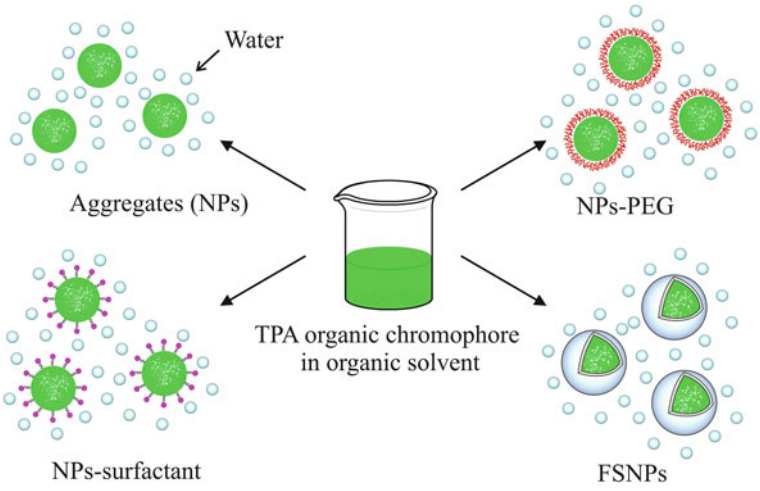

Fig. 2.8 Scheme of different methods to fabricate nanostructures from TPA chromophores

active TPA materials with high σ_{TPA} and η values such that when they are dispersed in water maintain their optical properties. In this section we will mention some methods that have emerged to incorporate hydrophobic materials into aqueous suspensions. These methods comprise the fabrication of organic nanomaterials in the range from 1 to 100 nm. Figure 2.8 presents schematically different possibilities to generate nanoparticles, i.e., nanoaggregates (NPs), nanoparticles covered by a biocompatible polymer (NPs-PEG) and fluorescent silica nanoparticles (FSNPs).

From the four preparation methods schematized in Fig. 2.8, the reprecipitation technique is the most facile and commonly used to assist the formation of NPs in aqueous media. Reprecipitation method induces the formation of nano-size aggregates that can be stabilized with a surfactant agent (CTAB, triton X-100, albumin, SDS, etc.). The use of surfactants not only stabilizes the suspensions but also protects the surfaces of the formed fluorescent NPs. According to experimental results, these NPs tend to conserve the nonlinear properties showed by the corresponding molecules in solution, although in some cases they showed high cytotoxicity [29, 30]. Recently, it has been demonstrated that the hydrophobic TPA material **23** (see Fig. 2.7; Table 2.1) can be nanostructured by the use micelles generated by dispersing an amphiphilic block copolymer, namely poly(methacrylic acid)-*block*-polystyrene (PMAA-*b*-PS), into water. The σ_{TPA} values for **23** in toluene solution is of 5300 GM and after it is processed into nanoparticles still exhibits a large σ_{TPA} (2790 GM) and high η (0.56) [31]. Another polymer used for the fabrication of NPs doped with hydrophobic TPA dyes is the poly (D,L-lactide-*co*-glycolide) which has the advantage of increasing the compatibility with biological environmental conditions [32].

To further reduce the cytotoxicity of NPs and increase their circulation time in vivo studied, they can be encapsulated with polyethylene glycol (PEG). PEG is considered an ideal biocompatible polymer with low toxicity and high water solubility. Some attractive TPA chromophores as silole and hexa-peri-hexabenzocorone

(∼1000 GM) have been covered with PEG derivatives to form NPs-PEG with nonlinearities ∼350 GM [33, 34].

It is important to note that specific inorganic materials, such as calcium phosphate, have been also used as shells of TPA organic materials to reduce the toxicity, protect and improve their transportation in biological medium. In particular, the inherent properties of calcium phosphate accentuate the potential of this system to enclosed low-weigh organic TPA dyes. A general method to encapsulate small fluorescent organic molecules in well-disperse calcium phosphate nanoparticles with diameter under 100 nm was reported [35].

The doping of fluorescent TPA materials (inorganic and organic) into silica NPs is also well-established in the literature. The fabrication of these fluorescent silica nanoparticles (FSNPs) is performed by using a microemulsion method. The advantages of FSNPs are their optical transparency, nonantigenicity, and rich surface chemistry for facile bioconjugation. The silica shell protects the dyes from photobleaching and prevents their interaction with the biological environment. The absorption and emission of the nanoparticles are determined by the properties of encapsulated fluorophores. One of the major disadvantages of using this type of nanoparticles is the phenomenon of aggregation induced fluorescence quenching of the loaded materials [36]. Organic chromophores can also be covalently encapsulated in silica nanoparticles. As an example of this, we can mention the photosensitizer **3** whose TPA properties were retained in the FSNPs, with approximately 1000 GM per unit [37, 38], although the total value per nanoparticle was estimated to be of the order of 8×10^6 GM. The TPA dye 9,10-bis[4′-(4″-aminostyryl)styryl] anthracene derivative (**1**) reported by Sehoon Kim et al., showed AIE in the aggregated state. The value of TPA cross-section of **1** in the aggregated state is 217 GM at 775 nm. This TPA dye was used to fabricated organically modified silica (ORMOSIL) nanoparticles with diameter <30 nm [39].

Our group has oriented investigations in the development of fluorescent TPA chromophores (small organic molecules, dendrimers and polymers) for the fabrication of NPs, NPs-PEG and FSNPs. For instance, we demonstrated that TPA properties of dye **4** ($\eta = 0.87$, $\sigma_{TPA} = 1000$ GM in THF) with architecture D-A-D is reduced with solvent polarity and hydrogen bonding. However, the formation of aggregates improve the photostability and tend to retain the third-order nonlinear properties ($\eta = 0.83$, $\sigma_{TPA} = 514$ GM in water) [30]. In addition, typical fluorescent chromophores as BODIPYs have been encapsulated with PEG polymers for bio-imaging applications, see for instance **20** [40]. Similarly, the polymer **29** was investigated in organic solvents and in the form of aggregated and encapsulated structures. In this case, such a polymer showed excellent optical properties, i.e., $\sigma_{TPA} = 9860$ GM and $\eta = 1$ in THF. When the polymer was processed into NP by using the reprecipitation method with CTAB as surfactant, the values of these optical parameters were $\sigma_{TPA} = 8481$ GM and $\eta = 0.95$. Further, for FSNPs fabricated by microemulsion technique the two-photon activity remained similar: $\eta = 0.75$, $\sigma_{TPA} = 8686$ GM. In addition, the photostability of **29** increased from THF solutions to silica nanoparticles comprising also high cell viability. With the use of this polymer we exemplified that is possible to process polymers into

nanostructures such that their TPA activity is conserved while simultaneously the requirements for biomedical applications are satisfied. These advantageous characteristics of polymer **29** were used to implement it as sensitive fluorescent contrast agent in TPM for the imaging of lung cancer cell line (A549) and human cervical cancer cell line (HeLa cells), as it is presented in Sect. 2.5 [41]. Thus, for TPM application is important that organic molecules maintain their TPA effect when they are processed into nanostructures. Other examples of organic molecules that tend to maintain their TPA activity are the molecules **1**, **3** and **17** (see Table 2.1). Contrary to this examples, other molecules exhibit detriment of such nonlinear optical property, see for instance the cases of **4**, **23** and **26**.

2.5 Biological Applications of TPA Organic Molecules

For organic NPs there are several scientific applications in biomedicine [42]. In this section we briefly describe those associated with TPA properties: two-photon laser scanning microscopy and photodynamic therapy.

2.5.1 Two-Photon Microscopy (TPM)

Fluorescent microcopy is one of the most versatile techniques in biomedical research. TPM is a three-dimensional imaging technology that was first demonstrated by Denk et al. [1] and is based on the detection of the fluorescence induced by TPA in biomedical samples. For instance, several biological systems often possess endogenous fluorophores, proteins such as tryptophan, tyrorosine, phycoerythrin and green fluorescent protein (GFP), neurotransmitter serotoin, coenzyme nicotinamide adenine dinucleotide phosphate [NAD(P)H], etc., such that they represent the source of fluorescence. Exogenous fluorophores can be also artificially added to the biological system under study to enhance the level of signal. The fluorescence produced either by exogenous or endogenous agents provides a direct mechanism for the visualization of cells or subcellular structures, tissue, biological processes and clinical imaging. It should be noted, however, that exogenous fluorophores can surpass in various orders of magnitude the TPA activity of endogenous ones.

To implement TPM a focused laser beam of long wavelength is used to scan the sample under study. In most of the cases the biological sample is stained with an exogenous fluorophores. The excitation is absorbed by the sample via the TPA exhibited by a fluorophore and the emitted fluorescence is collected to create an image point a point of the sample. TPM offers a number of unique advantages, such as reduced specimen photodamage, excitation at low energies (typically infra-red wavelengths) with emission in the visible, enhanced penetration depth, three-dimensional localization of the excitation volume, and high signal-to-background ratio fluorescence

detection [43]. Some of these advantages are consequence of the fact that being the TPA a nonlinear optical process, the magnitude of the induced absorption is intensity dependent so that it can be strongly confined to small volume of excitation within a femtoliter size. In practice, reduced volume of excitation is achieved by tightly focusing laser beams using powerful microscope objectives. Note that optical microscopy based in fluorescence induced by one photon excitation is not able to provide such small volumes of excitation as such absorption is not intensity dependent. Currently, one of the principal motivations in the field of fluorescence microscopy is the development of novel active materials with enhanced TPA properties in order to use them as exogenous fluorophores. These are also known as contrast agents or bio-markers.

The first TPA dyes studied in 1972 [44] were the Rhodamine derivatives which have σ_{TPA} values of 65 (Rhodamine 6G) and 140 GM (Rhodamine B) in methanol solution at the wavelength range 798–802 nm. Later a series of typical one-photon fluorophores (alexa, fluorescein, rhodamines and others) [45, 46] were also investigated for their TPA properties in water or other solvents compatible with biological medium.

Table 2.2 summarizes the optical properties of commercially available TPA dyes [46, 47]. Note that the commercially available dyes in Table 2.2 have rather weak optical properties compared with those novel dyes displayed in Table 2.1.

As mentioned previously (Sect. 2.3), recent investigations have produced a large variety of molecules with $\sigma_{TPA} > 1000$ GM. The optimization of the nonlinear properties of organic molecules has two central motivations: (a) the reduction of the laser excitation intensity required for imaging (less photodamage) and consequently (b) the opportunity of using less expensive laser systems. On the other hand, various processing methods are being implemented to give to these molecular systems advantages and viability for bio-applications [48]. Here some examples for TPA dyes in the form of NPs, NPs-PEG and FSNPs are presented when they are utilized in TPM to obtain bio imaging of several cell lines. In all cases, the searched features of TPA fluorescence-based contrast agents for TPM are: (a) high quantum yield and high two-photon absorption; (b) adequate dispersibility in the biological environment; (c) non-toxicity; (d) resistance to photobleaching; (e) in vitro and in vivo stability. For comparison purposes, some inorganic materials are also presented as reference.

Photoswitchable fluorescent NPs were fabricated and their surface was bioconjugated with anti-Her2 antibody, these NPs were employed to analyze the human breast cancer cell line (SK-BR-3) by TPM [49]. Polymers have been employed to protect and stabilized NPs to generate contrast agents. NPs fabricated from a fluorescent resonance energy transfer (FRET) pair, the known hexaphenylsilole and TPA dye **1** inside the micelle of amphiphilic block copolymers poly (methacrylic acid)-*b*-poly(styrene) (PMAA-*b*-PS), were employed to obtain high-quality fluorescent images of RAW cells [34]. Some biopolymers were used to protect NPs, in this context derivatives from PEG are the most employed. BODIPY **19** in NPs-PEG was used as red emissive contrast agent to obtain images of MCF-7 breast cancer cell [40]. Organic TPA dye (2-ter-butyl-0,10-di(naphthalene-2-yl) antracene (TBADN) was employed to fabricate NPs in which the surface was modified with the surfactant poly(maleic anhydride-alt-1-octadecene)-polyethylene

Table 2.2 TPA activity for commercial fluorophores in water

Dyes	Wavelength (nm)	$\eta \times \sigma_{TPA}$ (GM)
Alexa350	700	35
Alexa480	750	100
Alexa568	780	180
Alexa594	780	100
Bodipy	930	18
Ca-Crimson	870	100
Ca-Green	950	60
Cascade blue	740	2.5
Coumarine307[a]	800	15
DAPI	700	100
Di-4-ANEPPS[b]	950	5
Di-8-ANEPPS[b]	950	10
Dil[a]	700	95
dsRed	1000	110
eGFP	930	180
Fluorescein	780	38
Fluo-3	800	13
Riboflavina	700	1
Retinol	700	0.1
Folic acid	700	0.01
Lucifer yellow	850	1.4
mCerulean	850	78
mCFP	850	190
NADH in PBS	700	0.09

[a]Tested in methanol
[b]Tested in ethanol

glycol (C18PMH-PEG) and then bioconjugated with folic acid, bioimaging showed a selectivity for KB cell [50]. Folic acid-functionalized NPs-PEG of TPA chromophore **24** were used for targeting MCF-7 cancer cell by TPM technique [51]. Conjugated polymers are also attractive candidates to address the requirements for TPM imaging. NPs from conjugated polymer poly(p-phenylene ethylene) (**33**) were prepared by ultrafiltration technique. Average size for these NPs was of 8 nm and with a σ_{TPA} of 11,000 GM at 730 nm. The hydrophilicity and nontoxicity of **33**-NPs were employed to obtain several bio-images of endothelial cell by TPM [52]. In the case of inorganic materials with excellent luminescence and nonlinear properties, there are many examples of how NPs have been also applied as contrast agents in TPM. For instance, bio-conjugated QDs (CdSe/CdS/ZnS) with anti-caludin-4 were reported as optical contrast agent for imaging pancreatic cell in vitro using transferrin as targeting biomolecule [53]. In another example, aqueous dispersable $NaYF_4$ nanocrystals of 20–30 nm coped with RE ions Tm^{3+} and Yb^{3+} (UCNPs) were applied for in vitro TPM imaging, while the red emission ($\sim$800 nm) of UCNPs was used for obtain the imaging of pancreatic cancer cell, no apparent

cytotoxicity was observed [54]. Many other examples of inorganic nanoparticles employed for bio-imaging can be found in the literature [27].

Fluorescent SNPs have received strong interest in various cancer imaging applications [55–57]. FSNPs loaded with 25 % of TPA chromophore **1** (∼2500 molecules per nanoparticles) were used as efficient probes for TPM with extraordinary signal output, without any sign of cytotoxicity in Hela cell [58]. FSNPs doped with TPA dye **2** were fabricated and the surface bioconjugated with folic acid; these FSNP were employed to study in vitro the selectivity for HeLa cell cancer by TPM [59]. To increase the stability of FSNPs for in vivo imaging PEG derivatives are often introduced to their surface (FSNP-PEG). FSNPs-PEG doped with derivate 2-(2,6-bis((E)-2-(7-(diphenylamino)-9,9-diethyl-9Hfluoren-2-yl) vinyl)-4H-pyran-4-ylidene) malononitrile (DFP) bioconjugated with folic acid derivate have been employed to mark HeLa cells due to folate receptor interaction for in vivo analysis [60]. Of course, the use of SNPs loaded with inorganic materials has been also extensively reported in the literature. For instance, SNPs doped with Gold NPs were fabricated, these materials glow brightly when are excited by near-infrared light exhibiting σ_{TPA} of 2300 GM, which demonstrate the potential application to obtain biological imaging in bulk by two-photon-induced photoluminescence [61]. QDs and magnetic (Fe_3O_4) were co-encapsulated within SNPs and their surface was bioconjugated with transferrin, the magnetic properties of these SNPs were used in vitro to guide into Human pancreatic carcinoma (Pacn-1) line cell line and optical for obtain TPF-bioimaging [62].

Our group has fabricated NPs, NPs-PEG and FSNPs from organic dyes and polymers. One of our major interests is to study how nonlinearities can be conserved or changed as these TPA materials are processed into nano-structured systems intended to be used as contrast agents in TPM. Some of our results were presented in Sect. 2.4 regarding the conjugated polymer **29**, and it was discussed that this polymer tend to conserve its TPA action in the form of NPs, NPs-PEG and FSNPs as compared with that exhibited in molecular solution [41]. Taking advantage of this characteristic of our organic nanoparticles, the imaging of human cervical cancer cell line (HeLa cell) was performed. Figure 2.9 presents images from fluorescence microscopy obtained using the polymer **29** as contrast agent excited with either one-photon (488 nm) or two-photons (740 nm), showing the equivalence of the so obtained images, but in the latter case the use of infrared wavelengths is advantageous in the terms of less photodamage provoked (less invasive) to the biological specimen. For comparison purposes, we also present the images obtained for the same cellular line stained with the corresponding monomer of **29** (denoted as **M29**). **M29** and **29** were processed as NPs by reprecipitation technique and stabilized with surfactant (CTAB). These NPs showed large fluorescence and high photostability compared with the data collected in solution. The TPEF experiments for NPs of **M29** showed values of $\eta \sim 1$ and σ_{TPA} of 72 GM, while for NPs of **29** a higher value of σ_{TPA} (8481 GM) was obtained with $\eta = 0.95$. According to the images presented in Fig. 2.9, similar results are obtained with the use of **M29** or **29**. Nevertheless, the use of big molecules (polymers, hyperbranched polymers, dendrimers) as contrast agents is attractive because in

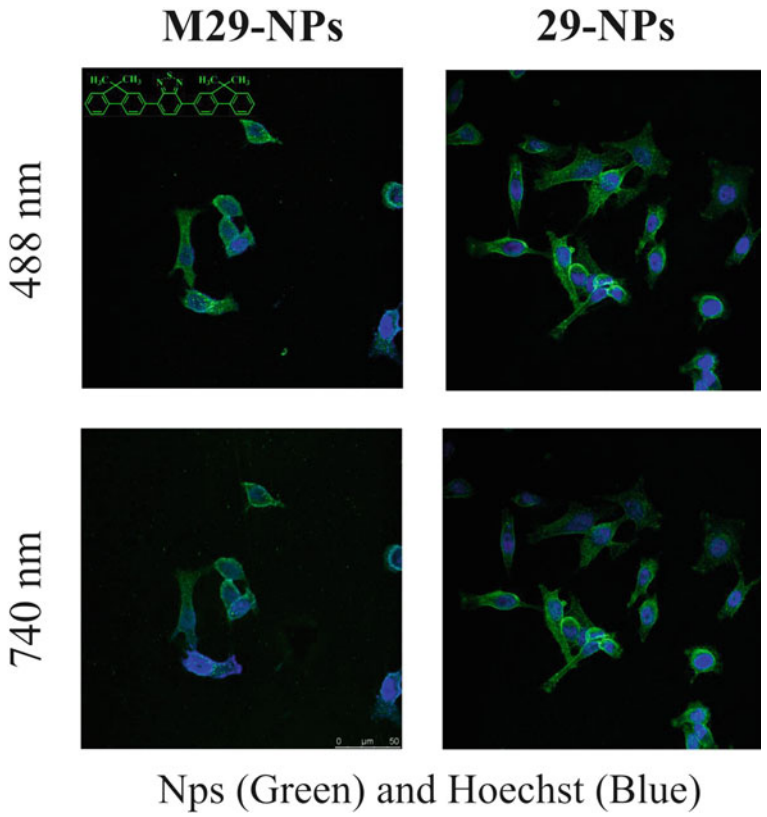

Fig. 2.9 One-photon (*first row*) and two-photon (*second row*) fluorescence images of HeLa cells treated with NPs of the monomer **M29** (*first column*) and the corresponding polymer **29** (*second column*). The excitation wavelengths are indicated to the *left of the columns*. The NPs penetrated nonspecifically into the cell and remained in the cytoplasm (*green emission*). The dye Hoechst 33258 was used to specifically stain the nucleus cell (*blue emission*). The fluorescence of this dye was obtained in all cases with one-photon excitation and the so obtained image merged to that corresponding to the two-photon excitation. The chemical structure of **M29** is shown in the picture of the first row and first column. The chemical structure of **29** is presented in Fig. 2.7

many cases they exhibit enhanced nonlinearities (per repeated unit of the polymer chain) in comparison to small organic molecules. Further, in our work it was demonstrated that it is possible to fabricate FSNPs with the polymer **29** to be used as contrast agents in TPM [41]. Notice that most of the attention given to FSNP in the literature is related to small organic molecules.

2.5.1.1 Photodynamic Therapy

Photodynamic therapy (PDT) has emerged as an alternative non-invasive and selective tool for blood purification and to destroy small cancerous tumors [8, 37, 63], i.e., for the

treatment of superficial tumors in oesophagus, bladder and melanoma cancer [64]. This technique involves the use of a photosensitizer (PS) which, upon irradiation at specific wavelengths in the presence of oxygen, leads to the generation of cytotoxic species (singlet oxygen $^1O_2$) and consequently to irreversible cell damage (Fig. 2.10). Usually, conventional photosensitizers (porfimer sodium Photofrin®, 5-aminovulinic acid ALA-Levulan®, verteporfin Visudyne® and methyl ester of ALA Metvix®) require very high intensity of excitation [65] (close to the threshold of tissue photodamage) at visible wavelengths. PDT combined with two-photon absorption in the near-IR region can circumvent this limitation. This approach offers new perspectives for the treatment of tumors providing a technique which is less invasive since the photodynamic effect can be limited to the area of interest, leaving the surrounding healthy tissues and cells undamaged. This is because, as it was discussed previously, the TPA is a process that depends on the intensity of excitation, and such a process only takes place when laser pulses are strongly focused in small volumes. Nevertheless, a bottle neck to make practical this application via TPA is that the commercially available PSs have weak two-photon absorption cross sections. Thus, there is an opportunity to develop new PS materials with a high TPA response in the biomedical window (650–1000 nm).

Recently novel organic materials and nanostructures have been tested as interesting supplies for PDT by using TPA properties [63]; some water soluble polymers [66], aggregated species [67] and modified silica nanoparticles [68] have been studied. In this respect, colloidal carriers for PSs, such as oil-dispersion, liposomes, low-density lipoproteins, polymeric micelles and silica nanoparticles, offer advantages as cell permeability and retention effect and active targeting by using surface modification. There are two main approaches for optimization of NPs systems for

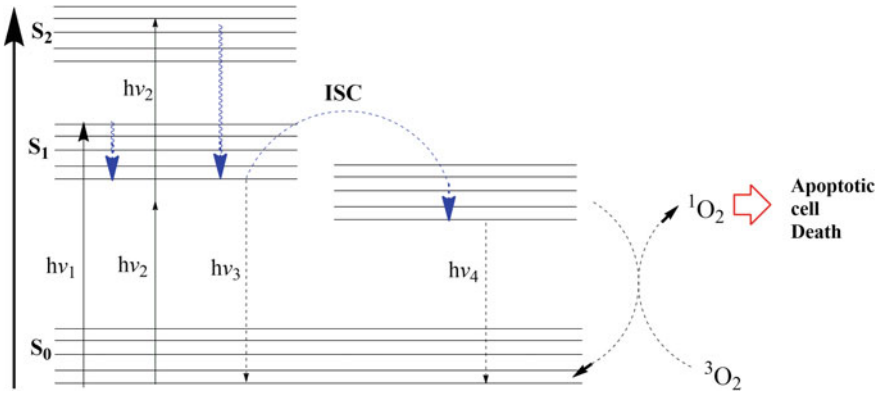

Fig. 2.10 Jablonski diagram depicting the photophysical processes for one-photon excitation and two-photon excitation of PDT. Excitation state of organic dyes is obtained by absorption of one or two photon (pulsed laser light). After excitation in either case, the molecule relaxes to the lowest vibrational level of the first singlet excited state. From here, it can emit photon (fluorescence) or undergo intersystem crossing (ISC) into the first triplet state. From the triplet state, this can emit phosphoresce or nonradiatively transfer its energy to convert the molecular oxygen $^3O_2$ to the cytotoxic singlet oxygen $^1O_2$. Singlet oxygen can then activate the apoptotic cell death pathway

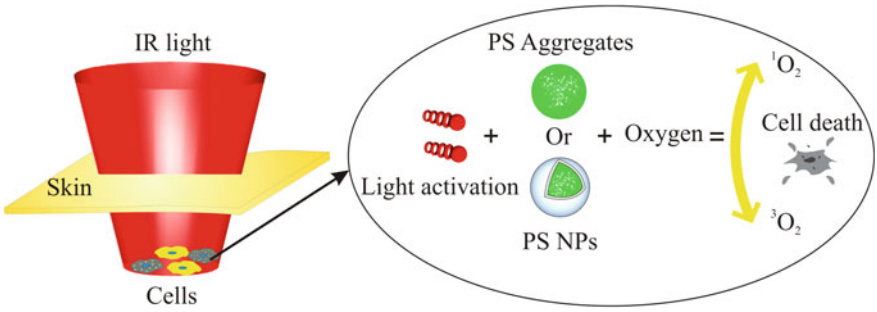

Fig. 2.11 Representation of organic nanomaterials with TPA properties employed in PDT. Infrared light activates nanoparticles (PS aggregates or NPs loaded with PS) through the absorption of two-photons. After sensitization the PS produces cytotoxic species (singlet oxygen $^1O_2$) able to produce cell damage

PDT (Fig. 2.11): (i) design of new photosensitizers or chemical modification of the existing ones to produce efficient sensitization through TPA process, (ii) employ the energy-transfer process from efficient TPA toward typical PS. For the latter, the PS (energy acceptor) is indirectly excited through fluorescent resonance energy transfer (FRET) from the TPA dye (energy donor) [69–71]. In general, commercial PS used in PDT as Verteporfin, Photofrin® and protoporphyrin IX (PpIX) have very low σ_{TPA} value, in this case 31, 7.5 and 10 GM, respectively [63, 72]. To increase their activity (cytotoxicity induced by the singlet oxygen generation) at infrared wavelengths they are encapsulate in SNPs with some efficient TPA dye (energy donor) [73]. As examples of this approach, we can mention the PDT employing SNPs doped with no commercial TPA dye **3** and bioconjugated with mannose to treat retinoblastoma cancer cells (Y-79) [74] or SNPs loaded with PpIX to treat HeLa cells [75].

Acknowledgements G. Ramos-Ortiz thanks financial support from the National Mexican Agency for Science and Technology (Conacyt).

References

1. W. Denk, J.H. Strickler, W.W. Webb, Two-photon laser scanning fluorescent microscopy. Science **248**(6), 73–76 (1990)
2. H.H. Fang, Q.D. Chen, J. Yang, H. Xia, Y.-G. Ma, H.-Y. Wang, H.-B. Sun, Two-photon excited highly polarized and directional upconversion emission from slab organic crystals. Opt. Lett. **35**(3), 441–443 (2010)
3. H. Guang, Y. Lixiang, P.N. Prasad, A. Abbotto, A. Facchetti, G.A. Pagani, Two-photon pumped frequency-upconversion lasing of a new blue-green dye material. Opt. Commun. **140** (1–3), 49–52 (1997)

4. J.E. Ehrlich, X.L. Wu, I.-Y.S. Lee, Z.-Y. Hu, H. Röckel, S.R. Marder, J.W. Perry, Two-photon absorption and broadband optical limiting with bis-donor stilbenes. Opt. Lett. **22**(24), 1843–1845 (1997)
5. P. Wei, O.F. Tan, Y. Zhu, G.H. Duan, Axial superresolution of two-photon microfabrication. Appl. Opt. **46**(18), 3694–3699 (2007)
6. N.S. Makarov, A. Rebane, M. Drobizhev, H. Wolleb, H. Spahni, Optimization two-photon absorption for volumetric storage. J. Opt. Soc. Am. B **24**(8), 1874–1885 (2007)
7. S.J. Pond, O. Tsutsumi, M. Rumi, O. Kwon, E. Zojer, J.L. Brédas, S.R. Marder, J.W. Perry, Metal-ion sensing fluorophores with large two-photon absorption cross sections: Aza-crown ether substituted donor-acceptor-donor distyrylbenzenes. Development of highly fluorescent silica nanoparticles chemically doped with organic dye for sensitive DNA microarray detection. J Am Chem Soc. **126**(30), 9291–9306 (2004)
8. S. Kim, T.Y. Ohulchanskyy, H.E. Pudavar, R.K. Pandey, P.N. Prasad, Organically modified silica nanoparticles co-encapsulating photosensitizing drugs and aggregation-enhanced two-photon absorbing fluorescent dye aggregates for two photon therapy. J. Am. Chem. Soc. **129**(9), 2669–2675 (2007)
9. M. Khurana, H.A. Collins, A. Karotki, H.L. Anderson, D.T. Cramb, B.C. Wilson, Quantitative *in* vitro demonstration of two-photon photodynamic therapy using photofrin and visudyne. Photochem. Photobio. **83**(6), 1441–1448 (2007)
10. M. Göppert-Mayer, Über Elementarakte mit zwei Quantensprüngen. Ann. Phys. (Leipzig) **9**, 273 (1931)
11. M.C. Rumi, J.W. Perry, Two-photon absorption: an overview of measurements and principles. Adv. Opt. Photon. **2**(4), 451–518 (2010)
12. M. Sheik-Bahae, A.A. Said, T.H. Wei, D.J. Hagan, E.W. Van Stryland, Sensitive measurement of optical nonlinearities using a single beam. IEEE LEOS NEWSLETTER **21** (1), 17–26 (2007). (Special 30th Anniversary Feature)
13. L. Antonov, K. Kamada, K. Ohta, Estimation of two-photon absorption characteristic by a global fitting procedure. Appl. Spectrosc. **56**(11), 1508–1511 (2002)
14. K. Kamada, K. Ohta, Y. Iwase, K. Kondo, Two-photon absorption properties of symmetric substituted diacetylene: drastic enhanced of the cross section near the one-photon absorption peak. Chem. Phys. Lett. **372**(3–4), 386–393 (2003)
15. C. Xu, W.W. Webb, Measurement of two-photon excitation cross section of molecular fluorophores with data from 690 to 1050 nm. J. Opt. Soc. Am. B **13**(3), 481–491 (1996)
16. A. Taouri, H. Derbal, J.M. Nunzi, R. Mountasser, M. Sylla, Two-photon absorption cross-section measurement by thermal lens and nonlinear transmission methods in organic materials at 532 and 1064 nm laser excitation. J. Optoelectronic Adv. Mater. **11**(11), 1696–1703 (2009)
17. C.V. Bindhu, S.S. Harilal, V.P.N. Nampoori, C.P.G. Vallabhan, Investigation of nonlinear absorption and aggregation in aqueous solution of rhodamine B using thermal lens technique. PRAMANA-J. Phys. **52**(4), 435–442 (1999)
18. C.V. Bindhu, S.S. Harilal, R.C. Issac, G.K. Varier, V.P.N. Nampoori, C.P.G. Vallabhan, Pulsed photoacoustic technique to study nonlinear processes in liquids: results in toluene. PRAMANA-J. Phys. **44**(3), 231–235 (1995)
19. M.A. Albota, C. Xu, W.W. Webb, Two-photon fluorescence excitation cross section of biomolecular probes from 690 to 960 nm. App. Opt. **37**(31), 7352–7356 (1998)
20. G.S. He, L.-S. Tan, Q. Zheng, P.N. Prasad, Multiphoton absorbing materials: molecular design, characterizations and applications. Chem. Rev. **108**(4), 1245–1330 (2008)
21. M. Pawlicki, H.A. Collins, R.G. Denning, H.L. Anderson, Two-photon absorption and the design of two-photon dyes. Angew. Chem. Int. Ed. **48**(18), 3244–3266 (2009)
22. M. Rumi, J.E. Ehrlich, A.A. Heikal, J.W. Perry, S. Barlow, Z. Hu, D. McCord-Maughon, T.C. Parker, H. Röckel, S. Thayumanavan, S.R. Marder, D. Beljonne, J.-L. Brédas, Structure-property relationship for two-photon absorbing chromophores: bis-donor diphenylpolyene and bis(styrylbenzene derivatives). J. Am. Chem. Soc. **122**(39), 9500–9510 (2000)

23. B.A. Reinhardt, L.L. Brott, S.J. Clarson, A.G. Dillard, J.C. Bhatt, R. Kannan, L. Yuan, G.S. He, P.N. Prasad, Highly active two-photon dyes: design, synthesis, and characterization toward application. Chem. Mater. **10**(7), 1863–1874 (1998)
24. H.M. Kim, B.R. Cho, Two-photon materials with large two photon cross section. Structure property relationship. Chem. Commun. **2**, 153–164 (2009)
25. F. NicoudJ, F. Bolze, X.-H. Sun, A. Hayek, P. Baldeck, Boron-containing two-photon absorbing chromophores. 3(1) one- and two-photon photophysical properties of *p*-carborane-containing fluorescent bioprobes. Inorg. Chem. **50**(10), 4272–4278 (2011)
26. H.Y. Woo, B. Liu, B. Kholer, D. Korystov, A. Mikhailovsky, G.C. Bazan, Solvent effects on the two-photon absorption of distyrylbenzene chromophores. J. Am. Chem. Soc. **127**(42), 14721–14729 (2005)
27. P. Sharma, S. Brown, G. Walter, S. Santra, B. Moudgil, Nanoparticles for bioimaging. Adv. Colloid Interface Sci. **123–126**, 471–485 (2006)
28. H. Kasai, H.S. Nalwa, H. Oikawa, S. Okada, H. Matsuda, N. Minami, A. Kakuta, K. Ono, A. Mukoh, H. Nakanishi, A novel preparation method of organic microcrystals. Jpn. J. Appl. Phys **3l**, L1132 (1992)
29. S. Kim, Q. Zheng, G.S. He, D.J. Bharali, H.E. Pudavar, A. Baev, P.N. Prasad, Aggregation-enhanced fluorescence and two-photon absorption in nanoaggregates of a 9,10-bis[4′-(4″-aminostyryl)styryl]anthracene derivative. Adv. Funct. Mater. **16**, 2317–2323 (2006)
30. J. Rodríguez-Romero, L. Aparicio-Ixta, M. Rodríguez, G. Ramos-Ortíz, J.L. Maldonado, A. Jiménez-Sánchez, N. Farfán, R. Santillan, Synthesis, chemical-optical characterization and solvent interaction effect of novel fluorene-chromophores with D-A-D structure. Dyes Pigm. **98**(1), 31–41 (2013)
31. Y. Tian, C.-Y. Chen, Y.-J. Cheng, A.C. Young, N.M. Tucker, A.K.-Y. Jen, Hydrophobic chromophores in aqueous micellar solution showing large two-photon absorption cross sections. Adv. Funct. Mater. **17**(10), 1691–1697 (2007)
32. K. Baba, T.Y. Ohulchanskyy, Q. Zheng, T.C. Lin, E.J. Bergey, P.N. Prasad, Infrared emitting dye and/or two photon excitable fluorescent dye encapsulated in biodegradable polymer nanoparticles for bioimaging. Mater. Res. Soc. Symp. Proc. **845**, 209–214 (2005)
33. Q. Zheng, T.Y. Ohulchanskyy, Y. Sahoo, P.N. Prasad, Water-dispersible polymeric structure co-encapsulation a novel hexa-peri-hexabenzocoronene core containing chromophore with enhanced two-photon absorption an magnetic nanoparticles for magnetically guided two-photon cellular imaging. J. Phys. Chem. C **111**(45), 16846–16851 (2007)
34. W.-C. Wu, C.-Y. Chen, Y. Tian, S.-H. Jang, Y. Hong, Y. Liu, R. Hu, B.Z. Tang, Y.-T. Lee, C.-T. Chen, W.-C. Chen, A.K.-Y. Jen, Enhancement of aggregation-induced emission in dye-encapsulating polymeric micelles for bioimaging. Adv. Funct. Mater. **20**, 1413–1423 (2010)
35. T.T. Morgan, H.S. Muddana, Eİ. Altinoğ, S.M. Rouse, A. Tabaković, T. Tabouillot, T. J. Russin, S.S. Shanmugavelandy, P.J. Butler, P.C. Eklund, J.K. Yun, M. Kester, J.H. Adair, Encapsulation of organic molecules in calcium phosphate nanocomposite particles for intracellular imaging and drug delivery. NanoLett. **8**(12), 4108–4115 (2008)
36. T.Y. Ohulchanskyy, I. Roy, K.-T. Yong, H.E. Pudavar, P.N. Prasad, High-resolution light microscopy using luminescent nanoparticles. WIREs Nanomed. Nanobiotechnol. **2**(2), 162–175 (2010)
37. M. Gary-Bobo, Y. Mir, C. Rouxel, D. Brevet, I. Basile, M. Maynadier, O. Vaillant, O. Mongin, M. Blanchard-Desce, A. Morère, M. Garcia, J.-O. Durand, L. Raehm, Mannose-functionalized mesoporous silica nanoparticles for efficient two-photon photodynamic therapy of solid tumors. Angew. Chem. **123**(48), 11627–11631 (2011)
38. C. Rouxel, M. Charlot, Y. Mir, C. Frochot, O. Mongin, M. Blanchard-Desce, Banana-shaped biophotonics quadrupolar chromophores: from fluorophores to biophotonic photosensitizers. New J. Chem. **35**, 1771–1780 (2011)

39. S. Kim, H.E. Pudavar, A. Bonoiu, P.N. Prasad, Aggregation-enhanced fluorescence in organically modified silica nanoparticles: a novel approach toward high-signal-output nanoprobes for two-photon fluorescence bioimaging. Adv. Mater. **19**(22), 3791–3795 (2007)
40. Z. Zhao, B. Chen, J. Geng, Z. Chang, L. Aparicio-Ixta, H. Nie, C.C. Goh, L.G. Ng, A. Qin, G. Ramos-Ortiz, B. Liu, B. Zhong, Red emissive biocompatible nanoparticles from tetraphenylethene-decorated BODIPY luminogens for two-photon excited fluorescence cellular imaging and mouse brain blood vascular visualization. Part. Part. Syst. Charact. **31** (4), 481–491 (2014)
41. L. Aparicio-Ixta, G. Ramos-Ortiz, J.L. Pichardo-Molina, J.L. Maldonado, M. Rodríguez, V.M. Tellez-Lopez, D. Martinez-Fong, M.G. Zolotukhin, S. Fomine, M.A. Meneses-Nava, O. Barbosa-García, Two-photon excited fluorescence of silica nanoparticles loaded with a fluorene-based monomer and its cross-conjugated polymer: their application to cell imaging. Nanoscale **4**, 7751–7759 (2012)
42. S. Krol, R. Macrez, F. Docagne, G. Defer, S. Laurent, M. Rahman, M.J. Hajipour, P. Kehoe, M. Mahmoudi, Therapeutic benefits from nanoparticles: the potential significance of nanoscience in diseases with compromise to the bold brain barrie. Chem. Rev. **113**(3), 1877–1903 (2013)
43. P.T.C. So, C.Y. Dong, B.R. Masters, K.M. Berland, Two-photon excitation fluorescence microscopy. Annu. Rev. Biomed. Eng. **2**, 399–429 (2000)
44. P. HermannJ, J. Ducuing, Dispersion of the two-photon cross section in rhodamine dyes. Opt. Commun. **6**(2), 101–105 (1972)
45. N.S. Makarov, M. Drobizhev, A. Rebane, Two-photon absorption standards in the 550–1600 nm excitation wavelength range. Opt. Express **16**(6), 4029–4047 (2008)
46. J.R. Lakowicz, *Principles of Fluorescence Spectroscopy*, 3rd edn. (Springer, Berlin, 2010). 2010
47. K. Svoboda, R. Yasuda, Principles of two-photon excitation microscopy and its applications to neuroscience. Neuron **50**, 823–839 (2006)
48. S.S. Agasti, S. Rana, M.-H. Park, C. Kim, C.-C. You, V. Rotello, Nanoparticles for detection and diagnostic. Adv. Drug Delivery Rev. **62**(3), 316–328 (2010)
49. M.-Q. Zhu, G.-F. Zhang, C. Li, M. Aldred, E. Chang, R. Drezek, A.D.Q. Li, Reversible two-photon photoswitching and two-photon imaging of immunofunctionalized nanoparticles target to cancer cells. J. Am. Chem. Soc. **133**(2), 365–372 (2011)
50. X. Diao, W. Li, J. Yu, X. Wang, X. Zhang, Y. Yang, F. An, Z. Liu, X. Zhang, Carrier-free, water dispersible and highly luminescent dye nanoparticles for targeted cell imaging. Nanoscale **4**, 5373–5377 (2012)
51. K. Li, Y. Jiang, D. Ding, X. Zhang, Y. Liu, J. Hua, S.S. Feng, B. Liu, Folic acid-functionalized two-photon absorbing nanoparticles for targeted MCF-7 cancer cell imaging. Chem. Commun. **47**, 7323–7325 (2011)
52. N.A. Abdul, W. McDaniel, K. Bardon, S. Srinivasan, V. Vickerman, P.T.C. So, J. Ho, Conjugated polymer nanoparticles for two-photon imaging of endothelial cells in a tissue model. Adv. Mater. **21**, 3492–3496 (2009)
53. J. QianYao, K.-T. Yong, I. Roy, T.Y. Ohulchanskyy, E.J. Bergey, Imaging pancreatic cancer using surface-functionalized quantum dots. J. Phys. Chem. B **111**, 6969–6972 (2007)
54. M. Nyk, R. Kumar, T.Y. Ohulchanskyy, E.J. Bergey, P.N. Prasad, High contrast in vitro and in vivo photoluminescence bioimaging using near infrared to near infrared up-conversion in TM3+ and Yb3+ doped fluoride nanophosphors. NanoLett. **8**, 3834–3838 (2008)
55. S. Santra, P. Zhang, K.M. Wang, R. Tapec, W.H. Tan, Conjugation of biomolecules with luminophore-doped silica nanoparticles for photostable biomarkers. Anal. Chem. **73**, 4988–4993 (2001)
56. J.E. Smith, C.D. Medley, Z.W. Tang, D. Shangguan, C. Lofton, W.H. Tan, Aptamer-conjugated nanoparticles for the collection and detection of multiple cancer cells. Anal Chem **79**, 3075–3082 (2007)
57. G. Yao, L. Wang, Y.R. Wu, J. Smith, J.S. Xu, W.J. Zhao, E.J. Lee, W.H. Tan, FloDots: luminescent nanoparticles. Anal. Bioanal. Chem. **385**, 518–524 (2006)

58. S.H. Kim, H. Huang, H.E. Pudavar, Y.P. Cui, P.N. Prasad, Intraparticle energy transfer and fluorescence photoconversion in nanoparticles: an optical highlighter nanoprobe for two-photon bioimaging. Chem. Mater. **19**, 5650–5656 (2007)
59. X. Wang, S. Yao, H.-Y. Ahn, Y. Zhang, M.V. Bondar, J.A. Torres, K.D. Belfield, Folate receptor targeting silica nanoparticles probe for two-photon fluorescence bioimaging. Biomed. Opt. Express **1**(2), 453–462 (2010)
60. X. Wang, A.R. Morales, T. Urakami, L. Zhang, M. Bondar, M. Komatsu, K.D. Belfield, Folate receptor-target aggregation-enhanced near-IR emitting silica nanoprobe for one-photon in vivo and two-photon ex vivo fluorescence bioimaging. Bioconjugate Chem. **22**(7), 1438–1450 (2011)
61. J. Park, A. Estrada, K. Sharp, K. Sang, J. Schwartz, D. Smith, C. Coleman, J.D. Payne, B.A. Korgel, A. Dunn, J.W. Tunell, Two-photon-induced photoluminescence imaging of tumors using near-infrared excited gold nanoshells. Opt. Express **16**(3), 1590–1599 (2008)
62. W.-C. Law, K.-T. Yong, I. Roy, G. Xu, H. Ding, E.J. Bergey, H. Zeng, P.N. Prasad, Optically and magnetically doped modified silica nanoparticles as efficient magnetically guide biomarker for two-photon imaging of live cells. J. Phys. Chem. C. **112**(21), 7972–7977 (2008)
63. J.P. Celli, B.Q. Spring, I. Rizvi, C.L. Evans, K.S. Samkoe, S. Verma, B.W. Pogue, T. Hasan, Imaging and photodynamic therapy: mechanisms, monitoring and optimization. Chem. Rev. **110**(5), 2795–2838 (2010)
64. M. Triesscheijn, P. Baas, J.H.M. Schellens, F. Stewart, Photodynamic therapy in oncology. Oncologist **11**, 1034–1044 (2006)
65. N. He, B. Li, H. Zhang, J. Hua, S. Jiang, Synthesis, two-photon absorption and optical limiting properties of new linear and multi-branched bithiazole-based derivatives. Synth. Met. **162**, 217–224 (2012)
66. X. Shen, L. Li, A.C.M. Chan, N. Gao, S.Q. Yao, Q.-H. Xu, Water-soluble conjugated polymers for simultaneous Two-photon cell imaging and Two-photon photodynamic therapy. Adv. Opt. Mater. **1**, 92–99 (2013)
67. L. Kelbauskas, W. Dietel, Internalization of aggregated photosensitizer by tumor cells: subcellular time-revolved fluorescence spectroscopy on derivatives of pyropheophorbide-a ethers and chlorin e6 under femtosecond one- and two-photon excitation. Photochem. Photobiol. **76**(6), 686–694 (2002)
68. S. Kim, T.Y. Ohulchanssky, H.E. Pudavar, R.K. Pandey, P.N. Prasad, Organically modified silica nanoparticles coencapsulating photosensitizing drug and aggregation-enhanced two photon absorbing fluorescent dye aggregates for two-photon photodynamic therapy. J. Am. Chem. Soc. **129**, 2669–2675 (2007)
69. W.R. Dichtel, J.M. Serin, C. Edder, J.M.J. Fréchet, M. Matuszewski, L.-S. Tang, T.Y. Ohulchanskyy, P.N. Prasad, Singlet oxygen generation via two-photon excited FRET. J. Am. Chem. Soc. **126**(17), 5380–5381 (2004)
70. M.A. Oar, J.M. Serin, W.R. Dichtel, J.M. Fréchet, Photosensitization of singlet oxygen via two-photon-excited fluorescence resonance energy transfer in water-soluble dendrimer. Chem. Mater. **17**, 2267–2275 (2005)
71. X. Shen, F. He, J. Wu, G.Q. Xu, S.Q. Yao, Q.-H. Xu, Enhanced two-photon singlet oxygen generation by photosensitizer-doped conjugate polymer nanoparticles. Langmuir **27**(5), 1739–1744 (2011)
72. K.S. Samkoe, A.A. Clancy, A. Karotki, B.C. Wilson, D.T. Cramb, Complete blood vessel occlusion in the chick chrioallantonic membrane using two-photon excitation photodynamic therapy: implications for treatment of wet age-related macular degeneration. J. Biomed. Opt. **12**(3), 034025-1–034025-14 (2007)
73. S.-H. Cheng, C.-C. Hsieh, N.-T. Chen, C.-H. Chu, C.-M. Huang, P.-T. Chou, F.-G. Tseng, C.-S. Yang, C.-Y. Mou, L.-W. Lo, Well-defined mesoporous nanostructure modulates three-dimensional interface energy transfer for two-photon activated photodynamic therapy. Nano Today **6**, 552–563 (2011)
74. M. Gary-Bobo, Y. Mir, C. Rouxel, D. Brevet, O. Hocine, M. Maynadier, A. Gallud, A. Silva, O. Mongin, M. Blanchard-Desce, S. Richeter, B. Loockd, P. Maillard, A. Morère, M. Garcia,

L. Raehm, J.-O. Durand, Multifuntionalized mesoporous silica nanoparticles for the *in vitro* treatment of retinoblastoma: drug deliver, one and two-photon photodynamic therapy. Int. J. Pharm. **432**, 99–104 (2012)
75. J. Qian, D. Wang, F. Cai, Q. Zhan, Y. Wang, S. He, Photosensitizer encapsulated organically modified silica nanoparticles for direct two-photon photodynamic therapy and *in vivo* functional imaging. Biomaterials **33**(19), 4851–4860 (2012)
76. C. Huang, C. Lin, A. Ren, N. Yang, Dicyanostilbene-derived two-photon fluorescence dyes with large two-photon absorption cross sections. J. Mol. Struct. **1006**(1–3), 91–95 (2011)
77. Y. Tan, Q. Zhang, J. Yu, X. Zhao, Y. Tian, Y. Cui, X. Hao, Y. Yang, G. Qian, Solvent effect on two-photon absorption (TPA) of three novel dyes with large TPA cross-section and red emission. Dyes Pigm. **97**(1), 58–64 (2013)
78. D. Xu, Z. Yu, M. Yang, Z. Zheng, L. Zhu, X. Zhang, L. Ye, J. Wu, Y. Tian, H. Zhou, 2,20-Bipyridine derivatives containing aza-crown ether: structure, two-photon absorption and bioimaging. Dyes Pigm. **100**, 142–149 (2014)
79. C. Huang, X. Peng, D. Yi, J. Qu, H. Niu, Dicyanostilbene-based two-photon thermo-solvatochromic fluorescence probes with large two-photon absorption cross sections: detection of solvent polarities, viscosities, and temperature. Sens. Actuators B **182**, 521–529 (2013)
80. F. Hao, Z. Liu, M. Zhang, J. Liu, S. Zhang, J. Wu, H. Zhou, Y.-P. Tian, Four new two-photon polymerization initiators with varying donor and conjugated bridge: Synthesis and two-photon activity. Spectrochim. Acta Part A Mol. Biomol. Spectrosc. **118**, 538–542 (2014)
81. H.A. Collins, M. Khurana, E.H. Moriyama, A. Mariampillai, E. Dahlstedt, M. Balaz, M.K. Kuimova, M. Drobizhev, V.X.D. Yang, D. Phillips, A. Rebane, B.C. Wilson, H.L. Anderson, Blood-vessel closure using photosensitizers engineered for two-photon excitation. Nature Photonics **2**, 420–424 (2008)
82. A.R. Morales, G. Luchita, C.O. Yanez, M.V. Bondar, O.V. Przhonska, K.D. Belfield, Linear and nonlinear photophysics and bioimaging of an integrin-targeting water-soluble fluorenyl probe. Org. Biomol. Chem. **8**(11), 2600–2608 (2010)
83. N. Aratani, D. Kim, A. Osuka, π-conjugation enlargement toward the creation of multi-porphyrinic systems with large two-photon absorption properties. Chem. Asian J. **4** (8), 1172–1182 (2009)
84. T.K. Ahn, K.S. Kim, D.Y. Kim, S.B. Noh, N. Aratani, C. Ikeda, A. Osuka, D. Kim, Relationship between two-photon absorption and the π-conjugation pathway in porphyrin arrays through dihedral angle control. J. Am. Chem. Soc. **128**(5), 1700–1704 (2006)
85. J.E. Raymond, A. Bhaskar, T. Goodson III, N. Makiuchi, K. Ogawa, Y. Kobuke, Synthesis and two-photon absorption enhancement of porphyrin macrocycles. J. Am. Chem. Soc. **130** (51), 17212–17213 (2008)
86. M. Velusamy, J.-Y. Shen, J.T. Lin, Y.-C. Lin, C.-C. Hsieh, C.-H. Lai, C.-W. Lai, M.-L. Ho, Y.-C. Chen, P.-T. Chou, J.-K. Hsia, A new series of quadrupolar type two-photon absorption chromophores bearing 11, 12-dibutoxydibenzo[a, c]-phenazine bridged amines; their applications in two-photon fluorescence imaging and two-photon photodynamic therapy. Adv. Funct. Mater. **19**(15), 2388–2397 (2009)
87. C. Wu, C. Szymanski, Z. Cain, J. McNeill, Conjugated polymer dots for multiphoton fluorescence imaging. J. Am. Chem. Soc. **129**(43), 12904–12905 (2007)
88. Q. Zheng, G. Xu, P.N. Prasad, Conformationally restricted dipyrromethene boron difluoride (BODIPY) dyes: highly fluorescent, multicolored probes for cellular imaging. Chem. Eur. J. **14**, 5812–5819 (2008)
89. S. Zeng, X. Ouyang, H. Zeng, W. Ji, Z. Ge, Synthesis, tunable two and three-photon absorption properties of triazine derivatives by branches. Dyes Pigm. **94**(2), 290–295 (2012)
90. T.-C. Lin, Y.-H. Lee, B.-R. Huang, C.-L. Hu, Y.-K. Li, Two-photon absorption and effective optical power-limiting properties of small dendritic chromophores derived from functionalized fluorene/oxadiazole units. Tetrahedron **68**(25), 4935–4949 (2012)

91. Y. Jiang, Y. Wang, J. Hua, J. Tang, B. Li, S. Qian, H. Tian, Multibranchedtriarylamine end-capped triazines with aggregation induced emission and large two-photon absorption cross-sections. Chem. Commun. **46**, 4689–4691 (2010)
92. R. Castro-Beltran, G. Ramos-Ortiz, C.K.W. Jim, J.L. Maldonado, M. Häußler, D. Peralta-Dominguez, M.A. Meneses-Nava, O. Barbosa-Garcia, B.Z. Tang, Optical nonlinearities in hyperbranched polyyne studied by two-photon excited fluorescence and third-harmonic generation spectroscopy. Appl. Phys. B **97**, 489–496 (2009)
93. Y. Wan, L. Yan, Z. Zhao, X. Ma, Q. Guo, M. Jia, P. Lu, G. Ramos-Ortiz, J.L. Maldonado, M. Rodríguez, A. Xia, Gigantic two-photon absorption cross sections and strong two-photon excited fluorescence in pyrene core dendrimers with fluorene/carbazole as dendrons and acetylene as linkages. J. Phys. Chem. B **114**, 11737–11745 (2010)
94. H. Xiao, C. Mei, B. Li, N. Ding, Y. Zhang, T. Wei, Synthesis, solvatochromism and large two-photon absorption cross-sections of water-soluble dipicolinate-based pyridinium salts. Dyes Pigm. **99**, 1051–1055 (2013)
95. M. Drobizhev, A. Karotki, A. Rebane, Dendrimer molecules with record large two-photon absorption cross section. Opt. Lett. **26**(14), 1081–1083 (2001)
96. N. Rendón, A. Bourdolle, P.L. Baldeck, H. Le, C. Andraud, S. Brasselet, C. Copéret, O. Maury, Bright luminescent silica nanoparticles for two-photon microscopy imaging via controlled formation of 4,4′-diethylaminostyryl-2, 2′-bipyridine Zn(II) surface complexes. Chem. Mater. **23**, 3228–3236 (2011)
97. A. Narayanan, O. Varnavski, O. Mongin, J.-P. Majoral, M. Blanchard-Desce, T. Goodson III, Detection of TNT using a sensitive two-photon organic dendrimer for remote sensing. Nanotechnology **19**, 115502 (2008). (6 p)
98. H. Wang, T.B. Hufft, D.A. Zweifelt, W. Het, P.S. Lowt, A. Weit, J.-X. Cheng, In vitro and in vivo two-photon luminescence imaging of single gold nanorods. PNAS **102**(4), 15752–15756 (2005)
99. D.R. Warren, R. Zipfel, R. Williams, S. Clark, M. Bruchez, F. Wise, W. Webb, Water-soluble quantum dots for multiphoton fluorescence imaging in vivo. Science **30**, 1434–1436 (2003)

Chapter 3
Optical Properties of Ultrathin InGaN/GaN Quantum Wells Subject to Indium Surface Segregation

Oleksiy V. Shulika, Mykhailo V. Klymenko and Igor A. Sukhoivanov

Abstract We investigate theoretically the influence of indium surface segregation in InGaN/GaN single quantum wells on its optical properties. Obtained results show that the influence of the surface segregation on the dipole matrix element is not equal for all optical transition. This effect results from the joint action of the piezoelectric polarization and indium surface segregation which change selection rules. Quantum well structures having different indium amount are analyzed and found that the influence of the indium surface segregation on absorption spectra is more pronounced in quantum well structures with high indium amount, in particular it shall be taken into account in structures containing over 10 % of indium.

3.1 Introduction

InGaN/GaN quantum-well structures are basic materials for optoelectronic devices operating in the spectral range from the visible up to the ultraviolet [1, 2]. Designing and following improvement of laser diodes, light-emitting diodes and electro-optical modulators based on these structures are rather difficult due to the fact that all their optical characteristics are strongly dependent on the growth conditions [3] consisting of the substrate temperature, components fluxes etc. One of the difficulties of the growth of nitride semiconductor structures is lack of cheap substrate lattice matched to the heterostructure. At the moment three kinds of the

O.V. Shulika (✉) · I.A. Sukhoivanov
Departamento de Ingeniería Electrónica, DICIS, Universidad de Guanajuato, Salamanca 36885, México
e-mail: oshulika@ugto.mx

I.A. Sukhoivanov
e-mail: i.sukhoivanov@ieee.org

M.V. Klymenko
Department of Chemistry, B6c, University of Liege, 4000 Liege, Belgium
e-mail: mklymenko@ulg.ac.be

O. Shulika and I. Sukhoivanov (eds.), *Contemporary Optoelectronics*,
Springer Series in Optical Sciences 199, DOI 10.1007/978-94-017-7315-7_3

substrates are used for epitaxial growth of nitride heterostructures: the sapphire (Al_2O_3), gallium nitride (GaN), and silicon carbide (SiC) [4, 5]. The best quality of a heterostructure one achieve using GaN substrate due to its best matching to the lattice of a nitride heterostructure. However, it is rarely used in mass production of nitride optoelectronic devices due to the cost issues in the growth of bulk GaN monocrystals. Due to difficulties in making GaN substrates of large area, these substrates are few orders of magnitude costly than GaAs substrates [5]. Although the growth technology of Al_2O_3 and SiC is mature and cheaper, lattice mismatch of these substrates to gallium nitride and indium nitride is large; the lattice constant of the sapphire is 1.5 times larger of the gallium nitride lattice constant [6], which results in high density of the crystalline defects. A way to decrease the defect density is to use the GaN buffer layer grown at low temperatures [6]. The buffer layer is incorporated in between the substrate and the active region. As it is shown in Fig. 3.1 the buffer layer contains a lot of crystalline defects due to large mismatch of the lattices. The vertical lines on the figure represent defects on the edges between volumes with different polarity of the crystalline lattice (directions [0001] and $[000\bar{1}]$ in the wurtzite lattice are not equivalent which results in two different polarities of the crystalline lattice).

Two principal methods of epitaxial growth of InGaN/GaN quantum well heterostructures are molecular-beam epitaxy (MBE) and metalorganic chemical vapour deposition (MOCVD). Figure 3.2 shows spatial distribution of indium in InGaN/GaN three-quantum-well heterostructure grown by MBE. The distribution shown has been obtained by transmission electron microscopy [7]. These data together with data from other works [8–12], are evidence of gradual variation of the indium mole fraction from zero to 10 % on the heterojunction instead of sharp distribution. The indium mole fraction deviates from the nominal one in the whole area of the quantum wells, and fission is observed in the vicinity of heterojunctions. The difficulty to obtain a heterojunction with sharp variation of the indium mole

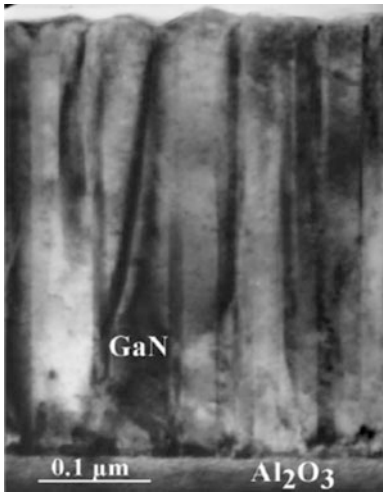

Fig. 3.1 Cross-sectional transmission electron microscopy image of the buffer *GaN* layer on the sapphire substrate, [4]

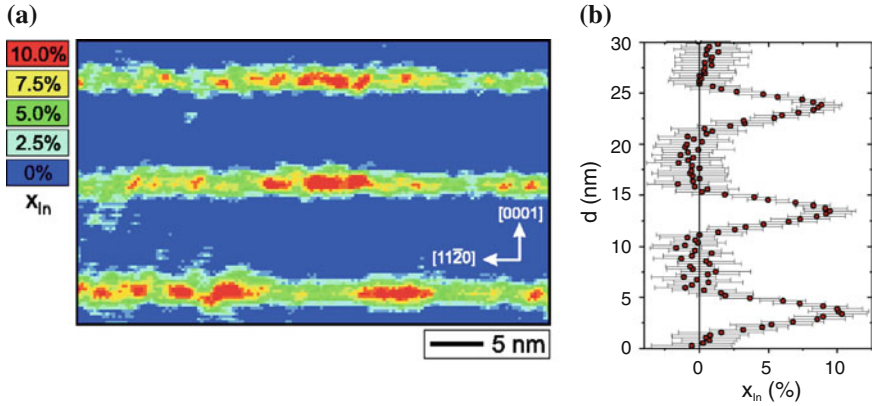

Fig. 3.2 Indium surface segregation (adopted from [7]). **a** Measurement data of TEM; **b** Indium distribution along [0001] direction averaged along [11$\bar{2}$1]

fraction is connected with the effect of surface segregation which arises due to large difference between enthalpies in GaN and InN [8].

Degree of segregation depends on the growth method. However, comparison of MBE and MOCVD made in [9], suggest that both methods lead to the surface segregation, although in a different extent. The MBE shows more pronounced effect of segregation. However, MOCVD shows more pronounce cauterization at weaker segregation. Indium spatial distribution in MBE made heterostructures can be viewed as reaction of crystalline structure to switching on/off of the indium evaporator. It results in different potential profiles of the leading and trailing edges of the quantum well.

There are several direct and indirect methods for observation of indium surface segregation (ISS) in *InGaN/GaN* quantum wells. They are transmission electron microscopy (TEM) [3, 10] reflection high-energy electron diffraction (RHEED) [11], X-ray diffraction (XRD) [13], and cathodeluminescence (CL) [14]. However, all of them have substantial drawbacks which influence precision of measurements, when applying to the *InGaN/GaN* quantum wells. TEM can lead to additional strain effects in the crystalline lattice due to prolonged exposure to electron beam [12]. Degree of strain depends on intensity and time of exposure. This effect leads to a systematic error in a measured data. RHEED measurements are usually made during the growth process, in situ, and cannot be applied to the grown structure. XRD is characterized by low sensitivity to the inhomogeneities less than 1 nm, and quantum well thickness of ultrathin quantum wells is 0.5–10 nm. Another drawback of XRD method is complexity to interpret the measured data which is angular distribution of the intensity of diffracted X-ray radiation. These data shall be processed using complex mathematical model in order to obtain measured parameters like composition of solid solution and thickness of the layers. TEM and RHEED, in contrast to XRD, produce more intuitive data which are more accessible for direct interpretation. CL method allows analysis of indium distribution only on the sample surface.

Laser spectroscopy is devoid of majority of the drawbacks described, but needs a theoretical model allowing interpretation of its data. Here we present briefly theoretical model of the optical response of a InGaN/GaN quantum well heterostructure and investigate various aspects of manifestation of indium surface segregation in optical absorption spectra. We will focus on the ISS effect in the Ga-face grown $In_xGa_{1-x}N$/GaN single quantum well (SQW) structures having different indium molar fractions. The first one is 4 nm $In_{0.1}Ga_{0.9}N$/GaN SQW structure [15], the second one is 2 nm $In_{0.37}Ga_{0.63}N$/GaN SQW structure [16].

Up to now, the influence of ISS on the optical characteristics have been studied in relation to the substrate temperature and ratio of III/V components fluxes which have effect on the segregation lengths. However, there is significant lack of information about the influence of the indium molar fraction on optical manifestations of the ISS. In this paper, we will show that even if the segregation lengths are independent on the indium flux, there is strong dependence of ISS optical manifestations on the indium molar fraction which is realized via the interplay between the piezoelectric polarization and ISS.

3.2 Indium Distribution and Potential Profiles

The potential profile or the band diagram defines dispersion of the charge carriers, which is starting point for calculation of the gain and absorption spectra [17, 18], gain suppression factor [19] (also known as gain compression and nonlinear gain factors), Auger recombination rate [20], and charge transport in the real space [21–23]. However, the theory is lacking for describing connection between the optical spectroscopic data and parameters of the structure imperfections with quantitative accuracy. It makes difficult to interpret the measured photoluminescense spectra and predict the optical spectral characteristics of the ultrathin QWs. The indium surface segregation appears during the crystal growth due to large difference between free binding enthalpies of GaN and InN semiconductor materials [8]. This effect was observed in many experiments including the transition electron microscopy [24], reflected high energy electron diffraction [11], cathodoluminescence [14] and X-rays diffraction [13]. As has been reported in [9], both molecular beam epitaxy and metalorganic vapour phase epitaxy are accompanied by the ISS with slight distinctions.

We use error functions to parameterize the indium distribution profile across the QW [8]:

$$n_{In}(z) = \begin{cases} 0, & z \le z_1 \\ n_0 \mathbf{erf}\left(\frac{z-z_1}{L_1}\right) & z_1 < z < z_2 \\ n_0 \mathbf{erf}\left(\frac{z_2-z_1}{L_1}\right)\left[1 - \mathbf{erf}\left(\frac{z-z_2}{L_2}\right)\right] & z_2 \le z \end{cases}, \tag{3.1}$$

here $n_{In}(z)$ is the indium distribution profile, n_0 is the nominal molar fraction of indium in the quantum well layer, z_1 and z_2 are coordinates of quantum well interfaces, L_1 and L_2 are the segregation lengths.

This expression gives an asymmetric indium distribution with two fitting parameters. It leads to better agreement with experimental data as compared with the symmetrical one. Usually, segregation lengths L_1 and L_2 are not equal. Existing kinetic theory of the MBE growth [3] gives dependencies of segregation lengths on the substrate temperature and ratio of III/V component fluxes. They states that the segregation lengths are independent on the indium flux at high substrate temperatures. Hereafter, we consider only this case deeming the segregation lengths are the same for both SQW heterostructures under examination.

In the $In_xGa_{1-x}N/GaN$ heterostructures, the indium distribution determines potential profiles of the band edges. A large indium amount leads to the significant mismatch of the lattice constants in semiconductor layers. The lattice mismatch causes strong strain giving origin to piezoelectric effects [25]. In this work, we neglect the spontaneous polarization that is a good approximation if the indium amount in the $In_xGa_{1-x}N$ alloy is large enough. To compute the piezoelectric polarization, we use non-linear relations for ternary alloys derived in [25]. The resulted internal electrostatic field in the quantum well is a superposition of electric fields formed by the piezoelectric charges and space charge of depletion layers produced due to doping. In the quantum well, computed internal electric field equals 0.5 MV/cm for the 4 nm $In_{0.1}Ga_{0.9}N/GaN$ SQW structure and 4.3 MV/cm for the 2 nm $In_{0.37}Ga_{0.63}N/GaN$ SQW structure. In barrier layers, internal fields equal 0.6 and 1.1 MV/cm respectively.

3.3 Band Structure

The computation of the interband absorption requires knowing of the band structure. In this paper, conduction and valence band structures have been computed separately using the envelope function approximation [26]. The conduction band structure and corresponding envelope functions have been obtained using the BenDaniel-Duke Hamiltonian [27]. For the valence band, we apply the six-band model including into consideration band mixing effects between the subbands. Such an approach is widely used for semiconductor nitrides with wurtzite crystal structure [2]. The numerical solution of resulted differential equations has been obtained by applying the finite difference method [28] with Dirichlet boundary conditions. Excepting the band gap energies, all position-dependent material parameters have been computed using linear interpolation formulas. For the band gaps, we use the second order interpolation with bowing parameters. Band structure parameters for the constituent binary semiconductors have been taken from [29].

The ISS has an effect on optical characteristics via the influence on the potential relief of band edges. As is illustrated in Fig. 3.3, the bottom of the potential well undergoes significant energy blueshift $\Delta E_c = 288$ meV if the piezoelectric

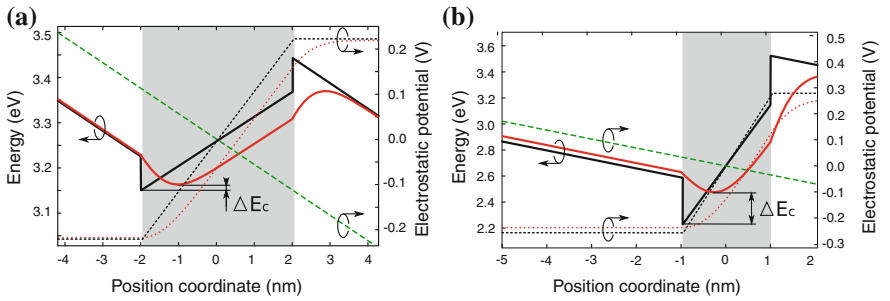

Fig. 3.3 Positional dependence of conduction band edges (*solid curves*), piezoelectric potential (*dotted curves*) and depletion layers potential (*dashed curve*) for **a** 4 nm $In_{0.1}Ga_{0.9}N/GaN$ SQW and **b** 2 nm $In_{0.37}Ga_{0.63}N/GaN$ SQW with ISS (*red curves*) and without ISS (*black curves*). Segregation lengths equal 2 nm in both cases

polarization is strong enough. In the case of weak internal fields, the shift ΔE_c is small, being of 17 meV. In both cases, segregation lengths have been taken as $L_1 = L_2 = L_s = 2$ nm. The magnitude of the piezoelectric polarization is related to the indium molar fraction. Therefore, changes in the potential profile caused by the ISS effect are dependent on the nominal indium molar fraction in the quantum well.

Such a behavior of potential profiles reflects on the transition energy dependence on the indium molar fraction. Comparing results for three cases presented in Fig. 3.4, one can separately estimate contributions to the transition energy form the ISS and piezoelectric polarization. Results of the band structure computations evidence that increasing of the indium molar fraction leads to the red shift of the transition energy. This is caused by the piezoelectric polarization which gives rise to the quantum confinement Stark effect [30]. In this case, the energy shift is dependent on the quantum well width [16]. The ISS has also effect on the transition energy leading to the blue shift for all magnitudes of the molar fraction. This result

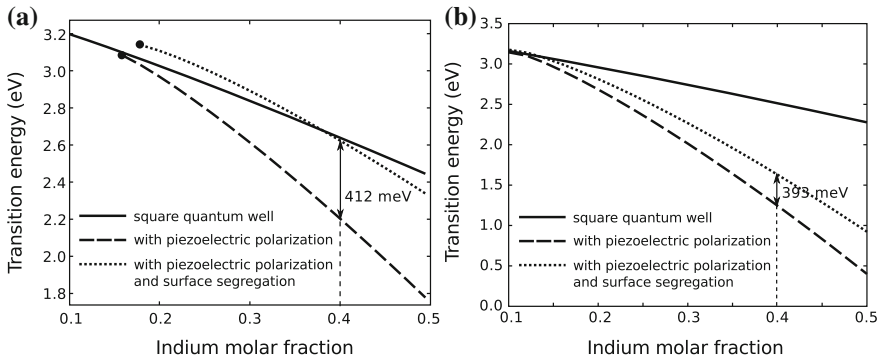

Fig. 3.4 Indium molar fraction dependence of the transition energy between the first conduction subband and first valence subband for the quantum well width of **a** 2 nm and **b** 4 nm

coincides with that one obtained in [31]. As follows from Fig. 3.3a, b, the energy shift caused by the ISS is dependent on internal electric fields that is manifestation of the interplay between the piezoelectric polarization and ISS. In turn, the piezoelectric polarization is determined by the indium molar fraction that makes the ISS effect be dependent on the indium amount even if the segregation lengths are invariable. At the same time, the influence of the quantum well width on the ISS effect is not so dramatic. Especially, this emerges at large indium amounts. For example, in structures having the indium molar fraction of 0.4, the energy shifts caused by the ISS equal to 412 meV in the 2 nm wide quantum well and 392 meV in the 4 nm wide quantum well. The difference amounts 20 meV that is approximately 5 % of the maximal magnitude. Variations of the quantum well width has more pronounced effect on the manifestation of the ISS effect only in ultrathin quantum wells. For narrow quantum wells, electron or holes wave function is affected by the ISS at both interfaces, while in wide quantum well the wave functions undergo the ISS effect only at one interface where charge carriers are localized. For the last case, increasing of the width does not change the shape of the wave functions for electrons and holes leading only to their shift in space relative each other. In other words, wave functions does not fill both heterointerfaces being localized by the piezoelectric polarization at the only one of heterojunctions.

In 4 nm wide quantum wells, localized states of electrons and holes exist for all considered magnitudes of the indium molar fraction. If the quantum well width equals 2 nm, there are no localized states for the indium molar fraction been less than 0.18. If the ISS is neglected, the localization is observed starting from the molar fraction of 0.16. These magnitudes are denoted by the black thick points in Fig. 3.4a. Thus, appearing of localized states in the quantum well is also affected by the ISS.

3.4 Global Sensitivity Analysis

Overall conclusion of the previous section is that increasing of segregation lengths leads to decreasing of the matrix element. However, segregation at each interface of a QW is not equal. Therefore, to resolve its influence much more data should be analyzed. To do that we use here global sensitivity analysis [32]. This approach allow to estimate the sensitivity of the matrix elements with respect to variations of ISS parameters separately and without large number of computations.

Using the global sensitivity analysis we try to clarify how strong the response of the system on the ISS effect is, what ME the most sensitive to the segregation is, and what segregation parameter having the strongest effect on the dipole matrix element is.

As a rule, the global sensitivity analysis is performed in connection with the Monte-Carlo method. In this paper, the procedure of the analysis is as follows.

1. First, we set the $N \times M$ matrix of parameters using a random-number generator. We use uniform distributions of random numbers. N is a number of Monte-Carlo experiments, and M is a number of input parameters. In our case, the input parameters are the segregation lengths L_1 and L_2 ($M = 2$).
2. The investigated mathematical model **S** acts N times on randomly generated input parameters.

$$\begin{bmatrix} L_1^{(1)} & L_2^{(1)} \\ \vdots & \vdots \\ L_1^{(j)} & L_2^{(j)} \\ \vdots & \vdots \\ L_1^{(N)} & L_2^{(N)} \end{bmatrix} \xrightarrow{\mathrm{S}} \begin{bmatrix} \mu_{11}^{(1)} & \mu_{13}^{(1)} \\ \vdots & \vdots \\ \mu_{11}^{(j)} & \mu_{13}^{(j)} \\ \vdots & \vdots \\ \mu_{11}^{(N)} & \mu_{13}^{(N)} \end{bmatrix}. \tag{3.2}$$

   The output parameters are dipole matrix elements μ_{11} and μ_{13} at the center of the Brillouin zone ($\mathbf{k}_{||} = 0$) in the case of TE polarization.
3. After series of Monte-Carlo numerical experiments, one obtains the matrix of output parameters. Indexes of columns correspond to different dipole matrix elements, and row indexes reflect the order number of a numerical experiment. The computed data can be plotted as a scatterplot. Then, dependences of output parameters on input ones is approximated by linear functions applying the least-square linear regression. From the linear dependence, one can get sensitivity coefficient defined as:

$$s_{L_m}^{\mu_{ij}} = \frac{\sigma_{L_m}}{\sigma_{\mu_{ij}}} \frac{\partial \mu_{ij}}{\partial L_m}, \tag{3.3}$$

   here σ_{L_m} and $\sigma_{\mu_{ij}}$ are standard deviations for segregation lengths and dipole matrix elements respectively.

The result of the global sensitivity analysis is set of sensitivity indices which are shown in Fig. 3.5. The magnitude of each index indicates relative sensitivity of the given output parameter to variations of the input parameter of the system.

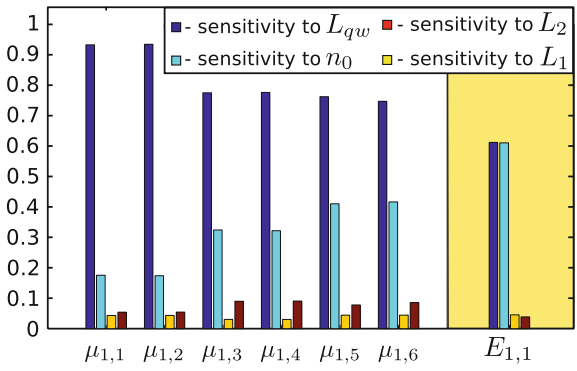

Fig. 3.5 Impact of the indium distribution parameters on the dipole matrix elements

With increasing of the number of a subband, the impact of the quantum-well width is decreased while the influence of the indium molar fraction is increased. At the same time, the indium surface segregation effect at each heterointerface remains the same for all subbands being less than one order of magnitude in comparison with other parameters.

3.5 Absorption Spectra

Absorption spectra have been computed using semiconductor Bloch equations in the quasi-equilibrium approximation. At the same time, electron-electron interactions are considered at the Hartree-Fock level of the approximation applying the constant dephasing time for high-order correlations. The dephasing time has been taken to be 41 ps. The temperature dependence of characteristics is modelled using semi-empirical Varshni formula [2]. This set of approximations allows to take into account excitonic effects and the transition energy renormalization caused by the exchange interactions [33].

Composition fluctuations in lateral directions cause the inhomogeneous broadening of the spectral characteristics. For the 4 nm $In_{0.1}Ga_{0.9}N$/GaN SQW structure, we use inhomogeneous broadening with FWHM = 31 meV that has been derived in [7]. For the 2 nm $In_{0.37}Ga_{0.63}N$/GaN SQW, the FWHM of the inhomogeneous broadening is taken as 38 meV.

The obtained results are shown in Figs. 3.6 and 3.7 and indicate that the inhomogeneous broadening leads to disappearing of excitonic resonances in absorption spectra. However, even when the inhomogeneous broadening equals zero, excitonic effects are very weak despite high exciton binding energy in the bulk GaN semiconductor [34]. This anomalous behavior can be explained considering expression for the interband Coulomb interaction potential in a quantum well [33]:

$$V_{i,j}(q) = \frac{2\pi e^2}{\varepsilon_0 L^2 q} \int \mathrm{d}z\mathrm{d}z' |\phi_{v,i}(z)|^2 |\phi_{c,j}(z')|^2 \mathrm{e}^{-q|z-z'|}, \tag{3.4}$$

where L is the lateral length of the heterostructure, q is the wave number for in-plane directions, z and z' are position coordinates in the growth direction, i and j are subband indices, $\phi_{c,j}(z)$ and $\phi_{v,i}(z)$ are electron and hole envelope functions. It is evident from (3.4) that better overlap between envelope functions $\phi_{c,j}(z)$ and $\phi_{v,i}(z)$ leads to stronger coupling between electron and holes which form excitons. In InGaN/GaN quantum well structures, electrons and holes are straddling in the space due to the piezoelectric polarization. According to (3.4), this leads to significant decay of the binding energies and, therefore, excitonic resonances in absorption spectra. Thus, excitonic effects are more pronounced in the thin quantum well where space separation of electrons and holes is not so large.

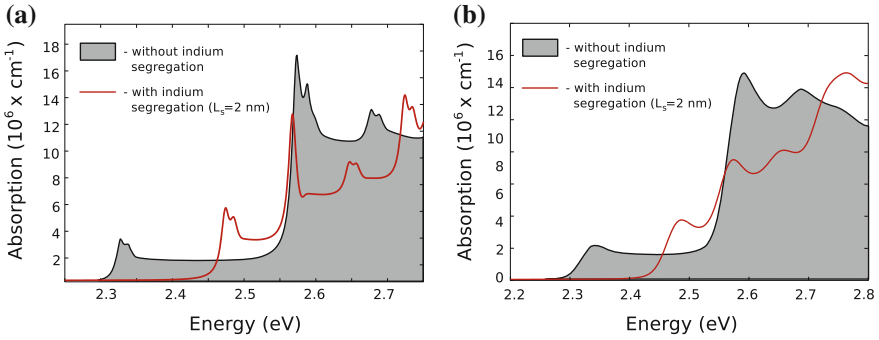

Fig. 3.6 Absorption spectra for the 2 nm $In_{0.37}Ga_{0.63}N/GaN$ SQW characterized by the inhomogeneous broadening with a FWHM of **a** 0 meV and **b** 38 meV

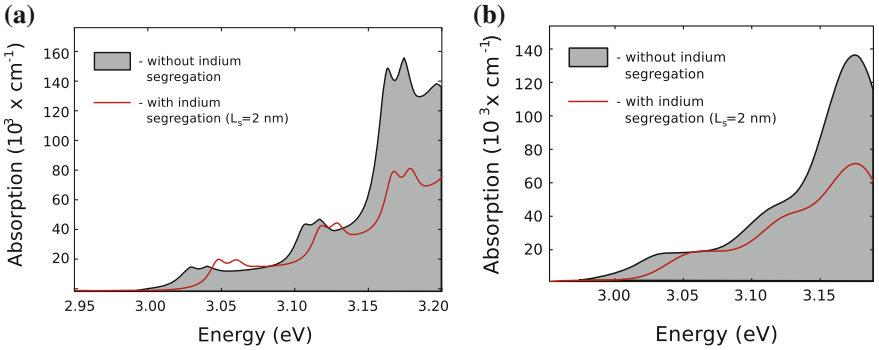

Fig. 3.7 Absorption spectra for the 4 nm $In_{0.1}Ga_{0.9}N/GaN$ SQW characterized by the inhomogeneous broadening with a FWHM of **a** 0 meV and **b** 31 meV

The results of our mathematical modelling affirm that the ISS leads to the blue shift of spectral characteristics [31] (see Figs. 3.6 and 3.7). In the case of the $In_{0.1}Ga_{0.9}N/GaN$ SQW structure, the ISS leads to the spectral shift of 15 meV, while for the another structure this value amounts 112 meV. Thus, the ISS effect is observed more clear for large magnitudes of the piezoelectric polarization. This dependence is resulted from the joint action of the piezoelectric polarization and surface segregation. When the piezoelectric polarization is high enough, carriers are localized near the quantum well interfaces where the indium segregation appears. Obtained results suggest that even when the segregation lengths are relatively large, the ISS effect is negligibly small in the square quantum well where the resulted internal field equals zero. However in this case manifestations of the ISS are determined by the quantum well width for narrow quantum wells.

3.6 Summary

In summary, we discover that the interplay between the piezoelectric polarization and ISS makes the structure with high indium amount more sensitive to the ISS effect. Hence, the influence of the ISS on absorption spectra is more pronounced for the large indium molar fractions. The obtained results evidence that neglecting of the ISS leads to high inaccuracy of simulation data if the indium molar fraction is large. However, if the indium molar fraction is less than or equal to 0.1, it is a good approximation. Results for this case has been affirmed in [35] by comparison computed and measured gain spectra.

References

1. P. Kiesel, F. Renner, M. Kneissl, N. Johnson, G. Dhler, Physica Status Solidi **188**(1)
2. J. Piprek (ed.), *Nitride Semiconductor Devices: Principles and Simulation* (Wiley, New York, 2007), p. 519
3. I. Stanley, G. Coleiny, R. Venkat, J. Cryst. Growth **251**, 23 (2003)
4. P. Ruterana, M. Albrecht, J. Neugebauer (eds.), *Nitride Semiconductors: Handbook on Materials and Devices* (Wiley, New York, 2003)
5. D. Ehrentraut, E. Meissner, M. Bockowski (eds.), *Technology of Gallium Nitride Crystal Growth* (Springer, Berlin, 2010)
6. A.G. Bhuiyan, A. Hashimoto, A. Yamamoto, J. Appl. Phys. **94**(5), 2779 (2003)
7. B. Witzigmann, V. Laino, M. Luisier, U.T. Schwarz, G. Feicht, W. Wegscheider, K. Engl, M. Furitsch, A. Leber, A. Lell, V. Härle, Appl. Phys. Lett. **88**(2), 021104 (2006)
8. O. Mayrock, H.J. Wünsche, F. Henneberger, Phys. Rev. B **62**, 16870–16880 (2000)
9. V. Potin, E. Hahn, A. Rosenauer, D. Gerthsen, B. Kuhn, F. Scholz, A. Dussaigne, B. Damilano, N. Grandjean, J. Cryst. Growth **262**(1–4), 145 (2004)
10. D. Biswas, S. Kumar, T. Das, Thin Solid Films **515**(10), 4488 (2007). The Third International Conference on Materials for Advanced Technologies (ICMAT 2005)
11. S. Martini, A.A. Quivy, T.E. Lamas, M.J. da Silva, E.C.F. da Silva, J.R. Leite, J. Cryst. Growth **251**(1–4), 101 (2003). Proceedings of the Twelfth International Conference on Molecular Beam Epitaxy
12. T. Li, E. Hahn, D. Gerthsen, A. Rosenauer, A. Strittmatter, L.R. Mann, D. Bimberg, Appl. Phys. Lett. **86**(24), 241911 (2005)
13. S. Pereira, M.R. Correia, E. Pereira, K.P. O'Donnell, E. Alves, A.D. Sequeira, N. Franco, I.M. Watson, C.J. Deatcher, Appl. Phys. Lett. **80**(21), 3913 (2002)
14. H. Wang, D.S. Jiang, U. Jahn, J.J. Zhu, D.G. Zhao, Z.S. Liu, S.M. Zhang, H. Yang, Thin Solid Films **518**(17), 5028 (2010)
15. M. Klymenko, O.V. Shulika, I. Sukhoivanov, IEEE J. Sel. Top. Quantum Electron. **17**(5), 1374 (2011)
16. M. Klymenko, O.V. Shulika, in *2010 10th International Conference on Laser and Fiber-Optical Networks Modeling (LFNM)* (2010), pp. 1–4
17. V. Lysak, H. Kawaguchi, I. Sukhoivanov, T. Katayama, A. Shulika, IEEE J. Quant. Electron. **41**(6), 797 (2005)
18. M. Klymenko, V. Lysak, I. Sukhoivanov, A. Shulika, Superlattices Microstruct. **46**(4), 603 (2009)
19. I.A. Sukhoivanov, Optic. Quant. Electron. **31**, 997 (1999)

20. I. Sukhoivanov, O. Mashoshyna, V. Kononenko, D. Ushakov, Microelectron. J. **36**(3–6), 264 (2005). Low Dimensional Structures and Devices Conference, LDSD'2004
21. O.V. Shulika, I.M. Safonov, I.A. Sukhoivanov, V.V. Lysak, Microelectron. J. **36**(3–6), 350 (2005)
22. V. Lysak, I. Sukhoivanov, O. Shulika, I. Safonov, Y. Lee, IEEE Photonics Technol. Lett. **18** (12), 1362 (2006)
23. I.M. Safonov, I.A. Sukhoivanov, O.V. Shulika, V.V. Lysak, Superlattices Microstruct. **43**(2), 120 (2008)
24. M. Takeguchi, M.R. McCartney, D.J. Smith, Appl. Phys. Lett. **84**(12), 2103 (2004)
25. V. Fiorentini, F. Bernardini, O. Ambacher, Appl. Phys. Lett. **80**(7), 1204 (2002)
26. G. Bastard, *Wave Mechanics Applied to Semiconductor Heterostructures* (Wiley, New York, 1991)
27. D.J. BenDaniel, C.B. Duke, Phys. Rev. **152**, 683–692 (1966)
28. S.L. Chuang, C.S. Chang, Semicond. Sci. Technol. **12**(3), 252 (1997)
29. I. Vurgaftman, J.R. Meyer, J. Appl. Phys. **94**(6), 3675 (2003)
30. H. Masui, J. Sonoda, N. Pfaff, I. Koslow, S. Nakamura, S.P. DenBaars, J. Phys. D Appl. Phys. **41**(16), 165105 (2008)
31. A. Dussaigne, B. Damilano, N. Grandjean, J. Massies, J. Cryst. Growth. **251**(1–4), 471–475 (2003)
32. A. Saltelli, F. Campolongo, J. Cariboni, D. Gatelli, F. Pennoni, M. Ratto, M. Saisana, S. Tarantola, *Global Sensitivity Analysis: A Primer* (Wiley, New York, 2008)
33. W.W. Chow, S.W. Koch, *Semiconductor Laser Fundamentals: Physics of the Gain Materials* (Springer, Berlin, 1999)
34. J.F. Muth, J.H. Lee, I.K. Shmagin, R.M. Kolbas, J.H.C. Casey, B.P. Keller, U.K. Mishra, S. P. DenBaars, Appl. Phys. Lett. **71**(18), 2572 (1997)
35. J. Hader, J.V. Moloney, S.W. Koch, Appl. Phys. Lett. **89**(17), 171120 (2006)

Part II
Metamaterials for Contemporary Optoelectronics

Chapter 4
Grating Resonances on Periodic Arrays of Sub-wavelength Wires and Strips: From Discoveries to Photonic Device Applications

Tatiana L. Zinenko, Volodymyr O. Byelobrov, Marian Marciniak, Jiří Čtyroký and Alexander I. Nosich

Abstract This chapter reviews the nature and the history of discovery of the high-quality natural modes existing on periodic arrays of many sub-wavelength scatterers as specific periodically structured open resonators. Although such modes can be found on various finite and infinite arrays made of metallic and dielectric elements, we concentrate our discussion around infinite arrays of silver wires and strips in the optical range. The grating modes (G-modes), like any other natural modes, are the "parents" of the corresponding resonances in the electromagnetic-wave scattering and absorption. Their wavelengths in either case are determined mainly by the period and the angle of incidence that has been a reason of their misinterpretation as Rayleigh anomalies. On the frequency scans of the reflectance or transmittance coefficients, G-mode resonances are usually observed as Fano-shape (double-extremum) spikes, while in the absorption they always display conventional Lorentz-shape peaks. If a grating is made of sub-wavelength size noble-metal elements, G-modes exist together with better known localized surface-plasmon modes (LSP-modes) whose wavelengths lay in the optical range. Thanks to high tunability and considerably higher Q-factors, the G-mode resonances can potentially supplement or even replace the LSP-mode resonances in the design of nanosensors, nano-antennas, and nanosubstrates for solar cells and surface-enhanced Raman scattering.

T.L. Zinenko · V.O. Byelobrov · A.I. Nosich (✉)
Institute of Radiophysics and Electronics NASU, Vul. Proskury 12,
Kharkiv 61085, Ukraine
e-mail: anosich@yahoo.com

M. Marciniak
National Institute of Telecommunications, Szachowa 1, 00-894 Warsaw, Poland

M. Marciniak
Kielce University of Technology, Al. Tysiaclecia Panstwa Polskiego 7,
25-314 Kielce, Poland

J. Čtyroký
Institute of Photonics and Electronics AS CR, v.v.i., Chaberská 57,
18251 Prague 8, Czech Republic

O. Shulika and I. Sukhoivanov (eds.), *Contemporary Optoelectronics*,
Springer Series in Optical Sciences 199, DOI 10.1007/978-94-017-7315-7_4

4.1 Introduction

Noble-metal nanowires are known to display intensive localized surface-plasmon (LSP) resonances in the visible range if illuminated with the H-polarized light (i.e. polarized orthogonally to the scatterer axis). The LSP resonance wavelengths depend primarily on the shape of the scatterer cross-section. For instance, a thin circular metal wire of the relative dielectric permittivity ε_{met} located in an infinite host medium with $\varepsilon_h > 0$ has a single broad peak in the scattering and absorption cross-sections slightly above the wavelength value λ^P where $\mathrm{Re}\,\varepsilon_{met}(\lambda^P) = -\varepsilon_h$. For a silver wire in free space, this yields $\lambda^P \approx 350\,\mathrm{nm}$ [1]. The plane-wave scattering by such a wire can be studied analytically using the separation of variables and can be further simplified using the small-argument asymptotics of cylindrical functions. This study shows that the wire possesses infinite number of closely spaced double-degenerate LSP eigenmodes of the azimuth orders $n = 1, 2, \ldots$, appearing as complex poles of the field as a function of the wavelength. However the corresponding resonance peaks overlap because the noble metals are lossy in the visible range, although the largest contribution comes from the dipole terms with $n = 1$. Non-circular wire scattering analysis needs more elaborated techniques such as volume or boundary integral equations. They also reveal shape dependent LSP-modes of different types and symmetries.

In scattering, LSP-resonances are the signatures of the underlying LSP-modes. If the shape of a metal wire is fixed, their wavelengths are specific for every host medium that makes possible the "sensing" of the medium refractive index by means of measuring the LSP wavelength [2]. The Q-factors of the LSP-resonances are low, of the order of $-\mathrm{Re}\,\varepsilon_{met}(\lambda^P)/\mathrm{Im}\,\varepsilon_{met}(\lambda^P) \approx 10$ in the visible range.

Although the optical properties of LSP modes of pairs (dimers) or small clusters of coupled metal wires or strips have been well documented [3], large periodic ensembles of them, i.e. chains, arrays and gratings, remain less studied and interpretation of the other, periodicity caused G-resonances is still controversial. Below we present a brief narrative of related publications and demonstrate the remarkable properties of these non-LSP resonances on nanogratings of circular wires and thin strips. For simplicity, the gratings are assumed to be suspended in free space.

4.2 Circular-Wire Gratings

The scattering of plane waves by free-standing *infinite* periodic gratings of *circular cylinders or wires* (see Fig. 4.1) made of metals and dielectrics has been extensively studied as a canonical scattering problem since the late 1890s [4–10]. Here, important research instrument was introduced by Rayleigh [5]: Floquet expansion of the field function in terms of spatial harmonics also called diffraction orders. Each Floquet harmonic is a homogeneous or inhomogeneous plane wave depending on the wavelength λ, period d and angle of incidence β.

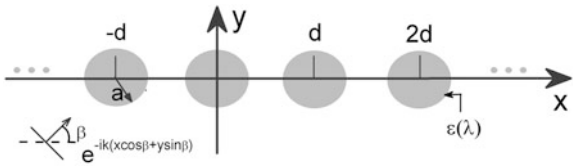

Fig. 4.1 Cross-sectional geometry of an infinite grating made of circular cylinders or wires

It was in 1979 when Ohtaka and Numata reported [11], apparently for the first time, that the scattering of light by an infinite one-period grating of thin dielectric circular cylinders showed unusually narrow total-reflection resonances. For the host medium with dielectric constant ε_h they appear near to (but not precisely at) the Rayleigh-Wood anomalies (RA) or "passing-off wavelengths,"

$$\lambda_{\pm m}^{RA} = (d\sqrt{\varepsilon_h}/m)(1 \mp \cos\beta), \quad m = 1, 2, \ldots \tag{4.1}$$

These are the resonances on G-modes. However the found effect did not attract any specific attention of research community and remained unclaimed for the next 25 years. Thus, it is an example of discovery that was done ahead of its time.

Although the G-resonances on dielectric-wire gratings in the cases of both E- and H-polarization can be noticed in some earlier papers (for instance, see Figs. 4.2 and 4.3 of [10]), they became an object of specific investigation only in 2006 [12–14]. In these papers, the authors used the dipole approximation to study the narrow total reflection resonances appearing on the extinction spectra just above the RA wavelengths. Experimental verification of this effect has been published in [15].

As already mentioned, the scattering resonances of various types are caused by the presence of the "parent" complex-valued poles of the field as a function of the wavelength. Unlike them, RAs are associated with the branch points and exist only for the infinite gratings. Therefore one can guess that the reason of the misinterpretation of the G-resonances in the studies related to infinite dielectric and metal wire gratings before 2006 was their extreme proximity to the RA branch-point wavelengths λ_m^{RA}, especially for the gratings made of thin wires.

Narrow resonances and high-Q eigenmodes need fine computational tools able to provide numerical results with many correct digits. Such a full-wave analysis of both wave-scattering and eignenvalue problems for the *dielectric-wire* gratings in free space was presented in [16, 17] using the meshless mode-expansion algorithm whose convergence is guaranteed. It refined earlier approximate results of [10–14].

Effects of both G- and LSP-resonances on infinite gratings of *silver* wires in free space (in the H-polarization case) have been studied numerically in [17, 18]. Here, the dielectric function ε_{met} was taken from [1]. Sample spectra of reflectance, transmittance and absorbance of silver-wire gratings are shown in Fig. 4.2.

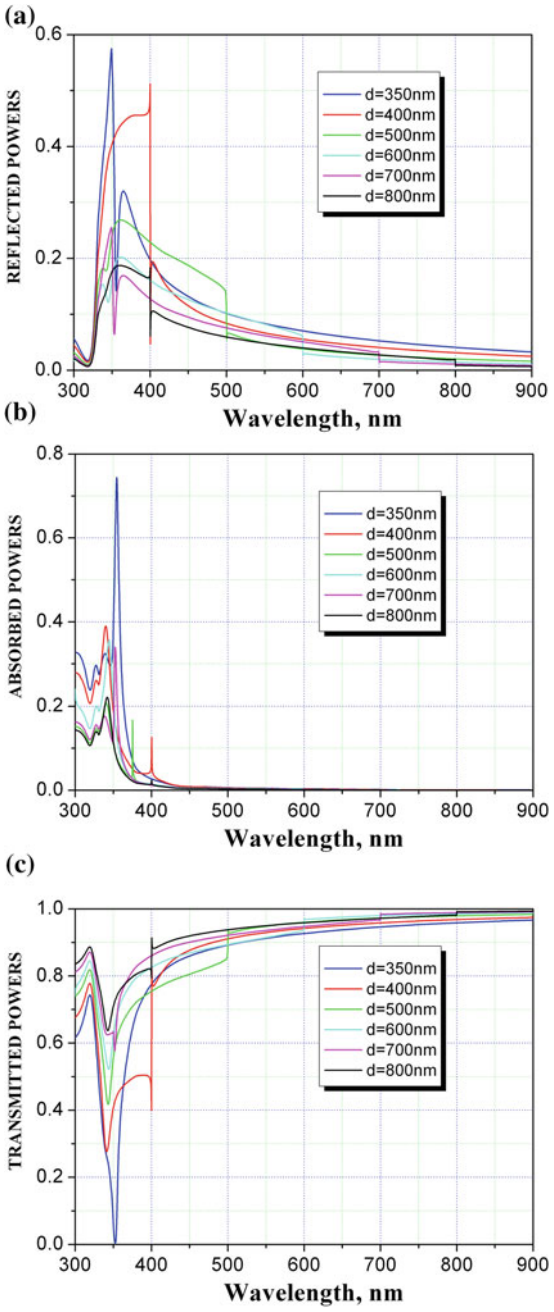

Fig. 4.2 Spectra of reflectance (**a**), transmittance (**b**), and absorbance (**c**) of infinite circular silver wire gratings of different periods with wire radius $a = 48.85$ nm. H-polarization, normal incidence

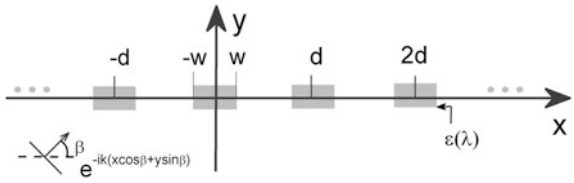

Fig. 4.3 Cross-sectional geometry of an infinite flat grating made of thin flat strips

As seen in Fig. 4.2, the LSP-resonance is present as a broad Lorentz peak near to 350 nm for all gratings. The G-modes usually display Fano-shape resonances in the reflectance and transmittance however simple Lorentz shape in absorbance. Important finding relates to the case of high-Q G-resonance on a grating of infinite number of wires with period tuned exactly to the wavelength of low-Q LSP-resonance. In this situation, the G-mode induces a narrow band of optical transparency cutting through the much wider band of intensive reflection associated with the LSP mode—see the curves for d = 350 and 700 nm.

In [18], new asymptotic expression for the complex-valued frequencies of G-modes was derived; it showed that if the wire radius or its dielectric contrast goes to zero then their wavelengths $\lambda^{G}_{\pm m}$ tend to the purely real RA wavelengths (4.1). Hence their Q-factors rise to infinity both for lossless and lossy wires.

In [16, 17] it has been discovered that if the grating is made of quantum wires (i.e. can be pumped to display gain) then the G-modes demonstrate ultra-law thresholds of lasing that can be much lower than the threshold of the SP-mode.

It is interesting to check how these optical effects manifest themselves on *finite* gratings that possess no RAs. Finite gratings of *many* thin wires remain relatively unclaimed area of research although early theoretical [6] and experimental papers [7, 19] noted unusual effects taking place near to the RA wavelengths. Accurate results of numerical study obtained by the convergent algorithm of [16, 17] have been published in [18, 20] for finite silver nanowire gratings where LSP and G-modes exist together. The resonances on G-modes become visible in the spectra of reflectance and transmittance (see [20] for the definition of these quantities for finite gratings) provided that the number of wires is at least N = 10. If it gets larger, the mode Q-factors tend to their limit values observed for infinite gratings.

4.3 Thin-Flat-Strip Gratings

Flat gratings made of thin *noble-metal strips* (see Fig. 4.3) have been always attractive in optics as easily manufactured components able to provide the wavelength and polarization discrimination. The scattering by strip gratings was initially studied assuming their infinite extension, zero thickness, perfect electric conductivity (PEC), and free-space location [4, 21–23].

Under these rude assumptions, the reflection and transmittance spectra of *infinite* gratings show only the RAs at wavelengths λ_m^{RA}. In contrast, a gold-strip grating lying on a dielectric substrate displays both LSP and G-resonances [24] provided that the substrate is sufficiently thick; and even a PEC-strip grating on a dielectric substrate has no LSP-resonances however has strong G-resonances [25].

The G-resonances on the free-standing *infinite* non-PEC strip gratings were found at first for thin dielectric strips in 1998 [26] although in the H-case narrow peaks of G-resonances were missed because of too coarse grid of computation points. This was clarified in the subsequent studies of impedance-strip [27] and silver-nanostrip [28] gratings. In [28], it has been shown analytically that the wavelengths of G-modes tend to λ_m^{RA} if the strip width or thickness gets smaller (see also (4.2) further in this section). Numerical study of both LSP and G-resonances on *finite* gratings of many silver strips has been published in [29–31].

It should be added that G-resonances have been also studied theoretically and experimentally on chains and gratings of 3-D particles—see, for instance, [32–42].

The controversy around the G-resonances on various gratings of metal scatterers consists in the fact that, in the early studies, they were frequently mixed up with more conventional LSP resonances. The failure to recognize their specific nature can be seen in the use of plasmon-related terminology such as "radiatively non-decaying plasmons," "supernarrow plasmon resonances," "subradiant lattice plasmons," and "plasmon resonances based on diffraction coupling of localized plasmons." This started changing recently when the terms like "collective resonance" of [39–41] and "photonic resonance" of [42] appeared. The fact that the G-modes and resonances exist in the scattering by the gratings of both metallic and dielectric elements and in the both of two principal polarizations makes it clear that they are caused solely by the periodicity and are not exotic plasmons.

To highlight the inter-relation between the conventional LSP-resonances and G-resonances in the visible-light scattering by periodic noble-metal scatterers, we present some numerical data computed using the convergent algorithm, based on the analytical regularization [28], for an *infinite* grating of thin silver strips illuminated by a normally incident H-polarized plane wave of the unit amplitude. The dispersion of the complex dielectric permittivity of silver has been taken into account using the measured data for the real and imaginary parts from [1].

The plots of reflectance, transmittance and absorbance as a function of the wavelength are presented in Fig. 4.4. The silver strip dimensions are taken as 50×150 nm^2 that results in the same area of cross-section as for the circular wires corresponding to Fig. 4.2. They demonstrate one broad LSP-resonance of enhanced reflection and absorption at 410 nm, associated with the first-order standing-wave mode built on the short-range surface plasmon wave bouncing between the edges of each strip. Besides, one can see one or two much sharper G-resonances at the wavelengths slightly larger than the period and half-period of the grating; these resonances, if well separated from LSP-ones, display the Fano shapes (two closely spaced extremums). If the wavelength of one of them coincides with the LSP-mode, a narrow-band optically induced transparency is observed.

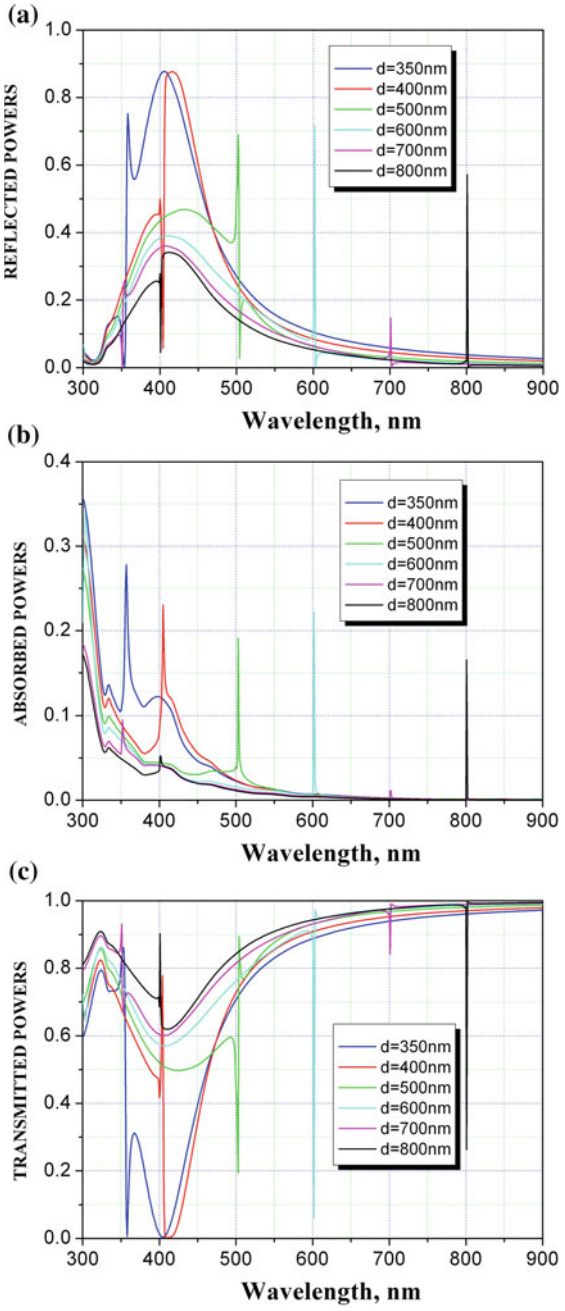

Fig. 4.4 Spectra of reflectance (**a**), transmittance (**b**), and absorbance (**c**) of infinite strip gratings of different periods with silver strip dimensions of $50 \times 150\,\text{nm}^2$, H-polarization, normal incidence

In Fig. 4.5, we demonstrate this effect in detail for the grating made of 10-nm thin silver strips. Such a reduced thickness is usual for today's nanotechnologies operating with electron-beam lithography and other techniques. Here one can see two broad LSP-resonances in the visible-light range around 640 and 380 nm, associated with the first and third-order LSP modes on each strip. Besides of them, one can also see an extremely sharp band of the optically induced transparency at the wavelength slightly larger than the period—see zoom in Fig. 4.5b. This is the effect of the G-mode resonance whose near-field patterns are shown in Figs. 4.6 and 4.7.

According to [28], in the normal-incidence case the normalized frequencies $\kappa = d/\lambda$ of the G-modes on a material strip grating with thickness $h/d \ll 1$ have the following asymptotic values:

$$\kappa_m^{GE,GH} = m - m^3(\chi_{E,H} 2\pi w h)^2 d^{-4} + O(|\varepsilon|\chi_{E,H}^2 m^4 h^4 d^{-4}), \tag{4.2}$$

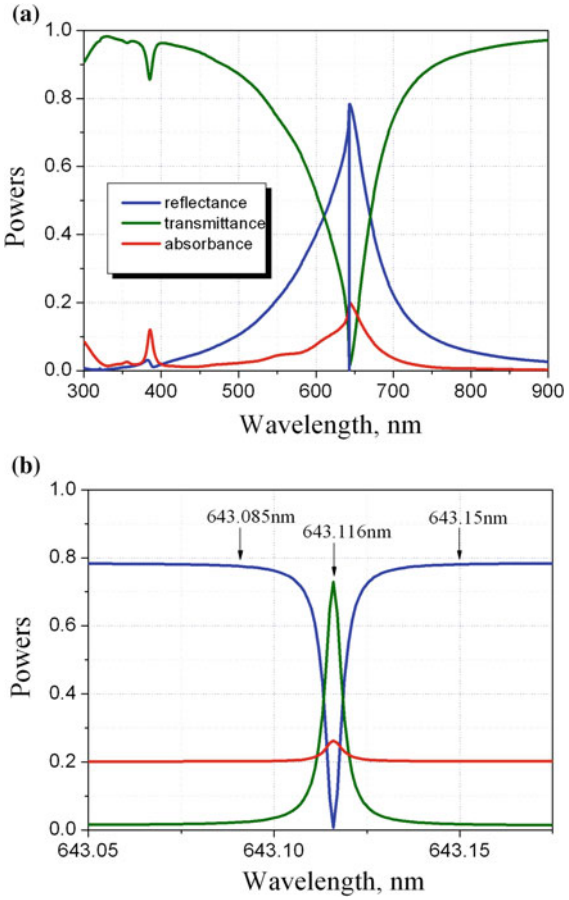

Fig. 4.5 Reflectance, transmittance, and absorbance spectra for the scattering of the H-polarized plane wave by infinite grating of silver nanostrips. The angle of incidence is $\beta = \pi/2$, the strip width is $2w = 150$ nm, the thickness is $h = 10$ nm, and the grating period is $d = 643$ nm

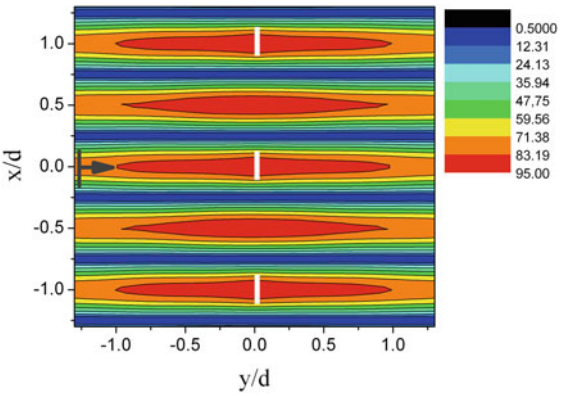

Fig. 4.6 The near-field pattern on three spatial periods for the scattering of the H-wave by infinite grating of thin silver nanostrips (shown using *white boxes*) in the combined LSP-G resonance (λ = 643.116 nm). Other parameters are the same as for Fig. 4.5

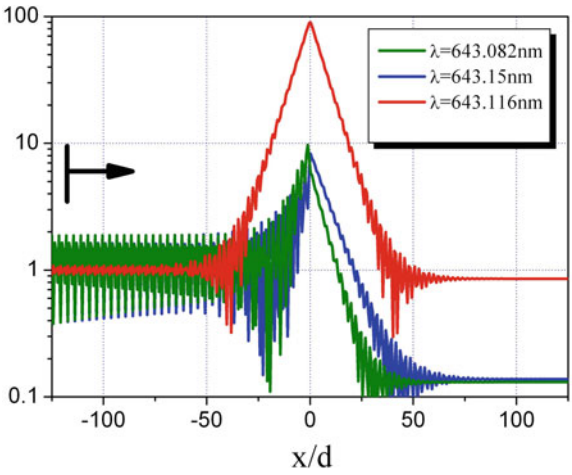

Fig. 4.7 The profile of the near field magnitude along the line $y = 0$ for the scattering of the H-wave around combined LSP-G resonance at λ = 643.082, 643.116, and 643.15 nm. Other parameters are the same as for Fig. 4.5

where $\chi_E = \varepsilon$ and $\chi_H = 1$. This means that, unlike LSP-mode, the G-mode quality factors $Q_m = -\mathrm{Im}\,\kappa_m / 2\mathrm{Im}\,\kappa_m$ tend to infinity if $h/d \to 0$ both for the lossy and lossless dielectric and metal materials in either polarization.

In the scattering problem, if the incident wave length approaches the real part of the mth natural G-mode wavelength, then the mth Floquet harmonic amplitude a_m takes a large value proportional to the mode Q-factor. This value is not restricted by the power conservation law because $\mathrm{Re}\,\kappa_m < m$ and hence the mth harmonic exponentially decays in the normal to the grating direction.

In resonance, under the normal incidence, the optical field near the grating is dominated by the intensive standing wave built of two identical Floquet harmonics with numbers $\pm m$. For the plots in Fig. 4.5, $m = 1$ and hence

$$H \approx 2a_1 e^{ik\alpha_1|x|} \cos(k\beta_1 y) \approx Q_{G1} \exp(-|x/d|Q_{G1}^{-1}) \cos(2\pi y/d). \quad (3)$$

This is fully consistent with the near field patterns observed in Figs. 4.6 and 4.7. Note that, in the G-resonance, very large values of the near field stretch to the distance of some 50 periods on the both sides of the silver-strip grating and the peak value is around 95. This is $\sim$25 times larger than in the LSP-resonance whose near-field bright spots are small and stick to the strips [28].

In the case of *finite* silver-strip gratings, the G-mode near-field pattern is well visible along the grating except a few periods near the ends. Additionally, in-G-resonance far field scattering patterns demonstrate intensive sidelobes in the plane of grating, explained by the mentioned Floquet modes excitation [29, 30]. Note that Q-factors of G-modes on *finite* grating depend on the number of strips N.

4.4 Comparison Between Two Shapes and Two Polarizations

The LSP-mode resonances are always observed on the deep sub-wavelength metal scatterers with $\mathrm{Re}\,\varepsilon_{met}(\lambda^P) < 0$. This is because the underlying physical phenomena have essentially static nature. Indeed, as it was shown in [43], the associated 2-D static problem of a non-magnetic cylinder in the uniform electric field possesses a set of discrete eigenvalues $\bar{\varepsilon}$ in terms of the dielectric constant. They depend on the shape of cylinder's cross-section and are negative real values. For a circular cylinder in free space, the single eigenvalue is $\bar{\varepsilon} = -1$, while for a rectangle it depends on the side lengths ratio. These eigenvalues have their projections to the H-polarized wave-scattering characteristics of the same 2-D metal scatterers whose dielectric permittivity is a function of the wavelength. The resonances on the LSP modes are found at the wavelengths near to those where $\mathrm{Re}\,\varepsilon_{met}(\lambda) = \bar{\varepsilon}$.

Note that in the E-polarization case, duality of the magnetic and electric fields suggests that similar properties take place for the magnetic permeability function $\mu(\lambda)$. However for all non-magnetic objects, there are no eigenvalues of ε and hence no E-polarized LSP-modes and associated to them scattering resonances.

Keeping in mind manufacturing issues and applications, it is interesting to compare the characteristics of gratings made of comparable silver wires and silver strips. To verify the polarization selectivity of considered gratings, it is also necessary to compare the scattering and absorption by each type of gratings in two alternative polarization regimes. Such comparison is presented in Fig. 4.8.

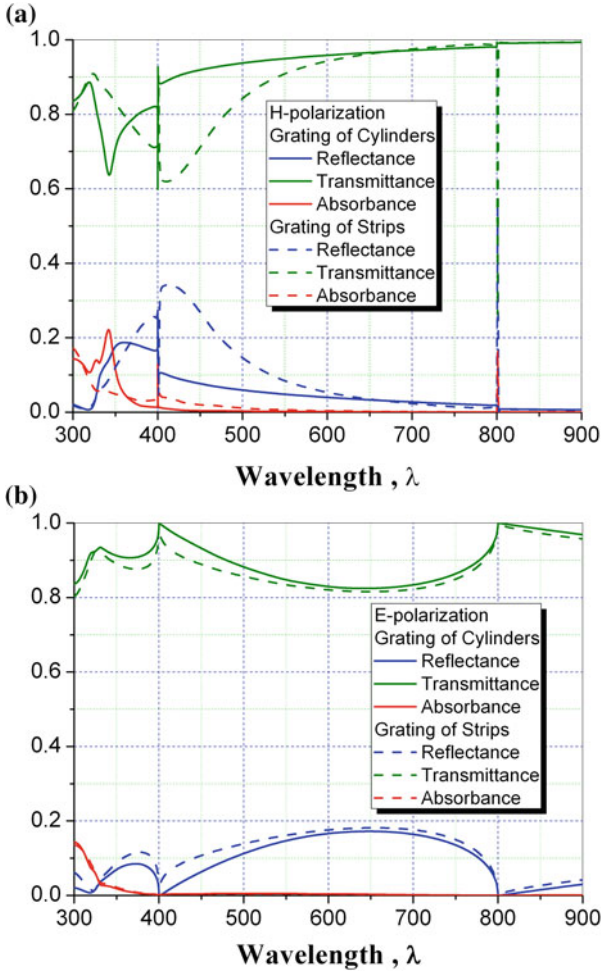

Fig. 4.8 Optical characteristics spectra of infinite silver gratings with period d = 800 nm illuminated by the H-polarized (**a**) and E-polarized (**b**) normally incident plane waves. The strip width is $2w$ = 150 nm and the thickness is h = 50 nm, while the wire radius is a = 48.85 nm

Here the wire and strip have the same area of cross-section, and the period is fixed at d = 800 nm. As one can see, in the case of H-polarization (Fig. 4.8a) each grating displays a broad Lorentz-shape SP-resonance at the corresponding wavelength. Besides of that, each grating produces two super-narrow G-resonances at the wavelengths slightly red-shifted from the ±1-st and ±2-nd RAs in accordance to (4.2). Note that LSP-mode wavelengths are generally different however the G-mode ones agree well provided that the cross-sectional areas of elements are the same. The optical response to the G-modes varies from the universal Fano shape to the optically induced transparency after tuning to the LSP-mode wavelength.

In the case of E-polarization depicted in Fig. 4.8b, no resonances are visible. As mentioned above, no E-polarized LSP-mode poles exist on any metal grating. The G-mode poles, in contrast, exist for both dielectric and metal gratings in both polarizations—see [11–16, 26, 28]. The reason that they are not seen in Fig. 4.8b can be found on examining (4.2): the Q-factors of G-modes in the E-case are in $|\varepsilon|^2$ times lower than in the H-case that is a factor varying from 25 at 400 nm to 1100 at 800 nm. This "invisibility" of G-modes in the E-polarization scattering regime has apparently hindered correct identification of their nature because it had suggested that they might have something common to LSP modes, non-existing in this regime at all. Still if a metal nanograting is placed on a dielectric substrate, the G-resonances become visible in the E-polarization spectra as well [24, 25].

The only visible feature of the optical spectra of either grating in the E polarization is the transmittance maxima exactly at the RAs (4.1). The curves of equal-area gratings are very close to each other in the whole visible range. Note that the largest difference in the optical responses for two alternative polarizations takes place near to the H-polarization LSP and G-mode resonances for either grating.

4.5 Applications to Photonic Devices

One of the main applications of conventional localized LSP-resonances is the sensing of the changes of refractive index of the medium hosting a plasmonic scatterer [2]. This is performed by measuring the position of the peak scattering or extinction and considered as key enabling technology in biological and chemical nanosensors. Therefore it is not a surprise that remarkable properties of the recently verified G-mode resonances have immediately attracted attention of scientists and engineers designing the sensors based on metallic nanogratings. In this community, such devices are called (erroneously) "Rayleigh-anomaly sensors" apparently because of the nearness of the G-resonances to the RA wavelengths [44–47]. The paper [47] is remarkable for the expressed there confidence that these resonances and Rayleigh anomalies are different phenomena (although G-mode resonances are still interpreted as some specific plasmons). Such sensors were proposed in [46] where a concentric gold ring nanograting was placed on the facet of optical fiber. As the G-resonance wavelength is given, in the main term, just by the RA value of (4.1), one can expect very attractive linear dependence of the scattering peak on the refractive index. Then the sensitivity, in wavelengths per refractive-index-unit, equals to the grating period. This is true however only provided that the analyte material is infinitely thick, while in practice it is usually a liquid making a finite overlay. Hence the location of the G-mode peak strongly depends on the overlay thickness, so that thinner than the wavelength overlays seem impractical. Only for thicker overlays the refractive-index sensitivity approaches the ultimate bulk-index sensitivity value of such a sensor [47].

4.6 Conclusions

We have demonstrated and discussed the main features of the grating or lattice resonances on the periodic arrays of circular silver wires and strips. As it became clear rather recently, these resonances are caused by specific poles of the field function and the associated modes have much higher Q-factors than those of the LSP modes. Therefore the G-resonances may serve as a superior alternative to LSP ones for various applications in chemical and biological sensing, photovoltaics, and SERS. The interplay between two types of resonances depends on the angle of incidence and the grating period and to a lesser extent on the size of each wire or strip. Choosing these parameters in optimal manner may help design nanosensors, absorbers, and SERS substrates with improved features.

Acknowledgements T.L.Z. and V.O.B. have contributed equally to this chapter. This work was supported, in part, by the National Academy of Sciences of Ukraine via the State Target Program "Nanotechnologies and Nanomaterials" and the International Visegrad Fund via the Ph.D. Scholarship to V.O.B.

References

1. P.B. Johnson, R.W. Christy, Optical constants of the noble metals. Phys. Rev. B **6**, 4370–4378 (1972)
2. J. Homola, Surface plasmon resonance sensors for detection of chemical and biological species. Chem. Rev. **108**(2), 462–493 (2008)
3. N.P. Stognii, N.K. Sakhnenko, Plasmon resonances and their quality factors in a finite linear chain of coupled metal wires. IEEE J. Sel. Topics Quant. Electron. **19**(3), 4602207 (2013)
4. H. Lamb, On the reflection and transmission of electric waves by a metallic grating. Proc. London Math. Soc. **29**, 523–544 (1898)
5. L. Rayleigh, On the dynamical theory of gratings. Proc. Royal Soc. London **A-79**, 399–416 (1907)
6. V. Twersky, On a multiple scattering theory of the finite grating and the Wood anomalies. J. Appl. Phys. **23**(10), 1099–1118 (1952)
7. A.W.K. Pursley, *The transmission of electromagnetic radiation through wire gratings*. Tech. Report Project 2351, Eng. Res. Inst., Univ. Michigan Ann Arbor (1956)
8. A.Z. Elsherbeni, A.A. Kishk, Modeling of cylindrical objects by circular dielectric and conducting cylinders. IEEE Trans. Antennas Propagat. **40**(1), 96–99 (1992)
9. D. Felbacq, G. Tayeb, D. Maystre, Scattering by a random set of parallel cylinders. J. Opt. Soc. Am. A: **11**(9), 2526–2538 (1994)
10. K. Yasumoto, H. Toyama, T. Kushta, Accurate analysis of 2-D electromagnetic scattering from multilayered periodic arrays of circular cylinders using lattice sums technique. IEEE Trans. Antennas Propagat. **52**(10), 2603–2611 (2004)
11. K. Ohtaka, H. Numata, Multiple scattering effects in photon diffraction for an array of cylindrical dielectrics. Phys. Lett. **73-A**(5–6), 411–413 (1979)
12. R. Gomez-Medina, M. Laroche, J.J. Saenz, Extraordinary optical reflection from sub-wavelength cylinder arrays. Opt. Exp. **14**(9), 3730–3737 (2006)
13. M. Laroche, S. Albaladejo, R. Gomez-Medina, J.J. Saenz, Tuning the optical response of nanocylinder arrays: an analytical study. Phys. Rev. B **74**(9), 245422/10 (2006)

14. D.C. Marinica, A.G. Borisov, S.V. Shabanov, Second harmonic generation from arrays of subwavelength cylinders. Phys. Rev. B **76**(8), 085311/10 (2007)
15. P. Ghenuche, G. Vincent, M. Laroche, N. Bardou, R. Haidar, J.-L. Pelouard, S. Collin, Optical extinction in single layer of nanorods. Phys. Rev. Lett., **109**, 143903/5 (2012)
16. V.O. Byelobrov, J. Ctyroky, T.M. Benson, R. Sauleau, A. Altintas, A.I. Nosich, Low-threshold lasing modes of infinite periodic chain of quantum wires. Opt. Lett. **35**(21), 3634–3636 (2010)
17. V.O. Byelobrov, T.M. Benson, A.I. Nosich, Binary grating of sub-wavelength silver and quantum wires as a photonic-plasmonic lasing platform with nanoscale elements. IEEE J. Sel. Topics Quant. Electron. **18**(6), 1839–1846 (2012)
18. D.M. Natarov, V.O. Byelobrov, R. Sauleau, T.M. Benson, A.I. Nosich, Periodicity-induced effects in the scattering and absorption of light by infinite and finite gratings of circular silver nanowires. Opt. Exp. **19**(22), 22176–22190 (2011)
19. D.W. Kerr, C.H. Palmer, Anomalous behavior of thin-wire gratings. J. Opt. Soc. Am. **61**(4), 450–456 (1971)
20. D.M. Natarov, R. Sauleau, A.I. Nosich, Periodicity-enhanced plasmon resonances in the scattering of light by sparse finite gratings of circular silver nanowires. IEEE Photonics Techn. Lett. **24**(1), 43–45 (2012)
21. Z.S. Agranovich, V.A. Marchenko, V.P. Shestopalov, Diffraction of a plane electro-magnetic wave from plane metallic lattices. Sov. Phys. Tech. Phys. **7**, 277–286 (1962)
22. T. Uchida, T. Noda, T. Matsunaga, Spectral domain analysis of electromagnetic wave scattering by an infinite plane metallic grating. IEEE Trans. Antennas Propagat. **35**(1), 46–52 (1987)
23. A. Matsushima, T. Itakura, Singular integral equation approach to plane wave diffraction by an infinite strip grating at oblique incidence. J. Electromagn. Waves Applicat. **4**(6), 505–519 (1990)
24. A. Christ, T. Zentgraf, J. Kuhl, S.G. Tikhodeev, N.A. Gippius, H. Giessen, Optical properties of planar metallic photonic crystal structures: experiment and theory. Phys. Rev. B **70**(12), 125113/15 (2004)
25. R. Rodríguez-Berral, F. Medina, F. Mesa, M. García-Vigueras, Quasi-analytical modeling of transmission/reflection in strip/slit gratings loaded with dielectric slabs. IEEE Trans. Microwave Theory Tech. **60**(3), 405–418 (2012)
26. T.L. Zinenko, A.I. Nosich, Y. Okuno, Plane wave scattering and absorption by resistive-strip and dielectric-strip periodic gratings. IEEE Trans. Antennas Propag. **46**(10), 1498–1505 (1998)
27. T.L. Zinenko, A.I. Nosich, Plane wave scattering and absorption by flat gratings of impedance strips. IEEE Trans. Antennas Propagat. **54**(7), 2088–2095 (2006)
28. T.L. Zinenko, M. Marciniak, A.I. Nosich, Accurate analysis of light scattering and absorption by an infinite flat grating of thin silver nanostrips in free space using the method of analytical regularization. IEEE J. Sel. Topics Quant. Electron. **19**(3), 9000108/8 (2013)
29. O.V. Shapoval, A.I. Nosich, Finite gratings of many thin silver nanostrips: optical resonances and role of periodicity. AIP Adv. **3**(4), 042120/13 (2013)
30. O.V. Shapoval, R. Sauleau, A.I. Nosich, Modeling of plasmon resonances of multiple flat noble-metal nanostrips with a median-line integral equation technique. IEEE Trans. Nanotechnol. **12**(3), 442–449 (2013)
31. O.V. Shapoval, J. Ctyroky J., A.I. Nosich, Resonance effects in the optical antennas shaped as finite comb-like gratings of noble-metal nanostrips, Proc. SPIE, Integr. Optics: Phys. Simulat., **8781**, 87810U/8 (2013)
32. K.T. Carron, W. Fluhr, M. Meier, A. Wokaun, H.W. Lehmann, Resonances of two-dimensional particle gratings in surface-enhanced Raman scattering. J. Opt. Soc. Am. B **3**(3), 430–440 (1986)
33. S. Zou, N. Janel, G.C. Schatz, Silver nanoparticle array structures that produce remarkably narrow plasmon lineshapes. J. Chem. Phys. **120**(23), 10871/5 (2004)

34. E.M. Hicks, S. Zou, G.C. Schatz, K.G. Spears, R.P. Van Duyne, L. Gunnarsson, T. Rindzevicius, B. Kasemo, M. Kall, Controlling plasmon line shapes through diffractive coupling in linear arrays of cylindrical nanoparticles fabricated by electron beam lithography. Nano Lett. **5**(6), 1065–1070 (2005)
35. N. Felidj, G. Laurent, J. Aubard, G. Levi, A. Hohenau, J.R. Krenn, F.R. Aussenegg, Grating-induced plasmon mode in gold nanoparticle arrays. J. Chem. Phys. **123**(22), 221103/5 (2005)
36. F.J.G. Garcia de Abajo, Colloquium: light scattering by particle and hole arrays. Rev. Mod. Phys. **79**(4), 1267–1289 (2007)
37. Y. Chu, E. Schonbrun, T. Yang, K.B. Crozier, Experimental observation of narrow surface plasmon resonances in gold nanoparticle arrays. Appl. Phys. Lett. **93**(18), 181108/3 (2008)
38. V.G. Kravets, F. Schedin, A.N. Grigorenko, Extremely narrow plasmon resonances based on diffraction coupling of localized plasmons in arrays of metallic nanoparticles. Phys. Rev. Lett. **101**(8), 087403/4 (2008)
39. B. Auguie, W.L. Barnes, Collective resonances in gold nanoparticle arrays. Phys. Rev. Lett. **101**(14), 143902/4 (2008)
40. V. Giannini, G. Vecchi, J. Gomez Rivas, Lighting up multipolar surface plasmon polaritons by collective resonances in arrays of nanoantennas. Phys. Rev. Lett. **105**, 266801/4 (2010)
41. S.R.K. Rodriguez, M.C. Schaafsma, A. Berrier, Gomez Rivas. J. Collect. Reson. Plasm. Crystals: Size Matters. Phys. B **407**(3), 4081–4085 (2012)
42. T.V. Teperik, A. Degiron, Design strategies to tailor the narrow plasmon-photonic resonances in arrays of metallic nanoparticles. Phys. Rev. B **86**(24), 245425/5 (2012)
43. D.R. Fredkin, I. Mayergoyz, Resonant behavior of dielectric objects (electrostatic resonances). Phys. Rev. Lett. **91**, 3902–3905 (2003)
44. P. Offermans, M.C. Schaafsma, S.K.R. Rodriguez, Y. Zhang, M. Crego-Calama, S.H. Brongersma, J. Gomez Rivas, Universal scaling of the figure of merit of plasmonic sensors. ACS Nano **5**(6), 5151–5157 (2011)
45. A.G. Nikitin, A.V. Kabashin, H. Dallaporta, Plasmonic resonances in diffractive arrays of gold nanoantennas: near and far field effects. Opt. Exp. **20**(25), 27941–27952 (2012)
46. S. Feng, S. Darmawi, T. Henning, P.J. Klar, X. Zhang, A miniaturized sensor consisting of concentric metallic nanorings on the end facet of an optical fiber. Small **8**, 1937–1944 (2012)
47. A. Ricciardi, S. Savoia, A. Crescitelli, E. Esposito, V. Galdi, A. Cusano, Surface versus bulk sensitivity of sensors based on Rayleigh anomalies in metallic nanogratings. Proc. SPIE, Optical Sens. **8774**, 87741 V/9 (2013)

Chapter 5
Electromagnetic Wave Diffraction by Periodic Planar Metamaterials with Nonlinear Constituents

V. Khardikov, P. Mladyonov, S. Prosvirnin and V. Tuz

Abstract We present a theory which explains how to achieve an enhancement of nonlinear effects in a thin layer of nonlinear medium by involving a planar periodic structure specially designed to bear a trapped-mode resonant regime. In particular, the possibility of a nonlinear thin metamaterial to produce the bistable response at a relatively low input intensity due to a large quality factor of the trapped-mode resonance is shown. Also a simple design of an all-dielectric low-loss silicon-based planar metamaterial which can provide an extremely sharp resonant reflection and transmission is proposed. The designed metamaterial is envisioned for aggregating with a pumped active medium to achieve an enhancement of quantum dots luminescence and to produce an all-dielectric analog of a 'lasing spacer'.

5.1 Introduction

One of the current trends in the theory of metamaterials is the development of two-dimensional planar periodic systems (metasurfaces, metamaterials) constructed in the form of arrays of resonant metallic or dielectric particles, which are arranged periodically on a thin (compared with the wavelength) dielectric layer. It is known that such planar metamaterials can create an environment whose electromagnetic characteristics are similar to those achieved in the traditional cavity resonators, but, unlike the latter, planar structures can have a much smaller size.

The metamaterial optical properties significantly depend on the resonant features of its constituent particles. It turns out that the particles with a special form of

V. Khardikov · P. Mladyonov · S. Prosvirnin (✉) · V. Tuz
Institute of Radio Astronomy of National Academy of Sciences of Ukraine,
4, Krasnoznamennaya Street, Kharkiv 61002, Ukraine
e-mail: prosvirn@rian.kharkov.ua

V. Khardikov · S. Prosvirnin · V. Tuz
School of Radio Physics, V.N. Karazin Kharkiv National University, 4, Svobody Square,
Kharkiv 61077, Ukraine

O. Shulika and I. Sukhoivanov (eds.), *Contemporary Optoelectronics*,
Springer Series in Optical Sciences 199, DOI 10.1007/978-94-017-7315-7_5

symmetric split rings or squares exhibit resonant properties, which result in a sudden change in the effective parameters of the metamaterial in a certain frequency band [1, 2]. Such resonances have quasi-static nature, since the size of the unit cell of the metamaterial is small. Thus, the particles can be seen as an oscillatory circuit, which has its eigen frequency and quality factor. Unfortunately, the presence of large radiation losses which appear due to the strong electromagnetic coupling of the system to free space, and a relatively small size (compared with the wavelength) of particles do not allow to reach the high-Q resonances in conventional planar metamaterials.

Nevertheless there is a possibility to achieve strong electromagnetic field confinement and localization in planar metamaterials which support a trapped-mode resonant regime [3, 4]. These resonances exist in two-dimensional planar periodic metamaterials with complex doubly or multi-connected metallic or dielectric particles, which have a low degree of asymmetry. In the near-infrared band it was shown theoretically [5] and confirmed experimentally [6] that introducing two slightly asymmetric metallic elements into the periodic cell can lead to the antiphase current trapped-mode excitation. In this case the electromagnetic coupling of conductive elements with free space is very weak, which provides low radiation losses and, therefore, high Q-factor resonances.

Such strong field localization in the mentioned metamaterials opens prospects for their application in laser and nonlinear optics. Thus, in [7, 8], the idea of using resonant enhancement of the electromagnetic field which is strongly localized on the surface of metallic nanoparticles is proposed to create nanoscale devices, in order to amplify or generate radiation in the visible and infrared bands. Further, in the development of this idea, a compact planar periodic structure is considered [9]. The proposed system provides strong field localization due to the trapped-mode excitation and acts like a conventional laser cavity.

In the present days, the theory of nonlinear metamaterials is actively developing [10–13] in the fields of controlling light with light [14], and parametric conversion of optical harmonics [15]. Here a particular interest is to study the peculiarities of intense light interaction with planar structures which sustain the trapped-mode resonant regime, and contain nonlinear components. In our opinion, strong field localization, which can be achieved in such structures, opens wide prospects for their application in the area of nonlinear optics.

5.2 Planar Metamaterials with Metallic Particles

5.2.1 Trapped-Modes: Concept

Let us assume an electromagnetic plane wave

$$\vec{E}^i = \vec{P}\exp[-j(\vec{k}^i \cdot \vec{r})] \tag{5.1}$$

incidents on a doubly periodic planar array of identical particles with a complex shape which are placed on a thin dielectric substrate. In (5.1) $\vec{P}$ is the polarization vector. Throughout this chapter the time dependence is assumed to be $\exp(j\omega t)$. The reflected and transmitted fields can be represented as a superposition of partial waves

$$\vec{E}^r = \sum_{m=-\infty}^{\infty} \sum_{m=-\infty}^{\infty} \vec{a}_{mn} \times \exp\{-j[\vec{\chi}_{mn}\vec{\rho} + \gamma(\vec{\chi}_{mn})z]\}, \quad z \geq 0, \tag{5.2}$$

$$\vec{E}^t = \sum_{m=-\infty}^{\infty} \sum_{m=-\infty}^{\infty} \vec{b}_{mn} \exp\{-j[\vec{\chi}_{mn}\vec{\rho} + \gamma(\vec{\chi}_{mn})(z+h)]\}, \quad z \leq -h, \tag{5.3}$$

where $\vec{\chi}_{mn} = \vec{e}_x(k_x^i + 2\pi n/d_x) + \vec{e}_y(k_y^i + 2\pi n/d_y)$, d_x and d_y are the periods of the array, $\vec{\rho} = \vec{e}_x x + \vec{e}_y y$, $\gamma(\vec{\chi}) = \sqrt{k^2 - \chi^2}$, and $\mathrm{Re}\,\gamma \geq 0$, $\mathrm{Im}\,\gamma \leq 0$.

Let us note that the propagation direction of any spatial partial wave in the reflected (5.2) and transmitted (5.3) fields depends only on directions of periodicity in the plane of array, sizes of its periods, the direction of initial plane wave incidence, and the wavelength. If a plane wave is incident on the double periodic array, the defined set of spatial partial waves is formed in space. As it can be easily derived, the propagation directions of spatial partial waves in this set do not change if the initial plane wave is incident upon the same array at any other direction provided that this direction coincides with the propagation direction of any spatial partial wave in the set.

The method of moments is generally used to solve the problem of electromagnetic scattering by arrays of metallic particles [16]. In the framework of this method it is implied that the metallic pattern is a very thin conductor. The method also takes into account the fact that the array is placed on a thin lossy dielectric substrate. By enforcing the impedance boundary condition

$$\vec{E}_{\tan}\big|_{z=0} = Z_s \vec{J}_s, \tag{5.4}$$

a vector integral equation is derived which is related to the current induced on a particular particle (here Z_s represents the surface impedance of this particular particle). The integral equation is reduced to an algebraic one by using the standard spectral-Galerkin technique. So, using the method of moments allows us to determine both the distribution and magnitude of the current J which flows along the metallic particles and further to calculate the reflection r and transmission t coefficients.

As a result of calculations of the current distribution and optical response of planar metamaterials with particles of different shape it is revealed that if these particles possess specific structural asymmetry, in a certain frequency band, the antiphase current oscillations with almost the same amplitudes appear on the

particles parts (arcs). The scattered electromagnetic field produced by such current oscillations is very weak, which drastically reduces its coupling to free space and therefore radiation losses. Indeed, both the electric and magnetic dipole radiations of currents oscillating in the arcs of the neighbor particles are cancelled. As a consequence, the strength of the induced current can reach very high value and therefore ensure a high-Q resonant optical response. Such a resonant regime is referred to so-called 'trapped-modes', since this term is traditionally used in describing electromagnetic modes which are weakly coupled to free space.

The most remarkable property of the trapped-modes is that they allow in principle to achieve high-Q resonances in a very thin structure. The trapped-modes are normally inaccessible in the systems with particles of a symmetrical form, but can be excited if these particles have a certain structural asymmetry that allows reaching weak coupling to free space. Nevertheless, in the arrays with symmetric configuration of particles the excitation of the trapped-modes is also possible if the shape of these particles is specially designed. It is important that in the latter case the system can become polarization-insensitive.

Further we consider two particular configurations of metallic particles with asymmetric [4] and symmetric [17] designs which can support the trapped-mode excitation (see Fig. 5.1). In the first case, the unit cell consists of metallic particles in the form of asymmetrically split rings (ASRs). Each ASR contains two identical strip elements positioned opposite each other. The right-hand split between the strips φ_1 is a little different from the left-hand one φ_2, so that the square unit cell is asymmetric with regard to the y-axis. In the second case, the unit cell of the studied metamaterial contains a single double-ring (DR). The radii of the outer and inner rings are fixed at a_1 and a_2, respectively. Suppose the width of the metal rings in both configurations is $2w$, and the arrays are placed on a thin dielectric substrate

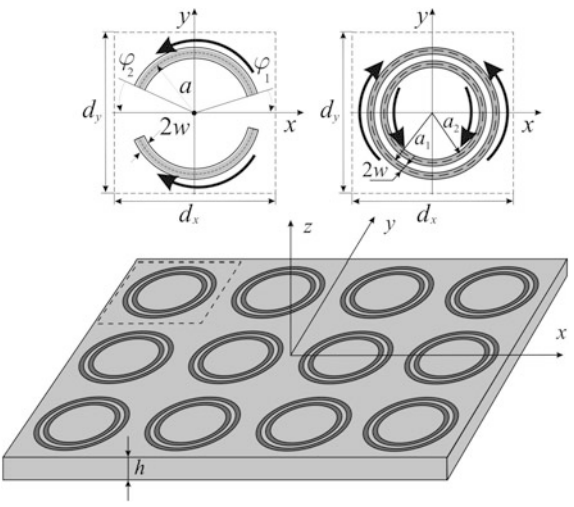

Fig. 5.1 Fragment of the planar metamaterial and its elementary unit cells

with thickness h and permittivity ε. We consider a normal incidence on the structure of a linearly polarized monochromatic plane wave with an amplitude A and frequency ω. Assume that the direction of the vector $\vec{E}$ of the incident wave coincides with the direction of the y-axis.

In the case of such a polarization of the incident field, in the structure of the first type, the trapped-mode excitation can be reached. Due to the 4-fold symmetry of the unit cell of the structure of the second type, its resonant properties do not depend on the direction of the vector $\vec{E}$ of the normally incident wave, i.e., as it was mentioned before, the second configuration is polarization-insensitive.

Typical frequency dependences of the transmission coefficient and current magnitudes calculated with the method of moments for ASR and DR structures are presented in Fig. 5.2. One can see that at the dimensionless frequency nearly æ = $d/\lambda \approx 0.3$, a sharp resonance occurs in the structures of both types (see the shaded areas in Fig. 5.2). This resonance corresponds to the excitation of a trapped-mode because equal and opposite directed currents in the two arcs of each complex particle of array radiate a little in free space. The resonance has a high-Q factor, and the current magnitude reaches its maximum exactly at this frequency. Remarkably,

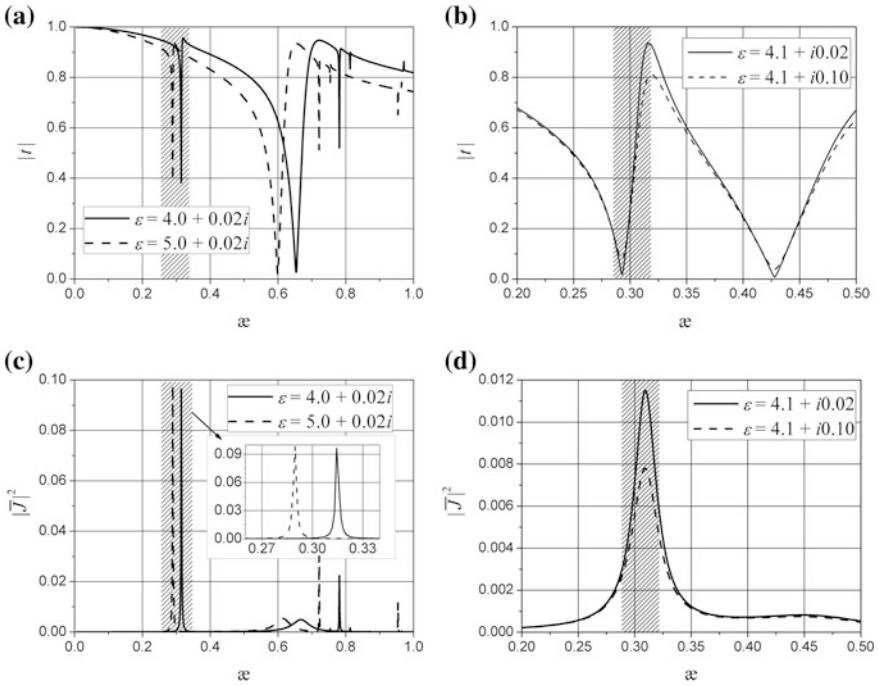

Fig. 5.2 Frequency dependences (æ = d/λ) of magnitudes of the transmission coefficient and squared average current (in a.u.) of the metamaterial with (**a**, **c**) ASR and (**b**, **d**) DR particles; (**a**, **c**) $d = d_x = d_y = 900$ nm, $\varphi_1 = 15°$, $\varphi_2 = 25°$; (**b**, **d**) $d = d_x = d_y = 800$ nm

as the permittivity of the substrate increases, the resonant frequency shifts down to low values (Fig. 5.2a). Also as the value of ohmic losses in the metamaterial substrate increases, the magnitude of current and quality factor of the resonance decrease (Fig. 5.2b) but, nevertheless, the resonance remains to be well observed. We expect that such a high-Q resonant regime is promised to enhance some non-linear effects, since at the frequency of trapped-mode excitation the field is strongly localized inside the system.

5.2.2 Inner Field Intensity Estimation

In order to understand the ability of the proposed structures to enhance some non-linear effects, it is required to estimate the intensity of the inner field which is localized within the system. The special geometry of the metamaterial with symmetrical DR allows us to obtain an analytical expression for this demand [12, 13]. So, at the trapped-mode resonance, the electromagnetic energy is confined to a very small region between the rings. Therefore, the approximation based on the transmission line theory is used here to estimate the field intensity between the rings. According to this theory, conductive rings are considered as two wires with a distance b between them. Along these wires the currents flow in opposite directions. Thus the electric field strength is defined as

$$E_{in} = V/b, \tag{5.5}$$

where $V = ZJ$ is the line voltage, $b = a_1 - a_2 - 2w$, J is the magnitude of current which flows along the DR-element, and Z is the impedance of line. The impedance is determined at the resonant dimensionless frequency $æ_0 = d/\lambda_0$,

$$Z = æ_0 \frac{60l}{dC_0}, \tag{5.6}$$

where $l = \pi(a_1 + a_2)/2$, and

$$C_0 = \frac{1}{4}\ln\left[\frac{p}{2w} + \sqrt{\left(\frac{p}{2w}\right)^2 - 1}\right], \tag{5.7}$$

is the capacity in free space per unit length of line, $p = a_1 - a_2$. From this model it follows that the electric field strength between the rings is directly proportional to the current magnitude J. Since the unit cell is small in comparison with the wavelength, the current magnitude J can be substituted with its value averaged along the metallic ring, $\bar{J}$. From our estimations it can be concluded that the intensity of the incident field $I_{in}(\bar{J})$ which is enough for the nonlinearity to become apparent is about 10 kW/cm^2.

5.2.3 Optical Bistability and All-Optical Switching

The effect of optical bistability (or, generally, multistability) is a basis of numerous applications such as all-optical switching, differential amplification, unidirectional transmission, power limiting, pulse shaping, optical digital data processing, and others [14, 18]. A classical example of the bistable device is a Fabry-Perot interferometer filled with a Kerr-type nonlinear material. In this case, the resonator provides feedback, which is essential to obtain a multivalued intensity at the structure's output. However, in such a system, both relatively strong light power and/or large enough volume of the nonlinear optical material are generally needed to achieve a sizeable nonlinear response.

A promising way to realize an optical switching in compact devices can be found in using planar metamaterials. In particular, at the trapped-mode resonance the electromagnetic energy is confined to a limited extent around the particles, where the energy density reaches substantially high values. This makes the response of the metamaterial operating in the trapped-mode regime extremely sensitive to the dielectric properties of the substrate.

If a metamaterial is under an action of intense light (i.e. in the nonlinear regime), the substrate permittivity ε becomes to be depended on the value of the average current $\bar{J}(\varepsilon = \varepsilon_1 + \varepsilon_2 I_{in}(\bar{J}))$. Thus, the appropriate average current magnitude for a given ε can be found using the next nonlinear equation

$$\bar{J} = \tilde{A} F_{\bar{J}}(\omega,\ \varepsilon(I_{in}(\bar{J}))), \tag{5.8}$$

where $\tilde{A}$ is a dimensionless coefficient which depicts how many times the incident field magnitude A is greater than 1 V/cm. Thus, the magnitude A is a parameter of (5.8), and, at a fixed frequency ω, the solution of this equation is the average current magnitude $\bar{J}$ which is depended on the magnitude of the incident field ($\bar{J} = \bar{J}(A)$). Further, on the basis of the current $\bar{J}(A)$ found by a numerical solution of (5.8), the permittivity of the nonlinear substrate $\varepsilon = \varepsilon(I_{in}(\bar{J}))$ is obtained and the reflection and transmission coefficients are calculated as functions of the frequency and magnitude of the incident field.

If the structure substrate is made of a Kerr-type nonlinear material, the curves of the average current magnitude versus incident field magnitude have a form of *S*-like hysteresis loops (Fig. 5.3a) [10]. Such a form of the input-output characteristic of the studied metamaterial is inherent to the most optical bistable devices. The presence of hysteresis results in abrupt switching between two distinct states with small and large levels of transmission nearly the frequency of the trapped-mode excitation (Fig. 5.3b).

The origin of such a bistable response can be explained as follows. Suppose that the trapped-mode resonant frequency is slightly higher than the incident field frequency. As the intensity of the incident field rises, the magnitude of currents on the metallic particles increases. This leads to increasing the field strength inside the substrate and its permittivity as well. As a result, the frequency of the resonant

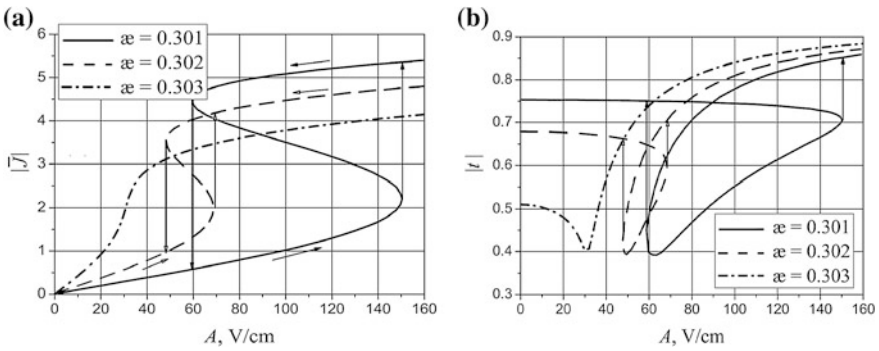

Fig. 5.3 The square of **a** the current magnitude (in a.u.) averaged along split ring and **b** the magnitude of the transmission coefficient versus the incident field magnitude in the case of the ASR nonlinear metamaterial ($\varepsilon_1 = 4 + 0.02i$, $\varepsilon_2 = 5 \times 10^{-3}$ cm^2/kW). The *arrows* indicate a bistable switching between two distinct levels of transmission. All other parameters are the same as in Fig. 5.2

mode decreases and shifts toward the frequency of incident wave, which, in turn, enhances further the coupling between the current modes and the inner field intensity in the nonlinear substrate. This positive feedback increases the slope of the rising edge of the transmission spectrum, as compared to the linear case. As the frequency extends beyond the resonant mode frequency, the inner field magnitude in the substrate decreases and the permittivity goes back towards its linear level, and this negative feedback keeps the resonant frequency close to the incident field frequency.

At once, the frequency dependence of the transmission coefficient magnitude manifests some impressive discontinuous switches to different values of transmission, as the frequency increases and decreases in the resonant range for the sufficiently large intensity of the incident wave. The shifting of the peak of the resonance and the onset of a bistable transmissivity through the ASR structure is similar to that of the reflection from a Fabry-Perot cavity (Fig. 5.4a). However, the trapped-mode resonance is Fano-shaped rather than the Lorentzian, as is the characteristic of 1D Fabry-Perot cavities. This Fano resonance can lead to a peculiar transmission spectra and bistable behavior. In particular, the transmission resonance of the ASR structure may loop back on themselves (Fig. 5.4b).

The most appropriate form for the realization of optical switching has the spectral characteristics of the DR-metamaterial [11–13]. While the dependence of the inner field intensity versus the incident field magnitude has the form of the *S*-like hysteresis loop (Fig. 5.5a), the frequency dependence of the magnitude of the transmission coefficient has a sharp asymmetric Fano-shape of the spectral line where the transmission coefficient changes from low to high level in a very narrow frequency range (Fig. 5.5b). Such a form of resonance is very suitable to obtain great amplitude of switching since there are gently sloping bands of the high reflection and transmission before and after the resonant frequency.

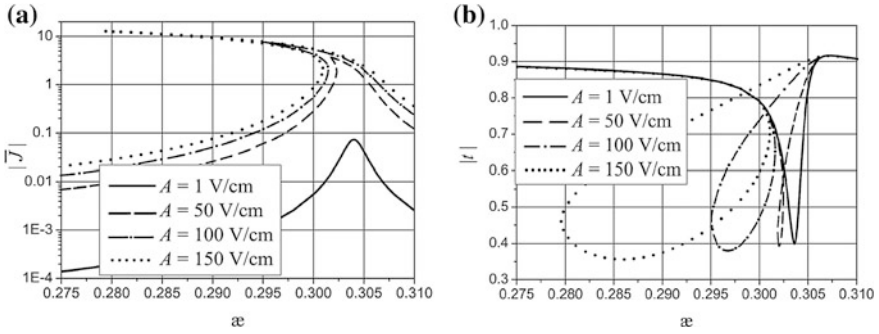

Fig. 5.4 Frequency dependences of **a** the square of the current magnitude (in a.u.) averaged along split ring (on the logarithmic scale) and **b** the magnitude of the transmission coefficient in the case of the ASR nonlinear metamaterial ($\varepsilon_1 = 4 + 0.02i$, $\varepsilon_2 = 5 \times 10^{-3}$ cm^2/kW). All other parameters are the same as in Fig. 5.2

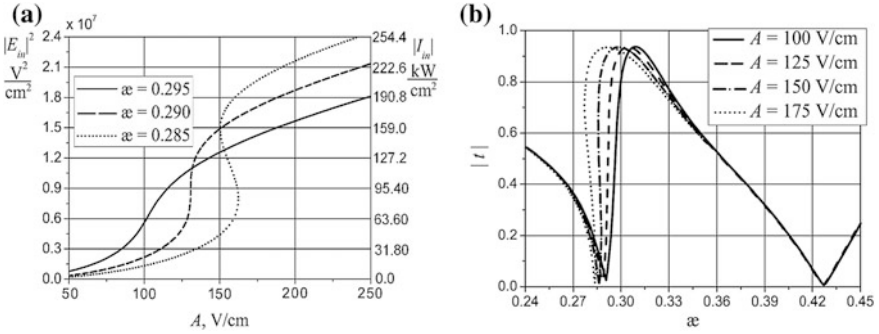

Fig. 5.5 Magnitude of the inner field intensity **a** versus magnitude of the incident field and **b** the frequency dependences of the magnitude of the transmission coefficient in the case of the DR nonlinear metamaterial ($\varepsilon_1 = 4.1 + 0.02i$, $\varepsilon_2 = 5 \times 10^{-3}$ cm^2/kW). All parameters are the same as in Fig. 5.2

5.2.4 *Strong Field Confinement in Bilayer-Fish-Scale System*

Another type of metamaterials which supports Fano-shape trapped-mode resonances is a planar metamaterial which consists of an equidistant array of continuous meandering metallic strips placed on a thin dielectric substrate (the fish-scale structure [19]). In this system the trapped-mode resonance appears due to a special form of strips, and this form is designed in view of the polarization of the incident field. A way to expand the functionality of such a fish-scale structure lies in the placement of the second grating on the back side of a thin dielectric substrate. In this case additional trapped-mode resonance can appear due to interaction of the

antiphase current oscillations between two adjacent gratings [20, 21]. This configuration is of particular interest in the case when the substrate is made of a field intensity dependent material (for example, a Kerr-type medium) because the strong field localization between the gratings can significantly enhance the nonlinear effects.

We consider a bilayer structure which consists of two gratings of planar perfectly conducting infinite strips placed on each side ($z = 0$, $z = -h$) of a thin dielectric substrate (Fig. 5.6). The unit cell of the structure under study is a square with sides $d_x = d_y = d$. The width of the metal strips and their deviation from a straight line, respectively, are $2w/d = 0.05$ and $\Delta/d = 0.25$. Suppose that the normally incident field is a plane monochromatic wave polarized in parallel to the strips (x-polarization).

Due to the bilayer configuration of the structure under study there are two possible current distributions which correspond to the trapped-mode resonances. The first distribution is the antiphase current oscillations in the arcs of each grating. In this case the structure can be considered as a system of two coupled resonators which operate at the same frequency because the gratings are identical. We have labeled this resonant frequency in Fig. 5.7 by the letter æ$_1$. Obviously that the distance h between the gratings will strongly effect on the resonant frequency position since this parameter defines the electromagnetic coupling degree. The Q-factor of this resonance is higher in the bilayer structure than that one existed in a single-layer structure but their similarity lies in the fact that the current magnitude in the metallic pattern depends relatively weakly on the thickness and permittivity of the substrate.

The second distribution is the antiphase current oscillations between two adjacent gratings. Similarly we have labeled this resonant frequency in Fig. 5.7 by the letter æ$_2$. It is well known that the closer are the interacting metallic elements, the higher is the Q-factor of the trapped-mode resonance. Thus varying both the distance between the gratings and substrate permittivity changes the trapped-mode

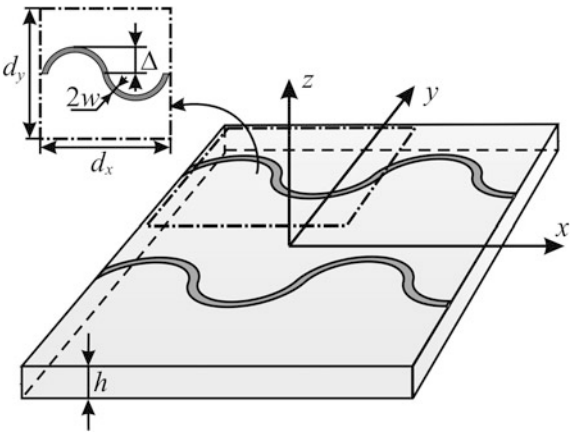

Fig. 5.6 Fragment of the bilayer-fish-scale metamaterial and its elementary unit cell

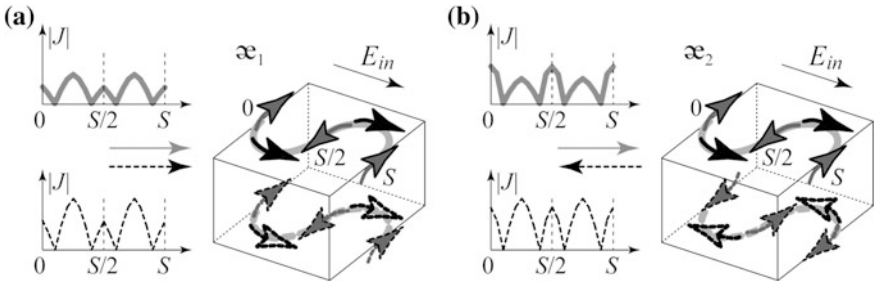

Fig. 5.7 The surface current distribution along the strips in the bilayer structure composed of gratings with wavy-line metal strips

resonant conditions and this changing manifests itself in the current magnitude. Remarkably that in this type of current distribution the field is localized between the gratings, i.e. directly in the substrate, which can sufficiently enhance the nonlinear effects if the substrate is made of field intensity dependent material.

This circumstance is depicted in Fig. 5.8 where typical curves of the inner field intensity and the transmission coefficient magnitude are given as functions of the frequency and the incident field intensity in the nonlinear regime.

For these calculations the structure parameters are chosen in such a way that the both resonances are closely settled and the frequency $æ_1$ of the first resonance is less than the frequency $æ_2$ of the second one ($æ_1 < æ_1$). One can see that as the intensity of the incident field rises, the frequency dependences of the inner intensity magnitude take a form of the bent resonances and a bistable regime occurs. An important point is that this bending is different for the first and second type of resonances due to the difference in the current magnitude changing at these two

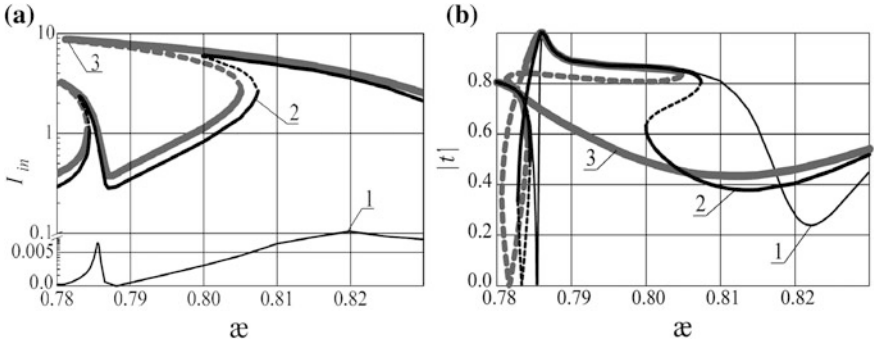

Fig. 5.8 The frequency dependences of **a** the inner field intensity (on the logarithmic scale) and **b** the transmission coefficient magnitude versus the different incident field intensity in the case of the nonlinear permittivity ($\varepsilon = \varepsilon_1 + \varepsilon_2 |I_{in}|^2$, dimension of I_{in} is in kW/cm^2); ε_1 = 3.0, ε_2 = 0.005 cm^2/kW; curve 1—I_0 = 1 kW/cm^2, curve 2—I_0 = 200 kW/cm^2, curve 3—I_0 = 300 kW/cm^2

frequencies. Thus at the resonant frequency $æ_2$ the magnitude of currents which flow along the strips of both gratings are significant, and they are greater than the magnitude of currents which flow nearly the resonant frequency $æ_1$ (Fig. 5.8a), and, in the nonlinear regime, the bending of the peak $æ_2$ is greater than that one of the peak $æ_1$. As a result, the spectral curves of the transmission coefficient magnitude experience different changes nearly the trapped-mode resonant frequencies. At the frequency $æ_1$ the curve transforms into a closed loop that is typical for the sharp nonlinear Fano-shape resonances. The second resonance $æ_2$ is smooth but it undergoes more distortion in the wider frequency band, and at a certain incident field intensity this resonance can overlap the first one (Fig. 5.8b). Evidently that in this case the transmission coefficient has more than two stable states, i.e. the effect of multistability occurs.

5.3 All-Dielectric Planar Metamaterials

5.3.1 Trapped-Modes in All-Dielectric Arrays

Unfortunately huge energy dissipation which is inherent to metal in the infrared and visible parts of spectrum results in increasing ohmic losses in plasmonic metamaterials [22–25] and decreasing Q-factor of the trapped-mode resonance [5]. Moreover, the trapped-mode resonance completely degrades in metamaterials with low degree of the particle asymmetry. Thus, using all-dielectric low-loss structures which are capable to support the trapped-mode excitation in the infrared and visible ranges is extremely good idea [26].

Let us consider the plane wave diffraction on a double-periodic structure which consists of two dielectric elements within the periodic cell (Fig. 5.9). These

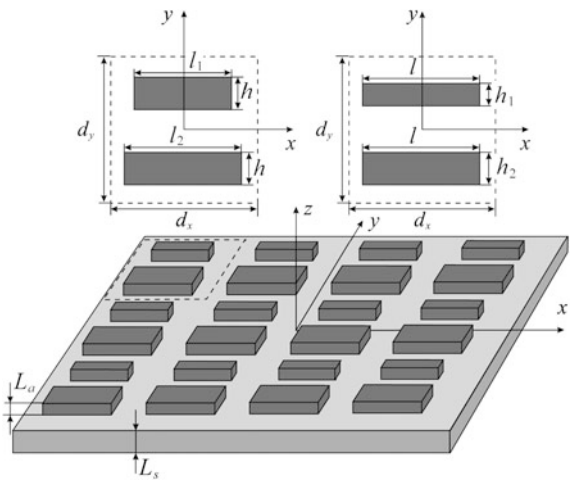

Fig. 5.9 Fragment of the all-dielectric metamaterial and its elementary unit cells

dielectric elements create an electromagnetic environment similar to that one existed in the open dielectric resonators, and, unlike structures with metallic particles, a form of these dielectric elements does not entail a substantial increase of the resonant wavelength. Note that a material with high refractive index is required for designing the array of subwavelength elements to provide the resonant light interaction with the system. In particular, we propose to construct such elements in the form of two closely spaced parallelepipeds with different length or width similar to those ones which are shown in Fig. 5.9. In particular, in this figure the double-periodic array of dielectric bars placed on a silica substrate with thickness L_s is presented. The unit cell of the array includes a pair of dielectric bars which have different length ($l_1 \leq l_2$, $h_1 = h_2 = h$) or width ($h_1 \leq h_2$, $l_1 = l_2 = l$) but are identical in thickness (L_a) and are made from the same material. The sizes of the square periodic cell are chosen to be identical $d_x = d_y = d$. The period cells of both structures are symmetric relative to the line drawn through the cell center parallel to the y-axis.

We suppose a normal incidence of the linearly x-polarized plane waves on the structure. The resonant response of the array is studied in the near-infrared wavelength range from 1000 to 2500 nm. The substrate is assumed to be made from the synthetic fused silica whose refractive index is approximately 1.44 in the wavelength range under consideration [27]. Refractive index of the dielectric bars is n_d. The diffraction problem is solved numerically using the mapped PSTD method [28, 29].

The wavelength dependences of the reflection coefficient magnitude of the arrays with a single dielectric bar (lines 1 and 2) and a pair of dielectric bars (line 3) within the periodic cell are shown in Fig. 5.10. In this figure the arrows and Roman numeral I indicate the high-Q resonance which appears in the array consisted of a pair of dielectric bars with different length. Each dielectric bar within the periodic cell interacts with light like a half-wavelength open dielectric resonator and the resulting field has antiphase distribution within the pair of these resonators, and, hence, this resonant regime can be referred to the trapped-mode excitation [6]. The main distinctive feature of the trapped-mode resonance in the two-element dielectric array is a great red shift of its wavelength compared to the resonant wavelengths of the corresponding single-element arrays (see Fig. 5.10). This feature of the trapped-mode resonant regime of the proposed all-dielectric metamaterial is quite important in view of its possible application in the infrared and visible parts of spectrum. First, the ratio of the array pitch to the wavelength may be decreased to design more homogeneous metamaterials. Second, as the resonant wavelength shifts up the field confinement increases since the radiation losses decrease. Remarkably, these behaviors are especially important when designing artificial nonlinear and gain artificial media.

The proposed array can be made of semiconductor in the wavelength range where semiconductor has a transparency window. In particular, the transparency windows of germanium and silicon lie between 1.9 and 16 μm, and 1.2 and 14 μm, respectively [30]. The semiconductor interacts with light as a good dielectric within these transparency windows. The typical value of the dissipation losses tangent of

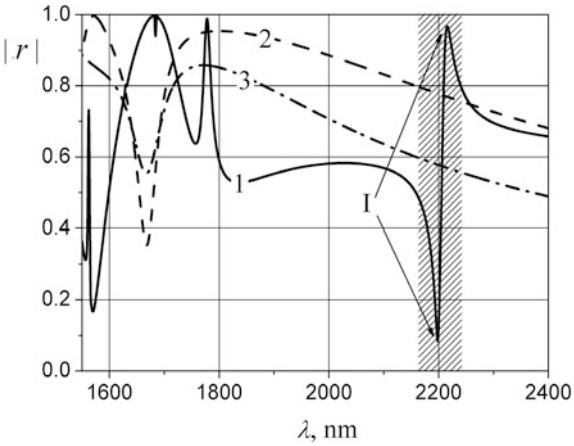

Fig. 5.10 Wavelength dependences of the reflection coefficient magnitude of the metamaterial with single dielectric bar (lines *2* and *3*) and pair of dielectric bars (line *1*) in periodic cell; $d = 975$ nm, $L_s = \infty$, $L_a = h = 195$ nm, $n_d = 5.5$. Line *1* corresponds to bars with sizes $l_1 = 780$ nm and $l_2 = 877$ nm, line *2* corresponds to bars with size $l = 877$ nm, and line *3* corresponds to bars with size $l = 780$ nm

the mentioned semiconductors within these bands do not exceed 10^{-3}. Also the semiconductor refractive index has extremely small variation of its value within the transparency windows. The germanium refractive index changes from 4.15 to 4.0, and silicon refractive index changes from 3.41 to 3.52, respectively.

The wavelength dependences of the reflection coefficient magnitude for the periodic array made from a pair of germanium bars in the periodic cell are shown in Fig. 5.11. One can see that both the Q-factor and the value of red shift of the trapped-mode resonance increase as the asymmetry of bars within the periodic cell decreases. The calculated Q-factors of the trapped-mode resonances are 203 and 1080 for the structures with germanium bars having geometrical parameters $l_1 = 780$ nm, $l_2 = 877$ nm and $l_1 = 838$ nm, $l_2 = 877$ nm, respectively (see lines 2 and 3 in Fig. 5.11). These values of Q-factor are ten orders of magnitude greater than those ones reached in the plasmonic metamaterials.

5.3.2 *Saturation Effect in Active Metamaterial*

We have proposed a simple design of an all-dielectric low-loss silicon-based planar metamaterial [31] which can produce an extremely sharp resonant reflection and transmission in the wavelength of about 1550 nm due to both low dissipation losses and the trapped-mode excitation. The Q-factor of the resonance exceeds in ten times

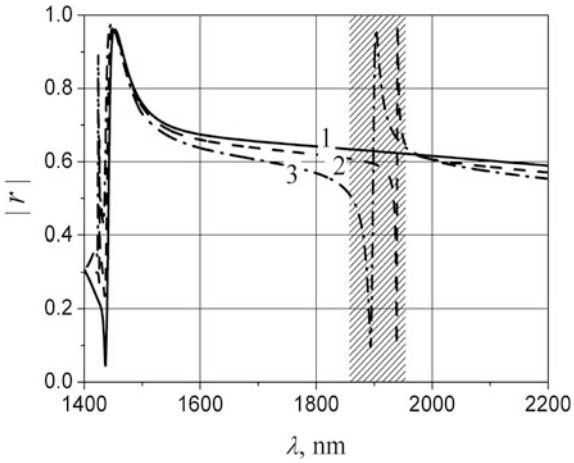

Fig. 5.11 Wavelength dependences of the reflection coefficient magnitude of the metamaterial with pair of germanium bars in periodic cell; d = 975 nm, $L_s = \infty$, $L_a = h$ = 195 nm, l_2 = 877 nm, the germanium refractive index is $n_d = 4.12$ which is actual for wavelength 1900 nm. Line *1*, *2* and *3* correspond to bars with sizes l_1 = 877 nm, l_1 = 838 nm, and l_1 = 780 nm, respectively

the Q-factor of resonances in known plasmonic structures. The designed metamaterial is envisioned for aggregating with a pumped gain medium to achieve an enhancement of luminescence, and we report that in the designed metamaterial the essential enhancement of luminescence (more than 500 times) in a layer which consists of pumped quantum dots (QD) can be reached. This value significantly exceeds the known values of the luminescence enhancement in known plasmonic planar metamaterials [32].

The model of a gain nonlinear medium assumes the introducing negative frequency dependent conductivity in the form:

$$\sigma(\omega) = \frac{1}{1 + I/I_s} \cdot \frac{\sigma_0(1 + i\omega\tau)}{(1 + \omega_0^2\tau^2) + 2i\omega\tau - \omega^2\tau^2}, \tag{5.9}$$

where $\omega_0 = 1.26 \times 10^{15}$ s^{-1} corresponds to the wavelength λ_0 = 1550 nm, $\tau = 4.85 \times 10^{-15}$ s, $\varepsilon_{QD} = 2.19$ corresponds to the refractive index $n_{QD} = 1.48$ of the non-pumped quantum dot laser medium, and $\sigma_0 = -500$ Sm/m corresponds to an emission factor $\mathrm{tg}\delta_e = -0.021$ by analogy with a lossy factor of media. Small value of τ results in a wide-band QD spectral line and enables us to exclude from consideration the effects caused by displacement of metamaterial dissipation peak and maximum of exciton emission line of QDs. Let us notice that the pump level (σ_0) is in one order of magnitude less than it is needed in the case of plasmonic metamaterials because there is a low degree of losses in the all-dielectric array. The factor $(1 + I/I_s)^{-1}$ allows us to consider the effect of the luminescence enhancement of the gain saturation effect which is inherent to the active media. Here the parameter

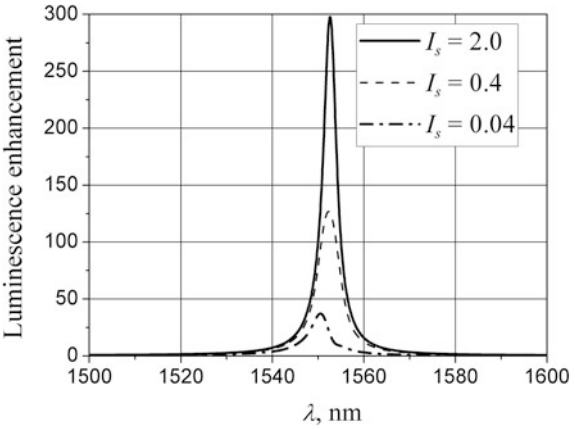

Fig. 5.12 The wavelength dependences of the luminescence enhancement (in a.u.) of the QD layer hybridized with the all-dielectric metamaterial for different value of I_s

I_s is proportional to the saturation intensity and displays the effect of inversion population reducing in the gain medium by simulated emission. It is proportional to the maximum of the internal field (I). The saturation factor $[(1 + I/I_s)^{-1}]$ is calculated separately for each point of the spatial grid which takes into account the heterogeneity of the QD layer. We should note that the small value of an emission factor results in independence of the QD refractive index on the saturation factor. Thus the effect of saturation versus the luminescence enhancement of QD layer hybridized with the all-dielectric metamaterial can be considered under this model.

The diffraction approach proposed in [31] is further used to calculate the luminescence enhancement in the QD layer hybridized with the all-dielectric metamaterial. This approach consists of evaluation of considered structure luminescence through the difference of the energy dissipation in the passive and active (pumped) structure. The dissipation energy is calculated from the solution of the corresponding diffraction problem for the separate plane wave. The luminescence enhancement equals to the ratio of the luminescence of the hybridized structure to the luminescence of the 210 nm homogeneous QD layer placed on 50 nm silica substrate. The wavelength dependences of the luminescence enhancement of the QD layer hybridized with the all-dielectric metamaterial for different values of the saturation intensity are shown in Fig. 5.12. The reducing of the luminescence enhancement with decreasing of the saturation intensity can be explained by exciting strong local field in the hybridized structure which results in the saturation factor decreasing. The distribution of the saturation factor in cross section ($z = -155$ nm) is depicted in Fig. 5.13. One can see the burning holes appearance in the distribution (see dark areas in Fig. 5.13). The energy of optical pumping within these holes is completely spent by simulated emission. The effect of gain saturation does not strongly affect on the photoluminescence in the system but it needs to be taken into account when designing optical amplifiers and lasing spacers.

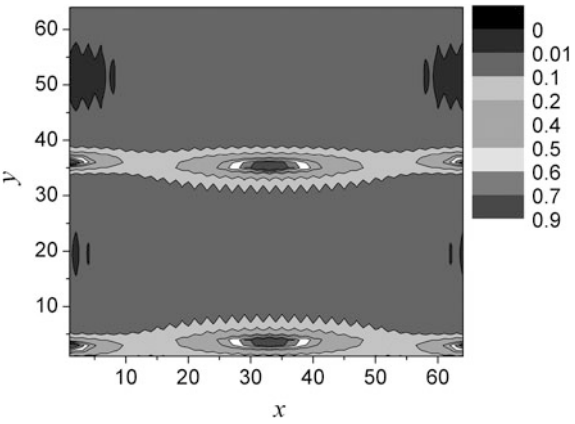

Fig. 5.13 The distribution of saturation factor in the cross section $z = -155$ nm; $\lambda = 1553$ nm; $I_s = 0.4$

Acknowledgements This work was supported by the Ukrainian State Foundation for Basic Research, the Project no. Φ54.1/004, and National Academy of Sciences of Ukraine, Program 'Nanotechnologies and Nanomaterials', the Project no. 1.1.3.17.

References

1. C. Rockstuhl, T. Zentgraf, H. Guo, N. Liu, C. Etrich, I. Loa, K. Syassen, J. Kuhl, F. Lederer, H. Giessen, Resonances of split-ring resonator metamaterials in the near infrared. Appl. Phys. B **84**(1–2), 219–227 (2006)
2. N. Liu, H. Guo, L. Fu, H. Schweizer, S. Kaiser, H. Giessen, Electromagnetic resonances in single and double split-ring resonator metamaterials in the near infrared spectral region. Phys. Stat. Sol. (b) **244**(4), 1251–1255 (2007)
3. S. Prosvirnin, S. Zouhdi, Resonances of closed modes in thin arrays of complex particles, in *Advances in Electromagnetics of Complex Media and Metamaterials*, ed. by S. Zouhdi, M. Arsalane (Kluwer Academic Publishers, Dordrecht, 2003), pp. 281–290
4. V.A. Fedotov, M. Rose, S.L. Prosvirnin, N. Papasimakis, N.I. Zheludev, Sharp trapped-mode resonances in planar metamaterials with a broken structural symmetry. Phys. Rev. Lett. **99** (14), 147401 (2007)
5. V. Khardikov, E. Iarko, S. Prosvirnin, Trapping of light by metal arrays. J. Opt. **12**(4), 045102 (2010)
6. Z.L. Samson, K.F. MacDonald, F. DeAngelis, B. Gholipour, K. Knight, C.C. Huang, E. Di Fabrizio, D.W. Hewak, N.I. Zheludev, Metamaterial electro-optic switch of nanoscale thickness. Appl. Phys. Lett. **96**(14), 143105 (2010)
7. D.J. Bergman, M.I. Stockman, Surface plasmon amplification by stimulated emission of radiation: quantum generation of coherent surface plasmons in nanosystems. Phys. Rev. Lett. **90**(2), 027402 (2003)
8. D.J. Bergman, M.I. Stockman, Can we make a nanoscopic laser? Laser Phys. **14**(3), 409–411 (2004)
9. N.I. Zheludev, S.L. Prosvirnin, N. Papasimakis, V.A. Fedotov, Lasing spacer. Nature Photonics **2**(6), 351–354 (2008)
10. V. Tuz, S. Prosvirnin, L. Kochetova, Optical bistability involving planar metamaterials with broken structural symmetry. Phys. Rev. B **82**(23), 233402 (2010)

11. V. Tuz, S. Prosvirnin, All-optical switching in metamaterial with high structural symmetry—bistable response of nonlinear double-ring planar metamaterial. Eur. Phys. J. Appl. Phys. **56** (3), 30401 (2011)
12. V. Tuz, V. Butylkin, S. Prosvirnin, Enhancement of absorption bistability by trapping-light planar metamaterial. J. Opt. **14**(4), 045102 (2012)
13. V. Dmitriev, S. Prosvirnin, V. Tuz, M. Kawakatsu, Electromagnetic controllable surfaces based on trapped-mode effect. Adv. Electromagn. **1**(2), 89–95 (2012)
14. H.M. Gibbs, *Optical bistability: controlling light with light* (Academic, Orlando, 1985)
15. M.W. Klein, C. Enkrich, M. Wegener, S. Linden, Second-harmonic generation from magnetic metamaterials. Science **313**(5786), 502–504 (2006)
16. S.L. Prosvirnin, S. Zouhdi, Multi-layered arrays of conducting strips: switchable photonic band gap structures. AEÜ Int. J. Electron. Commun. **55**(4), 260–265 (2001)
17. S.L. Prosvirnin, N. Papasimakis, V. Fedotov, S. Zouhdi, N. Zheludev, Trapped-mode resonances in planar metamaterials with high structural symmetry, in *Metamaterials and Plasmonics: Fundamentals, Modelling, Applications*, ed. by S. Zouhdi, et al. (Springer, The Netherlands, 2009), pp. 201–208
18. S.I. Tarapov, YuP Machekhin, A.S. Zamkovoy, *Magnetic resonance for optoelectronic materials investigating* (Collegium, Kharkov, 2008)
19. V.A. Fedotov, P.L. Mladyonov, S.L. Prosvirnin, N.I. Zheludev, Planar electromagnetic metamaterial with a fish scale structure. Phys. Rev. E **72**(5), 056613 (2005)
20. N. Papasimakis, V.A. Fedotov, N.I. Zheludev, S.L. Prosvirnin, Metamaterial analog of electromagnetically induced transparency. Phys. Rev. Lett. **101**(25), 253903 (2008)
21. P.L. Mladyonov, S.L. Prosvirnin, Wave diffraction by double-periodic gratings of continuous curvilinear metal strips placed on both sides of a dielectric layer. Radio Physics and Radio Astronomy **1**(4), 309–320 (2010)
22. C. Jansen, I. Al-Naib, N. Born, M. Koch, Terahertz metasurfaces with high Q-factors. Appl. Phys. Lett. **98**(5), 051109 (2011)
23. I. Al-Naib, R. Singh, C. Rockstuhl, F. Lederer, S. Delprat, D. Rocheleau, M. Chaker, T. Ozaki, R. Morandotti, Appl. Phys. Lett. **101**(7), 071108 (2012)
24. S. Zhang, D.A. Genov, Y. Wang, M. Liu, X. Zhang, Plasmon-induced transparency in metamaterials. Phys. Rev. Lett. **101**(4), 047401 (2008)
25. Z.-G. Dong, H. Liu, M.-X. Xu, T. Li, S.-M. Wang, S.-N. Zhu, X. Zhang, Plasmonically induced transparent magnetic resonance in a metallic metamaterial composed of asymmetric double bars. Opt. Express **18**(17), 18229–18234 (2010)
26. V. Khardikov, E. Iarko, S. Prosvirnin, A giant red shift and enhancement of the light confinement in a planar array of dielectric bars. J. Opt. **14**(3), 035103 (2012)
27. I.H. Malitson, Interspecimen comparison of the refractive index of fused silica. J. Opt. Soc. Am. **55**(11), 1205–1208 (1965)
28. G. Xian, M.S. Mirotznik, S. Shi, D.W. Prather, Applying a mapped pseudospectral time-domain method in simulating diffractive optical elements. J. Opt. Soc. Am. A **21**(5), 777–785 (2004)
29. V.V. Khardikov, E.O. Iarko, S.L. Prosvirnin, Using transmission matrix and pseudospectral time-domain method to study of light diffraction on planar periodic structures. Radiophysics and Radioastronomy **13**(2), 146–158 (2008)
30. H.H. Liu, Refractive index of silicon and germanium and its wavelength and temperature derivatives. J. Phys. Chem. Ref. Data **9**(3), 561–658 (1980)
31. V.V. Khardikov, S.L. Prosvirnin, Enhancement of quantum dot luminescence in all-dielectric metamaterial. arXiv:1210.4146 [physics.optics], October 2012
32. K. Tanaka, E. Plum, J.Y. Ou, T. Uchino, N.I. Zheludev, Multifold enhancement of quantum dot luminescence in plasmonic metamaterials. Phys. Rev. Lett. **105**(22), 227403 (2010)

Chapter 6
Gaussian Beam Tunneling Through a Gyrotropic-Nihility Finely-Stratified Structure

Vladimir R. Tuz and Volodymyr I. Fesenko

Abstract The three-dimensional Gaussian beam transmission through a ferrite-semiconductor finely-stratified structure being under an action of an external static magnetic field in the Faraday geometry is considered. The beam field is represented by an angular continuous spectrum of plane waves. In the long-wavelength limit, the studied structure is described as a gyroelectromagnetic medium defined by the effective permittivity and effective permeability tensors. The investigations are carried out in the frequency band where the real parts of the on-diagonal elements of both effective permittivity and effective permeability tensors are close to zero while the off-diagonal ones are non-zero. In this frequency band the studied structure is referred to a gyrotropic-nihility medium. It is found out that a Gaussian beam keeps its parameters unchanged (beam width and shape) when passing through the layer of such a medium except of a portion of the absorbed energy.

6.1 Introduction

The conception of *nihility* was firstly introduced in the paper [1] for a hypothetical medium, in which the following constitutive relations hold $\vec{D} = 0, \vec{B} = 0$. So, nihility is the electromagnetic nilpotent, and the wave propagation cannot occur in nihility, because $\nabla \times \vec{E} = 0$ and $\nabla \times \vec{H} = 0$ in the absence of sources therein.

V.R. Tuz · V.I. Fesenko
Institute of Radio Astronomy of NASU, Kharkiv, Ukraine

V.R. Tuz (✉)
School of Radio Physics, V.N. Karazin Kharkiv National University, Kharkiv, Ukraine
e-mail: tvr@rian.kharkov.ua

V.I. Fesenko
Lab. "Photonics", Kharkiv National University of Radio Electronics, Kharkiv, Ukraine
e-mail: volodymyr.i.fesenko@gmail.com

O. Shulika and I. Sukhoivanov (eds.), *Contemporary Optoelectronics*,
Springer Series in Optical Sciences 199, DOI 10.1007/978-94-017-7315-7_6

Further, in [2], this conception of nihility was extended for an isotropic chiral medium whose constitutive relations are: $\vec{D} = \varepsilon\vec{E} + i\rho\vec{H}, \vec{B} = \mu\vec{H} - i\rho\vec{E}$, where$\rho$ is the chirality parameter. Thus, a possible way for composing such a medium in the microwave band was proposed using canonical chiral wire particles. The effective material parameters are calculated on the basis of the Maxwell-Garnett mixing rule, and in a certain narrow frequency band it is found out that the real parts of both effective permittivity and effective permeability become close to zero ($\varepsilon' \approx 0, \mu' \approx 0$) while the real part of the chirality parameter is maintained at a finite value ($\rho' \neq 0$). It was revealed that in such an isotropic *chiral-nihility* medium there are two eigenwaves with right (RCP) and left (LCP) circularly polarized states, whose propagation constants depend only on the chirality parameter, and these propagation constants of the RCP (γ^+) and LCP (γ^-) waves are equal in magnitude but opposite in sign to each other ($\gamma^{\pm} = \pm k_0, \rho = \pm\gamma$). Thereby one of these eigenwaves experiences the forward propagation while the other one experiences the backward propagation. Here, the sign of the chirality parameter, which in turn depends on the chiral particles handedness, determines which of the eigenwaves appears as a backward propagating one. In particular, this feature results in some exotic characteristics in the wave transmission through and reflection from a single layer and multilayer systems which consist of such a chiral-nihility medium [3, 4].

Besides chiral media, the circularly polarized eigenwaves are also inherent to magneto-optic gyrotropic materials (e.g. ferrites or semiconductors) in the presence of an external static magnetic field, when this field is biased to the specimen in the longitudinal geometry relative to the direction of wave propagation (in the Faraday configuration) [5]. Such gyrotropic media are characterized by the permeability or permittivity tensor $\vec{D} = \hat{\varepsilon}\vec{E}, \vec{B} = \hat{\mu}\vec{H}$ with non-zero off-diagonal elements (gyrotropic parameters). Apart from getting double-negative conditions [6–10], combining together gyromagnetic (ferrite) and gyroelectric (semiconductor) materials into a certain unified gyroelectromagnetic structure [6] allows one to reach the *gyrotropic-nihility* effect within a narrow frequency band [11]. In particular, in a finely stratified ferrite-semiconductor structure such a condition is valid in the microwave band nearly the frequencies of ferromagnetic and plasma resonances. In this case the real parts of on-diagonal elements of both effective permeability and effective permittivity tensors of such an artificial medium simultaneously acquire zero while the off-diagonal ones are non-zero. It is revealed that in this medium the backward propagation can appear for one of the circularly polarized eigenwaves which leads to some unusual optical features of the system and provides an enhancement of the polarization rotation, impedance matching to free space, and complete light transmission.

Since a gyrotropic-nihility medium with appropriate parameters can support backward propagating eigenwaves and is impedance matched to free space, it becomes substantial to study the focusing properties of a finite thickness slab in which the gyrotropic-nihility condition holds [12]. It involves consideration of the field in the form of a spatially finite wave beam, in particular, as a Gaussian beam which is presented as a continual superposition of plane waves. On the other hand,

it is also known that there are several beam phenomena such as displacement of the beam axis, beam splitting, focal and angular shifts which are not found in the reflection and transmission of separate plane waves [13–16], and so they require particular consideration. These studies are usually based on a two-dimensional beam formulation, which is quite efficient [17, 18]. Nevertheless, in gyrotropic media a three-dimensional model of beam representation should be considered to take into account the polarization effects and to predict the change in the ellipticity of the scattered beam [19, 20].

In this chapter, we demonstrate the phenomenon of the three-dimensional Gaussian beam transmission through a ferrite-semiconductor finely-stratified structure being under an action of an external static magnetic field biased along the structure periodicity. The investigations are carried out for two different frequencies. The first one is chosen to be far from frequencies of the ferromagnetic and plasma resonances and the second one is selected to be at the gyrotropic-nihility frequency. The main goal is to show that such a finely-stratified structure is able to tunnel a Gaussian beam practically without any distortion of its form when the gyrotropic-nihility condition holds.

6.2 Problem Formulation and Methods of Solution

6.2.1 Magnetic Multilayer Structure Under Study

A stack of N identical double-layer slabs (unit cells) which are arranged periodically along the z axis is investigated (Fig. 6.1). Each unit cell is composed of ferrite (with constitutive parameters $\varepsilon_1, \hat{\mu}_1$) and semiconductor (with constitutive parameters $\hat{\varepsilon}_2, \mu_2$) layers with thicknesses d_1 and d_2, respectively. The structure's period is $L = d_1 + d_2$, and in the x and y directions the system is infinite. We suppose that the structure is finely-stratified, i.e. its characteristic dimensions d_1, d_2 and L are significantly smaller than the wavelength in the corresponding layer $d_1 \ll \lambda, d_2 \ll \lambda, L \ll \lambda$ (the long-wavelength limit). An external static magnetic field $\vec{M}$ is directed along the z-axis. The input $z \leq 0$ and output $z \geq NL$ half-spaces are homogeneous, isotropic and have constitutive parameters ε_0, μ_0.

We use common expressions for constitutive parameters of normally magnetized ferrite and semiconductor layers with taking into account the losses. They are defined in the form [21–23]:

$$\varepsilon_1 = \varepsilon_f, \quad \hat{\mu}_1 = \begin{pmatrix} \mu_1^T & -i\alpha & 0 \\ i\alpha & \mu_1^T & 0 \\ 0 & 0 & \mu_1^L \end{pmatrix}, \quad \hat{\varepsilon}_2 = \begin{pmatrix} \varepsilon_2^T & -i\beta & 0 \\ i\beta & \varepsilon_2^T & 0 \\ 0 & 0 & \varepsilon_2^L \end{pmatrix}, \quad \mu_2 = \mu_s, \quad (6.1)$$

where for ferrite the auxiliary values are $\mu_1^T = 1 + \chi' + i\chi''$, $\chi' = \omega_0\omega_m\left[\omega_0^2 - \omega^2(1 - b^2)\right]D^{-1}$, $\chi'' = \omega\omega_m b\left[\omega_0^2 - \omega^2(1 + b^2)\right]D^{-1}$, $\alpha = \Omega' + i\Omega''$, $\Omega' = \omega\omega_m$

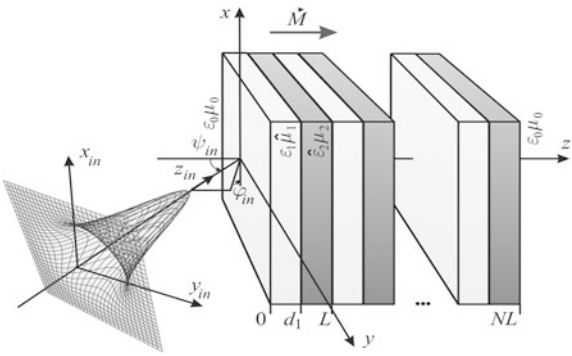

Fig. 6.1 A periodic stack of one-dimensional double-layer ferrite-semiconductor structure under the Gaussian beam illumination

$\left[\omega_0^2 - \omega^2(1+b^2)\right]D^{-1}$, $\Omega'' = 2\omega^2\omega_0\omega_m bD^{-1}$, $D = \left[\omega_0^2 - \omega^2(1+b^2)\right]^2 + 4\omega_0^2\omega^2 b^2$, ω_0 is the Larmor frequency and b is a dimensionless damping constant; for semiconductor layers the auxiliary values are $\varepsilon_2^L = \varepsilon_0\left[1 - \omega_p^2[\omega(\omega+iv)]^{-1}\right]$, $\beta = \varepsilon_0\omega_p^2\omega_c\left[\omega((\omega+iv)^2 - \omega_c^2)\right]^{-1}$, $\varepsilon_2^T = \varepsilon_0\left[1 - \omega_p^2(\omega+iv)[\omega((\omega+iv)^2 - \omega_c^2)]^{-1}\right]$, ε_0 is the part of permittivity attributed to the lattice, ω_p is the plasma frequency, ω_c is the cyclotron frequency and v is the electron collision frequency in plasma.

The frequency dependences of the permeability and permittivity parameters calculated using (6.1) are presented in Fig. 6.2. Note that the values of $\mathrm{Im}(\mu_1^T)$, $\mathrm{Im}(\alpha)$ and $\mathrm{Im}(\varepsilon_2^T)$, $\mathrm{Im}(\beta)$ are so close to each other that the curves of their frequency dependences coincide in the corresponding figures.

6.2.2 *Gaussian Beam Representation*

The auxiliary coordinate system x_{in}, y_{in}, z_{in} (see, Fig. 6.1) is introduced to describe the incident beam field [13, 14, 20]. In it, the incident field $\vec{\psi}_{in} = \vec{E}_{in}$, $\vec{H}_{in}$ is defined as a continued sum of the partial plane waves with the spectral parameter $\vec{\kappa}_{in}$ (it has a sense of the transverse wave vector of the partial plane wave):

$$\vec{\psi}_{in} = \vec{v}\int\limits_{-\infty}^{\infty} U(\vec{\kappa}_{in})\exp[i\vec{\kappa}_{in}(\vec{r}_{in} + \vec{a}_{in}) + i\gamma_{in}(z_{in} + a_3)]d\vec{\kappa}_{in}. \qquad (6.2)$$

In (6.2) the vector $\vec{v}$ is related to E ($\vec{v} = \vec{e}_{in}$) or H ($\vec{v} = \vec{h}_{in}$) field, respectively; $\vec{e}_{in} = \vec{P}V_p - \vec{b}_{in} \times \vec{P}V_s$, $\vec{h}_{in} = \vec{P}V_s + \vec{b}_{in} \times \vec{P}V_p$ where the vector $\vec{P} = \vec{z}_0 \times \vec{n}$ describes the field polarization. In the structure's coordinates x, y, z, the vector $\vec{n}$ is characterized via the next components $(\cos\theta_{in}\cos\varphi_{in}, \cos\theta_{in}\sin\varphi_{in}, 0)$, where

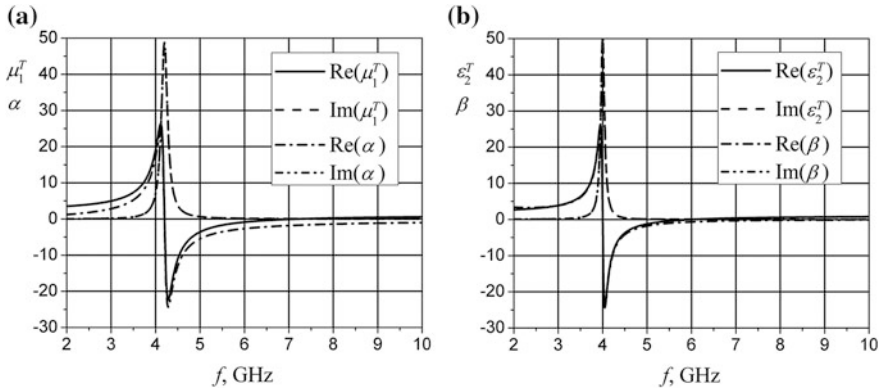

Fig. 6.2 Frequency dependences of the permeability and permittivity of ferrite (**a**) and semiconductor (**b**) layers, respectively. We use typical parameters for these materials in the microwave region. For the ferrite layers, under saturation magnetization of 2000 G, parameters are $\omega_0/2\pi = 4.2$ GHz, $\omega_m/2\pi = 8.2$ GHz, $b = 0.02$, $\varepsilon_f = 5.5$. For the semiconductor layers, parameters are: $\omega_p/2\pi = 4.5$ GHz, $\omega_c/2\pi = 4.0$ GHz,$\nu/2\pi = 0.05$ GHz, $\varepsilon_0 = 1.0$, $\mu_s = 1.0$

$\theta_{in} = 90^\circ - \psi_{in}$; $\vec{z}_0$ is the basis vector of z-axis, and the vector $\vec{b}_{in} = (\cos\theta_{in}\cos\varphi_{in},\ \cos\theta_{in}\sin\varphi_{in},\ -\sqrt{\varepsilon_0\mu_0 - \cos^2\theta_{in}})$ describes the direction of the incident beam propagation; $U(\vec{\kappa}_{in})$ is the spectral density of the beam in the plane $z_{in} = 0$; $\gamma_{in} = \sqrt{k_0^2 - \vec{\kappa}_{in}\cdot\vec{\kappa}_{in}}$, $0 < \arg(\sqrt{k_0^2 - \vec{\kappa}_{in}\cdot\vec{\kappa}_{in}}) < \pi$, and $\vec{a}_{in} = (a_1, a_2)$.

The transformation from the structure's coordinate system $\{x, y, z\}$ to the beam's one $\{x_{in}, y_{in}, z_{in}\}$ can be realized in the standard means [24]: by rotating around the z-axis on the angle φ_{in}; by rotating around the y-axis on the angle ψ_{in}; by shifting the point of origin to the point $(a_1,\ a_2,\ a_3)$. Taking into account the coordinate system transformation, the reflected and transmitted fields are obtained as follows:

$$\begin{aligned}
\vec{\psi}_{ref} &= \vec{P}V_{\upsilon}\int\limits_{-\infty}^{\infty} U(\vec{\kappa}_{in})R^{\upsilon\upsilon}\exp[i\vec{\kappa}\cdot\vec{r} - i\gamma z]d\vec{\kappa}_{in} \\
&\pm \vec{b}_{ref}\times\vec{P}V_{\upsilon'}\int\limits_{-\infty}^{\infty} U(\vec{\kappa}_{in})R^{\upsilon'\upsilon}\exp[i\vec{\kappa}\cdot\vec{r} - i\gamma z]d\vec{\kappa}_{in}, \\
\vec{\psi}_{tr} &= \vec{P}V_{\upsilon}\int\limits_{-\infty}^{\infty} U(\vec{\kappa}_{in})T^{\upsilon\upsilon}\exp[i\vec{\kappa}\cdot\vec{r} + i\gamma(z - NL)]d\vec{\kappa}_{in} \\
&\pm \vec{b}_{tr}\times\vec{P}V_{\upsilon'}\int\limits_{-\infty}^{\infty} U(\vec{\kappa}_{in})T^{\upsilon'\upsilon}\exp[i\vec{\kappa}\cdot\vec{r} + i\gamma(z - NL)]d\vec{\kappa}_{in},
\end{aligned} \tag{6.3}$$

where $\gamma = \sqrt{k_0^2 - \vec{\kappa} \cdot \vec{\kappa}}$, $0 < \arg(\sqrt{k_0^2 - \vec{\kappa} \cdot \vec{\kappa}}) < \pi$; $R^{\upsilon\upsilon}$, $R^{\upsilon'\upsilon}$ and $T^{\upsilon\upsilon}$, $T^{\upsilon'\upsilon}$ are the complex reflection and transmission coefficients ($\upsilon, \upsilon' = s, p$) of the partial plane electromagnetic waves, respectively. They depend on the frequency of the incident field, angles ψ_{in}, φ_{in} and other electromagnetic and geometric parameters of the structure. The coefficients with coincident indexes ($\upsilon\upsilon$) describe the transformation of the incident wave of the perpendicular ($\upsilon = s$) or the parallel ($\upsilon = p$) polarization into the co-polarized wave, and the coefficients with distinct indexes ($\upsilon'\upsilon$) describe the transformation of the incident wave into the cross-polarized wave at the structure output. The left and right indexes correspond to the polarization states of the incident and reflected (transmitted) waves, respectively. The corresponding reflection and transmission coefficients are determined through the rigorous solution of the Cauchy problem related to the tangential field components on the structure's boundaries; the reader is referred here to [5, 11] for further details.

6.2.3 *Effective Medium Theory*

In the long-wavelength limit, when the characteristic dimensions of the structure (d_1, d_2, L) are *significantly smaller* than the wavelength in the corresponding layer ($d_1 \ll \lambda$, $d_2 \ll \lambda$, $L \ll \lambda$), the interactions of electromagnetic waves with a periodic gyromagnetic-gyroelectric structure can be described analytically using the effective medium theory. From the viewpoint of this theory, the periodic structure is represented approximately as an anisotropic (gyroelectromagnetic) *uniform* medium whose optical axis is directed along the structure periodicity, and this medium is described with some effective permittivity and permeability tensors $\hat{\varepsilon}$ and $\hat{\mu}$ [11]. By this means, the investigation of the wave interaction with an inhomogeneous periodic structure is reduced to the solution of the boundary-value problem of conjugations of an equivalent homogeneous anisotropic layer with surrounding spaces.

Let us consider a unit cell of the studied structure. It is made of two layers $0 \le z \le d_1$ and $d_1 \le z \le L$ of dissimilar materials whose constitutive relations are as follows:

$$\left.\begin{aligned} \vec{D} &= \varepsilon_1 \vec{E} \\ \vec{B} &= \hat{\mu}_1 \vec{H} \end{aligned}\right\} \quad 0 \le z \le d_1, \quad \left.\begin{aligned} \vec{D} &= \hat{\varepsilon}_2 \vec{E} \\ \vec{B} &= \mu_2 \vec{H} \end{aligned}\right\} \quad d_1 \le z \le L. \tag{6.4}$$

In general form, in the Cartesian coordinates, the system of Maxwell's equations for each layer has a form

$$\begin{aligned} ik_y H_z - \partial_z H_y &= -ik_0 (\hat{\varepsilon}_j \vec{E})_x, & ik_y E_z - \partial_z E_y &= ik_0 (\hat{\mu}_j \vec{H})_x, \\ \partial_z H_x - ik_x H_z &= -ik_0 (\hat{\varepsilon}_j \vec{E})_y, & \partial_z E_x - ik_x E_z &= ik_0 (\hat{\mu}_j \vec{H})_y, \\ ik_x H_y - ik_y H_x &= -ik_0 (\hat{\varepsilon}_j \vec{E})_z, & ik_x E_y - ik_y E_x &= ik_0 (\hat{\mu}_j \vec{H})_z, \end{aligned} \tag{6.5}$$

where $\partial_z = \partial/\partial z$, k_x and k_y are the wavevector transverse components, $k_0 = \omega/c$ is the free-space wavenumber, $j = 1, 2$, $\hat{\varepsilon}_1$ and $\hat{\mu}_2$ are the tensors with ε_1 and μ_2 on their main diagonal and zeros elsewhere, respectively ($\hat{\varepsilon}_1 = \varepsilon_1 \hat{I}$, $\hat{\mu}_2 = \mu_2 \hat{I}$, $\hat{I}$ is the identity tensor). From six components of the electromagnetic field $\vec{E}$ and $\vec{H}$, only four are independent. Thus the components E_z and H_z can be eliminated from the system (6.5) and derived a set of four first-order linear differential equations related to the transversal field components inside each layer of the structure [5]. For the ferrite ($0 \le z \le d_1$) and semiconductor ($d_1 \le z \le L$) layers these systems, respectively, are:

$$\partial_z \begin{pmatrix} E_x \\ E_y \\ H_x \\ H_y \end{pmatrix} = ik_0 \begin{pmatrix} 0 & 0 & k_x k_y/k_0^2\varepsilon_1 + i\alpha & \mu_1^T - k_x^2/k_0^2\varepsilon_1 \\ 0 & 0 & -\mu_1^T + k_y^2/k_0^2\varepsilon_1 & -k_x k_y/k_0^2\varepsilon_1 + i\alpha \\ -k_x k_y/k_0^2\mu_1^L & -\varepsilon_1 k_0^2 + k_x^2/k_0^2\mu_1^L & 0 & 0 \\ \varepsilon_1 - k_y^2/k_0^2\mu_1^L & k_x k_y/k_0^2\mu_1^L & 0 & 0 \end{pmatrix} \begin{pmatrix} E_x \\ E_y \\ H_x \\ H_y \end{pmatrix}, \tag{6.6}$$

$$\partial_z \begin{pmatrix} E_x \\ E_y \\ H_x \\ H_y \end{pmatrix} = ik_0 \begin{pmatrix} 0 & 0 & k_x k_y/k_0^2\varepsilon_2^L & \mu_2 - k_x^2/k_0^2\varepsilon_2^L \\ 0 & 0 & -\mu_2 + k_y^2/k_0^2\varepsilon_2^L & -k_x k_y/k_0^2\varepsilon_2^L \\ -k_x k_y/k_0^2\mu_2 - i\beta & -\varepsilon_2^T + k_x^2/k_0^2\mu_2 & 0 & 0 \\ \varepsilon_2^T - k_y^2/k_0^2\mu_2 & k_x k_y/k_0^2\mu_2 - i\beta & 0 & 0 \end{pmatrix} \begin{pmatrix} E_x \\ E_y \\ H_x \\ H_y \end{pmatrix}. \tag{6.7}$$

The sets of (6.6) and (6.7) can be abbreviated by using a matrix formulation:

$$\partial_z \vec{\Phi}(z) = ik_0 \mathbf{A}(z) \vec{\Phi}(z), \quad 0 < z < L. \tag{6.8}$$

In this equation, $\vec{\Phi} = \{ E_x, \quad E_y, \quad H_x, \quad H_y \}^T$ is a four-component column vector (here upper index T denotes the matrix transpose operator), while the 4×4 matrix function $\mathbf{A}(z)$ is piecewise uniform as

$$\mathbf{A}(z) = \begin{cases} \mathbf{A}_1, & 0 < z < d_1, \\ \mathbf{A}_2, & d_1 < z < L, \end{cases} \tag{6.9}$$

where the matrices $\mathbf{A}_1$ and $\mathbf{A}_2$ correspond to (6.6) and (6.7), respectively.

Since the vector $\vec{\Phi}$ is known in the plane $z = 0$, the (6.7) is related to the Cauchy problem [25] whose solution is straightforward, because the matrix $\mathbf{A}(z)$ is piecewise uniform. Thus, the field components referred to boundaries of the double-layer period of the structure are related as[1]

[1]The series $\exp(\mathbf{X}) = \mathbf{I} + \sum_{m=1}^{\infty} \frac{1}{m!} \mathbf{X}^m$ converges for square matrices $\mathbf{X}$, i.e. function $\exp(\mathbf{X})$ is defined for all square matrices [25].

$$\vec{\Phi}(L) = \mathbf{M}_2\vec{\Phi}(d_1) = \mathbf{M}_2\mathbf{M}_1\vec{\Phi}(0) = \mathbb{M}\vec{\Phi}(0) = \exp[ik_0\mathbf{A}_2d_2]\exp[ik_0\mathbf{A}_1d_1]\vec{\Phi}(0), \tag{6.10}$$

where $\mathbf{M}_j$ and $\mathbb{M}$ are the transfer matrices of the corresponding layer and the period, respectively.

Suppose that γ_j is the eigenvalue of the corresponding matrix $k_0\mathbf{A}_j$ ($\det[k_0\mathbf{A}_j - \gamma_j\mathbf{I}] = 0$), $j = 1, 2$ and $\mathbf{I}$ is the 4×4 identity matrix. When $|\gamma_j|d_j \ll 1$ (i.e., both layers in the period are electrically thin), the next long-wave approximations can be used [26]

$$\exp[ik_0\mathbf{A}_2d_2]\exp[ik_0\mathbf{A}_1d_1] \simeq \mathbf{I} + ik_0\mathbf{A}_1d_1 + ik_0\mathbf{A}_2d_2. \tag{6.11}$$

Let us now consider a single layer of effective permittivity $\hat{\varepsilon}_e$, effective permeability $\hat{\mu}_e$ and thickness L. Quantity $\mathbf{A}_e$ is defined in a way similar to (6.6), (6.7):

$$\partial_z\begin{pmatrix} E_x \\ E_y \\ H_x \\ H_y \end{pmatrix} = ik_0\begin{pmatrix} 0 & 0 & k_xk_y/k_0^2\varepsilon_e^L + i\alpha_e & \mu_e^T - k_x^2/k_0^2\varepsilon_e^L \\ 0 & 0 & -\mu_e^T + k_y^2/k_0^2\varepsilon_e^L & -k_xk_y/k_0^2\varepsilon_e^L + i\alpha_e \\ -k_xk_y/k_0^2\mu_e^L - i\beta_e & -\varepsilon_e^T + k_x^2/\mu_e^Lk_0^2 & 0 & 0 \\ \varepsilon_e^T - k_y^2/k_0^2\mu_e^L & k_xk_y/k_0^2\mu_e^L - i\beta_e & 0 & 0 \end{pmatrix}\begin{pmatrix} E_x \\ E_y \\ H_x \\ H_y \end{pmatrix}, \tag{6.12}$$

and (6.10):

$$\vec{\Phi}(L) = \mathbf{M}_e\vec{\Phi}(0) = \mathbb{M}\vec{\Phi}(0) = \exp[ik_0\mathbf{A}_eL]\vec{\Phi}(0). \tag{6.13}$$

Provided that γ_e is the eigenvalue of the matrix $k_0\mathbf{A}_e$ ($\det[k_0\mathbf{A}_e - \gamma_e\mathbf{I}] = 0$) and $|\gamma_e|L \ll 1$ (i.e., the entire composite layer is electrically thin as well), the next approximation follows

$$\exp[ik_0\mathbf{A}_eL] \simeq \mathbf{I} + ik_0\mathbf{A}_eL. \tag{6.14}$$

Equations (6.11) and (6.14) permit us to establish the following equivalence between bilayer and single layer:

$$\mathbf{A}_e = f_1\mathbf{A}_1 + f_2\mathbf{A}_2, \quad f_j = d_j/L. \tag{6.15}$$

In the case when the directions of both wave propagation and static magnetic field are coincident ($k_x = k_y = 0$), the following simple expressions for the effective constitutive parameters of the homogenized medium can be obtained:

$$\mu_e^T = f_1\mu_1^T + f_2\mu_2, \quad \varepsilon_e^T = f_1\varepsilon_1 + f_2\varepsilon_2^T, \quad \alpha_e = f_1\alpha, \quad \beta_e = f_2\beta. \tag{6.16}$$

The effective constitutive parameters calculated according to the formula (6.16) are given in Fig. 6.3. The whole frequency range can be divided into three specific

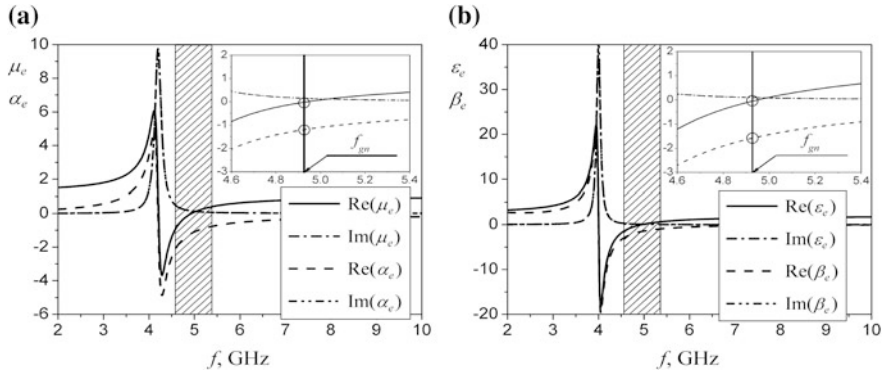

Fig. 6.3 Frequency dependences of **a** effective permeability and **b** effective permittivity of the homogenized ferrite-semiconductor medium. Parameters of the ferrite and semiconductor layers are the same as in Fig. 6.2; d_1 = 0.05 mm, d_2 = 0.2 mm. The *circles* mark the situation when $\mathrm{Re}(\mu_e^T)$ and $\mathrm{Re}(\varepsilon_e^T)$ are close to zero while $\mathrm{Re}(\alpha_e) \neq 0$, $\mathrm{Re}(\beta_e) \neq 0$ and losses in the ferrite and semiconductor layers are small

bands where parameters of the tensors $\hat{\mu}_e$ and $\hat{\varepsilon}_e$ acquire different properties. In the first band, located between 2 and 3 GHz, μ_e^T, ε_e^T, α_e and β_e have positive values of their real parts and small imaginary parts. In the second band, between 3 and 4.5 GHz, the real parts of parameters vary from positive values to negative ones as the frequency increases. These transitions occur at the frequencies of the ferromagnetic resonance of ferrite (f_{fr} = 4.2 GHz) and the cyclotron resonance of semiconductor f_{pr} = 4.0 GHz), respectively. In this band the medium losses are very significant. Finally, in the third frequency band, located from 4.5 to 5.5 GHz, the real parts of parameters have a transition from negative to positive values while their imaginary parts are small. The latter band is given in the insets of Fig. 6.3 on a larger scale. One can see that there is a frequency $f_{gn} \approx 4.94$ GHz where real parts of μ_e^T and ε_e^T simultaneously reach zero. It is significant that, by special adjusting ferrite and semiconductor type, external static magnetic field strength and thicknesses of layers, it is possible to obtain the condition when real parts of μ_e^T and ε_e^T acquire zero at the same frequency. Exactly this situation is marked in the insets of Fig. 6.3 with circles. Note that at this frequency, the real parts of α_e and β_e are far from zero and the medium losses are small.

6.2.4 Eigenvalue Problem

The formulation of the eigenvalue problem on the matrix $\mathbf{A}_e$ ($\det[\mathbf{A}_e - \eta_e \mathbf{I}] = 0$), whose coefficients are defined as (6.16), gives us the characteristic equation on the effective refractive index η_e of the medium:

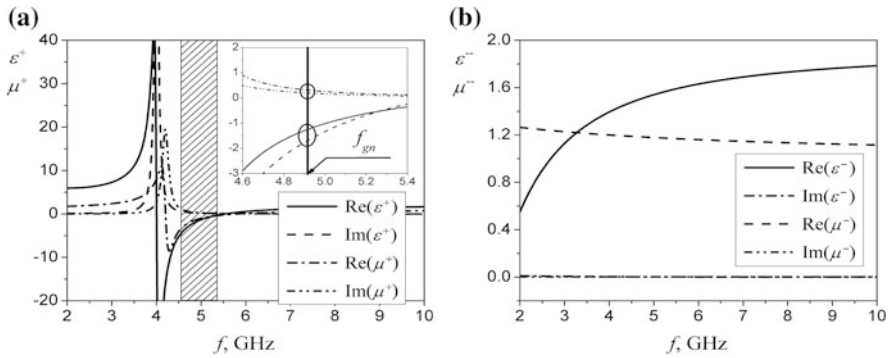

Fig. 6.4 Frequency dependences of the material parameters of the equivalent gyrotropic medium for the **a** RCP and **b** LCP eigenwaves. Parameters of the ferrite and semiconductor layers are the same as in Fig. 6.2; $d_1 = 0.05$ mm, $d_2 = 0.2$ mm

$$\eta_e^4 - 2\eta_e^2\left(\varepsilon_e^T\mu_e^T + \alpha_e\beta_e\right) + \left(\varepsilon_e^T\mu_e^T\right)^2 - \left(\mu_e^T\beta_e\right)^2 - \left(\varepsilon_e^T\alpha_e\right)^2 + \left(\alpha_e\beta_e\right)^2 = 0, \tag{6.17}$$

whose solutions are

$$\left(\eta_e^{\pm}\right)^2 = \left(\varepsilon_e^T \pm \beta_e\right)\left(\mu_e^T \pm \alpha_e\right) = \varepsilon^{\pm}\mu^{\pm}. \tag{6.18}$$

Here the signs '±' are related to two different eigenwaves with propagation constants $\gamma_e^{\pm} = k_0\eta_e^{\pm}$. It is well known that in an unbounded gyrotropic medium they have right (RCP, γ_e^+) and left (LCP, γ_e^-) circular polarizations [21].

Especially interesting situation appears if the real parts of μ_e^T and ε_e^T are close to zero and the medium losses are small. In this case there is $|\varepsilon^{\pm}\mu^{\pm}| \approx |\alpha_e'\beta_e'|$, and the propagation constants become as:

$$\gamma_e = -\gamma_e^+ = \gamma_e^- \approx k_0\sqrt{|\alpha_e'\beta_e'|}. \tag{6.19}$$

Thus, the propagation constants of the RCP (γ_e^+) and LCP (γ_e^-) waves are equal in the magnitude but opposite in sign to each other, and the *backward propagation* appears for the RCP wave while for the LCP wave it is forward one (see also, Chap. IV of [27]). Recall that the backward wave is the wave in which the direction of the Poynting vector is opposite to that of its phase velocity [28]. The similar peculiarity of the RCP and LCP waves propagation occurs also in the chiral-nihility media [2–4], so in the analogy with them, the condition (6.19) is related to the *gyrotropic-nihility* media [11]. The frequency band, at which the gyrotropic-nihility condition is satisfied for the RCP wave, is depicted in Fig. 6.4. Particularly, the gyrotropic-nihility frequency f_{gn} is marked in the inset of this figure with circles.

6.3 Numerical Results: Reflected and Transmitted Fields

6.3.1 Spectral and Angular Behaviors

It is anticipated that if the frequency of the electromagnetic wave which incidents on a finite layer of such a composite medium is chosen to be nearly the frequency f_{gn} of the gyrotropic-nihility condition, the transmitted and reflected fields will acquire some unusual properties. In order to demonstrate this, in the long-wavelength limit, the reflection and transmission coefficients can equivalently be calculated using the rigorous solution (6.10) or the approximate solution (6.13) of (6.8) because these solutions give the same result. In particular, we are interested here in the study of the energy relations between the transmitted and reflected fields, i.e. the polarization effects do not discuss in this chapter. Nevertheless we refer the reader to [11] where some polarization features of the studied structure are revealed.

So, the transmittance is calculated as a function of the frequency and the angle of incidence (Fig. 6.5a). One can see that this function exhibits an expanded flat area of the transmittance at the frequency where the gyrotropic-nihility condition holds. At this frequency the complete transmission of the partial plane monochromatic waves takes a place almost in the entire range of angles of incidence except the range of glancing angles. Such a high transmittance appears due to the peculiarities of the medium impedances ($Z^{\pm} = \sqrt{\mu^{\pm}/\varepsilon^{\pm}}$) related to the RCP and LCP waves. It is particularly remarkable that in the vicinity of the gyrotropic-nihility frequency f_{gn}, the parameters α_e and β_e are close in value to each other and their real parts approach to unit which can be clearly seen in Fig. 6.3. It leads to the fact that the medium becomes to be impedance matched to free space [11]. Directly at the

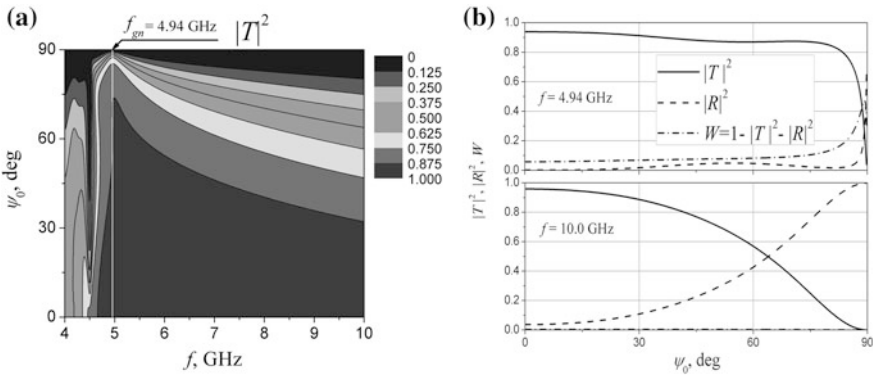

Fig. 6.5 **a** Transmittance as a function of the frequency and the angle of incidence of the plane monochromatic wave for the equivalent gyrotropic layer with finite thickness (NL = 2.5 mm). **b** The angular dependences of the transmittance, reflectance and absorption coefficient at the gyrotropic-nihility frequency (*top figure*) and far from it (*bottom figure*). Parameters of the ferrite and semiconductor layers are the same as in Fig. 6.2; d_1 = 0.05 mm, d_2 = 0.2 mm

gyrotropic-nihility frequency, the impedances related to the RCP and LCP waves become indistinguishable: $Z = Z^{+} = Z^{-} = \sqrt{|\alpha'_e|/|\beta'_e|}$.

This feature is also confirmed by the data plotted in Fig. 6.5b where the reflectance, transmittance and absorption coefficient are calculated at two different frequencies for a comparison. Thus the first frequency is chosen at the gyrotropic-nihility condition and the second one is selected to be far from the frequencies of gyrotropic-nihility condition and the ferromagnetic and plasma resonances. At the frequency of $f = 10$ GHz, the curves have typical form where the transmittance monotonically decreases and the reflectance monotonically increases as the angle of incidence rises. On the other hand, at the gyrotropic-nihility frequency, the curves of the transmittance and reflectance are different drastically from that ones in the first case. Thus, the level of the transmittance/reflectance remains to be invariable almost down to the glancing angles. At the same time, the reflectance is small down to the glancing angles because the medium is impedance matched to free space.

6.3.2 Gaussian Beam Transmission

Since the beam field is represented by an angular continuous spectrum of plane waves, the transmitted beam distribution depends on the angular characteristic of the transmission coefficient of spatial plane monochromatic waves at a particular frequency. We consider an incident Gaussian beam with the spectral density assigned due to the law $U(\vec{\kappa}_{in}) = \exp[-(\vec{w} \cdot \vec{\kappa}_{in})^2 \big/ 16] H_m(k_{x_{in}} w_x \big/ \sqrt{2}) H_n (k_{y_{in}} w_y \big/ \sqrt{2})$, where $\vec{w} = \{w_x, w_y\}$, w_x and w_y are the beam widths along x_{in} and y_{in} axis, respectively, $H_\upsilon(\cdot)$ is the Hermit polynomial of υ-th order ($\upsilon = m, n$). In this chapter we restrict ourselves to the case of the zero-order ($m = n = 0$) beam. The final distribution of the transmitted beam is presented in Figs. 6.6 and 6.7 in two- and three-dimensions. As before the results are obtained for two distinct frequencies.

So, at the frequency f_{gn} where the gyrotropic-nihility condition holds, the studied gyroelectromagnetic medium is well impedance matched to free space, and spatial plane monochromatic waves can completely pass through the system up to the glancing angles. As a result, the transmitted beam pattern does not acquire any significant distortion of its form nearly the frequency f_{gn}, while this feature is not inherent to the pattern of the transmitted beam to be far from this frequency. It should be noted that this shape retention of the transmitted beam pattern remains unchanged even under the oblique incidence of the primary beam and this effect is polarization insensitive.

In conclusion, the peculiarities of the Gaussian beam interaction with a ferrite-semiconductor finely-stratified structure being under an action of an external static magnetic field in the Faraday geometry is presented in this chapter. In the

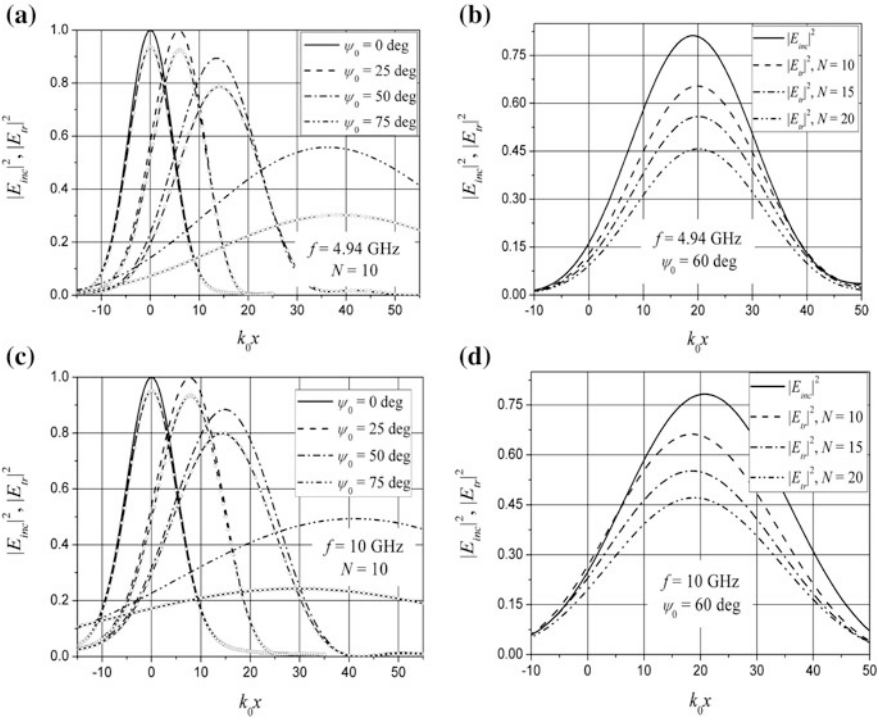

Fig. 6.6 The two-dimensional distribution of the absolute value of the incident beam $|E_{inc}|^2$ and the transmitted beam $|E_{tr}|^2$ for different (**a**, **c**) angles of incidence of the primary beam and (**b**, **d**) number of structure's periods. The field distribution is normalized to the maximum value of the normally incident beam. Parameters of the ferrite and semiconductor layers are the same as in Fig. 6.2. The incident beam parameters are: $k_0w_x = k_0h = 10$, $\varphi_{in} = 0°$. Other structure parameters are: $d_1 = 0.05$ mm, $d_2 = 0.2$ mm

long-wavelength limit, when the structure layers are optically thin, the effective medium theory is developed, and the effective constitutive parameters of the equivalent uniform anisotropic medium are obtained analytically. On the basis of these parameters the peculiarities of the eigenwaves propagation are studied and the possibility of achieving the gyrotropic-nihility condition is predicted.

The reflection, transmission and absorption of waves in the system are studied in vicinity of the gyrotropic-nihility frequency. It is found out that under the oblique incidence of the spatial plane monochromatic wave on the studied structure, the level of the transmission/reflection remains to be invariable almost down to the glancing angles when the gyrotropic-nihility condition is satisfied. As a result, at the frequency of the gyrotropic-nihility condition the Gaussian beam can pass through such a system keeping its parameters unchanged (beam width and shape) except of a portion of the absorbed energy even under the oblique incidence of the primary beam.

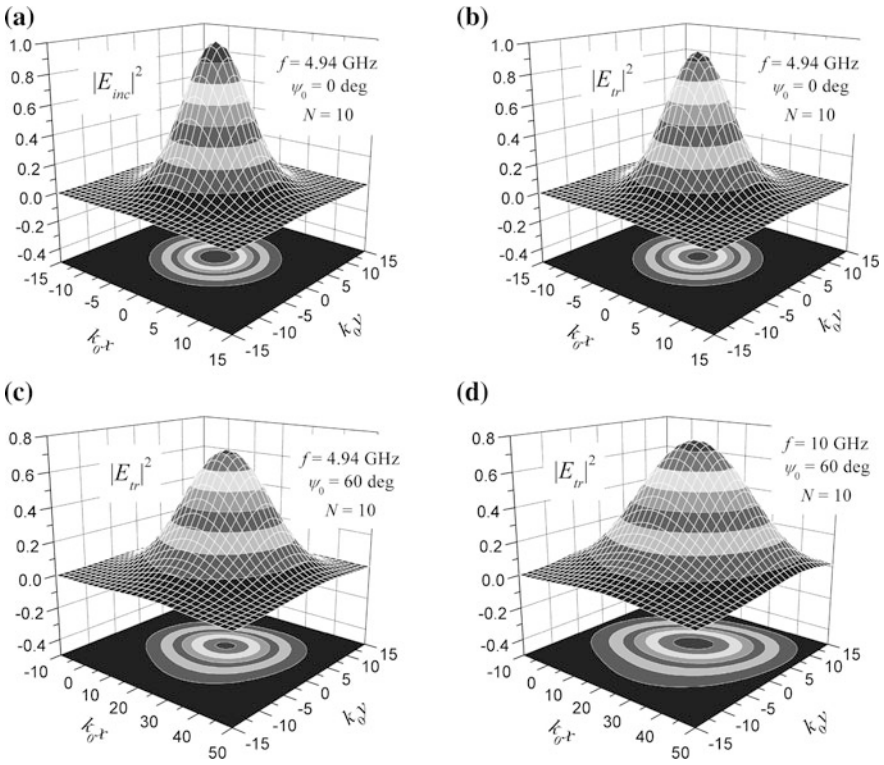

Fig. 6.7 The three-dimensional distribution of the absolute value of **a** the incident beam $|E_{inc}|^2$ and **b–d** the transmitted beam $|E_{tr}|^2$. The field distribution is normalized to the maximum value of the normally incident beam. Parameters of the ferrite and semiconductor layers are the same as in Fig. 6.2. The incident beam parameters are: $k_0 w_x = k_0 w_y = k_0 h = 10$, $\varphi_{in} = 0°$. Other structure parameters are: $d_1 = 0.05$ mm, $d_2 = 0.2$ mm

Acknowledgments This work was partially supported (V.R. Tuz) by Ministry of Education and Science of Ukraine under the Program "Electrodynamics of layered composites with chiral properties and multifunctional planar systems", Project No. 0112 U 000561.

References

1. A. Lakhtakia, An electromagnetic trinity from "negative permittivity" and "negative permeability". Int. J. Infrared Millimeter Waves **22**, 1731–1734 (2001)
2. S. Tretyakov, I. Nefedov, A.H. Sihvola, S. Maslovki, C. Simovski, Waves and energy in chiral nihility. J. Electromagn. Waves Appl. **17**, 695–706 (2003)
3. C.-W. Qiu, N. Burokur, S. Zouhdi, L.-W. Li, Chiral nihility effects on energy flow in chiral materials. J. Opt. Soc. Am. A **25**, 55–63 (2008)
4. V. Tuz, C.-W. Qiu, Semi-infnite chiral nihility photonics: parametric dependence, wave tunelling and rejection. Prog. Electromagn. Res. **103**, 139–152 (2010)

5. V.R. Tuz, M.Y. Vidil, S.L. Prosvirnin, Polarization transformations by a magneto-photonic layered structure in the vicinity of a ferromagnetic resonance. J. Opt. **12**, 095102 (2010)
6. E. Prati, Propagation in gyroelectromagnetic guiding systems. J. Electromagn. Waves Appl. **17**, 1177–1196 (2003)
7. R.H. Tarkhanyan, D.G. Niarchos, Effective negative refractive index in ferromagnet-semiconductor superlattices. Opt. Express **14**, 5433–5444 (2006)
8. A.V. Ivanova, O.A. Kotelnikova, V.A. Ivanov, Gyrotropic left-handed media: energy flux and circular dichroism. J. Magn. Magn. Mat. **300**, e67–e69 (2006)
9. R.X. Wu, T. Zhao, J.Q. Xiao, Periodic ferrite–semiconductor layered composite with negative index of refraction. J. Phys. Condens. Matter **19**, 026211 (2007)
10. O.V. Shramkova, Transmission spectra in ferrite-semiconductor periodic structure. Prog. Electromagn. Res. M **7**, 71–85 (2009)
11. V.R. Tuz, O.D. Batrakov, Y. Zheng, Gyrotropic-nihility in ferrite-semi-conductor composite in Faraday geometry. Prog. Electromagn. Res. B **41**, 397–417 (2012)
12. Yi Jin, Sailing He, Focusing by a slab of chiral medium. Opt. Express **13**, 4974–4979 (2005)
13. S.N. Shulga, Two-dimensional wave beam scattering on an anisotropic half-space with anisotropic inclusion. Opt. Spectrosc. **87**, 503–509 (1999)
14. A.V. Malyuskin, D.N. Goryushko, S.N. Shulga, A.A. Shmatko, in *Scattering of a Wave Beam by Inhomogeneous Anisotropic Chiral Layer*. International conference *on* mathematical methods EM theory (MMET 2002), Kyiv, Ukraine, pp. 566–568, 10–13 Sept 2002
15. T.M. Grzegorczyk, X. Chen, J. Pacheco Jr, J. Chen, B.-I. Wu, J.A. Kong, Reflection coefficients and Goos–Hänchen shifts in anisotropic and bianisotropic left-handed metamaterials. Prog. Electromagn. Res. **51**, 83–113 (2005)
16. W.T. Dong, L. Gao, C.-W. Qiu, Goos-Hänchen shift at the surface of chiral negative refractive media. Prog. Electromagn. Res. **90**, 255–268 (2009)
17. R.-L. Chern, P.-H. Chang, Negative refraction and backward wave in pseudochiral mediums: illustrations of Gaussian beams. Opt. Express **21**, 2657–2666 (2013)
18. R.-L. Chern, P.-H. Chang, Negative refraction and backward wave in chiral mediums illustrations of Gaussian beams. J. Appl. Phys. **113**, 153504 (2013)
19. K.M. Luk, A.L. Cullen, Three-dimensional Gaussian beam reflection from short-circuited isotropic ferrite slab. IEEE Trans. Antennas Propag. **41**, 962–966 (1993)
20. V. Tuz, Three-dimensional Gaussian beam scattering from a periodic sequence of bi-isotropic and material layers. Prog. Electromagn. Res. B **7**, 53–73 (2008)
21. A.G. Gurevich, *Ferrites at Microwave Frequencies* (Heywood, 1963)
22. R.E. Collin, *Foundation for Microwave Engineering* (Wiley, New York, 1992)
23. F.G. Bass, A.A. Bulgakov, *Kinetic and Electrodynamic Phenomena in Classical and Quantum Semiconductor Superlattices* (Nova Science, 1997)
24. G.A. Korn, T.M. Korn, *Mathematical Handbook for Scientists and Engineers: Definitions, Theorems, and Formulas for Reference and Review* (McGraw-Hill Book Co., 1968)
25. V.A. Jakubovich, V.H. Starzhinskij, *Linear Differential Equations with Periodic Coefficients* (Wiley, New York, 1975)
26. A. Lakhtakia, C.M. Krowne, Restricted equivalence of paired epsilon-negative and mu-negative layers to a negative phase-velocity materials (alias left-handed material). Optik **114**, 305–307 (2003)
27. V.G. Veselago, The electrodynamics of substances with simultaneously negative values of ε and μ. Sov. Phys. Usp. **10**, 509–514 (1968)
28. V.V. Shevchenko, Forward and backward waves: Three definitions and their interrelation and applicability. Phys.-Usp. **50**, 287–290 (2007)

Chapter 7
Gyrotropic Metamaterials and Polarization Experiment in the Millimeter Waveband

S.I. Tarapov, S. Yu Polevoy and N.N. Beletski

Abstract The paper deals with the analysis of modern situation in physics of artificial gyrotropic media. Most widespread techniques of experimental and theoretical finding constitutive parameters are under analysis. Besides, the original results obtained by authors while studying polarization features for some types of magnetically controllable metamaterials, possessing the gyrotropic/chiral features in the millimeter wavelength range are presented. The results of measurements are under discussion.

7.1 Introduction

It is well known that the term "gyrotropy", which was used for description of condensed media dozens years ago, can be applied successfully to the electrodynamics of artificial media (metamaterials). Moreover, a lot of terms, which describe the ability of medium to rotate the polarization of linearly polarized wave ("chirality", "magnetoactivity", "bianisotropy") came from the condensed media physics. They are used widely in physics of metamaterials today. Let consider them more detailed.

In most general case the constitutive parameters ($\dot{\varepsilon}$ and $\dot{\mu}$) for the bianisotropic medium [1, 2], represent themselves matrixes, where all components are not equal to zero. The gyrotropic medium as the special case of bianisotropic medium, has anti-symmetric tensor parameters $\dot{\varepsilon}$ and $\dot{\mu}$ [3] with non-zero nondiagonal components ($a_{12} = -a_{21} \neq 0$). If the gyrotropic medium has nondiagonal components $a_{12}(\vec{k}) = a_{12}(-\vec{k})$, $a_{21}(\vec{k}) = a_{21}(-\vec{k})$, where $\vec{k}$ is the propagation constant of the media, it is a non-reciprocal medium. Note this medium is represented in our paper by magnetoactive media. The chiral medium, as another special case of gyrotropic medium is a reciprocal medium [4, 5] with nondiagonal components

S.I. Tarapov (✉) · S.Y. Polevoy · N.N. Beletski
O. Ya Usikov Institute for Radiophysics and Electronics of NAS of Ukraine, Kharkiv, Ukraine
e-mail: tarapov@ire.kharkov.ua

O. Shulika and I. Sukhoivanov (eds.), *Contemporary Optoelectronics*,
Springer Series in Optical Sciences 199, DOI 10.1007/978-94-017-7315-7_7

$a_{12}(\vec{k}) = -a_{12}(-\vec{k})$, $a_{21}(\vec{k}) = -a_{21}(-\vec{k})$. Note that the wave propagation in the gyrotropic media for the condensed media were studied in details (for example, [6, 7]), namely for the physics of crystals for the optical frequency band.

The paper presented should be considered as a next step in experimental research of artificial gyrotropic media with electrical and magnetic activity in microwave band. Namely main objectives of study are:

- the development of the experimental technique for determining the effective constitutive parameters of chiral media in the millimeter waveband;
- learning the possibility of experimental control of the rotation angle of the polarization plane of electromagnetic wave by changing the "specific density" of the structure;
- to study both theoretically and experimentally the polarization properties of one-layered and multilayered magnetoactive metamaterial depending on static magnetic field;
- the experimental and numerical demonstration of the Faraday effect enhancement for the case of gyrotropic magnetic layer inserted into special one-dimensional (1D) photonic crystal.

The task of research of chiral metamaterials is interesting both for fundamental and for applied physics. These structures can be used for design the compact magnetically controllable microwave devices, (for inst. polarizers, using the Faraday effect).

Bulk chiral metamaterials are promising, because they can realize rotation of polarization plane of the electromagnetic waves on large angles in the millimeter wavelength range. For example, in [8, 9], the chiral metamaterials used for the rotation of the polarization plane at angles up to several hundred degrees per wavelength, which is several orders of magnitude larger than for the natural media with optical activity. In spite a lot of studies are carrying out now (for example [10, 11]), a plenty of tasks for the millimeter waveband which is important today from the application point of view, are unsolved yet.

Probably, Hetch and Barron [12], Arnaut and Davis [13] were the first who introduced planar (2D) chiral structures into the electromagnetic research. However, 2D chirality does not lead to the same electromagnetic effects which are conventional for 3D chirality so, it became a subject of special intense investigations [14]. It is known, that bulk (3D) chiral artificial structures [1] manifest a reciprocal optical activity [15]. The typical constructive object of 3D chiral media is a spirally conducting cylinder. Besides, in some particular cases, quasi-2D planar chiral metallic structures can be asymmetrically combined with isotropic substrates to distinguish a reciprocal optical response inherent to true 3D chiral structures. In such metamaterials, at normal incidence of the exciting wave, an optical activity appears only in the case, when their constituent metallic elements have finite thickness, which provides an asymmetric coupling of the fields at the air and substrate interfaces.

The planar chiral structure placed on a ferrite substrate [10, 15] (one layered magnetoactive structure) and multilayered ferrite-dielectric structures [16] are even more interesting objects from both fundamental and application points of view. The

appearance of so-called Faraday Effect Enhancement (FEE) has significant application perspectives. Namely, they can be used successfully to design non-reciprocal magnetically controllable microwave devices based on the Faraday effect.

A number of principal features of gyrotropy of magnetoactive medium can be extracted while studying the bounded photonic crystal (PC) [17]. In particular, we note the appearance of a sharp transparency peak (Tamm peak) in the band gap of such a structure. This effect is based on the well-known Tamm state effect [18, 19]. This phenomenon is well studied experimentally for magnetoactive one-dimensional and two-dimensional periodical media [20–23] (in non-gyrotropic approximation). But the presence of gyrotropy is in such medium is of special interest. The wave propagation in the photonic crystal substantially depends on the material which includes into PC, and on the material placed as a boundary of the PC. For the gyrotropic boundary medium we can obtain the Faraday Effect Enhancement (FEE) [17] also. It reveals here as a strong rotation of the polarization plane by such PC on the frequency of Tamm state. A significant Faraday Effect Enhancement (FEE) in the case when magneto-optical PC, bounded by almost reflecting medium was described theoretically in [16]. The FEE for microwave band was observed for bounded PC, which is formed by magnetoactive elements [17]. So the FEE effect can be considered as a resonance effect in gyrotropic resonator without intrinsic volume.

Note that in contrast to optical frequency range photonic crystals, in the microwave band we are dealing with magnetic gyrotropy instead electric gyrotropy. One of the most actual directions of the photonic and magnetophotonic crystals study is searching ways to control the spectral properties of such structures in the microwave frequency range. It allows to produce a novel generations of high-speed electronically controlled devices that may find wide application in the area of telecommunications, computing and physical electronics.

7.2 The Polarization Rotation Enhancement in the Dielectric Bulk Chiral Metamaterial

7.2.1 The Experimental Setup

The experimental setup for the determination of effective constitutive parameters of chiral media is shown on Fig. 7.1 [24]. Investigated bulk chiral structure is placed between the transmitting and receiving rectangular horns which are fitted to the Vector Network Analyzer Agilent N5230A by means of coaxial-waveguide junctions and cables. The main functions of the Analyzer are measuring S-parameters, its processing and transforming into the graphical form. Absorbing screen can be placed in the vicinity of the structure under study to eliminate the influence of diffraction on the edges.

The horns are located on the same axis passing perpendicularly to the structure through its center at a distance larger than ten wavelengths. If necessary, the phase-correction lenses can be placed close the horns that make the wavefront flat.

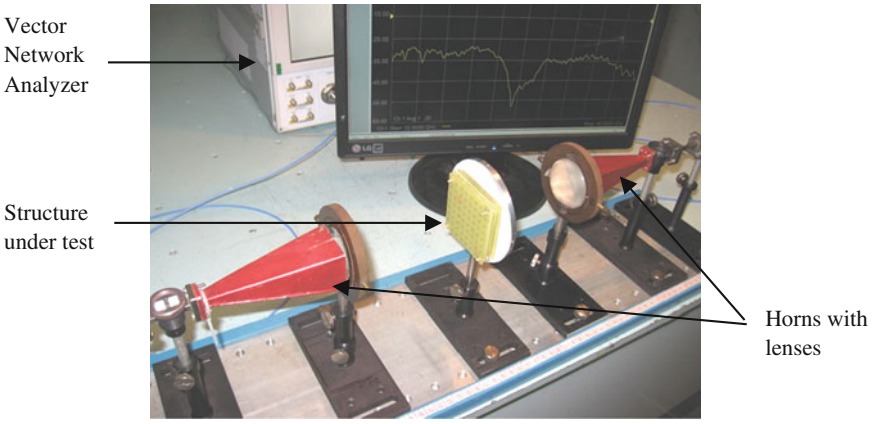

Fig. 7.1 The experimental setup for study of gyrotropic/chiral metamaterials

Receiving horn can be rotated around its axis. With help of the analyzer the parameters S_{21} and S_{11} in the frequency range of 22–40 GHz are registered. The calibrating procedure for the measuring setup provides the reduction in the influence of parasitic reflections occurred due to the non-ideality matching of the spatial elements.

The determination of the chirality parameter was carried out using the model bulk dielectric chiral structure (Fig. 7.2). It consists of several subsequent layers of planar chiral structures in the form of 2D array of chiral elements on the fiberglass substrate. Planar chiral structures were etched on the foil side of the fiberglass by

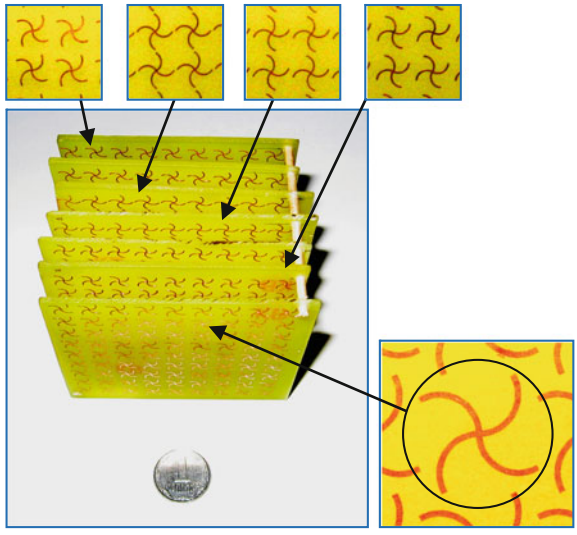

Fig. 7.2 Model dielectric bulk chiral structure under study

photolithography. Chiral elements are rotated around its axis by 15° relative to the elements in each subsequent layer.

7.2.2 Determination of the Effective Constitutive Parameters of Chiral Media

To obtain the comprehensive information about the gyrotropic medium it is necessary to have technique of mathematical description of its constitutive parameters. Since there are several forms of writing the constitutive equations for chiral media, so first we must select a convenient form of the constitutive equations, such as [4, 25]:

$$\vec{D} = \dot{\varepsilon}\vec{E} + i\dot{\kappa}\vec{H}, \quad \vec{B} = \dot{\mu}\vec{H} - i\dot{\kappa}\vec{E}, \tag{7.1}$$

where $\vec{E}$, $\vec{H}$ are vectors of the electric and magnetic fields intensity; $\vec{D}$, $\vec{B}$ are vectors of electric and magnetic induction, $\dot{\varepsilon}$, $\dot{\mu}$ are the complex permittivity and permeability; $\dot{\kappa}$ is the complex chirality parameter.

To make the problem clearer let's consider the task about the propagation of the electromagnetic wave through the chiral layer of finite thickness L. Let's consider the case of normal incidence of the plane electromagnetic waves. In this case, the chiral medium is a uniaxial medium in the direction of wave propagation (z axis).

Using the transfer matrix method, we can obtain the relations between the components of the electric and magnetic fields intensities (E_x, E_y, H_x, H_y) on the input and output boundary of the chiral layer ($z = 0$ and $z = L$) and its constitutive parameters ($\dot{\varepsilon}$, $\dot{\mu}$, $\dot{\kappa}$):

$$\Psi(L) = \hat{M}\Psi(0), \tag{7.2}$$

$$\Psi(L) = \begin{pmatrix} E_x(L) \\ E_y(L) \\ H_x(L) \\ H_y(L) \end{pmatrix}, \quad \Psi(0) = \begin{pmatrix} E_x(0) \\ E_y(0) \\ H_x(0) \\ H_y(0) \end{pmatrix},$$

where $\hat{M}$ is the transfer matrix 4×4 with coefficients:

$$M_{11} = M_{22} = M_{33} = M_{44} = \cos(\dot{k}L)\cos(k_0\dot{\kappa}L),$$

$$M_{12} = -M_{21} = M_{43} = -M_{34} = \cos(\dot{k}L)\sin(k_0\dot{\kappa}L),$$

$$M_{13} = M_{24} = -i\frac{\dot{\mu}}{\dot{n}}\sin(\dot{k}L)\sin(k_0\dot{\kappa}L),$$

$$M_{14} = -M_{23} = i\frac{\dot{\mu}}{\dot{n}}\sin(\dot{k}L)\cos(k_0\dot{\kappa}L),$$

$$M_{31} = M_{42} = i\frac{\dot{n}}{\dot{\mu}}\sin(\dot{k}L)\sin(k_0\dot{\kappa}L),$$

$$M_{41} = -M_{32} = i\frac{\dot{n}}{\dot{\mu}}\sin(\dot{k}L)\cos(k_0\dot{\kappa}L),$$

where $\dot{k} = k_0\dot{n}$, $\dot{n} = \sqrt{\dot{\varepsilon}\dot{\mu}}$, and k_0 is the propagation constant of the vacuum.

Thus, using the relation (7.2) and setting the constitutive parameters, we can find the transmission coefficients for the electric and magnetic fields intensity, and polarization characteristics of chiral layer.

However, an inverse problem of determining the effective constitutive parameters of such media using experimentally measured transmission and reflection coefficients exists as well. It appears to be even more important from the experimental point of view. There are several approaches of experimental determination of the effective constitutive parameters of uniaxial chiral media [5, 25].

The *first approach* described in [9, 25], consists of measuring the transmission and reflection coefficients of electromagnetic waves interacting with the metamaterial for two mutual orientations of transmitting and receiving horns. This means—the "parallel" (co-polarization) and "perpendicular" (cross-polarization) horns locations. Measured transmission and reflection coefficients for co-polarization ($\dot{T}_{||}$, $\dot{R}_{||}$), and for cross-polarization ($\dot{T}_{\perp}$, $\dot{R}_{\perp}$) are associated with the transmission and reflection coefficients of electromagnetic waves with right (RCP) and left (LCP) circular polarizations [9]:

$$\dot{T}_{\pm} = \dot{T}_{||} \mp i\dot{T}_{\perp}, \quad \dot{R}_{\pm} = \dot{R}_{||} = \dot{R}. \tag{7.3}$$

Calculating the values of $\dot{T}_{+}$ and $\dot{T}_{-}$ allows to calculate the chirality parameter $\dot{\kappa}$ and polarization characteristics: the rotation angle of the polarization plane of the transmitted wave θ and the ellipticity angle η [25].

Permittivity $\dot{\varepsilon}$, permeability $\dot{\mu}$ and chirality parameter $\dot{\kappa}$ for the chiral medium are determined by the following relations [25]:

$$\dot{\varepsilon} = \dot{n}/\dot{Z}, \quad \dot{\mu} = \dot{n}\dot{Z}, \quad \dot{\kappa} = (\dot{n}_{+} - \dot{n}_{-})/2, \tag{7.4}$$

where $\dot{n} = (\dot{n}_{+} + \dot{n}_{-})/2 = \sqrt{\dot{\varepsilon}\dot{\mu}}$ is the average refractive index for RCP and LCP waves. The refraction coefficients $\dot{n}_{+}$, $\dot{n}_{-}$ of the RCP and LCP waves and impedance $\dot{Z}$ are determined from transmission $\dot{T}_{\pm}$ and reflection $\dot{R}_{\pm}$ coefficients [25].

Thus, by measuring the transmission and reflection coefficients for the waves on co-polarization and cross-polarization with the horns, we can calculate the effective constitutive parameters of the structure, and its polarization characteristics.

There is also a *second approach* of determining the chirality parameter $\dot{\kappa}$ and the polarization characteristics of the transmitted wave for the chiral structure. It is suggests the direct measurement of the angle θ using the receiving horn, which can be rotated around its longitudinal axis [5]. The angle θ is that rotation angle of the

receiving horn at which the transmission coefficient of electromagnetic waves is maximal ($\dot{T}_{\max}$). If we measure the minimum transmission coefficient ($\dot{T}_{\min}$) at a rotation angle of the receiving horn $\theta + 90°$, then we can determine the ellipticity angle η of the transmitted wave by the following relation:

$$\eta = arctg \frac{\left|\dot{T}_{\min}\right|}{\left|\dot{T}_{\max}\right|}. \tag{7.5}$$

Let us find the relation between the polarization characteristics of the structure and its chirality parameter. The rotation angle of the polarization plane is directly proportional to the angular frequency ω, the real part of the chirality parameter and the chiral layer thickness [4, 26]:

$$\theta = k_0 L\kappa' = \frac{\omega L\kappa'}{c}. \tag{7.6}$$

The ellipticity angle of the transmitted wave depends on the imaginary part of the chirality parameter [27] as:

$$\eta = arctg[th(k_0 L\kappa'')]. \tag{7.7}$$

Finally according to the experimental values θ and η one can calculate the chirality parameter:

$$\dot{\kappa} = \frac{\theta}{k_0 L} + i\frac{arcth(tg\eta)}{k_0 L}. \tag{7.8}$$

7.2.3 Experimental Finding of Chirality Parameter Features

In order to investigate the dependence of the polarization properties of the dielectric bulk chiral structure on its "specific density" the experimental dependences of the rotation angle of the polarization plane $\theta(f)$ on the frequency of the electromagnetic wave $f = \omega/(2\pi)$ for four values of the structure thickness L (Fig. 7.3a) were analyzed [28]. Structure thickness L was varied from 10.5 to 12.6 mm by increasing the distance d between its layers from 1.5 to 1.8 mm. The "specific density" of the structure/metamaterial has been varied thereby. According to the experimental curves the frequency dependences of the chirality parameter real part $\kappa'(f)$ for several values of the structure thickness L (Fig. 7.3b) were calculated using the relation (7.8).

For the frequency dependence of the angle $\theta(f)$ for the structure thickness L = 10.5 mm (Fig. 7.3a, curve 1) near the frequency of 31.2 GHz the area of maximal dispersion of the $\theta = 90°$ at the ellipticity angle $\eta = 20°$ was defined. Near the frequency of 30 GHz the angle $\theta = 50°$ at the $\eta = 2°$. As can be seen, the

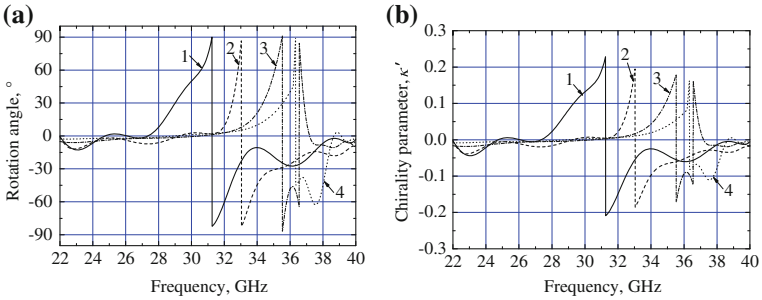

Fig. 7.3 Experimental frequency dependences: **a** $\theta(f)$ and **b** $\kappa'(f)$ for four values of the structure thickness L (*1*—10.5; *2*—11.2; *3*—11.9; *4*—12.6 mm)

frequency dependence of the chirality parameter $\kappa'(f)$ is resonant at the same frequencies as for $\theta(f)$. The maximum for chirality parameter module reaches about 0.23. The dependence $\kappa'(f)$ is similar to the dependence $\theta(f)$ in accordance with formula (7.8).

Figure 7.4a clearly shows a monotonic increasing of the frequency f_{res} of the area of the maximal dispersion of the angle θ from 31.2 to 36.3 GHz with the structure "specific density" increasing. Such behavior can be assigned to existence of high-quality "magnetic" mode [8, 29], appeared in the given chiral medium. This "magnetic mode" has anomalous frequency dependence, i.e., when the distance between the layers of the chiral structure increases its frequency increases too. Such dependence is typical for media with negative dispersion. Note that in this bulk chiral structure, as well as structures in [8, 30] exists the "electric" mode, which has a conventional frequency dependence, i.e., when the distance between the layers of the chiral structure (the "specific density") increases its frequency decreases.

Besides the decreasing of the maximum value of chirality parameter real part κ'_{res} from 0.23 to 0.16 (Fig. 7.4b) is registered at the same frequencies. The most probable reason for the decreasing of κ'_{res} is the exhausting of the structure with an increasing of the distance between its layers.

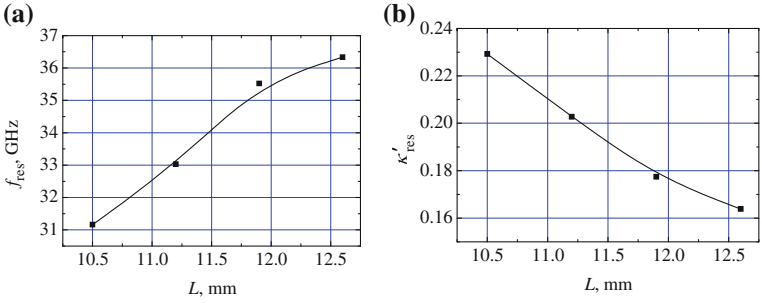

Fig. 7.4 Values of **a** $f_{res}(L)$ and **b** $\kappa'_{res}(L)$ for the "magnetic" mode

7.3 Faraday Effect Enhancement (FEE) in the Magnetoactive Bulk Metamaterial

7.3.1 The Experimental Technique

For the studying of the magnetoactive metamaterials with longitudinal magnetization another one experimental setup was design (Fig. 7.5). It is similar to the experimental setup described above, however, the structure and horns in it are located along the axis of the electromagnet that controlled by a computer. More detailed technique of this experiment is described in [15, 17].

The magnetoactive metamaterial being under investigation is designed as a single-layered structure, which consists of the planar chiral periodic structure placed on the ferrite (L14H) plane-parallel slab. The chiral structure is made of fiberglass, one side of which is covered with copper foil. The foil side of this structure is patterned with the periodic array whose square unit cell consists of the planar chiral rosette (see Fig. 7.2).

The polarization properties of the magnetoactive bulk metamaterial (Fig. 7.6), represents a multilayered structure. It consists from the set of single-layered magnetoactive structures described above.

7.3.2 Experimental. Polarization Rotation

Let consider some experimental results to demonstrate the influence of the magnetodependent elements involved into chiral media on its gyrotropy features under conditions of longitudinal magnetization:

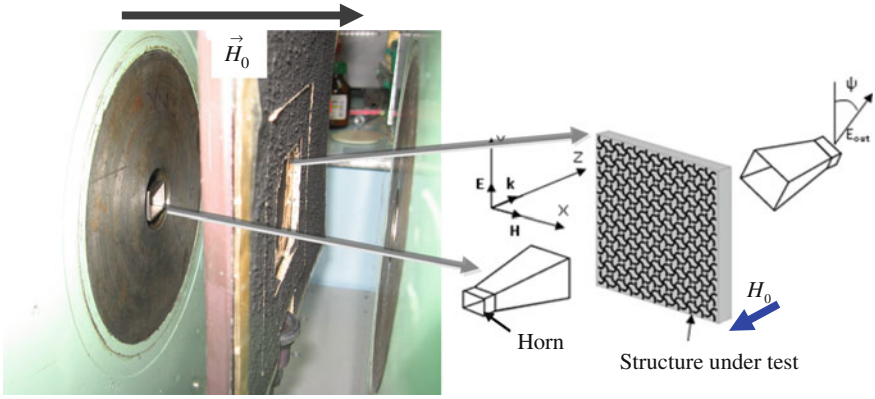

Fig. 7.5 The experimental setup for the study of magnetoactive structures with longitudinal magnetization

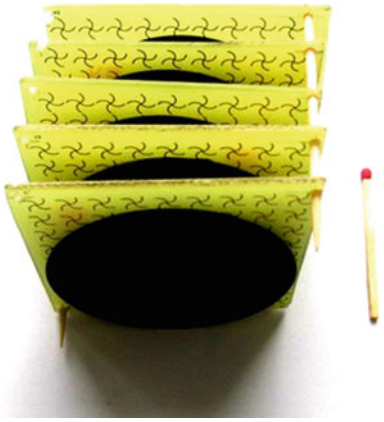

Fig. 7.6 The layered bulk magnetoactive metamaterial

- the polarization rotation angle θ of linearly polarized wave, propagating through a single ferrite slab (Fig. 7.7a);
- the polarization rotation angle θ of linearly polarized wave propagating through the magnetoactive bulk metamaterial consisting of planar chiral structure with period d = 5 mm loaded with a ferrite slab (Fig. 7.7b).

One can see that the surface plotted for the ferrite slab (Fig. 7.7a) is much smoother (colors variation is more weak) than that one for the one-layered magnetoactive metamaterial (Fig. 7.7b). Also, for the magnetoactive metamaterial, a monotonic growth of θ on the field strength takes place. Moreover, near the frequency of the metamaterial resonance dip (f_r = 25.5–26.5 GHz), this dependence acquires a pronounced resonant character (dashed line), and for $\theta \rightarrow \theta_r$ achieves significantly higher values than that one for the ferrite slab (up to $\theta_r \geq 45°$).

It can be seen that the value θ_r (Fig. 7.7b) also depends on the magnetic field strength, and the maximum of θ_r is observed at $H_0 \approx$ 4800 Oe (see arrow in

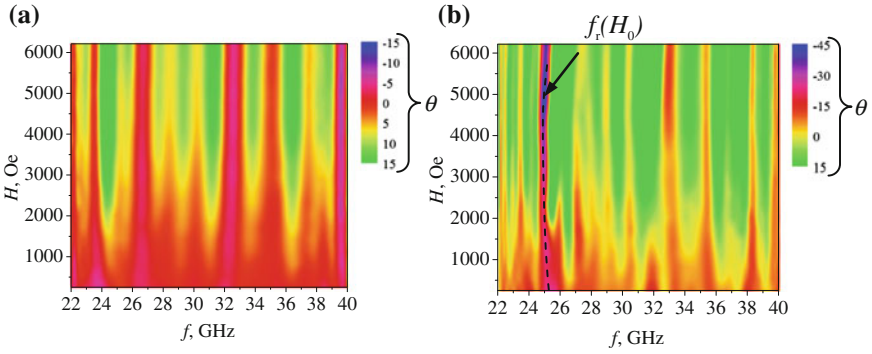

Fig. 7.7 Experimental dependencies of the polarization rotation angle $\theta(f, H_0)$ for: **a** the single ferrite slab; **b** the one-layered magnetoactive metamaterial

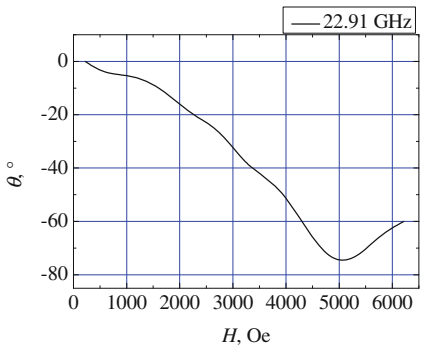

Fig. 7.8 The dependence of the rotation angle of the polarization plane on the static magnetic field for the layered bulk magnetoactive metamaterial

Fig. 7.7b). In this region the real part of permeability has extreme value, that explains the extreme in the dependency of $\theta_r(H_0)$.

The distinct feature of the bulk 1-layered magnetoactive chiral metamaterial is larger sensitivity of its polarization properties to the static magnetic field strength compared with single ferrite slab. This phenomenon can be explained by the fact that the resonant character of the magnetic permeability component of ferrite is superimposed on the resonant character of oscillations in the planar chiral structure.

Note that a similar situation, which was called as the amplification of the Faraday rotation has been detected by authors in the millimeter wave range earlier, but in more simple resonant structures (the two-mirror resonator [31]).

The similar measurements of the polarization characteristics for the layered bulk magnetoactive metamaterial (Fig. 7.6) were performed for the same values of the static magnetic field and microwave frequencies. At the frequency of 22.91 GHz at the static magnetic field of about 5000 Oe the rotation angle of the polarization plane reaches 75° (Fig. 7.8), that is sufficiently higher than for a single-layer magnetoactive chiral structure (Fig. 7.7b).

7.4 Faraday Effect Enhancement (FEE) in a Magnetoactive Bounded Photonic Crystal

7.4.1 The Experimental Technique

To realize the Faraday effect enhancement in the PC, that is limited by negative permittivity "boundary medium" described earlier experimental setup has been upgraded. The magentoactive element (ferrite disk) is placed between PC and the boundary medium (Fig. 7.9a). For the registration of the transmission coefficient of PCs in a given frequency range under the static magnetic field the technique [17] and the setup was used (Fig. 7.5). The electrodynamic cell (Fig. 7.9b) is a single-mode circular waveguide (with fundamental mode TE_{11}) contained the structure under research.

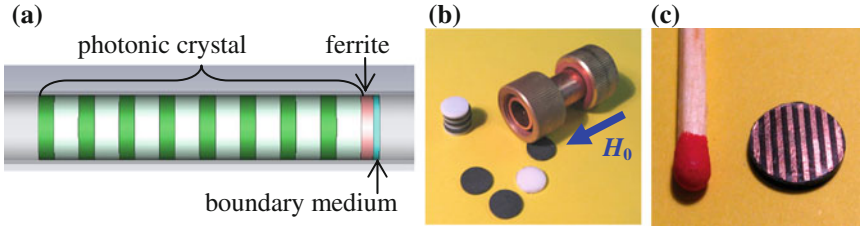

Fig. 7.9 **a** The model of investigated PC structure, loaded with magentoactive element and boundary medium; **b** The appearance of the electrodynamic cell for research in the cylindrical magnetophotonic structures; **c** the appearance of copper wire medium as the boundary of the photonic crystal

The investigated photonic crystal structures (Fig. 7.9b) consists of dielectric disks of different thicknesses and materials, so that the band gaps of such PC are located in the frequency range 22–40 GHz. As the boundary medium of PCs, the copper wire medium (Fig. 7.9c) and the copper thin film medium were used. The static magnetic field H_0 is directed along the axis of the cell.

7.4.2 *Polarization Rotation in Magnetoactive Bounded Photonic Crystal. Experiment*

Let consider the structures with the boundary medium as a thin metal film. Analysis of the transmission spectrum [17] of the unloaded PC (without boundary medium) and for the PC, loaded with ferrite slab and metal layer, shows that in the latter case, a surface state mode in the bandgap of PC ("surface peak" in Fig. 7.10) occurs. The peak has a common origin with the known Tamm peak [22, 32], so it will be also called as the Tamm peak.

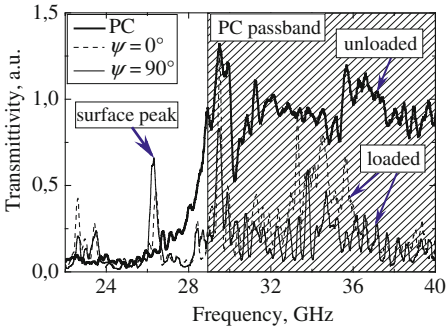

Fig. 7.10 The transmission spectrum of unloaded PC structure and PC structure loaded with ferrite slab and metal film for two different polarization angles of the incident wave

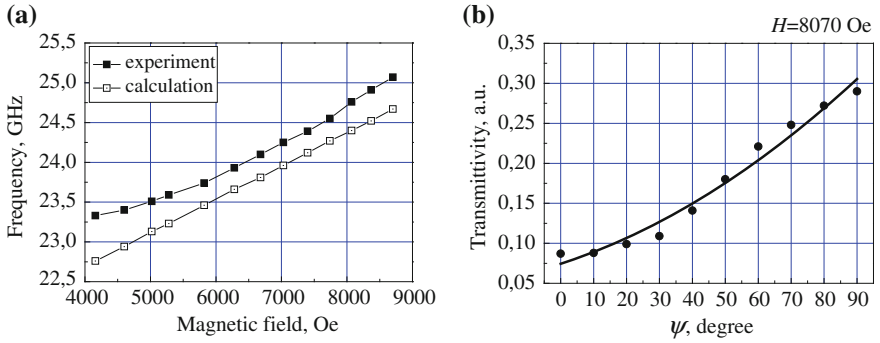

Fig. 7.11 **a** Tamm peak frequency versus: the static magnetic field; **b** the Tamm peak intensity versus the angle ψ

A detailed analysis allows to identify this peak as the peak associated with the excitation of TE_{11} mode, which is excited due Faraday effect in the ferrite layer. It can be seen (Fig. 7.10), when the angle between the polarization of the waveguide sections (transmitting and receiving) is $\psi = 90°$, we can see more intense signal on the Tamm peak frequency in comparison with the case $\psi = 0°$. Thus the Faraday effect enhancement takes place.

To check the nature of Tamm peak, we analyzed the dependence of its position on the static magnetic field, and the dependence of the peak intensity on the polarization angle (Fig. 7.11). It can be see that if the peak associated with the Faraday effect, while increasing the magnetic field shifts in the higher frequency range. The numerical calculations [17] lead to the same conclusion. Really, in Fig. 7.11a typical experimental and calculated frequency-field dependences of the Tamm-peaks exhibit a similar behavior.

Polarization properties of the structure were studied experimentally by rotating the transmitting and receiving sections relatively to each other. Figure 7.11b shows the typical dependence of the surface state peak intensity on the angle ψ at some certain magnetic field $H = 8070$ Oe. It can be seen that with the increasing of the angle ψ the transmission coefficient is also increases. Its maximum is occurred at $\psi = 90°$. This means that the polarization of the wave at the output of the structure is changed on 90° relative to the polarization at the input of the structure.

7.5 Conclusions

To conclude, let's list some outcomes of the research performed. Thus in the millimeter waveband:

1. Two experimental approaches for determining the effective constitutive parameters of the bulk chiral media are realized. The frequency dependence of

the real part of the chirality parameter of the bulk chiral metamaterial based on array of planar chiral structures is defined.
2. The ability to control the resonant frequency of the rotation angle of the polarization plane of electromagnetic wave by changing the "specific density" of the bulk metamaterial is demonstrated experimentally. The existence of left-handed "magnetic" mode is shown.
3. The transmission of electromagnetic waves through the multilayered and one-layered magnetoactive chiral metamaterial has been studied. The range of frequencies and magnetic field strength where the angle of polarization rotation appears essentially higher than that one related to a single ferrite slab (Faraday effect enhancement) is defined. The amplification of the polarization rotation for multilayered structure in comparison with one-layered structure is shown.
4. The surface state peak (the Tamm peak) was detected in the spectrum of the magnetoactive bounded photonic crystal. It was shown that the Tamm peak frequency depends on the external magnetic field.

Acknowledgments The authors thank Ruban V. P. for help in preparing of the investigating samples. The paper is supported partially by STCU grant #5714.

References

1. A. Serdyukov, I. Semchenko, S. Tretyakov, A. Sihvola, *Electromagnetics of Bi-anisotropic Materials: Theory and Applications* (Gordon and Breach Science Publishers, Amsterdam, 2001)
2. A. Sihvola, Metamaterials in electromagnetics. Metamaterials **1**(1), 2–11 (2007)
3. A.G. Gurevich, G.A. Melkov, *Magnetization Oscillations and Waves* (CRC Press, New York, 1996)
4. O.V. Ivanov, *Electromagnetic Wave Propagation in Anisotropic and Bianisotropic Layered Structures* (UlSTU, Ulyanovsk, 2010). (in Russian)
5. O.V. Osipov, A.N. Volobuev, On the physical sense of material equations of a chiral medium. Tech. Phys. Lett. **35**(8), 753–755 (2009)
6. V.M. Agranovich, V.L. Ginzburg, *Spatial Dispersion in Crystallooptics and the Theory of Excitons* (Wiley-Interscience, London, 1966)
7. F.I. Fedorov, *Theory of Gyrotropy* (Nauka i Tekhnika, Minsk, 1976). (in Russian)
8. E. Plum, J. Zhou, J. Dong, V.A. Fedotov, T. Koschny, C.M. Soukoulis, N.I. Zheludev, Metamaterial with negative index due to chirality. Phys. Rev. B. **79**(3), 035407 (2009)
9. R. Zhao, L. Zhang, J. Zhou, Th Koschny, C.M. Soukoulis, Conjugated gammadion chiral metamaterial with uniaxial optical activity and negative refractive index. Phys. Rev. B. **83**(3), 035105 (2011)
10. S.L. Prosvirnin, V.A. Dmitriev, Electromagnetic wave diffraction by array of complex-shaped metal elements placed on ferromagnetic substrate. Eur. Phys. J. Appl. Phys. **49**(3), 33005 (2010)
11. V.A. Fedotov, P.L. Mladyonov, S.L. Prosvirnin, A.V. Rogacheva, Y. Chen, N.I. Zheludev, Asymmetric propagation of electromagnetic waves through a planar chiral structure. Phys. Rev. Lett. **97**(16), 167401 (2006)

12. L. Hecht, L.D. Barron, Linear polarization Raman optical activity. The importance of the non-resonant term in the Kramers-Heisenberg-Dirac dispersion formula under resonance conditions. Chem. Phys. Lett. **225**(4–6), 519–524 (1994)
13. L.R. Arnaut, L.E. Davis, On planar chiral structures, in *Progress in Electromagnetic Research Symposium PIERS 1995,* July, Seattle, p. 165 (1995)
14. S. Zouhdi, G.E. Couenon, A. Fourrier-Lamer, Scattering from a periodic array of thin planar chiral structures—calculations and measurements. IEEE Trans. Antennas Propagat. **47**(6), 1061–1065 (1999)
15. S.Y. Polevoy, S.L. Prosvirnin, S.I. Tarapov, V.R. Tuz, Resonant features of planar Faraday metamaterial with high structural symmetry. Eur. Phys. J. Appl. Phys. **61**(3), 030501 (2013)
16. M. Inoue, R. Fujikawa, A. Baryshev, A. Khanikaev, P.B. Lim, H. Uchida, O.A. Aktsipetrov, T.V. Murzina, A.A. Fedyanin, A.B. Granovsky, Magnetophotonic crystals. J. Phys. D Appl. Phys. **39**(8), 151 (2006)
17. A.A. Girich, S.Y. Polevoy, S.I. Tarapov, A.M. Merzlikin, A.B. Granovsky, D.P. Belozorov, Experimental study of the Faraday effect in 1D-photonic crystal in millimeter waveband. Solid State Phenom. **190**, 365–368 (2012)
18. I.E. Tamm, O vozmozhnoi sviazi elektronov na poverkhnostiakh kristalla (in Russian). Zh. Eksp. Teor. Fiz. **3**(1), 34–35 (1933)
19. I.M. Lifshitz, S.I. Pekar, Tamm bounded states of electrons on the crystal surface and surface oscillations of lattice atoms (in Russian). Usp. Fiz. Nauk. **56**(8), 531–568 (1955)
20. S.V. Chernovtsev, S.I. Tarapov, D.P. Belozorov, Magnetically controllable 1D magnetophotonic crystal in millimetre wavelength band. J. Phys. D Appl. Phys. **40**(2), 295–299 (2007)
21. S.I. Tarapov, D.P. Belozorov, Microwaves in Dispersive Magnetic Composite Media (Review Article). Low Temp. Phys. **38**(7), 766–792 (2012)
22. A.P. Vinogradov, A.V. Dorofeenko, S.G. Erokhin, M. Inoue, A.A. Lisyansky, A.M. Merzlikin, A.B. Granovsky, Surface state peculiarities at one-dimensional photonic crystal interfaces. Phys. Rev. B **74**(4), 045128 (2006)
23. A.A. Bulgakov, A.A. Girich, M.K. Khodzitsky, O.V. Shramkova, S.I. Tarapov, Transmission of electromagnetic waves in a magnetic fine-stratified structure. JOSA B **26**(12), 156–160 (2009)
24. S.Y. Polevoy, S.L. Prosvirnin, S.I. Tarapov, Resonance properties of planar metamaterial, formed by array of gammadions on unmagnetized ferrodielectric substrate. Radiophys. Electron. **4**(18), N1, 42–46 (2013) (in Russian)
25. R. Zhao, T. Koschny, C.M. Soukoulis, Chiral metamaterials: retrieval of the effective parameters with and without substrate. Opt. Express **18**(14), 14553–14567 (2010)
26. I.V. Lindell, A.H. Sihvola, S.A. Tretyakov, A.J. Viitanen, *Electromagnetic Waves in Chiral and Bi-Isotropic Media* (Artech House, Boston/London, 1994)
27. C. Menzel, C. Rockstuhl, T. Paul, F. Lederer, Retrieving effective parameters for quasiplanar chiral metamaterials. Appl. Phys. Lett. **93**(23), 233106 (2008)
28. S.Y. Polevoy, Experimental determination of constitutive parameters of the chiral media in the millimeter wavelength range. Radiophys. Electron. **4**(18), N4, 42–46 (2013) (in Russian)
29. S.Y. Polevoy, S.I. Tarapov, Frequency dispersion of the polarization properties of chiral structure in the millimeter waveband, in *The processings of the eighth international Kharkov symposium on physics and engineering of microwaves, millimeter and submillimeter waves MSMW 2013,* June 23–28, Kharkov, Ukraine, pp. 98–100 (2013)
30. J. Dong, J. Zhou, T. Koschny, C. Soukoulis, Bi-layer cross chiral structure with strong optical activity and negative refractive index. Opt. Express **17**(16), 14172–14179 (2009)
31. S.I. Tarapov, Y.P. Machekhin, A.S. Zamkovoy, *Magnetic Resonance for Optoelectronic Materials Investigation* (Collegium, Kharkov, 2008)
32. E. Yablonovitch, Inhibited spontaneous emission in solid-state physics and electronics. Phys. Rev. Lett. **58**(20), 2059–2062 (1987)

Chapter 8
Dynamic Singular Vector Speckle Fields and Their Hurst Exponent Time Analysis

Marat Soskin and Vasyl Vasil'ev

Abstract The generic developing vector speckle fields were realized first by the "optical-damage" effect in the photorefractive crystal $LiNbO_3$:Fe. Singularities evolve through loop and chain reactions. *Loop* trajectories are limited in time and evolve in one speckle. *Chain* reactions are not limited in space and time. They obey installed *topological sum rules*: equal quantity of paired nucleations, annihilations and dislocation lines interconnections. Techniques of the Hurst (H) exponent, firstly used in dynamic singular optics, allowed install *space-time autocorrelation* of speckle fields development. Measured high values of the exponent H = 0.56–0.89 for the C points chain reactions witness realization of the *long-term positive autocorrelation* processes during generic development of singular vector speckle fields.

8.1 Introduction

Classical optics was cardinally changed when lasers were realized in sixties. They create new chapters of modern optics: nonlinear optics, laser spectroscopy, holography, etc. The physical backgrounds of *singular optic* were created by J. Nye and M. Berry in 1974 [1], summarized in J. Nye monograph [2] and first review [3]. They have considered basic unique properties of optical singularities, where wavefront parameters are undefined in their centers. At the beginning of nineties, the new actual and rapidly developing chapter of modern optics "*singular optics*" was established. Our division in Institute of physics NAS of Ukraine (Kiev, Ukraine) was focused firstly on experimental realization of singular laser beams from smooth Gaussian beams by computer generated "fork" holograms [4]. Systematic investigations of singular light beams basic properties were performed.

M. Soskin (✉) · V. Vasil'ev
Institute of Physics, NAS of Ukraine, Prospect Nauki 46, Kiev 680028, Ukraine
e-mail: marat.soskin@gmail.com

O. Shulika and I. Sukhoivanov (eds.), *Contemporary Optoelectronics*,
Springer Series in Optical Sciences 199, DOI 10.1007/978-94-017-7315-7_8

Speckled scattering of propagating laser beam was discovered immediately after lasers realization. In general, speckle phenomena play essential role in modern optics and optical quantum electronics [5, 6]. Singularities are evolving especial interest in *developing* optical fields. In general, this subject belongs to the *dynamic singular optics* started by us [7]. In reality, successful development of dynamic singular optics started, when unique "optical damage effect" [8] in photorefractive media was exploiting [9]. It opened firstly possibility realize and investigate comprehensively the topological regularities of singular scalar and vector speckle fields development.

Today state-of-art of this subject together with latest new results is presented in this overview.

8.2 Experimental Technique and Data Processing

Our main new approaches to the investigation of wave fields with optical singularities are their comprehensive *topological analysis*. It demands in turn the precise measurement of all actual parameters of singularities and establishment of general topological regularities of speckles field with nested singularities development. The ideal space resolution of optical measurements of any type is limited by pixel size of used CCD camera. We have used CCD camera with 5.7×4.6 mm^2 input screen and 576×720 pixels of 8×8 μm^2 dimensions.

The optimized schemes for writing of dynamic *scalar* and *vector* speckle fields and for their comprehensive analysis is presented in Fig. 8.1. We call for short fields with fixed (changeable) orientation of electric vector $\boldsymbol{E}$ as "scalar" (vector) ones.

The lens L diminishes the chosen scattered-light fragment to $\sim 1.5 \times 10^{-4}$ srad divergence. The *scalar* developing speckle fields are created, when laser beam propagates orthogonal to the crystal axis c with *fixed* orientation of electrical vector $\boldsymbol{E}$ orthogonal to both of them (Fig. 8.1). The developing *vector* speckle fields were created sequentially by two shown orientations of the polarization vector in the incident laser beam Fig. 8.1b. For the beginning, electrical vector $\boldsymbol{E}$ was oriented perpendicularly to beam axis c as in previous case of scalar field writing [the position (a)]. It was written during 1800s up to practical saturation of scalar speckle field created by "optical-damage" effect. $\boldsymbol{E}$ was turned then to angle 56° by rotation of λ/2 plate (Fig. 8.1). This allowed realize full gamut of induced noisy diffraction gratings and the polarization ellipses accordingly. The collimated speckle field fragments allowed usage the standard stokes-polarimetry technique [10]. All Stokes parameters were obtained by combination of quarter-wave plate (λ/4) and polarizer P with various orientations of polarization vector needed for measurement of the Stokes parameters of the incident laser beam. Laser beam was blocked by movable screen S during all time of optical elements readjustment what eliminated fully possible distortions of measured dynamics for the developing speckle fields.

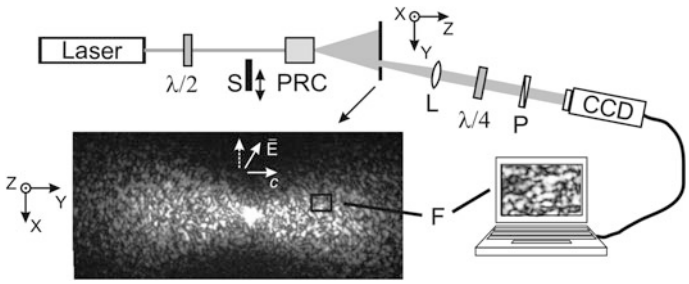

Fig. 8.1 Optical schemes for writing and investigation of developing "scalar", i.e. linearly polarized in one direction (**a**) and *vector* (**b**) speckle fields. Structure of vector speckle fields and morphology of C points were measured by the short-time Stokes-polarimetry [9]. The small fragment of scattered light cone propagating after crystal was cut by 5 mm diameter hole in screen and projected on the CCD camera input window

Linearly polarized Gaussian beam of standard He-Ne laser (633 nm) with 0.5 mm diameter and 0.5 W/cm^2 intensity irradiates lithium niobate crystal. Measurement of each Stokes component was realized faster than 15 ms and four of them during 100 ms. The used 15 s interval between measured cadres allowed fix all stages of topological/morphological dynamics for developing singular speckle fields. Therefore, all presented trajectories are dotted lines. The transverse coordinates and topology of dynamic singularities were measured in the output plane of PRC (Fig. 8.1a). Its image was projected on input screen of used CCD camera.

8.3 Topology of Dynamic Vector Speckle Fields and Optical Singularities. "Sign Paradox"

Investigated vector speckle fields develop due to the unique "optical-damage" effect in photorefractive crystals (PRC) [8] (in our case $LiNbO_3$:Fe crystal) firstly used by us in stationary and dynamic singular optics [7, 9]. Speckle fields in laser beam after its propagation through PRC appear due to initial random distribution of Fe^{3+} ions and drift of exited electrons in conduction band due to inner electrical fields [8]. When they recombine with empty traps, the new dynamic local inhomogeneities of refraction index are created in crystal matrix. This "optical-damage" effect is developing in time, what induces in turn development of created speckle field. The interference of scattered light components with random directions and polarization produces family of random gratings, which possess micron-scale space period. Propagating laser beam diffracts on them and self-interferes. As a result, developing speckle field is created. Its scattered light diagram possesses the "butterfly" form oriented along crystal *c* axis, where electro-optical tensor possesses the largest value. The "optical-damage" effect for typical photorefractive crystal $LiNbO_3$:Fe develops nearly 1 h up to practical saturation. Main stages of its development are

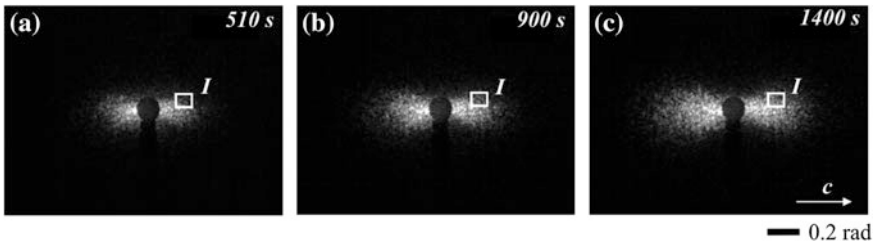

Fig. 8.2 Structure and space diagram of scattered light, which possess "butterfly" form with pronounced speckle structure. It is oriented across crystal axis *c*. The *round* screen in the center of the scattered light blocks direct incident laser beam. Small *white rectangle* on "butterfly" right periphery marks the part of scattered light used for measurements [9]. Only in this case, obtained results show the real properties of singular speckle fields and are *generic* ones

shown in Fig. 8.2 for initial stage 510 s (a), mean time 900 s (b), and for 1400 s, when optical damage started saturate (c).

Genericity is general property of surfaces, field structure etc. It has strict mathematical definition. This fundamental notion was introduced to physical optics by J. Nye with new sense: "Generic means that the object in question occurs without special preparation and conditions" [2]. According to it, OVs with topological charges ±1 are generic once. All written and investigated structures and phenomena in such developing speckle fields were *generic* ones automatically, because they appear really in natural way "without special preparation and conditions".

The minima between two speckles become exactly zero in some point. This moment pair of *generic* single-charged optical vortices (OVs) is born in this point and propagates inside the incident laser beam.

Space and phase structures of OVs are described by the simple formula (8.1):

$$\Psi_l(\vec{r}) = u(r,z)\mathrm{e}^{-ikz}\mathrm{e}^{-il\theta} \tag{8.1}$$

Zero-amplitude center of an OV in cross-section appears due to full *destructive* interference of scattered light in this point. It possesses the *indefinite* phase and *handedness* automatically contrary to all other ordinary points on the OV wave front with their *definite* values. The zero-amplitude **z** axis of an OV is the *dislocation* line [2]. This is very important for singularities dynamics. Scalar wave front around z axis possesses *helicoidal* form with right/left handedness. Namely this is the origin of term "optical vortex" [11].

Each point of vector speckle field possesses random elliptical polarization. Their parameters vary inhomogeneously from point to point during development of induced vector speckle fields. Each polarization ellipse can be decomposed on left and right circular components with different amplitude and phase values. The

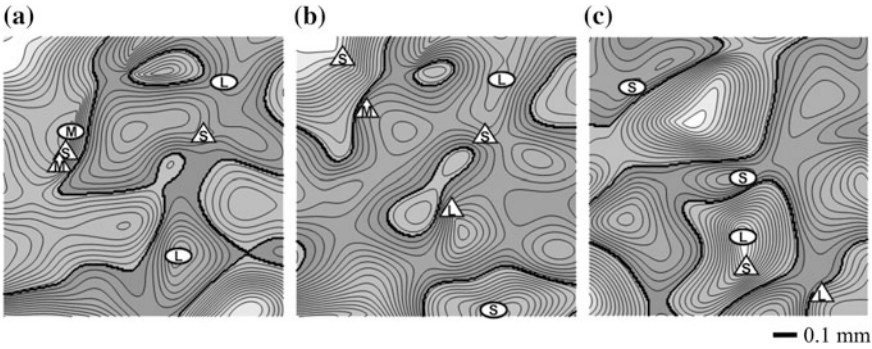

Fig. 8.3 The measured polarization structure of generated elliptic speckle fields. Areas with RH/LH polarizations are shown by *grey/white* colors at 495 s (**a**), 750 s (**b**) and 1650 s (**c**). They are delimited by *black linearly* polarized L lines [3]. Fragments of the dynamic elliptic singular speckle field are presented as distribution of $b(x, y)$ axis amplitudes of polarization ellipses and field handedness distribution. As it is seen, C points with all morphological forms are attended

stronger circular component defines its general handedness. When smaller component becomes zero in the center of OV, polarization ellipse transforms automatically to the circularly polarized *singular* C point [2]. As the result, all C points are located *exactly above* centers of correspondent OVs. This is starting point of the fixed "sign paradox" in singular vector speckle fields, when handedness of all C points and surrounding ellipses is *equal* in the frames of closed linearly polarized L lines [2] contrary to *opposite* signs of underlying pairs of positive/negative charged OVs.

Experiment shows that the polarization ellipses in vector speckle fields form compact areas with *equal* right or left handedness delimited by the *closed linearly polarized* L lines [2] (Fig. 8.3).

Specific is the arrangement of ellipses around C points. M. Berry and J. Hannay have shown analytically that each C point arranges the long axes of surrounding ellipses in *three* possible morphological configurations: *stars* (S), *monstars* (M) *and lemons* (L) [12] for right/left polarized C points (Fig. 12.2 in J. Nye monograph [2]). This is not mistake and misprint. It shows that around C points ellipses rotate *clockwise* for stars, and *counterclockwise* for monstars and lemons for *both* signs of C points. Therefore, their indices equal $-½$ for stars and $+½$ for monstars and lemons don't depend from handedness of surrounding ellipses. But what parameters of underlined OVs define them? We have supposed that this is done by their *handedness*. Indeed, *direction of rotation* of polarization ellipses around a C point and their morphological forms during circumference around it are defined automatically: *clockwise* for stars, *counterclockwise* for monstars and lemons for C points of *both signs*. To confirm experimentally correctness of our explanation of the fixed "sign paradox" we have chosen two fragments of vector field with opposite handedness (Fig. 8.4).

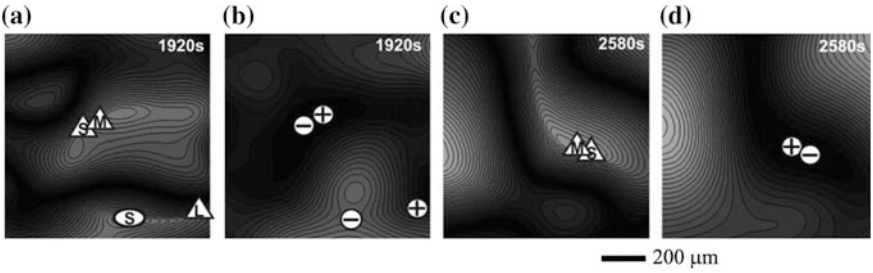

Fig. 8.4 Morphology of C points in **a** the left handed and **c** the right handed fragments of vector speckle fields. The handedness of underlined OVs in the left and the right fragments of these vector speckle fields is shown in (**b**, **d**) pictures. They were measured with right/left polarized reference waves for left/right polarized vector fields

Obtained structures show unambiguously that for *both* polarizations the S/L morphologies are realized for negative/positive charged OVs in full accord with our suggestion. These results confirm completely our explanation of the "sign paradox" and resolve it completely.

Let us move now to analyses of general distribution of ellipses handedness in the *real* developing speckle fields. One remark has to be given for the beginning. As was shown by I. Freund, all polarization singularities are accompanied by so called "optical diabolos" (OD) [13]. Their surfaces are formed by minor axes b of surrounding ellipses. ODs were realized firstly in our group [14]. ODs possess two forms: *elliptic* and *hyperbolic* ones according to structure of their cross-section. Elliptics have Poincaré index $I_P = +1$ and are realized when C point is located on the *top* of a speckle. They are marked by the *oval*. Hyperbolics with $I_P = 0$ are settled on speckle *slopes*. They are marked by the *triangle.* Both elliptic and hyperbolic C points are seen in Fig. 8.3.

Experiment confirmed that the polarization ellipses form compact areas with *equal* right or left handedness ellipses delimited by the *closed linearly polarized* L lines (Fig. 8.3). L lines are new type of singularities, namely *singularities of handedness*! The shown fragments possess three left-handed C points. The lower L and middle S are located in neighbor speckles. As will be shown later, pair of elliptic and hyperbolic C points of equal handedness nested in neighbor speckles gives origin of singular topological *chain* reactions. Figure 8.3b, c demonstrates essential changes of vector speckle field topology during field development.

It happens due to *indefinite* phase in the zero-amplitude centers of vortices, which underline each C point pair. This nontrivial property is the first essential feature of the "*sign paradox*" fixed and resolved by us firstly due to our knowledge. As was shown, each C point besides handedness possesses one of three possible morphological forms, which don't depend from C point sign. But what OV features define morphology of upperlying C points? We have supposed that this is done by the *handedness* underlined OVs: *direction of rotation* of polarization ellipses and correspondent morphological forms is defined automatically: *clockwise* for stars,

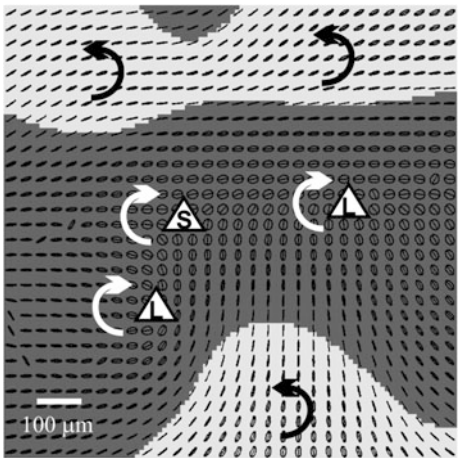

Fig. 8.5 All ellipses in *right* (*grey*) and *left* (*white*) polarized areas delimited by linearly polarized L lines possess *equal* handedness indeed

counterclockwise for monstars and lemons for C points of *both signs*. This is the *second* nontrivial feature of the "sign paradox". To confirm it experimentally we have chosen two fragments of vector field with opposite handedness (Fig. 8.4). It shows unambiguously that for *both* polarizations S/L are realized for negative/positive charged OVs in accord with our suggestion.

Last essential item of general properties of vector speckle field is distribution of the *handedness* of polarization ellipses as the function of C point morphology (Fig. 8.5). It shows that C points of *arbitrary* morphology possess the same handedness in accord with mentioned Fig. 12.2 in [2].

8.4 Loop and Chain Trajectories

The one of main goals of our investigations are *topological regularities* of dynamic vector speckle field development, when multitude of singularities are born and annihilate. They are defined by properties of born pairs of vector singularities, trajectory of their movement during PRC illumination by a laser beam up to their annihilation. Of course, they are accompanies by opposite handedness OVs. Optical singularities nucleate, interact and annihilate as *pair*.

Only *two* types of trajectories are allowed topologically: when born and moving singularities interact (1) in pairs or (2) with singularities from other pairs born independently. The simplest *loop* trajectories developing in frame of one speckle are realized in the first case (Fig. 8.6).

There are no topological obstacles for annihilation of born pair in the frames of the same speckle. Namely this circumstance defines short time of the loops existence. Typical example of the measured loop trajectory is shown in Fig. 8.6a. It starts from nucleation of star-monstar pair at 720 s in common speckle (b). They

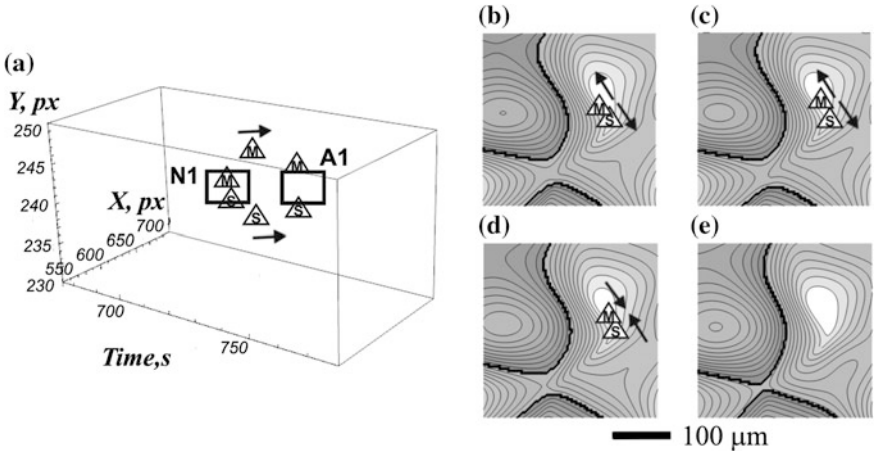

Fig. 8.6 The loop trajectory: **a** the space-time structure, **b–e** nucleation, movement and annihilation of polarization singularities pair in one speckle

repel at 735 s (c), attract then at 750 s (d) and annihilate finely at 765 s. Most of reactions in developing generic speckle fields are loops.

Another type of topological reactions is realized in the second category of topologically allowed trajectories when interact singularities from independent singularities pairs. We have shown that they aren't limited in space and time. We call them *chain* trajectories due to their analogy to well known *nuclear* and *chemical* chain reactions [15, 16]. Nuclear reaction can start even from one active neutron. Topology of particles don't play crucial role in both chain reactions.

Topological chain reactions originate then and only then, when born C point pair attract strongly and occupies *different* neighbor speckles (central lower elliptic lemon and higher hyperbolic star in Fig. 8.3a, b). Therefore, there are *two* types of topological chain reactions: star (S) and lemon (L) ones with the starting and conserving total charge −1/+1. Regularities of topological chain reactions are defined completely by general topological lows of singular optics. Chain reactions are realized, when born C points pair (star S and lemon L) are located on two *neighbor* speckles, what prevent them from immediate easy annihilation. Each of such singularities can start independent chain reactions of S or L type. Figure 8.7 presents complicated elucidate structure of L type chain reaction.

Trajectory in Fig. 8.7a exists during its more than 1500 s development. It started at 0 s from sequence of L singularities. Pair of S and L singularities nucleates at 75 s. S and first L approach and annihilate at 150 s. This moment upper and lower fragment reconnect and lower L link #1 moves long way nearly 1400 s to next annihilations. In between new pair of S-M nucleates, and star and lemon links #2, 3 moves. Ends of first and second chains annihilate at 1415 s and second reconnection takes place.

The chain reaction of L type (Fig. 8.7a) contains short link #1 from previous link and #2 of L and S singularities accordingly and three extra long links #3–5 of L singularities. Two nucleations take place at 75 and 450 s. They initiate two annihilations A1 and A2 of S-L pairs at 150 and 1415 s followed by two instantaneous reconnections of links 1 and 3, 3 and 5. The reason of appearance of extra long #3–5 is lows of topology. Indeed, pair of opposite sign singularities can annihilate then and only then, when they are located in the frame of common speckle. But it is seen that they are arranged in *different* speckles during neighbor links development. They annihilate indeed when neighbor links #1, 2 and 3, 4 attract, C points with opposite sign get in *one* speckle and annihilate soon: events A1 and A2.

Something other scenario is realized in **S**-type chain reaction (Fig. 8.7b). The upper links #1 comes from previous chain. Two pairs of opposite sign C points nucleate independently at 1315 and 2340 s in different points. The links #1 and #3 approach and annihilate at 795 s. Then links #2 and #4 approach and annihilate also at 895 s. Left link #5 remains and moves to next links as in previous chain reaction.

It is seen that both chain reaction differ in space structure but obey the same "iron" topological scenario. The measured topological chain reactions allow install their simple sum rules: $N_{nucl} = N_{an} = N_{recon}$.

Description of shown chain reactions by the structure of correspondent speckles is presented in Figs. 8.8 and 8.9. One preliminary topological remark has to proceed. Each transformation of speckle field is realized with minimal changes of its structure. Due to this only S-M pair is realized during nucleation and annihilation of C points pair because their two auxiliary morphological straight lines are parallel in these moments [2]. But M form is unstable and transforms to L when S-M pair repel. All these transformations are seen in Figs. 8.8 and 8.9.

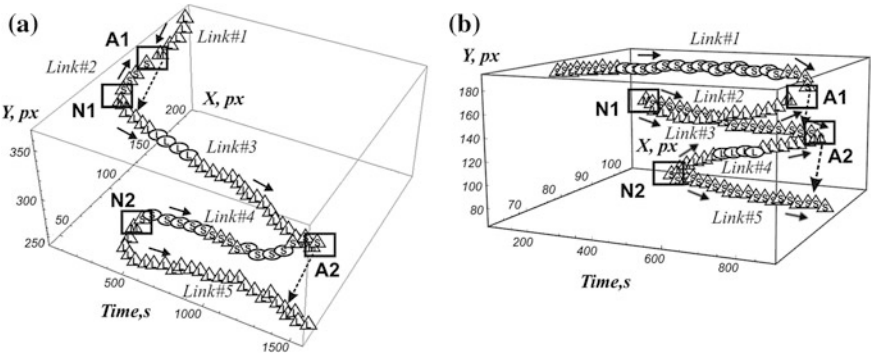

Fig. 8.7 Space-time chain trajectories of L (**a**) and S (**b**) types. *Arrows* show directions of singularities movement after their nucleation to annihilation. Moments of C point pair nucleation/annihilation are marked by *rectangles* N/A. Instantaneous reconnection of two chain trajectories lines after singularities pairs annihilations are shown by *dotted arrows*

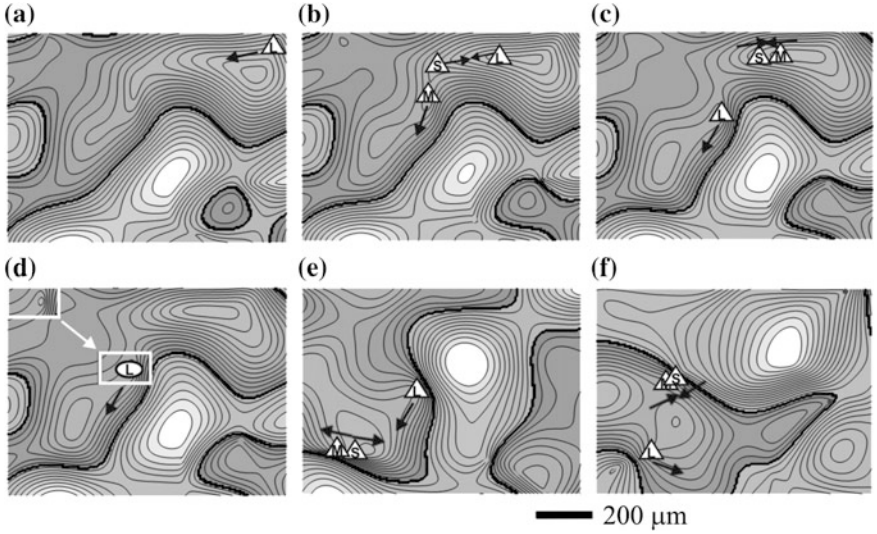

Fig. 8.8 Topology of chain reaction (Fig. 8.7a) presented throw evolution of correspondent speckles structure. The starting speckle **a** contains coming L singularity. Pair of S-M singularities is born (**b**). S moves to L and they annihilate soon (**c**). The left lower M transforms to L form and travels (**d**). Second S-M nucleates and S moves to L (**e**). Finally it annihilates with lemon transformed to monstar and left M transformed to L travels (**f**)

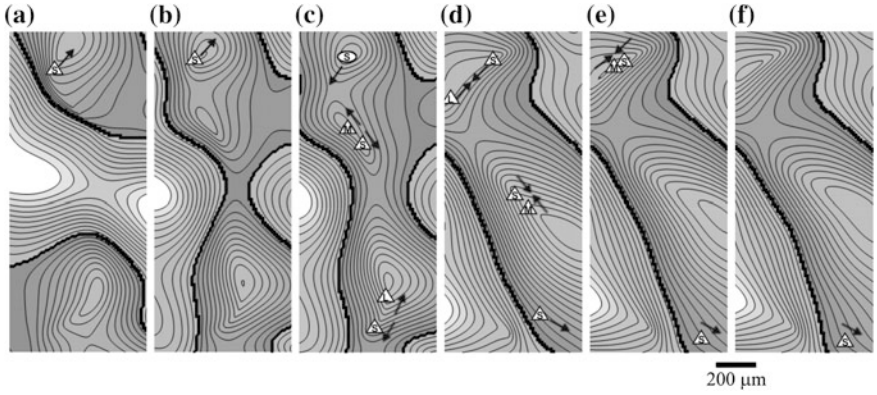

Fig. 8.9 Topology of chain reaction shown in Fig. 8.7b presented by evolution of correspondent speckles structure. Singularity S is coming from preceding link of S-type chain reaction (**a**) and travels (**b**–**c**). Two new C pairs nucleate (**c**). Two pairs of C points annihilate then (**d**) and left S started its long way (**d**–**f**)

8.5 Space-Time Autocorrelation of Dynamic Speckle Fields Development Installed by the Hurst Exponent Technique

As we see, birth, movement and topological reaction of singularities are defined by *local* transformations of developing speckle fields. The last crucial question of dynamic singular optics is checking of the *time correlation* for all perturbation processes during singular speckle field generic development. It's evident that the loop trajectories are fully correlated because they appear and develop up to annihilation in the frames of single speckle with very stable structure. But this is not evident for totality of chain reactions not limited in space and time. English scientist Hurst has discovered the essential statistical method called normalized scope (R/S), or H exponent method, which can answer this principal question [17]. H exponents' method is used often enough for analysis of the fractal time series [18]. The H values in the range $0.5 < H < 1$ indicates the time series with long-term positive autocorrelation.

Figure 8.8 shows space-time correlation of L type chain reaction (Figs. 8.10 and 8.11).

In general, linear dependence was founded for all measured chain reactions with exponent values 0.56–0.89. This witnesses high level of autocorrelation during

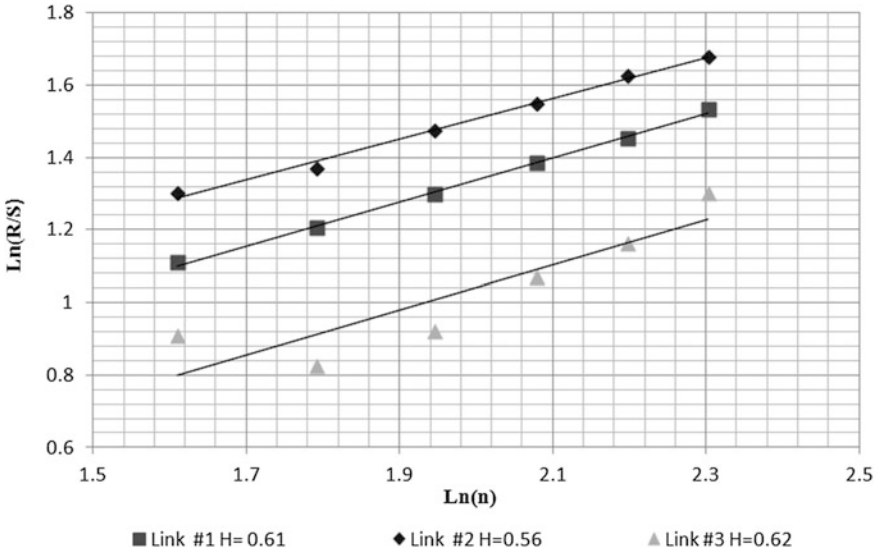

Fig. 8.10 Space-time autocorrelation of dynamic speckle fields development (L chain reaction) installed by the Hurst exponent technique

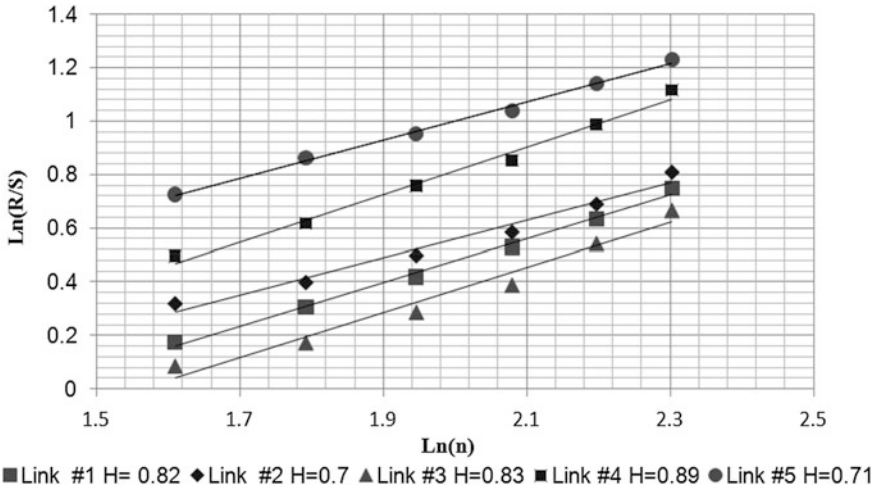

Fig. 8.11 Space-time autocorrelation of dynamic speckle fields development (S chain reaction) installed by the Hurst exponent technique

dynamic speckle field development. Shown long-time trajectories of chain reactions explain this essential result in natural way. Indeed, they develop in frame of single speckles, which are auto correlated automatically.

8.6 Conclusion

1. The generic developing vector speckle fields were realized first by the "optical-damage" effect in the photorefractive crystal $LiNbO_3$:Fe. They were investigated by advanced methods of dynamic singular optics and technique of the Hurst exponent. They develop through topological short-time *loop* in frame of *one* speckle and space/time unlimited *chain* reactions developing in *different* speckles. Their topological space-time regularities were established.
2. The morphological form of ellipses arrangement around each C point of *any sign* is defined by the helicity of underlying circularly polarized OVs (established and resolved "sing paradox").
3. The measured extra long-time links of chain reactions appeared due to existence of *alone* singularities in actual speckles against needed pair of opposite-sign C points for their annihilation. Their existence explains measured high values of the Hurst exponent $H \approx 0.56–0.89$.

References

1. J.F. Nye, M.V. Berry, Dislocations in wave trains. Proc. R. Soc. London A **336**, 165–199 (1984)
2. J.F. Nye, *Natural Focusing and Finer Structure of Light* (Institute of Physics Publishing, Bristol, 1999)
3. M.S. Soskin, M.V. Vasnetsov, Singular optics. Progress Opt. **42**(4), 219–276 (2001)
4. V.Y. Bazhenov, M.V. Vasnetsov, M.S. Soskin, Laser beams with screw dislocations of wave fronts. JETP Lett. **52**(8), 429–451 (1990)
5. J.W. Goodman, *Speckle Phenomena in Optics: Theory and Applications* (Robert and Company Publishers, CO, USA, 2007)
6. C. Dainty (ed.), *Laser Speckle and Related Phenomena* (Springer, Berlin, 1984)
7. M.S. Soskin, V.I. Vasil'ev, Nonlinear singular optics: topological dynamics of optical singularities, in *Technical Digest of International Workshop "Nonlinear Physics and Mathematics"* (Kiev, Ukraine, 2006), p. 52
8. S.G. Odoulov, B.I. Sturman, Photorefraction with the photovoltaic charge transport, in *Progress in Photorefractive Nonlinear Optics* (Taylor & Frances, London, New York, 2002)
9. V. Vasil'ev, M. Soskin, Topological and morphological transformations of developing singular paraxial vector light fields. Opt. Commun. **281**, 5527–5540 (2008)
10. M. Born, E. Wolf, *Principle of Optics*, 7th edn. (Pergamon, New York, 1999)
11. P. Coullet, L. Gil, F. Rocca, Optical vortices. Opt. Commun. **73**, 403–408 (1989)
12. M.V. Berry, J.H. Hannay, Umbilic points on Gaussian random surfaces. J. Phys. A Math. Gen. **10**, 1809–1821 (1977)
13. I. Freund, Optical diabolos: configurations, nucleations, transformations, and reactions. Opt. Commun. **272**, 293–309 (2007)
14. R.I. Egorov, M.S. Soskin, I. Freund, Experimental optical diabolos. Opt. Lett. **31**, 2048–2050 (2006)
15. J. Lamarsh, A. Baratta, *Introduction to Nuclear Engineering* (Prentice Hall, Upper Saddle River, NJ, 2001)
16. R.H. Petrucci et al., *General Chemistry Principles and Modern Applications*, 9th edn. (Pearson Prentice Hall, Upper Saddle River, NJ, 2007)
17. H.E. Hurst, R.P. Black, Y.M. Simeika, *Long-term Storage: An Experimental Study* (Comlake, London, 1965)
18. J. Feder, *Fractals* (Plenum Press, New York, 1988)

Part III
Devices of Contemporary Optoelectronics

Chapter 9
Synthetic Structures with Parity-Time Symmetry

Tsampikos Kottos and Alejandro B. Aceves

Abstract Parity-time (PT) symmetric wave mechanics is a rapidly developed field with applications in various areas of physics and mathematics. Although originally proposed in the framework of Quantum Field Theory, it was recently recognized to be a natural mathematical language necessary to describe novel wave transport phenomena in synthetic structures where balanced gain and loss mechanisms coexist. Examples of its successful implementation can be found in areas ranging from integrated photonics and electronic circuitry to antenna theory and meta-materials. The objective of this chapter is to highlight some of these successes, both in modeling and experimental implementations, of PT-symmetric optical and electronic systems.

9.1 Introduction

Modern history in Optics provides multiple examples where system properties and functionalities emerge in direct analogies with quantum mechanical counterparts. Examples include, photonic band-gap crystals, quasi-crystals, Anderson localization of light, tunneling etc. [1]. In all these cases the index of refraction (the equivalent of the potential in quantum mechanics framework) of the optical medium was considered to be real. Recently, however, it was proposed to extend the optics/quantum mechanics analogies to cases where optical gain and loss mechanisms are involved. In the quantum-mechanical framework this scenario assumes the existence of complex potentials associated to non-Hermitian Hamiltonians. Although such extension of traditional quantum mechanics is highly controversial,

T. Kottos
Department of Physics, Wesleyan University, Middletown, CT 06459, USA

A.B. Aceves (✉)
Department of Mathematics, Southern Methodist University, Dallas, TX 75275, USA
e-mail: aaceves@smu.edu

O. Shulika and I. Sukhoivanov (eds.), *Contemporary Optoelectronics*,
Springer Series in Optical Sciences 199, DOI 10.1007/978-94-017-7315-7_9

Bender and colleagues have shown [2] that a class of non-Hermitian Hamiltonians, which commute with the joint parity-time (*PT*) symmetry, can emerge as a phenomenological description of systems in quantum field theories. *PT*-symmetry impose the following constrain to the complex potential $V(x) = V^*(-x)$ in Schrödinger's equation, which might result into situations where the spectrum can still be real. This concept has been brought to the optical framework by the authors of [3]. In their work, they assumed that the complex index of refraction has the same *PT*-symmetry property, $n(x) = n^*(-x)$. Not only this property is manageable in optical devices by engineering the loss/gain profile in the optical structure, but also the strength of this component can be tuned resulting to exotic phase transition phenomena. Moreover, one can enrich the overall dynamics by use of a nonlinear optical response. Finally, many of these studies can be carried out in an experimentally friendlier platform provided by RLC circuits.

This chapter illustrates the behavior of optical and electronic *PT*-symmetric structures. While it is by no means a comprehensive discussion, thus we do not cite the hundreds of publications on *PT*-symmetric wave mechanics, we hope that the examples discussed below illustrate the canonical dynamics dictating all these many different *PT*-symmetric models that have been reported in the literature and which can be summarizes as follows: *PT*-symmetric structures present the opportunity of phase transitions from a pseudo-conservative (Hamiltonian)-like behavior to an unstable dynamics which departs from the Hamiltonian-like nature.

9.2 A Simple Example of a PT-symmetric Optical Structure: The PT-symmetric Coupler

In this section we will briefly review the basic properties of the linear *PT*-symmetric coupler [2, 4–9]. In optics this simple *PT*-system can be realized in the form of two coupled waveguides, with only one of them being optically pumped to provide gain γ for the guided light, whereas the neighbor waveguide experiences equal amount of loss. For this system we will analyze the dependence of the propagation constants on the gain/loss parameter and the structure of the associated super-modes. Then we will investigate the beam evolution in the paraxial approximation. Finally we will discuss how the PT-dynamics is modified in the presence of a Kerr non-linearity.

9.2.1 Beam Dynamics of the Linear PT-symmetric Coupler

Using the coupled-mode approach, the optical-field dynamics in the two-coupled waveguides are described by the following set of equations:

$$i\frac{d\psi_1}{dz} + \psi_2 - i\gamma\psi_1 = 0; \quad i\frac{d\psi_2}{dz} + \psi_1 + i\gamma\psi_2 = 0, \tag{9.1}$$

where $\psi_{1,2}(z)$ are modal electric field amplitudes in the amplifying and lossy waveguide channels, z represents a dimensionless propagation distance, normalized in units of coupling lengths, and γ is a scaled gain (loss) coefficient, also normalized to the coupling strength. The Hamiltonian corresponding to the linear problem of (9.1), is written as

$$H = \begin{pmatrix} i\gamma & -1 \\ -1 & -i\gamma \end{pmatrix}. \tag{9.2}$$

It is straightforward to show that Hamiltonian H of (9.2) commutes with the combined PT operator. A surprising result associated with this class of problems is the possibility that such a PT-symmetric Hamiltonian H can have an entirely real energy spectrum, despite the fact that it is non-Hermitian [7, 8].

For the specific example of the non-Hermitian Hamiltonian of (9.2), a direct diagonalization gives the following set of eigenvalues [8]:

$$E_{\pm} = \pm\sqrt{1-\gamma^2}, \tag{9.3}$$

which are real as long as the gain (loss) parameter γ is smaller than some critical value, $\gamma_{PT} = 1$ (*exact PT*-symmetric phase). As the gain (loss) parameter γ increases above γ_{PT}, the eigenvalues becomes complex (*broken PT*-symmetric phase). The transition point for which the spectrum changes from a real-valued to a complex-valued is known as the *spontaneous PT-symmetric phase transition point*. The behavior of the eigenmodes is shown in Fig. 9.1 (left).

The eigenvector problem for the non-hermitian Hamiltonian (9.2) involves a left and right bi-orthogonal set of eigenvectors that are defined via the following set of equations:

$$H|\pm_R\rangle = E_{\pm}|\pm_R\rangle; \quad \langle\pm_L|H = E_{\pm}\langle\pm_L|, \tag{9.4}$$

with the ortho-normalization condition $\langle\pm_L|\pm_R\rangle = \delta_{+,-}$. The corresponding eigenvectors are then found to be [8]

$$\begin{aligned} |+\rangle &= \tfrac{1}{\sqrt{2\cos\alpha}}\begin{pmatrix} e^{i\alpha/2} \\ e^{-i\alpha/2} \end{pmatrix}; \\ |-\rangle &= \tfrac{1}{\sqrt{2\cos\alpha}}\begin{pmatrix} ie^{-i\alpha/2} \\ -ie^{i\alpha/2} \end{pmatrix}; \quad \sin(\alpha) = \gamma \end{aligned}. \tag{9.5}$$

In the exact PT-symmetric phase, both the H and PT operators share the same set of eigenvectors. In this regime, the mode intensity is symmetric with respect to the mirror axis of the two waveguides, see Fig. 9.1 (right). As γ increases above γ_{PT} the eigen-functions of H cease to be eigenfunctions of the PT operator, despite the fact

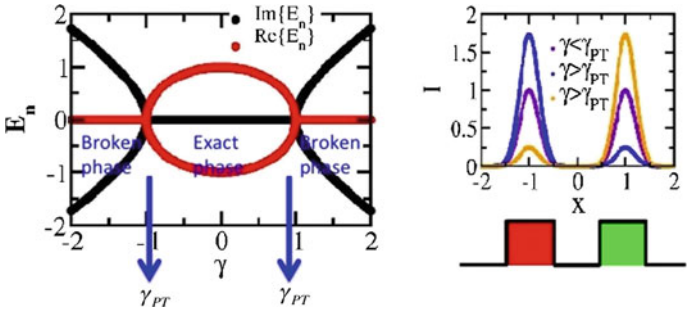

Fig. 9.1 *Left* Eigenvalue spectra of the Hamiltonian system (9.1, 9.2). *Red points* correspond to the real part of the eigenvalues while black to the imaginary part. At the exact phase, corresponding to $\gamma < |\gamma_{PT}|$, the imaginary part (*black points*) is zero. For gain/loss values greater than γ_{PT} (marked with the *blue arrows*) the spectrum becomes complex and the eigenvalues appear in pairs with elements that are complex conjugates of one another. *Right* Typical spatial distribution of the supermodes of a system consisting of two *PT*-symmetric coupled waveguides (*low inset*). For $\gamma < \gamma_{PT}$ (*maroon line*) the modal intensity is respecting the PT-symmetry of the problem and it is equally distributed between the two waveguides. As the gain/loss parameter increases beyond the spontaneous PT-symmetry breaking point, each of the two modes becomes isolated in each waveguide (*blue and yellow curves*)

that H and the PT operator still commute. This happens because the PT operator is anti-linear, and thus the eigenstates of H may or may not be eigenstates of PT. In the broken PT-symmetric phase, the spatial distribution of the modes is asymmetric, one of them living predominantly in the amplifying site and the other in the lossy one, see Fig. 9.1 (right). At the phase-transition point $\gamma = \gamma_{PT}$ the two eigenfunctions and their corresponding eigenvalues coalesce leading to an "exceptional" point singularity.

The beam dynamics associated with (9.1) was investigated theoretically in [6, 8]. It is relatively straightforward to analyze the dynamics. To this end the Hamiltonian (9.2) is first written in the form $H = |E_\pm| \vec{\sigma}\hat{n} = |E_\pm|\sigma_n$ where σ_n is the Pauli matrix along the $\hat{n} = (1/|E_\pm|)(1, 0, \gamma)$ direction. Using the identity $\exp(iz\sigma_n) = \cos(z)\hat{1} + i\sin(z)\sigma_n$ ($\hat{1}$ is the identity matrix), the effective evolution operator $\hat{U}(z)$ takes the form:

$$\hat{U}(z) = \exp(-izH) = \cos(|E_\pm|z)\hat{1} - i\sin(|E_\pm|z)H/|E_\pm|. \tag{9.6}$$

Application of the above operator to a generic initial preparation $\psi(z=0) = (c_1, c_2)^T$ allow us to evaluate the beam $\psi(z)$ at a propagation distance z

$$\psi(z) \equiv \begin{pmatrix} \psi_1(z) \\ \psi_2(z) \end{pmatrix} = \frac{1}{\cos\alpha} \begin{pmatrix} c_1 \cos(\frac{|E_\pm|z}{2} - \alpha) - c_2 i \sin(\frac{|E_\pm|z}{2}) \\ c_2 \cos(\frac{|E_\pm|z}{2} + \alpha) - c_1 i \sin(\frac{|E_\pm|z}{2}) \end{pmatrix} \tag{9.7}$$

The total light intensity $I(z) = |\psi_1(z)|^2 + |\psi_2(z)|^2$ is not any more a constant of motion. Its dependence on the paraxial distance z can be easily evaluated from (9.7):

$$I(z) = \frac{1}{2\cos^2\alpha}\left(\cos^2\left(\frac{|E_\pm|z}{2} - \alpha\right) + \cos^2\left(\frac{|E_\pm|z}{2} + \alpha\right) + 2\sin^2\left(\frac{|E_\pm|z}{2}\right)\right). \tag{9.8}$$

In Fig. 9.2 we plot the theoretical expressions (9.7, 9.8) describing the beam dynamics associated with the *PT*-symmetric coupler for some typical values of the gain/loss parameter γ [6]. The associated experimental measurements have been performed in [4, 5]. These authors recognized that as the gain (loss) parameter γ reaches γ_{PT}, the total beam power starts growing exponentially [see Fig. 9.2 (right)], while for $\gamma < \gamma_{PT}$ power oscillations are observed [see Fig. 9.2 (left)]. The former behavior is rooted in the complex nature of the propagating constants in the broken phase, while the latter is due to the bi-orthogonal nature of the super-modes. At $\gamma = \gamma_{PT}$ the intensity grows in a power law manner with respect to the propagation distance z. This is due to the existence of a defective eigenvalues (exceptional point). All these cases can be easily derived analytically from (9.7). In all cases the beam evolution is non-symmetric (see Fig. 9.2). Specifically, the beam propagation pattern differs depending on whether the initial excitation is on the left or right

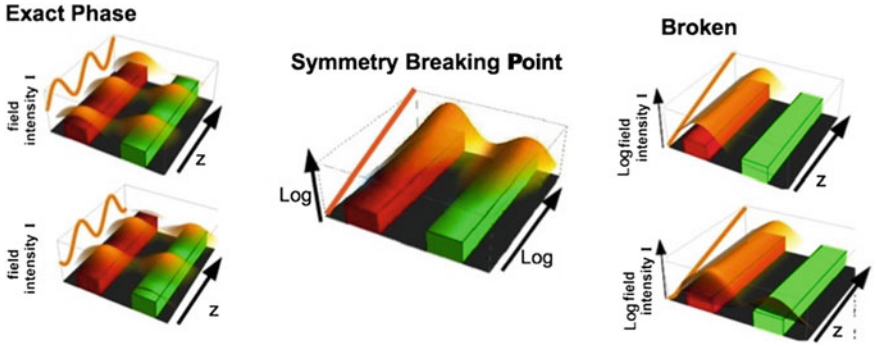

Fig. 9.2 Beam dynamics for a PT-symmetric coupler. The waveguides are colored according to the gain/loss parameter (*red* for gain and *green* for loss). *Left* At the exact phase, corresponding to $\gamma < \gamma_{PT}$ the system is in the exact phase, with real-valued propagation constants. The PT-symmetric nature of the dynamics can be seen in the variation of the total light intensity (*orange line*), which shows oscillatory behavior. Moreover the dynamics is non-symmetric for different initial conditions (e.g. incident beam at the gain—upper- or loss—lower—waveguides), with respect to the z-axis of symmetry of the structure. *Center* The beam dynamics at the exceptional point $\gamma = \gamma_{PT}$. Notice that now the total field intensity (*orange line*) grows in a power law with the propagation distance z. *Right* The beam dynamics in the broken phase corresponding to $\gamma > \gamma_{PT}$. In this case the beam intensity grows exponentially (notice the log-scale in the vertical axis), whereas the beam propagation is again non-symmetric with respect to the mirror axis of the two waveguides [6]

waveguide. This has to be contrasted with the $\gamma = 0$ case, where the beam propagation is insensitive to the initial condition i.e. if the incident beam is launched in the left or right waveguide.

9.2.2 *Beam Dynamics of the Non-linear PT-symmetric Coupler*

In this section, we review a new mechanism, first reported in [9], for unidirectional optical transport based on configurations involving nonlinear optical materials with *PT*-symmetry. Specifically it was shown that the interplay of non-symmetric dynamics arising from *PT*-symmetry, and self-trapping phenomena associated with Kerr nonlinearities [10], can mold the flow of light in a surprising way. Such novel directed dynamics could be exploited in the realization of a new generation of optical isolators.

Even though the validity of this mechanism can be demonstrated for a variety of non-linear *PT*-configurations, below, we will highlight its basic principles, using the simplest possible arrangement, consisting of two *PT*-coupled waveguide elements with Kerr nonlinearity of strength χ. Each of the waveguides is single-mode—one providing gain and the other an equal amount of loss (see Fig. 9.3). Nonlinear *PT*-symmetric optical coupled systems can be realistically synthesized on semiconductor wafers-known for their high Kerr-like nonlinearities [11].

We begin our presentation by providing the mathematical model that describes optical wave propagation in a Kerr nonlinear *PT*—symmetric coupled dual waveguide arrangement. The two modal field amplitudes are governed by the evolution equations:

$$i\frac{d\psi_1}{dz} + \psi_2 - i\gamma\psi_1 + \chi|\psi_1|^2\psi_1 = 0; \quad i\frac{d\psi_2}{dz} + \psi_1 + i\gamma\psi_2 + \chi|\psi_2|^2\psi_2 = 0 \quad (9.9)$$

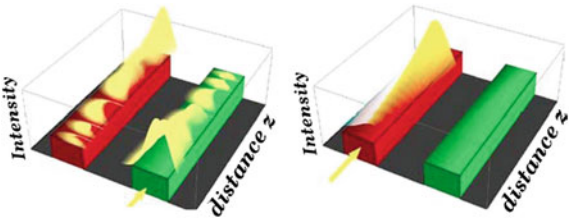

Fig. 9.3 Beam propagation in two coupled nonlinear waveguides with non-linearity strength χ and a complex *PT*-symmetric refractive index profile. Waveguides are color coded, indicating balanced gain (*red*) and loss (*green*) regions ($\gamma = 0.1$). *Left subfigure* Corresponds to an initial excitation at the gain waveguide port, while *right subfigure* corresponds to an initial excitation at the lossy waveguide. The non-linearity strength is $\chi = 8 > \chi_d$ [9]

where all variables are the same as the ones in (9.1)—and χ is the strength of the Kerr-nonlinearity. In (9.9) γ is a scaled gain/loss coefficient, also normalized to the coupling strength.

Equation (9.9) can be re-written in terms of the Stokes parameters $S_0 = |\psi_1|^2 + |\psi_2|^2$; $S_1 = \psi_1^*\psi_2 + \psi_1\psi_2^*$; $S_2 = i(\psi_1\psi_2^* - \psi_1^*\psi_2)$; and $S_3 = |\psi_1|^2 - |\psi_2|^2$. We note that Stokes parameters always satisfy the relation $S_0^2 - \vec{S}\cdot\vec{S} = 0$. In this representation, (9.9) take the form [9]:

$$\frac{dS_0}{dz} = \vec{E}\cdot\vec{S}; \quad \frac{d\vec{S}}{dz} = S_0\vec{E} + \vec{S}\times\vec{B}, \tag{9.10}$$

where $\vec{E} = (0, 0, 2\gamma)$, $\vec{B} = (2, 0, \chi S_3)$ and $\vec{S} = (S_1, S_2, S_3)$ is the three-dimensional Stokes vector.

For $\gamma = 0$ the dynamics has two constants of motion: The total energy H = $(\chi/2)S_3^2 + 2S_1$ and the total beam intensity S_0 inside the two waveguides. However, when $\gamma \neq 0$ these two quantities are not any more conserved. Instead PT-symmetry enforces two other constants of motion [9]:

$$C^2 = (\chi S_1 - 2)^2 + (\chi S_2)^2; \quad \mathrm{J} = S_0 + \frac{2\gamma}{\chi}\sin^{-1}\left(\frac{\chi S_1 - 2}{C}\right). \tag{9.11}$$

For the specific initial conditions $S_0(0) = 1, S_3(0) = \pm 1, S_1(0) = S_2(0)$ further theoretical calculations for the evaluation of the Stokes parameters can be carried out. It can be shown [9] that there is a critical value of nonlinearity $\chi_d = 4 - 2\pi\gamma$ for which the beam evolution is unidirectional, i.e., the output beam remains in the gain channel, irrespective from the input channel.

Examples of the resulting beam dynamics for $\gamma = 0.1$ and representative non-linearity strength $\chi = 8 > \chi_d$ is reported in Fig. 9.3. One can see that the output field always leaves the sample from the waveguide with gain (red-colored) irrespective of the preparation of the input beam. At the same time the output beam intensity at the lossy waveguide becomes zero for waveguides longer than some critical length z_d [9]. The behavior shown in Fig. 9.3 implies that such systems can be used to realize a new class of optical isolators. Finally, it is important to point that the nonlinear *PT*-symmetric isolator discussed in this section is polarization insensitive, it does not rely on higher harmonic generation and it can be fabricated as an on-chip element. Furthermore it provides a broadband nonreciprocal action.

The isolation action in the nonlinear *PT*-symmetric dimer is a result of dynamical decoupling. Above the critical value of non-linearity the input beam from the lossy channel experience a low index of refraction, therefore it tunnels to the gain waveguide. On the other hand, once the light is at the gain waveguide, it experiences a high index of refraction, which confines it to this waveguide. As a result it cannot tunnel back to the lossy waveguide. In the backward process the beam initiated from the gain waveguide from the very beginning is self-trapped and there is no tunneling to the lossy waveguide.

9.3 An Alternative Framework: PT-symmetric Electronics

While the impact of *PT*-symmetric wave mechanics ideas within the framework of non-Hermitian optics it possess various experimental difficulties (see, however, recent experimental results along these lines [4, 5, 12, 13]), it is possible to explore (generalized) *PT*-symmetry using electric circuits where complex potentials can be synthesized with the help of resistors and amplifiers [14]. In fact, there exist an exact isomorphism that maps an RLC array to a discrete Hamiltonian, termed a tight-binding (TB) Hamiltonian. TB Hamiltonians have been used in the past for the mathematical description of electrons on lattices, or wave propagation in coupled waveguide arrays. More recently TB Hamiltonians with *PT* symmetric potentials, were used in the theoretical studies of PT systems (see for example [15]).

To demonstrate the relation between a TB Hamiltonian and a generic RLC array with amplification and attenuation we consider the electrical circuit of classical impedances Z_n and z_n shown in the upper panel of Fig. 9.4. Application of Kirchhoff's Loop Rule to three successive unit cells of the circuit leads to the following linear relation between the voltages V in the $(n-1)$-th, n-th and $(n+1)$-th cells

$$b_n V_{n+1} + b_{n-1} V_{n-1} = (B_n + b_{n-1} + b_n - iG_n) V_n, \tag{9.12}$$

where $B_n = \Im m(Z_n^{-1})$, $\mathrm{b}_n = \Im m(z_n^{-1})$ are the corresponding susceptances and $G_n = \Re e(Z_n^{-1})$ is the conductance. At the same time the generalized TB Hamiltonian describing a particle moving on a lattice (lower panel of Fig. 9.4) is given by the equation:

$$h_n \psi_{n+1} + h_{n-1} \psi_{n-1} = (E - \varepsilon_n) \psi_n, \tag{9.13}$$

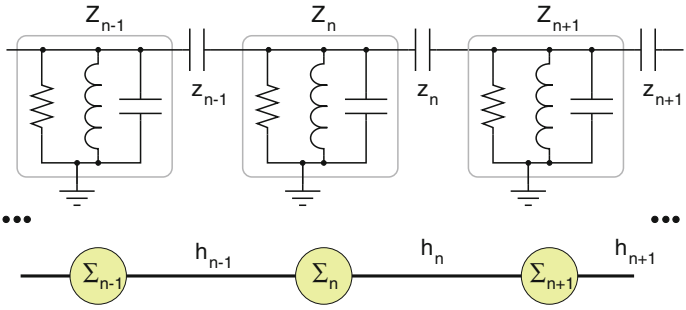

Fig. 9.4 *Up* Three sequential units of an RLC array coupled capacitively. *Down* The corresponding tight-binding system

where $n = 1, \ldots, N$ is the site index, ψ_n is the eigenmode amplitude at site n while h_n is the coupling element between nearby sites. Comparison between (9.12) and (9.13) indicate that these two equations are isomorphic if we assume $(h_n;\varepsilon_n;E) \rightarrow (b_n;\delta_n + iG_n;b_n + b_{n-1} + \bar{B})$. Here the value of the susceptance B_n is split into its mean value $\bar{B} = \langle B_n \rangle$ and a possible fluctuating part $\delta_n = \bar{B} - B_n$. In the simple case where $h_{n-1} = h_n = h$ the Hamiltonian described by (9.13) is *PT*-symmetric if the complex on-site potential $\varepsilon_n = b_n + i\gamma_n$ satisfies the constraint $\varepsilon_n = \varepsilon^*_{N+1-n}$. In this case, the isomorphism between (9.12) and (9.13) is complete once we set $\varepsilon_n/h = (\delta_n + iG_n)/b$ and $E/h = 2 + \bar{B}/b$. Obviously, *PT*-symmetry requires that $\delta_n + iG_n = \delta_{N+1-n} + iG_{N+1-n}$. The above discussion demonstrates that RLC lattices, appropriately augmented, with positive (attenuated) and negative (amplified) $\Re e(Z_n) = R_n$ elements, can be used for the experimental study of *PT*-dynamics.

9.3.1 Experimental Demonstration of PT-symmetric RLC Circuits

The authors of [14], have provided a simple experimental realization which displays all the novel phenomena encountered in a minimal *PT*-symmetric structure: a pair of coupled, active RLC circuits, one with amplification and the other with equivalent attenuation. This active dimer, illustrated at the left subpanel of Fig. 9.5, is implemented with simple electronics, and allows a direct observation of the spontaneous *PT*-symmetric breaking phase transition by measuring the

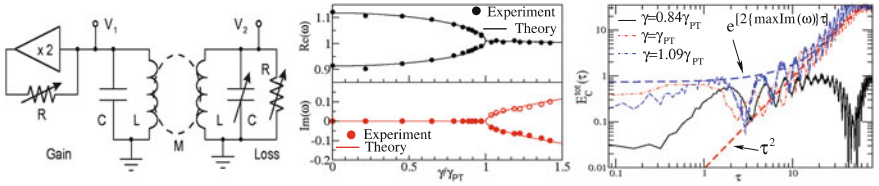

Fig. 9.5 *Left* Electronic implementation of a PT-symmetric dimer. The negative resistance (gain element) is provided by feedback from a voltage-doubling buffer. The coils are inductively coupled, and V_1 and V_2 provide access to the system variables; *Center* parametric evolution of the experimentally measured eigenfrequencies (in units of $\omega_0 = 1/\sqrt{LC}$), versus the normalized gain/loss parameter γ/γ_{PT}. A comparison with the theoretical results (*solid lines*) indicates an excellent agreement. In all cases, we show only the $\Re e(\omega_l) > 0$ eigenfrequencies. The *open circles* in the lower panel are reflections of the experimental data (*lower curve*) with respect to the $\Im m(\omega_l) = 0$ axis; *Right* Experimentally measured temporal dynamics of the capacitance energy $E_C^{tot}(\tau)$ of the total system for various γ-values. As $\gamma \rightarrow \gamma_{PT}$ the τ^2 behavior signaling the spontaneous *PT*-symmetry breaking is observed [14]

eigenfrequencies. Kirchhoff's laws, lead to the following set of equations for the charge Q_n on the capacitors ($n = 1$ correspond to the amplified and $n = 2$ to the lossy sides)

$$\begin{aligned}\frac{d^2Q_1}{d\tau^2} &= -\frac{1}{1-\mu^2}Q_1 + \frac{\mu}{1-\mu^2}Q_2 + \gamma\frac{dQ_1}{d\tau},\\ \frac{d^2Q_2}{d\tau^2} &= \frac{\mu}{1-\mu^2}Q_1 - \frac{1}{1-\mu^2}Q_2 - \gamma\frac{dQ_2}{d\tau},\end{aligned} \tag{9.14}$$

where $\tau \equiv \omega_0 t$, $\gamma = R^{-1}\sqrt{L/C}$ is the gain/loss parameter, $\mu = M/L$ is the rescaled mutual inductance and $\omega_0 = 1/\sqrt{LC}$ (see left subpanel of Fig. 9.5). Direct inspection of (9.14) indicates that they are invariant under a combined P (i.e. $n = 1 \leftrightarrow n = 2$) and T (i.e. $t \to -t$) transformation.

The measured eigen-frequencies are presented in the center panel of Fig. 9.5, indicating a transition from real (exact phase) to complex (broken phase) valued as the attenuation/amplification parameter γ increases. At the spontaneous *PT*-breaking point γ_{PT}, the normal modes coalesce and the relative phase differences of their components acquire a definite value dictated by the inductive coupling [14]. The consequences of the phase-transition in the spatiotemporal energy evolution (right subpanel of Fig. 9.5) were identified and traced back to the properties of the normal modes. Specifically, for $\gamma < \gamma_{PT}$, it was observed energy oscillations due to the bi-orthogonal nature of the eigen-modes, while an exponential increase of the energy was found for $\gamma > \gamma_{PT}$. It has to be stressed that the experimental realization of [14] was the first one that allowed for an actual spatio-temporal study of *PT*-symmetric structures. Work that will follow is to include nonlinear effects arising in the loss/gain term where $\gamma \to \gamma(1 - Q_j^2)$.[1] By use of weakly nonlinear theory (multiple-time scales) one derives modulation equations for the amplitudes of the linear eigenfunctions. We then expect to capture the correction to the bifurcation value and the subsequent nonlinear dynamics.

Other subsequent achievements involving *PT*-symmetric scattering set-ups can be found in [16–19]. Being free of theoretical approximations, and due to its relative simplicity in the experimental implementation, the RLC-network with *PT* symmetry can offer new insights into the study of *PT*-symmetric systems and a practical means for testing new concepts with direct applications in RF systems. It is also worth mentioning that RLC circuits are often used to describe the dynamics in split-ring resonator metamaterials. While in recent years the focus in metamaterial research has been to develop new avenues that will minimize the tremendous losses via integration of optical gain, it is expected that the investigations of *PT*-symmetric RLC circuitry will lead to new and more efficient design schemes.

[1]Notice that such a nonlinear RLC dimer was already realized experimentally in [19] where its scattering properties have been investigated.

9.4 Large PT-symmetric Array Systems

In this section we pay attention to large array systems formed by waveguides [20], lattices [15, 21–26], and similar to the RLC arrays presented above, metamaterial nano-resonators [27, 28] all of which have the *PT*-symmetry property. Starting with what would be a natural extension of the coupler previously discussed, the authors in [20] modified an otherwise homogeneous waveguide array by inserting a gain-loss coupler. What they observed in their numerical studies was that symmetry-breaking thresholds were different for planar versus circular array configurations, thus making PT-symmetry breaking topologically sensitive. It was shown that the beam dynamics is shaped by guides at locations away from the coupler, an indication of nonlocality. PT-symmetric lattices can have a spatially extended gain/loss region [21, 22] and can be nonlinear. As with classical optical lattice systems, modeling depends of whether you are considering truly discrete modes or extended (long-wave) modes. In the second case, it is common to find theoretical models like the nonlinear Schroedinger equation with a complex potential [22],

$$i\frac{\partial\psi}{\partial z}+\frac{\partial^2\psi}{\partial x^2}+V(x)\psi+\sigma|\psi|^2\psi=0, \tag{9.15}$$

where the lattice geometry is described by the periodicity of the complex potential $V(x+d)=V(x)$, the PT-symmetry results in the condition $V^*(-x)=V(x)$. In the linear regime, Floquet-Bloch (FB) modes have been found with novel dynamic properties like power oscillations and unique diffraction patterns, some exhibiting phase singularities [5]. In the simplest case where $V(x)=V_r(x)+i\gamma V_i(x)$, the starting point is the known solutions for $\gamma=0$ many of which had been known for a long time; one then uses continuation techniques from bifurcation theory to track the deformation of solutions of the Hamiltonian model up to a critical value where they no longer exist. As an example, in [23] the authors show solitons bifurcating from the FB-modes; these solitons are stable up to a critical value of the strength of the imaginary part of the potential and in some instances the unstable behavior leads to unbounded energy grow of the propagating beam (see Fig. 9 in [23]).

Interestingly, discrete models are by necessity binary-like. Three examples follow: the first one is of particular interest simply because it illustrates *PT*-symmetry in a discrete system outside the realm of optics and electronics. In the tight-binding model (Fig. 1 in [21]), the governing equations are

$$\begin{aligned} i\frac{da_n}{dt}&=-\kappa b_n-\sigma b_{n-1}-\rho e^{i\varphi}a_{n+1}-\rho e^{-i\varphi}a_{n-1}+iga_n,\\ i\frac{db_n}{dt}&=-\kappa a_n-\sigma a_{n+1}-\rho e^{i\varphi}b_{n+1}-\rho e^{-i\varphi}b_{n-1}-igb_n, \end{aligned} \tag{9.16}$$

where the loss/gain property is described by the last term in each equation. This model is a non-Hermitian extension of the Rice-Mele dimerized lattice of

conjugated diatomic polymers. In [21], the author demonstrates analytically and numerically that the PT-induced phase transition can be either convective or absolute.

Optical lattices with PT-symmetry have also been studied for different configurations and applications. In each case, the discrete symmetry allows to study optical phenomena of interest. In [24] the basic unit of the linear lattice is the one considered in the linear loss/gain coupler studied in Sect. 9.2. These lattices support the Talbot effect of self-imaging revivals for input patterns whose periodicity are dictated not only by the discreteness of the lattice but by the strength of the loss/gain parameter as well, which could be used for image quality control. A second geometry that has been studied is that the basic unit forms a honeycomb lattice [25] where conical diffraction solely depends on the gain/loss parameter. In fact, for linear lattices one can work on the "inverse" problem [26] where one simulates transformations among discrete PT-symmetric systems by suitable coupling maps so that the spectra remains real and then see the role nonlinearity plays in the dynamics.

Rather that discussing the analytical tools used for these models, we dedicate the remainder of this section to a more detailed discussion of recent work on an array of split-ring resonators studied in [27, 28]. The array shown in Fig. 9.6 (similar to Fig. 1 in [28]), whose governing equations for the charges in the odd and even resonators are,

$$\begin{aligned}
\frac{d^2A_m}{dt^2} + A_m &= -\lambda_M' \frac{d^2B_m}{dt^2} - \lambda_M \frac{d^2B_{m+1}}{dt^2} + \varepsilon_0 \sin(\Omega t) - \alpha A_m^2 - \beta A_m^3 - \gamma \frac{dA_m}{dt}, \\
\frac{d^2B_m}{dt^2} + B_m &= -\lambda_M \frac{d^2A_{m-1}}{dt^2} - \lambda_M' \frac{d^2A_m}{dt^2} + \varepsilon_0 \sin(\Omega t) - \alpha B_m^2 - \beta B_m^3 + \gamma \frac{dB_m}{dt},
\end{aligned} \tag{9.17}$$

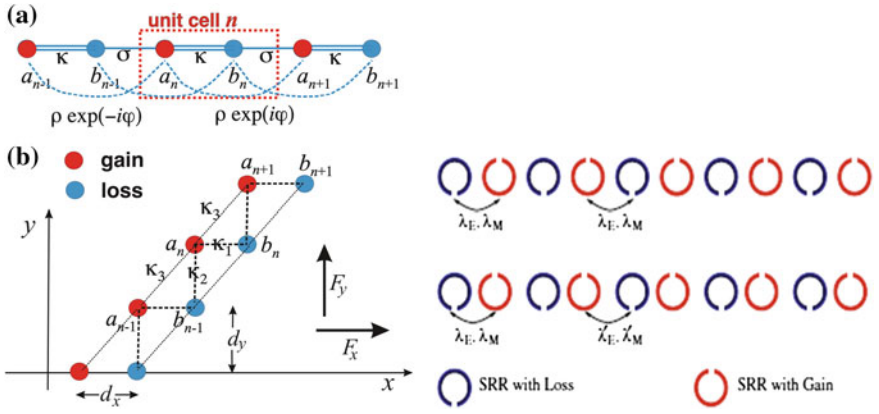

Fig. 9.6 *Left figure* Tight binding array model studied in [21]. *Right figure* Split ring resonator array studied in [27]

where as in the previous example, the last terms in the system describe loss/gain. In [28], the authors demonstrate numerically that discrete breathers in such a dimer chain are generic though their long-term stability is compromised when the balance between gain and loss is not exact. It is not clear though if a symmetry breaking bifurcation typical of PT-systems. Since it is the case that all coefficients in the right hand side of the model are small, we can apply weakly nonlinear (multiple time scale) theory to what at the first order of approximation are uncoupled identical oscillators. This approach gives equations for the slowly varying amplitude modulations,

$$a_m(\tau), b_m(\tau); A_m(t,\tau) = a_m(\tau)e^{it} + cc, B_m(t,\tau) = a_{bm}(\tau)e^{it} + cc, \tag{9.18}$$

where τ is the slow time. Because of the applied periodic voltage to the resonators, three regimes arise: at resonance ($\Omega = 1$), near resonance ($\Omega = 1 + \varepsilon\omega$; $\varepsilon \ll 1$) and far away from resonance. If in addition, we restrict the study to extended breathers where the continuum approximation is valid, one arrives to the coupled system (CME) of partial differential equations (for the non-resonant case):

$$\begin{aligned} -i\frac{\partial b}{\partial \tau} + \frac{\partial a}{\partial x} &= \frac{1}{\lambda_M}\left[\alpha_M a - 3\beta|b|^2 b + i\gamma b\right], \\ i\frac{\partial a}{\partial \tau} + \frac{\partial b}{\partial x} &= \frac{1}{\lambda_M}\left[-\alpha_M b + 3\beta|a|^2 a + i\gamma a\right], \end{aligned} \tag{9.19}$$

where the continuum approximation means:

$$a_n(\tau) \to a(x = n, \tau), b_n(\tau) \to b(x = n, \tau).$$

In [28], we found that for $\gamma = 0$ there are exact soliton solutions describing extended breathers in the array. In the general case, these breathers can propagate across the array. In the stationary regime, we find analytically that breathers persist up to the critical value $\gamma_c = |\alpha_M|$ at which a bifurcation arises. Work that will follow is what type of nonlinear modes and their corresponding bifurcation properties for the near resonant and the resonant cases described by the system below

$$\begin{aligned} -i\frac{\partial b}{\partial \tau} + \frac{\partial a}{\partial x} &= \frac{1}{\lambda_M}\left[\alpha_M a - 3\beta|b|^2 b + i\gamma b - i\frac{\varepsilon}{2}f\right], \\ i\frac{\partial a}{\partial \tau} + \frac{\partial b}{\partial x} &= \frac{1}{\lambda_M}\left[-\alpha_M b + 3\beta|a|^2 a + i\gamma a + i\frac{\varepsilon}{2}f\right], \end{aligned} \tag{9.20}$$

where $f = 1 (f = e^{i\delta\tau})$ for the in(near) resonance case. Finally, we expect to apply this approach and study long arrays of the coupled RLC circuits discussed in the previous section. The starting point as we did here is to find amplitude equations in the slow-time, long-wave limit and analyze them with techniques suitable for Hamiltonian PDE's.

9.5 Beam Dynamics in PT-symmetric Waveguides

In the previous section we mentioned that lattice potentials could be described in the continuum approximation by the NLSE. Similarly, planar nonlinear waveguides with gain (loss) for $x<(>)0$ are modeled by the same equation. Take for example a complex Scarff II potential $V(x) = V_0\text{sech}^2(x) + iW_0\text{sech}(x)\tanh(x)$. In [29], the authors obtained exact guided modes of (9.15) of the form:

$$\psi = A\text{sech}(x)e^{i\mu\tan^{-1}[\sinh(x)]+iz}, \quad \mu = W_0/3, \quad A = \sqrt{2 - V_0 + (W_0/3)^2}. \quad (9.21)$$

This solution was numerically tested to be linearly stable for values of the gain/loss coefficient W_0 above the bifurcation value $V_0 + 1/4$ of the linear case. The nontrivial phase form explains that the stable behavior results from the fact that the momentum $S = i/2[\psi\psi_x^* - cc] = (W_0A^2/3)\text{sech}^3(x)$ is always positive implying that power always flows from the gain to the loss direction. An exact balance of this flux allows for the existence of a stationary propagating mode.

While there is not much work reported in two-dimensional PT-symmetric structures, it would be interesting in particular to extend this work for two-dimensional nonlinear waveguides. For real 2d potentials (classical waveguide theory), at low powers linear-like guided modes exist, whereas a blow-up singularity triggered by the instability of the Townes soliton would destabilize such modes at high powers. The question is then what would be the role of having a gain/loss potential. One would expect a similar flux feature as in the 1-d case, which perhaps would stabilize confined beams at high powers.

9.6 Conclusions

As we indicated in the Introduction, this short review is by no means a complete presentation of the many new results on PT-symmetric structures that have appeared and continues to appear in the literature. For example, in our presentation we did not discuss optical structures with defocusing nonlinearities, where vortices play the role of solitons in the focusing regime [30]. Similarly, we did not review the unique scattering properties of PT-symmetric systems and their possible application in producing unidirectional reflectionless PT-metamaterials [31]. Finally, following the extension of PT-symmetry to optics and electronics, there are some recent studies investigating the possibility to realize (pseudo-)PT-symmetric dynamics in the framework of (ultra)-cold atoms [32–35]. If anything, this only suggests that the story is just beginning.

Acknowledgements The authors want to particularly thank our colleagues Hui Cao, Demetrios Christodoulides and Greg Salamo with whom we have had fruitful collaborations on this research topic. TK also acknowledge many useful discussions with F. Ellis on *PT*-electronics. Many of the

results reviewed here is the outcome of fruitful collaboration with N. Bender, D. Christodoulides, F. Ellis, Z. Lin, H. Ramezani, J. Schindler, D. Wang, M. Zheng. The National Science Foundation through the ECCS-1128593 IDR grant has supported this collaborative work.

References

1. S. Longhi, Quantum-optical analogies using photonic structures. Laser Photonic Rev. **3**(3), 243–261 (2009)
2. C.M. Bender, S. Boettcher, S. Phys. Rev. Lett. **80**, 5243 (1998)
3. R. El-Ganainy, K.G. Makris, D.N. Christodoulides, Z.H. Musslimani, Theory of coupled optical PT-symmetric structures. Opt. Lett. **32**, 2632 (2007)
4. A. Guo, G.J. Salamo, D. Duchesne, R. Morandotti, M. Volatier-Ravat, V. Aimez, G.A. Siviloglou, D.N. Christodoulides, Observation of P T symmetry breaking in complex optical potentials. Phys. Rev. Lett. **103**, 093902 (2009)
5. C.E. Ruter et al., Observation of parity–time symmetry in optics. Nat. Phys. **6**, 192 (2010)
6. T. Kottos, Nat. Phys. **6**, 166 (2010)
7. C.M. Bender, D.C. Brody, H.F. Jones, Phys. Rev. Lett. **89**, 270401 (2002)
8. C.M. Bender, Making sense of non-Hermitian Hamiltonians. Rep. Prog. Phys. **70**, 947 (2007)
9. H. Ramezani, T. Kottos, R. El-Ganainy, D.N. Christodoulides, Unidirectional nonlinear PT-symmetric optical structures. Phys. Rev. A **82**, 043803 (2010)
10. S.M. Jensen, IEEE J. Q. Electron. **18**, 1580 (1982)
11. B.E.A. Saleh, M.C. Teich, *Fundamentals of Photonics* (Wiley, NY, 1991)
12. A. Regensburger, C. Bersch, M.-A. Miri, G. Onishchukov, D.N. Christodoulides, U. Peschel, Parity-time synthetic photonic lattices. Nature **488**(7410), 167 (2012)
13. T. Eichelkraut, R. Heilmann, S. Weimann, S. Stutzer, F. Dreisow, D.N. Christodoulides, S. Nolte, A. Szameit, Mobility transition from ballistic to diffusive transport in non-Hermitian lattices. Nat. Commun. **4**, 2533 (2013)
14. J. Schindler, A. Li, M.C. Zheng, F.M. Ellis, T. Kottos, Experimental study of active LRC circuits with PT-symmetries. Phys. Rev. A **84**, 040101(R) (2011)
15. M.C. Zheng, D.N. Christodoulides, R. Fleischmann, T. Kottos, Phys. Rev. A **82**, 010103 (2010)
16. H. Ramezani, J. Schindler, F.M. Ellis, U. Gunther, T. Kottos, Bypassing the bandwidth theorem with PT symmetry. Phys. Rev. A **85**, 062122 (2012)
17. Z. Lin, J. Schindler, F.M. Ellis, T. Kottos, Experimental observation of the dual behavior of PT-symmetric scattering. Phys. Rev. A **85**, 050101(R) (2012)
18. J. Schindler, Z. Lin, J.M. Lee, H. Ramezani, F.M. Ellis, T. Kottos, PT-symmetric electronics. J. Phys. A Math. Theor. **45**, 444029 (2012)
19. N. Bender, S. Factor, J.D. Bodyfelt, H. Ramezani, D.N. Christodoulides, F.M. Ellis, T. Kottos, Observation of asymmetric transport in structures with PT-symmetric nonlinearities. Phys. Rev. Lett. **110**, 234101 (2013)
20. A.A. Sukhorukov, S.V. Dmitriev, S.V. Suchkov, Y.S. Kivshar, Nonlocality in PT-symmetric waveguide arrays with gain and loss. Opt. Lett. **37**(11), 2148–2150 (2012)
21. S. Longhi, Convective and absolute PT symmetry breaking in tight-binding lattices. arXiv:1310.5004v1 [quant-ph] (2013)
22. K.G. Makris, R. El-Ganainy, D.N. Christodoulides, Z.H. Musslimani, PT-symmetric optical lattices. Phys. Rev. A **81**, 063807 (2010)
23. S. Nixon, L. Ge, J. Yang, Stability analysis for solitons in PT-symmetric optical lattices. Phys. Rev. A **85**, 023822 (2012)
24. H. Ramezani, D.N. Christodoulides, V. Kovanis, I. Vitebskiy, T. Kottos, PT-symmetric Talbot effect. Phys. Rev. Lett. **109**, 033902 (2012)

25. H. Ramezani, T. Kottos, V. Kovanis, D.N. Christodoulides, Exceptional-point dynamics in photonic honeycomb lattices with PT symmetry. Phys. Rev. A **85**, 013818 (2012)
26. D.A. Zezyulin, V.V. Konotop, Nonlinear modes in finite-dimensional PT-symmetric systems. Phys. Rev. Lett. **108**, 213906 (2012)
27. N. Lazarides, G.P. Tsironis, Gain-driven breathers in PT-symmetric nonlinear metamaterials. Phys. Rev. Lett. **110**, 053901 (2013)
28. D. Wang, A.B. Aceves, Modulation theory in PT-symmetric magnetic meta-material arrays in the continuum limit. Phys. Rev. A **88**, 043831 (2013)
29. Z.H. Musslimani, K.G. Makris, R. El-Ganainy, D.N. Christodoulides, Optical solitons in PT-periodic potentials. Phys. Rev. Lett. **100**, 030402 (2008)
30. V. Achilleos, P.G. Kevrekidis, D.J. Frantzeskakis, R. Carretero-Gonzalez, Dark solitons and vortices in PT-symmetric nonlinear media: from spontaneous symmetry breaking to nonlinear PT phase transitions. Phys. Rev. A **86**, 013808 (2012)
31. L. Feng, Y.-L. Xu, W.S. Fegadolli, M.-H. Lu, J.E.B. Oliveira, V.R. Almeida, Y.-F. Chen, A. Scherer, Experimental demonstration of a unidirectional reflectionless parity-time metamaterial at optical frequencies. Nat. Mater. **12**, 108–113 (2013)
32. C. Keller, M.K. Oberthaler, R. Abfalterer, S. Bernet, Tailored complex potentials and Friedel's law in atom optics. Phys. Rev. Lett. **79**, 3327 (1997)
33. M.K. Oberthaler, R. Abfalterer, S. Bernet, J. Schmiedmayer, A. Zeilinger, Atom waves in crystals of light. Phys. Rev. Lett. **77**, 4980 (1996)
34. M. Hiller, T. Kottos, A. Ossipov, Bifurcations in resonance widths of an open Bose-Hubbard dimer. Phys. Rev. A **73**, 063625 (2006)
35. E.-M. Graefe, Stationary states of a PT-symmetric two-mode Bose-Einstein condensate. J. Phys. A Math. Theor. **45**, 444015 (2012)

Chapter 10
Nonlinear Plasmonic Waveguides

José Ramón Salgueiro and Yuri S. Kivshar

Abstract Recent results on plasmonic waveguides are summarized. After a brief introduction to motivate the use of plasmonic structures for optical integrated devices and to present the main characteristics and potential applications, the metal-dielectric-metal slot waveguide is studied. The way to calculate the complex modes, which are necessary for a proper modeling taking optical losses into account, is presented for the linear and nonlinear cases. This calculations are then used to obtain the dispersion curves and to show the way modes transform when losses go from negligible to realistic values. The calculation of nonlinear modes leads to the study of the power dispersion curves considering optical losses and to the comparison with the non lossy case. Also, the way to simulate the propagation of light in this structures, using the finite-difference time-domain technique is discussed. The last part of the text deals with specific devices: nonlinear directional couplers applied to optical power switching. Finally, the use of tapered waveguides for the directional coupler is proposed, as a way to avoid the negative effect of optical loss and to enhance the coupler performance.

10.1 Introduction

The field of plasmonics has recently attracted a lot of attention from the scientific community due to many interesting optical properties of metals in the presence of electromagnetic fields and new effects which may have potential technological

J.R. Salgueiro (✉)
Departamento de Física Aplicada, Universidade de Vigo, As Lagoas, s/n,
32004, Ourense, Spain
e-mail: jrs@uvigo.es

Y.S. Kivshar
Nonlinear Physics Center, Research School of Physics and Engineering,
The Australian National University, Canberra, ACT 0200, Australia
e-mail: ysk@internode.on.net

O. Shulika and I. Sukhoivanov (eds.), *Contemporary Optoelectronics*,
Springer Series in Optical Sciences 199, DOI 10.1007/978-94-017-7315-7_10

applications [1–3]. Plasmonics deals with plasmons as elementary excitations. A plasmon is created by an electromagnetic wave interacting resonantly with collective electronic oscillations in a metal, that produces a coupled hybrid state. One of the most typical realizations of a plasmon wave is an optical mode propagating along an interface separating a dielectric medium and a metal. Boundary conditions for the electromagnetic field at the interface require the electric field to be polarized perpendicularly (the so-called TM mode) and that is why this modes are called *surface plasmon polaritons* [4, 5]. Exponential tails of a plasmon decaying into both dielectric and metal, define a range of the order of half-wavelength and skin-depth respectively.

A small skin depth into the metal makes possible a high confinement of the optical field in plasmonic structures, specially if the dielectric layer is bounded by metals on both sides resulting a structure of a three-layer plasmonic slot waveguide. The confinement can reach tenths of nanometers, two orders of magnitude smaller than the wavelength, making possible a design and fabrication of integrated circuits at the nanoscale [6, 7]. On the other hand, the optical field can penetrate nanometer apertures overpassing the diffraction limits [8]. The reason for this is the coupling of the optical field to the plasmon modes supported by the bored screen. Another interesting property is the possibility of nanofocusing since some optical modes do not possess a cutoff [9], even for arbitrarily narrow waveguide cores. The sizes reached for the optical modes and fabrication techniques used for patterning these integrated devices are compatible with those of nowadays electronics, making easy the fabrication of optoelectronic devices for guiding, high-sensitive sensing and signal processing. All this made plasmonics an actual and active research field on the development of devices at the nanoscale and led to the arising of what is now called nanoplasmonics [10].

The advantageous properties of plasmonic devices make them useful for many applications. For example, metals are excellent candidates for making metamaterials, particularly those presenting negative refractive index [11]. In fact, the requirements of negative electrical permittivity and magnetic permeability is naturally fulfilled for the permittivity in the case of metals. Collimators to obtain nanometric size beams can be possible using a screen with a nanometric hole surrounded by some structure patterned on the screen [5]. This beam can be useful for writing or reading information in high-density data-store devices. Also, the properties of surface plasmon polaritons are very sensitive to modifications in the properties of the media and this makes such systems suitable for high sensitivity optical sensors [12]. Another application is for high speed modulators [13]. In this case, a plasmon polariton is coupled (input) and decoupled (output) to an silica-aluminum interface by a diffraction grating patterned on the silica. The modulation takes place by irradiating the boundary with laser fs-pulses which control the propagating wave via nonlinear effects triggered into the metal. Finally, another interesting application is the performance enhancement of solar cells [14–16].

The main drawback of plasmonic devices are the large losses they present when operating at optical frequencies because at such frequencies metals are far from perfect conductors. This means that a small tail of the field exists inside the metallic

layers and this makes power conversion into heat via electronic collisions. Power losses could in principle be admissible in integrated devices due to the small dimensions implied but in any case, a realistic description and modeling of devices based on plasmonics require from taking into account such power losses.

The high confinement of optical fields possible with this kind of structures means high power densities and consequently high nonlinear effects. So, devices based on plasmonics are potentially suitable for nonlinear control of optical signals. Different nonlinear systems combining the properties of plasmons and solitons have been studied [17–19] as well as metal-dielectric interface waveguides [20–23] and slot waveguides [24] when the dielectric shows the Kerr nonlinearity. Different nonlinear processes have been also demonstrated in plasmonic systems as optical limiting and self-phase modulation with nanoparticles [25] or second harmonic generation [26–28]. Also, applications in signal processing as for instance the design of all-optical logic gates [29].

Here, recent results on plasmonic waveguides which are basic components of optical integrated devices are summarized. In the following section the basic aspects of linear and nonlinear waveguides, like mode calculation or dispersion properties, will be presented, while Sect. 10.3 deals with the specific application of nonlinear directional couplers applied to optical power switching.

10.2 Plasmonic Waveguides

The most basic device of an integrated circuit is a waveguide. When metals are present the simplest one is the single interface between a dielectric and a metal, able to support surface plasmon polaritons (SPP). However, other different types of waveguides made of three layers are also possible. In that way three layer waveguides presenting additional advantages as to make power coupling by the end-fire method more efficient, keeping the optical field better confined in a nanometric size (metal-dielectric-metal waveguide) or increase the sensitivity of the optical mode properties to external changes (dielectric-metal-dielectric waveguide) were proposed. The linear wave propagation in this kind of structures was studied in the past [9, 30–32]. Also the nonlinear propagation was already studied for single interface waveguides, when the dielectric shows the Kerr nonlinear response and the metal is considered linear [20–23]. On the other hand, slot nonlinear Kerr dielectric-metal waveguides were studied [24], and due to the fact that both interfaces are waveguides themselves, they can support asymmetric modes in a similar fashion as a nonlinear directional coupler.

The studies referred above do not consider optical losses in the metallic layers. Nevertheless, the need of taking them into account has been proved necessary because they influence strongly the behaviour of optical devices based on plasmonics. Additionally, metals are strongly dispersive media and a correct description

requires the use of a model to express the permittivity (ε_m) as a function of frequency (ω). The simplest one is the classical Drude's model which describes electric permittivity as

$$\varepsilon_m(\omega) = 1 - \frac{\omega_p^2}{\omega^2 + i\Gamma\omega} = \left(1 - \frac{\omega_p^2}{\omega^2 + \Gamma^2}\right) + i\left(\frac{\Gamma}{\omega}\frac{\omega_p^2}{\omega^2 + \Gamma^2}\right), \tag{10.1}$$

where ω_p is the plasma frequency and Γ the electronic collision frequency which ultimately describes the effect of power losses as it makes the permittivity a complex number.

Power losses usually spoil the performance of any guiding device at optical frequencies. However, it is well-known that at microwave frequencies metallic waveguides are currently used with a negligible effect of losses. The reason is the almost perfect conductive behaviour of metals at those frequencies, that prevents the electric field to exist inside any metallic layer (Fig. 10.1a). This avoids energy dissipation via electronic collisions, even though at such frequencies many collisions could take place in a wave period (the permittivity is a large negative imaginary number). Nevertheless, at optical frequencies, there is a negligible number of collisions in a wave period, but the fact that there is a significant fraction of the field inside the metal (Fig. 10.1b) makes losses relevant. In this case the permittivity is a complex number with a large negative real part and a small imaginary part. Finally, at very high frequencies ($\omega > \omega_p$) metals turn into transparent media because the electrons cannot follow the wave oscillations.

According to all this, a plasmonic waveguide at optical frequencies can be considered an intermediate case between the planar parallel guide used at microwave regime and the dielectric slab (Fig. 10.1), being losses the particular effect to take into account at this regime. Losses were already demonstrated to affect dramatically the performance of devices, not only decreasing optical power but also spoiling the operation efficiency as was demonstrated for instance for power switching using a nonlinear directional coupler [33]. Taking losses into account in a rigorous way requires the consideration of the so called evanescent modes, which

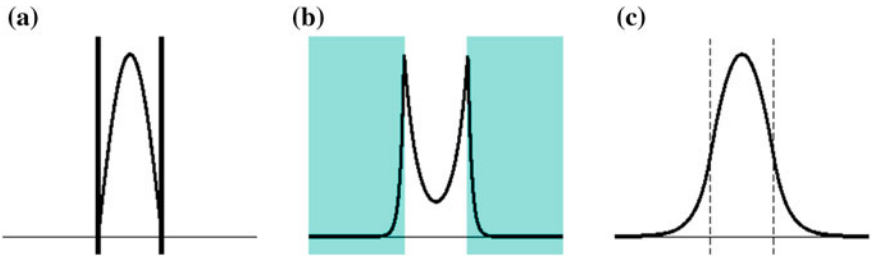

Fig. 10.1 Different types of waveguides and the shape of the fundamental supported modes. **a** Parallel-plate waveguide, **b** plasmonic slot waveguide, **c** dielectric slab waveguide

are complex fields with an also complex propagation constant, whose imaginary part induces a exponential decaying of the field amplitude upon propagation. This modes are usually overlooked in weak lossy systems since their decaying distance is small compared with the propagation of the optical field. In fact, the usual way to account for losses is to solve the problem as though there were no losses at all and then introduce losses as a perturbation to the non-lossy system. Nevertheless, in systems containing metals, losses can be so large that the field amplitude decays in a short propagation distance and complex evanescent modes become relevant for a proper description of the system.

Evanescent modes were already studied in waveguides and other plasmonic structures [34, 35], and the main results indicate that those modes transform themselves when losses increase and become mixed with the usual propagating modes, becoming undistinguishable when optical loss is large. This again reveals the need of taking such modes into account for a rigorous description of waveguiding systems with large optical losses.

10.2.1 Mode Calculation

Let us take a waveguide made of a dielectric core of width d embedded in metallic layers (cladding). The dielectric function is considered to be constant inside the core ($\varepsilon = \varepsilon_d$), and described by the classical Drude model (10.1) in the cladding [$\varepsilon = \varepsilon_m(\omega)$]. The calculation of modes is made using the Maxwell's equations to describe the evolution of the harmonic modal fields $\tilde{\mathbf{E}}(\mathbf{r}, t)$ and $\tilde{\mathbf{H}}(\mathbf{r}, t)$ of the form,

$$\tilde{\mathbf{E}}(\mathbf{r}, t) = \mathbf{E}(x) \exp[-i(\beta z - \omega t)], \tag{10.2}$$

$$\tilde{\mathbf{H}}(\mathbf{r}, t) = \mathbf{H}(x) \exp[-i(\beta z - \omega t)]/(\mu_0 c), \tag{10.3}$$

where μ_0 is the vacuum magnetic permeability, β the propagation constant, t the time and $\mathbf{r} = (x, y, z)$ are spatial coordinates normalized by the vacuum wavenumber $k_0 = \omega/c$, being c the speed of light. The structure is considered to lay along the x direction and the mode propagates along the z-direction. If we consider a TM mode $\mathbf{E} = E_x\hat{\mathbf{x}} + iE_z\hat{\mathbf{z}}$, $\mathbf{H} = H_y\hat{\mathbf{y}}$ and replace both fields into the Maxwell's equations the following system of differential equations for the mode components are got,

$$\partial_x H_y = -\varepsilon E_z, \tag{10.4}$$

$$\partial_x E_z = (1 - \beta^2/\varepsilon) H_y, \tag{10.5}$$

together with the relationship $\beta H_y = \varepsilon E_x$. This problem is equivalent to the following second order differential equation,

$$\left[\varepsilon(x)\,\partial_x\left(\frac{1}{\varepsilon(x)}\,\partial_x\right)+\varepsilon(x)\right]H_y=\beta^2 H_y, \tag{10.6}$$

which describes the usual eigenvalue problem to solve for modal shapes $[H_y(x)]$ and propagation constants (β^2).

The interest is now set on solutions with a general complex propagation constant $\beta=\beta_1+i\beta_2$ and so the field components in the equations above should be also complex. It is worthy to remark that even when losses are neglected, so that $\varepsilon(x)$ is a real function, the problem described by (10.5) or (10.6) still have complex solutions. The reason is the fact that the function $\varepsilon(x)$ changes its sign for different intervals of the domain as for metals it is a negative number [36]. This also makes that (10.6) cannot be considered a proper Sturm-Liouville type problem.

A slot metal-dielectric-metal waveguide is first considered in a linear regime, and then in a nonlinear regime with a dielectric core showing the Kerr nonlinearity. In such a way, since the metals will always be considered linear, there will exist analytical solution at the claddings in the form of exponential functions $A\exp(\mp\sqrt{\beta^2-\varepsilon_m}\;\;x)$, where the sign inside the exponential function is chosen to obtain a decaying behaviour when $x\to\pm\infty$ respectively. The numerical problem will consequently reduce to obtain the solution inside the core that fulfill the boundary conditions at both core-cladding interfaces, i.e. continuity of both fields H_y and E_z. This conditions are,

$$\sqrt{\beta^2-\varepsilon_m}\;\;H_y\pm\varepsilon_m E_z=0, \tag{10.7}$$

where ε_m is the value of the permittivity of the metal obtained from Drude's model (10.1). In the expression above the positive and negative signs are used respectively at the left and right boundaries. Once the solution at the core is numerically obtained, it is augmented into the cladding using the analytical expression above, where constant A is chosen to adapt the value at the boundaries to the one of the calculated solution inside the core.

The fact that in (10.5) appears the eigenvalue as β^2 means that two different solutions for β are got, being only one of them physically significant. There exist two types of modes, forward and backward, and there are two way to describe them at this point. The first one [36] considers all the modes propagating in a fix direction of z (say positive, $z>0$). Then, as the spatial phase evolves in the way $\exp(-i\beta z)$ (10.2) the physical solution is that with $\beta_2<0$, since the mode amplitude has to decrease as z increases. The sign of the real part of the propagation constant β_1 for this solution describes the modal type, forward (positive phase velocity) or backward (negative phase velocity). Another alternative description [35, 37] fixes the sign of β_1 (for instance $\beta_1>0$) and relies on the corresponding sign of β_2 to determine the direction of propagation: $z>0$ (forward modes) or $z<0$ (backward modes) so that amplitude decays upon propagation. We will use the second description.

The spectrum of modes can be divided in a discrete part (point spectrum), formed by the guided or proper modes, and a continuous part formed by the radiation or improper modes (see Fig. 10.2). The point spectrum is formed by real or propagating modes (imaginary part is null) and complex or evanescent modes (imaginary part different from zero) which lay on the continuous spectrum. Due to the negative value of ε_m, the point spectrum is not restricted to the region below the core permittivity value, in contrast to the case of a dielectric slab waveguide.

To solve the problem we will separate fields in their real and imaginary part as

$$H_y(x) = h_1(x) + \mathrm{i}h_2(x),$$
$$E_z(x) = e_1(x) + \mathrm{i}e_2(x). \tag{10.8}$$

Once these expressions are replaced into (10.4), (10.5) and (10.7) the problem is transformed in a real valued one. When the system is considered linear (10.4) and (10.5) are a complex eigenvalue problem and there exists analytical solution for the optical modes, though the values of the propagation constant have to be obtained by a numerical iterative method, solving an algebraic dispersion equation. The fact that the solutions to be hunted are complex makes the problem a little more complicated, but there are available methods like the argument principle method (APM) [36, 38]. On the other hand when the problem is nonlinear, the system of differential equations should be solved numerically (at least in regions presenting nonlinearities) to obtain modal fields and propagation constants. The need of using a numerical solving code for the nonlinear case, made recommendable to treat the linear problem also numerically (though there exists an analytical solution), and use the same code for the sake of simplicity.

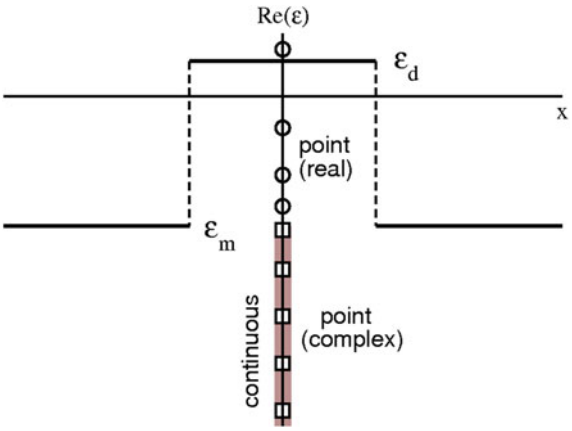

Fig. 10.2 Sketch of the general spectrum of a plasmonic waveguide (real part). The permittivity profile is shown for reference. The *coloured band* stands for the continuous spectrum (β pure imaginary). Points (*square*) overlapped to the band are the point complex spectrum. *Circle* points over ε_m level are the point real spectrum

As coordinates are rescaled by the wavenumber, from now on a rescaled frequency ω will be also used, in such a way that it takes the unity value $\omega = 1$ at a chosen reference wavelength λ_0. This can be always done, since according to (10.2) and (10.3) it only affects to the units taken for the time. For the calculations carried out the values of the taken parameters were $d = 0.5$ (waveguide width), $\varepsilon_d = 2.25$ (linear permittivity of the dielectric core) and $\varepsilon_m = -8.25$, corresponding to silver at a wavelength $\lambda_0 = 480$ nm [39] which will be also the chosen reference wavelength (for $\omega = 1$).

10.2.2 Dispersion of Linear Modes

When the complex field functions (10.8) are replaced in (10.4) and (10.5) a system of four differential equations involving the real-valued functions $h_{1,2}(x)$ and $e_{1,2}(x)$ is obtained. Also, since these equations constitute an eigenvalue problem, the system is completed with two additional equations for the propagation constant: $\partial_x \beta_1 = 0$, $\partial_x \beta_2 = 0$. This system is then numerically solved at the waveguide core using a relaxation method to obtain the modal fields and the values of the propagation constant. Along with the continuity of the fields at the core-cladding boundaries (four equations) two additional conditions are required and they come from the linearity of the problem. In fact, a solution can be multiplied by an arbitrary complex constant to get an equivalent solution. In such a way, the value of two of the functions is fixed at a particular point (say one of the boundaries x_b), obtaining the two necessary conditions, $h_1(x_b) = c_1$, $h_2(x_b) = c_2$, being c_1 and c_2 constants. Besides, to make easier the calculation of propagating (real propagation constant, i.e. $h_2(x) = 0$) and evanescent modes at a time it is quite convenient to fix $c_2 = 0$.

In Fig. 10.3 the dispersion curves for the linear modes are shown for the case when losses are neglected ($\Gamma = 0$) and for two different values of the electronic collision frequency which correspond to weak ($\Gamma = -0.01$) and strong ($\Gamma = -0.1$) loss. A realistic case would be in between these values. It is important to remark at this point that the negative sign of Γ is a result of the sign convention taken for the wave phase in (10.2) and (10.3). According to this, to get a z-decreasing amplitude wave it is necessary that the imaginary part of ε_m is negative what is fulfilled if $\Gamma < 0$ (10.1).

In Fig. 10.4 few examples of low order modes are shown. When losses are neglected ($\Gamma = 0$), the dielectric constant for the metallic cladding is real and modes with a real value of β (propagating modes) and an infinite number of modes with a complex value of β (evanescent modes), coming in complex conjugate pairs [36] may be found. In Fig. 10.3a, d we show the dispersion curves for the lowest order modes. For the particular taken values of the parameters, the waveguide supports only a propagating (fundamental) mode (see Fig. 10.4a) below the surface plasma resonance (ω_{sp}) and two (fundamental and first order) above the resonance.

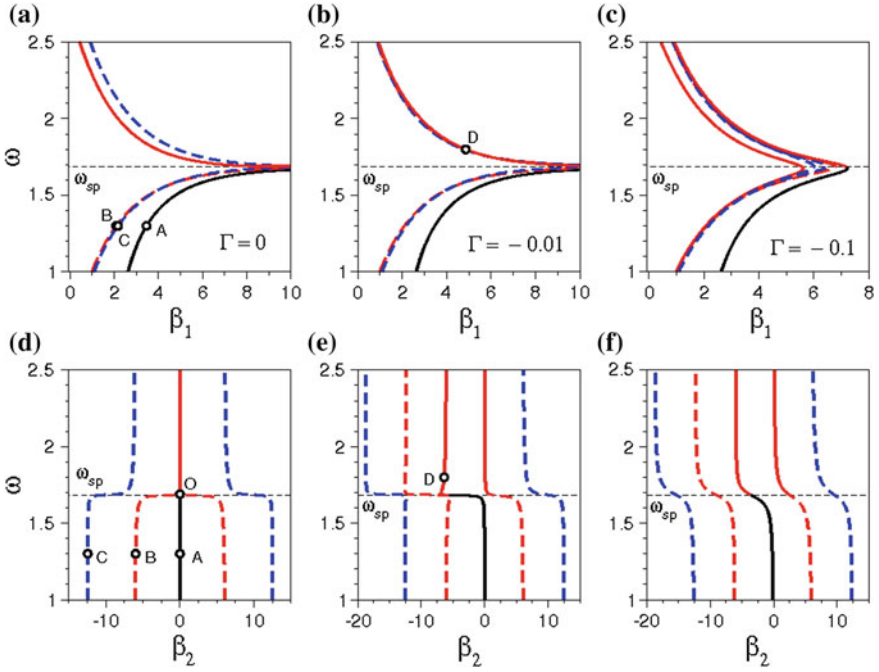

Fig. 10.3 Dispersion curves for the linear slot waveguide. The three columns correspond to three different values for the optical losses: no loss (**a**, **d**), weak loss (**b**, **e**) and strong loss (**c**, **f**). *Top row* shows the real part of the propagation constant, *bottom row* shows the imaginary part. *Points marked on the figure* correspond to the examples shown in Fig. 10.4. *Continuous and dashed lines* represent propagating and evanescent modes respectively. ω_{sp} represents the surface plasmon resonance frequency

The pair of first order modes, forward and backward, present conjugate propagation constants being described by symmetric branches whose imaginary part turn to zero and join together in a bifurcation point at $\omega = \omega_{sp}$ (point O in Fig. 10.3d). From this point, for increasing frequency, both modes are degenerated and propagating (zero imaginary part).

When losses are considered ($\Gamma \neq 0$) all modes become complex and they no longer come in complex conjugate pairs so the symmetry of the branches is destroyed. Both types of modes, propagating and evanescent, transform themselves and merge together. In Fig. 10.3 (second and third columns) we show the dispersion curves when passing from null to weak and then to strong loss. Degeneracy of the first order mode at ω_{sp} is removed and that mode joins to the first order backward mode. The fundamental (originally propagating) mode joins now at $\omega = \omega_{sp}$ to the the branch of the second mode (Fig. 10.4d). In general each mode joins at ω_{sp} to the next order mode of the same symmetry. These results are in agreement with previous studies [34, 35].

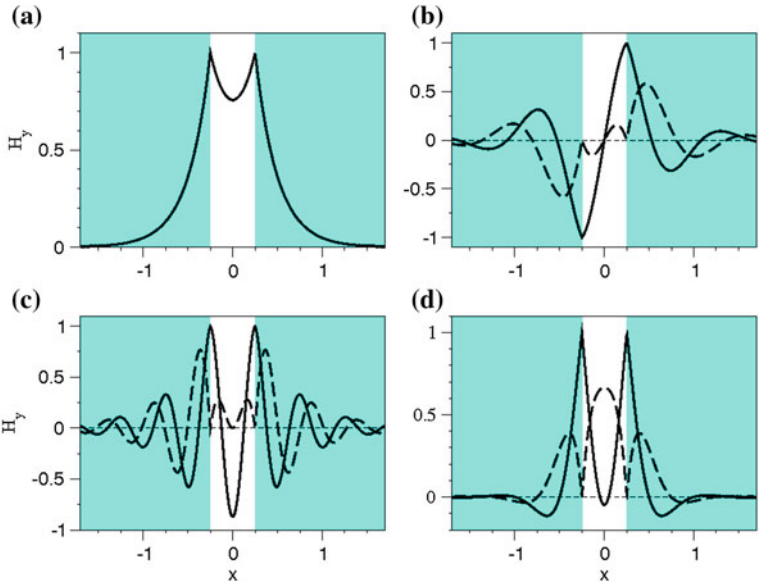

Fig. 10.4 Examples of propagating and evanescent modes when losses are neglected: fundamental propagating mode (**a**), first (**b**) and second (**c**) order evanescent modes. Also, the second order mode for the lossy case (**d**). The *labels* correspond to the points shown in Fig. 10.3. *Continuous and dashed lines* represent real and imaginary part respectively

10.2.3 Nonlinear Power Dispersion

In order to study the nonlinear modes a waveguide core made of a dielectric showing the nonlinear Kerr response is considered, i.e. described by a dielectric function $\varepsilon_d(x) = \varepsilon_l + \alpha|\mathbf{E}|^2$, being ε_l the linear dielectric constant and α the Kerr coefficient, which can be suppressed from equations just considering both fields **H** and **E** rescaled by a factor $\alpha^{-1/2}$. The numerical solution can be obtained in a similar way as for the linear case, after expressing the dielectric function above in terms of the components H_y and E_z, using (10.2) and (10.3) and the relation $\varepsilon E_x = \beta H_y$ to obtain the following cubic equation [40],

$$\varepsilon^3 - (\varepsilon_d + E_z^2)\varepsilon^2 - \beta^2 H_y^2 = 0. \tag{10.9}$$

It is easy to demonstrate that this equation has only one real solution which can be obtained using Cardano's method. Once this solution is replaced in (10.5) the system of ordinary differential equations is numerically solved in a similar way as for the linear problem.

This nonlinear problem has a family of solutions of different power parameterized by the propagation constant. Since the nonlinearity depends only on the field modulus but not on the phase, only part of the propagation constant (say the real

part) can be fixed so that it is necessary to solve for the other (imaginary part) as an eigenvalue. Consequently, the system has now only one additional equation ($\partial_x \beta_2 = 0$) and boundary condition: it is possible to arbitrary fix the phase of one of the fields (say **H**) at a particular point (say a boundary, x_b), $a\tan[h_2(x_b)/h_1(x_b)] = c$. For the sake of simplicity the constant c is taken as zero.

Dispersion curves are now calculated in terms of the mode power for a fixed value of the frequency ($\omega = 1$). When losses are not considered and for the taken values of the system parameters, the modes symmetric, antisymmetric and asymmetric are propagating [24]. The antisymmetric mode, however, is characterized by a negative power flux due to the small core width of the waveguide. As was studied in [24] the sign of the flux of the antisymmetric mode depends on the width of the waveguide core in such a way that it is negative for small width and positive for large width. For an intermediate width it can happen to exist a value of the propagation constant β for which the sign changes from negative to positive.

Power is obtained integrating the time-averaged Poynting vector, which for harmonic fields is $P = \int (\mathbf{E} \times \mathbf{H}^*)\hat{\mathbf{z}} dx = \beta \int (|H_y|^2/\varepsilon) dx$. In Fig. 10.5 (top) power

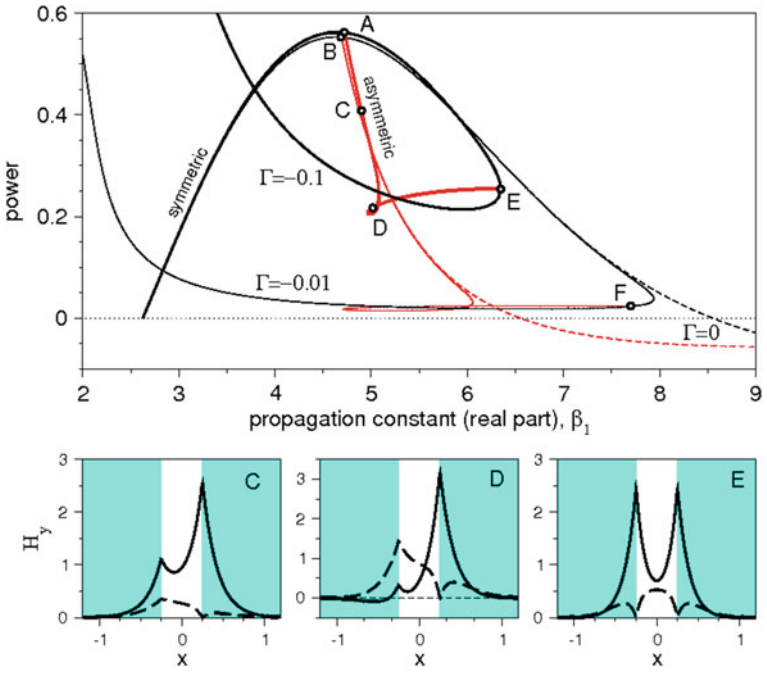

Fig. 10.5 *Top* Power dispersion curves for nonlinear modes, showing power against the real part of the propagation constant for the propagating symmetric and asymmetric modes of the waveguide. *Dashed, thin continuous, and thick lines* correspond respectively to the lossless ($\Gamma = 0$), weak lossy ($\Gamma = -0.01$) and strongly lossy case ($\Gamma = -0.1$). *Bottom* examples of some nonlinear asymmetric modes. *Labels* correspond to the points on the power diagram (*top*). *Thin and thick lines* are the real and imaginary part respectively

versus the real part of the propagation constant for the symmetric and asymmetric modes is plotted. Also, in Fig. 10.5 (bottom), some examples of modes for the case of a strong loss are presented. For the case $\Gamma = 0$ (no loss) the already studied power diagram is obtained (dashed lines) [24]. When losses are present the curve corresponding to the symmetric mode turns back at a certain value of β_1 and then, after describing a loop turns up so that power increases indefinitely. This is in sharp contrast with the non lossy case were power was limited to a maximum value and the propagation constant could reach arbitrarily large values. A possible explanation for this behavior is the fact that losses inside metallic layers induce a progressive decreasing in the negative contribution to power flux, allowing total power to increase due to the nonlinear contribution inside the core. The asymmetric mode, however, that bifurcates from the symmetric one at points *A* (strong loss) and *B* (weak or no loss) also turns back, describing a loop and joining again to the symmetric curve at new bifurcation points *E*, *F* that have no analog in the non lossy case.

10.2.4 Propagation and Stability

Modeling structures which are smaller than the wavelength and, additionally, strongly dispersive, requires the use of the finite-difference time-domain technique (FDTD). This technique discretizes Maxwell's equations in time and space and solves for the fields at subsequent time steps. Maxwell's equations are solved exactly and the goodness of the result depends directly on how good are the models used to describe the different media, i.e. how good is the model for the electrical permittivity and magnetic permeability functions.

In order to model metallic regions a scheme for cold plasmas based on Drude's theory was used, necessary to take into account the strong dispersion of metals. The dispersion is introduced in Maxwell's equations using a polarization current term [41] $\mathbf{J} = \partial_t \mathbf{P}$ which is introduced in the Ampère law equation, $\partial_t \mathbf{D} = \nabla \times \mathbf{H} - \mathbf{J}$, being *D* the electric displacement, and modeled by solving an additional differential equation, $\partial_t \mathbf{J} + \Gamma \mathbf{J} = \omega_p^2 \mathbf{E}$, where ω_p is the plasma frequency and Γ is the electron collision frequency describing the power losses. This equation is the time-domain version of Drude's model (10.1). Parameters ω_p and Γ can be obtained from the literature directly or from the optical constants. Using the normalized units described above, for silver at $\omega = 1$ ($\lambda_0 = 480$ nm), the optical constants are $\mathrm{Re}(\varepsilon) \approx -8.25$ and $\mathrm{Im}(\varepsilon) \approx 0.3$ [39], and so it is obtained from (10.1) $\omega_p = 3.043$ and $\Gamma = 0.031$.

For the dielectric showing the Kerr nonlinearity a model based on an instantaneous response of the medium [42, 43] is used, valid for a CW or even for non ultrashort pulses. According to this, the relationship $\mathbf{D} = \varepsilon(|\mathbf{E}|^2)\mathbf{E}$ is used taking the

nonlinear permittivity as described by the Kerr model $\varepsilon_d(x) = \varepsilon_l + \alpha|\mathbf{E}|^2$. For the simulations we took $\varepsilon_d = 2.25$ (pure silica) though the nonlinear model is general for any Kerr material just re-scaling back the fields by the factor $\alpha^{1/2}$, α is the Kerr coefficient, after the simulation. At each time step, after obtaining the magnetic component and then the two components for the displacement vector, D_x and D_z, the calculation of the electric field components requires the solution of a nonlinear cubic equation at each point of the mesh. This is efficiently done by a single Newton step, starting from the value of the electric components at the previous time step. The FDTD technique to model the metal and the nonlinear dielectric in the way described above will be used in the following section to simulate propagation of light through different coupling structures.

10.3 Plasmonic Nonlinear Couplers

A directional coupler is a very interesting and widely studied device because of its applications in telecommunications for optical signal processing and switching. Particularly when nonlinear effects are present it can be useful for power switching, i.e. the discrimination of signals according to their power level. The device is made of two waveguides running parallel and separated a distance so that the cladding tails of both modes overlap causing power to pass from one to the other. Since metal-dielectric interfaces are waveguides themselves the slot waveguide studied above is a kind of directional coupler, though more efficient devices can be obtained by placing two of such waveguides close together. Directional couplers of different geometries based on plasmonic waveguides were already studied [44–48]. They were also proposed for the mode transition from a dielectric waveguide into a plasmonic mode propagating along a metal stripe [49].

A directional coupler present two low order modes, one antisymmetric and another one symmetric (Fig. 10.6b, c), which are a result—at least for weakly coupling waveguides—of a combination of the fundamental modes of each separate waveguide. This fact is responsible for the periodic coupling of light from one guide to the other. For nonlinear devices there is also an asymmetric mode (Fig. 10.6d) which has no analog in linear systems and exists only above a power threshold. In the case of plasmonic waveguides, this asymmetric mode bifurcates from the antisymmetric mode [40] and is the key for power switching operation.

10.3.1 Switching

One of the applications of a nonlinear directional coupler is power switching. The idea is the change of state when power overpasses a certain threshold. For the coupler this shows as a change of the waveguide to which output power is directed.

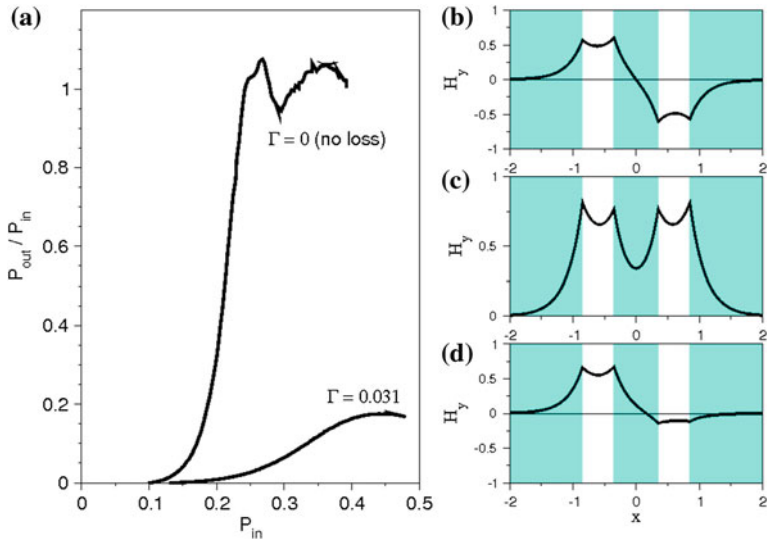

Fig. 10.6 **a** *Switching curve* ratio of the output power to the input power against input power for the case of null loss and realistic loss. **b–d** Shape of the modes antisymmetric, symmetric and asymmetric for $\beta = 5.0$

In Fig. 10.6a, the power switching curve for the dual-core plasmonic coupler is presented. Optical power is coupled to one of the waveguides and the output power is measured at the same waveguide after propagation by a beat length, i.e. the distance for which all power transfers to the second waveguide in a linear regime. The curve plots the ratio between output and input power against input power. According to this, for small input power the value of the ratio remains close to zero since most of the power transferred to the second waveguide. When power rises over the threshold where the asymmetric mode starts to exist, light remains mostly on the first waveguide producing an increase in the output power. The slope of the curve measures the efficiency of the optical switching when the threshold value is overpassed.

Losses have an important effect on the performance of the device as is shown in Fig. 10.6a where curves corresponding to both lossless and lossy cases are ploted. When losses are taken into account, the maximum of the power curve decreases since energy is lost (reaching a maximum of less than 20 %) but also the slope of the curve dramatically decreases revealing a degradation in the switching efficiency. In Fig. 10.7 both cases are illustrated as FDTD simulations. Images (a–c) respectively correspond to the low, intermediate and large power cases when losses are neglected, and illustrate how power remains in the first core when the threshold is overpassed. Images (d–f) are the same cases when losses are taken into account, revealing the decrease of power on propagation.

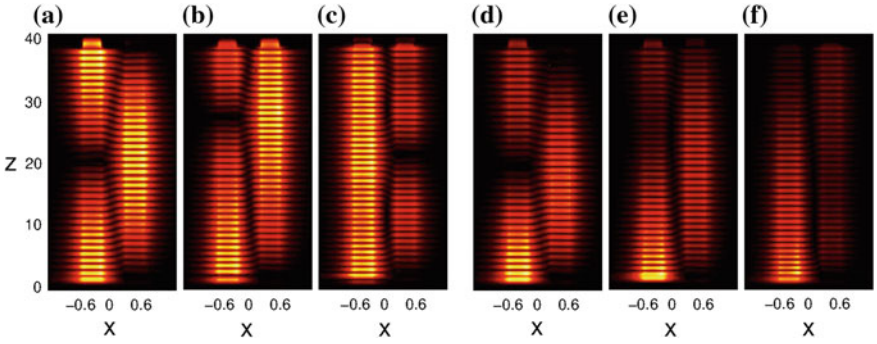

Fig. 10.7 FDTD simulations of the plasmonic coupler for different values of input power showing power switching. **a–c** are respectively the low, intermediate and high power cases when losses are neglected. **d–f** are the same cases taking losses into account. The images show the magnetic component modulus, $|H_y|$

10.3.2 Efficiency Enhancement Using Tapers

Tapered waveguides can be employed in the plasmonic directional coupler to overcome the effect of losses, increasing the field amplitude inside the cores and raising the switching efficiency. The increase of power density inside the core of a single waveguide was already demonstrated resulting that the phenomenon can even reach nanofocusing [50–52]. This solution is also effective to enhance the switching performance of plasmonic couplers. In order to measure performance we consider how fast is the change from one state of the coupler to the other when input power is increased. Ideally one would desire a fast change, but as it was shown in the previous section power losses in metals completely spoil the sharpness of the change [40].

First, the proper angle range leading to the compensation of loss has to be sought considering a linear regime. From a set of experiments for different taper angles, measuring total power at each waveguide and also the irradiance inside both cores, it is deduced that for angles slightly lower than $\theta = 2.0$ degrees loss is compensated by the focusing effect of the taper waveguides. It should be remarked that irradiance is a more convenient parameter than power for this study as it represents the optical density inside the waveguide core, so that it results enhanced by a progressive decrease of the core width. The total power, however, will always decrease as an effect of the optical loss in the metallic layers and this decrease is even larger for an increasingly narrow core. This is due to the fact that when the waveguide core width is smaller a larger fraction of the modal field lies inside the metallic cladding and relative loss increase. Nevertheless the irradiance inside the core increases when the angle increases because the power concentration inside the core partially compensates loss.

The switching properties of this nonlinear tapered coupler were then studied. In Fig. 10.8 we show images of FDTD simulations presenting the modulus of the field

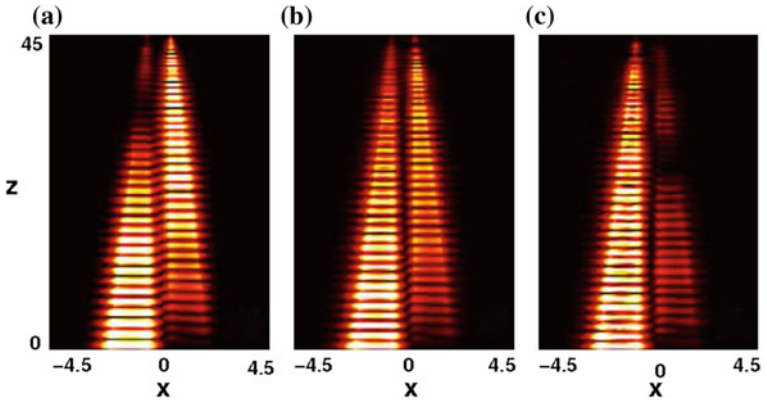

Fig. 10.8 Simulation of the nonlinear coupler with tapered waveguides. The three images correspond to the cases with no loss, weak losses and strong losses respectively

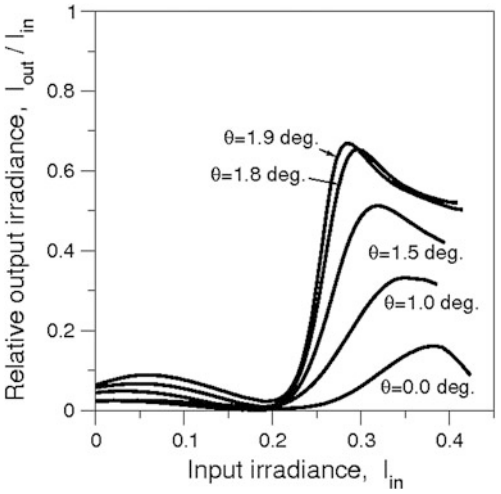

Fig. 10.9 Switching curves for different values of the taper angle. Ratio of the output power to the input one against input power

(magnetic component) for different power regimes using tapered waveguides at an angle of $\theta = 1.9\,deg$. The three images correspond to linear, intermediate and nonlinear regimes reached when input power is increasingly larger. Though loss still exist, the irradiance inside the core is enhanced and this is the reason why switching results more effective. This is clearly seen in the switching curves shown in Fig. 10.9 where the relative irradiance for a beat length is plotted against the input irradiance. As the taper angle increases, the curve slope becomes increasingly larger and reaches a larger fraction of the input irradiance, dramatically improving the efficiency of the device.

References

1. S.A. Maier, *Plasmonics: fundamentals and applications* (Springer, New York, 2007)
2. D. Sarid, W. Challener, *Modern Introduction to Surface Plasmons* (Cambridge University Press, Cambridge, 2010)
3. M.L. Brongersma, P.G. Kik (eds.), *Surface Plasmon Nanophotonics* (Springer, New York, 2007)
4. A.D. Boardman, *Electromagnetic Surface Modes* (Wiley, New York, 1982)
5. W.L. Barnes, A. Dereux, T.W. Ebbesen, Nature **424**, 824 (2003)
6. S.I. Bolzhevolnyi, V.S. Volkov, E. Devaux, J.Y. Laluet, T.W. Ebbesen, Nature **440**, 508 (2006)
7. H. Ditlbacher, J.R. Krenn, A. Leitner, F.R. Aussenegg, Appl. Phys. Lett. **81**(10), 1762 (2002)
8. D.K. Gramotnev, S.I. Bozhevolnyi, Nat. Photonics **4**, 2427 (2004)
9. R. Yang, M.A.G. Abushagur, Z. Lu, Opt. Expr. **16**, 20142 (2008)
10. M.I. Stockman, Opt. Expr. **19**(22), 22029 (2011)
11. J.B. Pendry, A.J. Holden, D.J. Robbins, W.J. Stewart, IEEE Trans. Microwave Theory Tech. **47**(11), 2075 (1999)
12. J. Homola, S.S. Yee, G. Gauglitz, Seensors Actuat. B **54**, 3 (1999)
13. K.F. MacDonald, Z.L. Sámson, M.I. Stockman, N.I. Zheludev, Nat. Photonics **3**, 55 (2009)
14. M. Westphalen, U. Kreibig, J. Rostalski, H. Lüth, D. Meissner, Sol. Energy Mater. Sol. Cells **61**, 97 (2000)
15. K.R. Catchpole, A. Polman, Opt. Expr. **16**(26), 21794 (2008)
16. J. Zhu, M. Xue, R. Hoekstra, F. Xiu, B. Zeng, K.L. Wang, Nanoscale **4**, 1978 (2012)
17. E. Feigenbaum, M. Orenstein, Opt. Lett. **32**(6), 674 (2007)
18. K.Y. Bliohkh, Y.P. Bliokh, A. Ferrando, Phys. Rev. A **79**, 041803 (2009)
19. C. Milián, D.E. Ceballos-Herrera, D.V. Skryabin, A. Ferrando, Opt. Lett. **37**(20), 4221 (2012)
20. V.M. Agranovich, V.S. Babichenko, V.Y. Chernyak, Sov. Phys. JETP Lett. **32**, 512 (1980)
21. G.I. Stegeman, C.T. Seaton, J. Ariyasu, R.F. Wallis, A.A. Maradudin, J. Appl. Phys. **58**, 2453 (1985)
22. D. Mihalache, G.I. Stegeman, C.T. Seaton, E.M. Wright, R. Zanoni, A.D. Boardman, T. Twardowski, Opt. Lett. **12**, 187 (1987)
23. A.D. Boardman, A.A. Maradudin, G.I. Stegeman, T. Twardowski, E.M. Wright, Phys. Rev. A **35**, 1159 (1987)
24. A.R. Davoyan, I.V. Shadrivov, Y.S. Kivshar, Opt. Expr. **16**, 21209 (2008)
25. N.C. Panoiu, R.M. Osgood, Nano Lett. **4**, 2427 (2004)
26. W. Fan, S. Zhang, N.C. Panoiu, A. Abdenour, S. Krishna, R.M. Osgood, K.J. Malloy, S.R. J. Brueck, Nano Lett. **6**, 1027 (2006)
27. J.A.H. van Nieuwstadt, M. Sandke, S. Enoch, L. Kuipers, Phys. Rev. Lett. **97**, 146102 (2006)
28. A.R. Davoyan, I.V. Shadrivov, Y.S. Kivshar, Opt. Expr. **17**(22), 20063 (2009)
29. T. Fujisawa, K. Masanori, J. opt. Soc. Am. B **23**(4), 684 (2006)
30. E.N. Economou, Phys. Rev. B **182**, 539 (1969)
31. J.J. Burke, G.I. Stegeman, T. Tamir, Phys. Rev. B **33**, 5186 (1986)
32. B. Prade, J.Y. Vinet, A. Mysyrowicz, Phys. Rev. B **44**(24), 13556 (1991)
33. J.R. Salgueiro, Y. Kivshar, Opt. Expr. **20**(9), 9403 (2012)
34. T. Yang, K.B. Crozier, Opt. Expr. **17**(2), 1136 (2009)
35. A.R. Davoyan, W. Liu, A. Miroshnichenko, I. Shadrivov, Y. Kivshar, S.I. Bozhevolnyi, Photonic Nanostruc. Fundam. Appl. **9**, 207 (2011)
36. S.E. Kocabas, G. Veronis, D.A.B. Miller, S. Fan, Phys. Rev. B **79**, 035120 (2009)
37. A.R. Davoyan, I.V. Shadrivov, S.I. Bozhevolnyi, Y.S. Kivshar, J. Nanophotonics **4**, 043509 (2010). doi:10.1117/1.3437397
38. M.S. Kwon, S.Y. Shin, Opt. Comun. **233**, 119 (2004)
39. P.B. Johnson, R.W. Christy, Phys. Rev. B **6**, 4370 (1972)
40. J.R. Salgueiro, Y.S. Kivshar, Appl. Phys. Lett. **97**, 081106 (2010)

41. S.A. Cummer, I.E.E.E. Trans, Antennas Propagat. **45**(3), 392 (1997)
42. R.M. Joseph, T. Allen, I.E.E.E. Phot, Tech. Lett. **6**(10), 1251 (1994)
43. I.S. Maksymov, A.S. Sukhorukov, A.V. Lavrinenko, Y.S. Kivshar, IEEE Antennas Wireless Propag. Lett. **10**, 143 (2011)
44. D.K. Gramotnev, K.C. Vernon, D.F.P. Pile, Appl. Phys. B **93**, 99 (2008)
45. Z. Chen, T. Holmgaard, S.I. Bozhevolnyi, A.V. Krasavin, A.V. Zayats, L. Markey, A. Dereux, Opt. Lett. **34**, 810 (2009)
46. T. Holmgaard, Z. Chen, S.I. Bozhevolnyi, L. Markey, A. Dereux, J. Lightwave Technol. **27**, 5521 (2009)
47. M. Conforti, M. Guasoni, C. De Angelis, Opt. Lett. **33**(22), 2662 (2008)
48. C. Milián, D.V. Skryabin, Appl. Phys. Lett. **98**, 111104 (2011)
49. A. Degiron, S.Y. Cho, T. Tyler, N.M. Jokerst, D.R. Smith, New J. Phys. **11**, 015002 (2009)
50. A.R. Davoyan, I.V. Shadrivov, A.A. Zharov, D.K. Gramotnev, Y.S. Kivshar, Phys. Rev. Lett. **105**(11), 116804 (2010)
51. A.R. Davoyan, I.V. Shadrivov, Y.S. Kivshar, D.K. Gramotnev, Phys. Status Solidi (RRL) **4**, 277 (2010)
52. S.I. Bozhevolnyi, K.V. Nerkararyan, Opt. Lett. **35**(4), 541 (2010)

Chapter 11
Oppositely Directional Coupler: Example of the Forward Backward Waves Interaction in the Metamaterials

A.I. Maimistov and E.V. Kazantseva

Abstract We consider the coupled electromagnetic waves propagating in a nonlinear coupler and in nonlinear waveguide array, which consists of alternating waveguides of positive and negative refraction indexes. The forward wave and backward wave interaction is realized in these devices. Gap solitons in a nonlinear oppositely directional coupler with one channel or both channels fabricated from nonlinear medium having negative refraction index are discussed. Generalization of the usually waveguide array is zigzag array. Due to zigzag configuration there are interactions between both nearest and next nearest neighboring waveguides exist. The system of evolution equations for coupled waves has the steady state solution describing the electromagnetic pulse running in the array. Numerical simulation demonstrates robustness of these solitary waves.

11.1 Introduction

If the phase velocity and the Pointing vector of the incident electromagnetic wave are directed in the same direction but the phase velocity and the Pointing vector of the refracted electromagnetic wave are opposite directed, than refraction angle is negative one. The Snell's formula can be used in this case, if the refractive index is considered as negative index. This phenomenon is referred to as negative refraction.

A.I. Maimistov (✉)
Department of Solid State Physics and Nanosystems, National Research Nuclear University Moscow Engineering Physics Institute, Kashirskoe sh 31, 115409 Moscow, Russia
e-mail: aimaimistov@gmail.com

A.I. Maimistov · E.V. Kazantseva
Department of Physics and Technology of Nanostructures, Moscow Institute of Physics and Technology, Dolgoprudnyi, 141700 Moscow, Russia

E.V. Kazantseva
Joint Institute for High Temperatures, Russian Academy of Sciences, 125412 Moscow, Russia

O. Shulika and I. Sukhoivanov (eds.), *Contemporary Optoelectronics*,
Springer Series in Optical Sciences 199, DOI 10.1007/978-94-017-7315-7_11

Antiparallel orientation of the phase velocity ($\boldsymbol{v}_{\mathrm{ph}}$) and the Pointing vector ($\boldsymbol{S}$) was first discussed in [1, 2]. In [3] it was indicated that antiparallel orientation of $\boldsymbol{v}_{\mathrm{ph}}$ and $\boldsymbol{S}$ results in negative refraction. Subsequently, this idea was developed by Mandelstam in [4]. It has been predicted that when the real parts of the dielectric permittivity and magnetic permeability in the medium simultaneously take on negative values in some frequency range, antiparallel orientation of $\boldsymbol{v}_{\mathrm{ph}}$ and $\boldsymbol{S}$ occurs [5, 6] and the property of negative refraction appears [7].

The existence of the media characterized by negative refractive index (NRI) was demonstrated experimentally first in the microwave and then in the near-infrared ranges [8–12]. Reviews of the properties NRI materials are presented in [13–16].

The present technological level does not yet allow for the fabrication of 3D materials of sufficient size and small enough losses for experiential verification of the effects described above. However, a considerable effort aimed at loss reduction and improvement of nanofabrication technology gives hope that the considered device will be manufactured.

It is well known that two closely located waveguides can be coupled due to the tunneling of light from one waveguide to the other. A coupler using tunneling, fabricated from materials with a positive refractive index (PRI), preserves the direction of light propagation, and for this reason it is named a *directional coupler*. It is much used device in integral optics.

If one of the waveguides of the coupler is fabricated from a material with a negative refractive index, this device is taking new features. The radiation entering one waveguide leaves the device through the other waveguide at the same end but in the opposite direction. For this reason, this device can be called the *oppositely directional coupler*. The properties of this coupler and different generalization of oppositely directional couplers will be discussed here.

11.2 Oppositely Directional Coupler

The principal property of the oppositely directional coupler is governed by the spectral features of linear wave. Unlike wave in usual directional coupler the spectrum of waves in the opposite directional coupler has the forbidden zone (i.e., gap). In this case the coupler acts like to distributed mirror.

11.2.1 Linear Oppositely Directional Coupler

The electric field of an optical wave propagating in linear directed coupler in the positive z direction can be represented as follows

$$E(x,y,z;t) = \sum_{J=1.2}\sum_{m} A_m^{(J)}(z,t)\Psi_m^{(J)}(x,y)\exp[-i\omega_0 t + i\beta_m^{(J)} z]. \tag{11.1}$$

The mode function for a particular m-th mode of channel J is denoted by $\Psi_m^{(J)}(x,y)$, and $A_m^{(J)}$ is a slowly varying envelope of the electric field corresponding to this mode. Parameters $\beta_m^{(J)}$ are propagation constants. Omitting the details we can write the general coupled equations which are governed by normalized envelopes $Q_J(\zeta,\tau) = A_m^{(J)}(z,t)A_0^{-1}$

$$i\tilde{k}_1\frac{\partial Q_1}{\partial z} + i\frac{1}{v_{g1}}\frac{\partial Q_1}{\partial t} + K_{12}Q_2\exp\{+i\Delta\beta z\} = 0,$$

$$i\tilde{k}_2\frac{\partial Q_2}{\partial z} + i\frac{1}{v_{g2}}\frac{\partial Q_2}{\partial t} + K_{21}Q_1\exp\{-i\Delta\beta z\} = 0.$$

The coefficients K_{12} and K_{21} are the coupling constants between neighboring waveguides. The phase mismatch is taking into account by $\Delta\beta = \beta_m^{(2)} - \beta_m^{(1)}$. v_{g1} and v_{g2} are group velocities. If in these equations we put $\tilde{k}_1 = +1$ and $\tilde{k}_2 = -1$ in corresponding to PRI and NRI cases respectively, we get the mathematical models describing the linear oppositely directional coupler.

It is suitable to introduce new variables

$$q_1 = \sqrt{K_{21}}Q_1\exp\{-i\Delta\beta z/2\}, \quad q_2 = \sqrt{K_{12}}Q_2\exp\{+i\Delta\beta z/2\}, \tag{11.2}$$

and the new variables according to following formulae $\zeta = z/L_c$, $\tau = t_0^{-1}(t - z/V_0)$, where $\delta = \Delta\beta L/2$ and

$$L_c = (K_{12}K_{21})^{-1/2}, \quad t_0 = L(v_{g1} + v_{g2})/2v_{g1}v_{g2},$$
$$V_0 = (v_{g2} - v_{g1})/2v_{g1}v_{g2}.$$

The system of the linear equations is rewritten as

$$i\left(\frac{\partial}{\partial\zeta} + \frac{\partial}{\partial\tau}\right)q_1 - \delta q_1 + q_2 = 0, \quad i\left(\frac{\partial}{\partial\zeta} - \frac{\partial}{\partial\tau}\right)q_2 + \delta q_2 - q_1 = 0. \tag{11.3}$$

Using the Fourier transformation we can find the dispersion relation for the harmonic waves $\omega = \delta \pm \sqrt{1 + k^2}$ (Fig. 11.1). Thus, this spectrum of harmonic waves has the gap $\Delta\omega = 2$. It should be pointed out that in the case of the PRI medium of both channels the gap is absent.

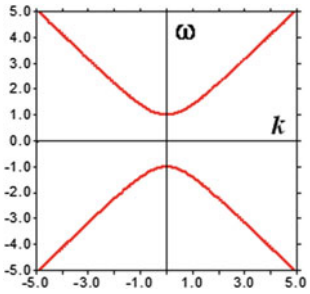

Fig. 11.1 The dispersion relation for linear waves in oppositely-directional couplers

11.2.2 Nonlinear Oppositely Directional Coupler

If the channels of directed coupler are prepared from a nonlinear medium, the system of the general coupled equations describing the nonlinear opposite directional coupler (NLODC) will contain additional terms. If normalized variables are used then the system of equations reads [17–19]

$$i\left(\frac{\partial}{\partial\zeta}+\frac{\partial}{\partial\tau}\right)q_1-\delta q_1+q_2+r_1|q_1|^2q_1=0, \tag{11.4}$$

$$i\left(\frac{\partial}{\partial\zeta}-\frac{\partial}{\partial\tau}\right)q_2+\delta q_2-q_1-r_2|q_2|^2q_2=0. \tag{11.5}$$

There parameters r_1 and r_2 are the nonlinearity measure for each waveguide [18]. By using real variables $q_{1,2}=a_{1,2}\exp(i\varphi_{1,2})$, one can obtains from (11.4) to (11.5) the system of the real variables equation.

$$\left(\frac{\partial}{\partial\zeta}+\frac{\partial}{\partial\tau}\right)a_1=a_2\sin\Phi,\quad \left(\frac{\partial}{\partial\zeta}-\frac{\partial}{\partial\tau}\right)a_2=a_1\sin\Phi,$$

$$\left(\frac{\partial}{\partial\zeta}+\frac{\partial}{\partial\tau}\right)\varphi_1=-\delta+\frac{a_2}{a_1}\cos\Phi+r_1a_1^2, \tag{11.6}$$

$$\left(\frac{\partial}{\partial\zeta}-\frac{\partial}{\partial\tau}\right)\varphi_2=\delta-\frac{a_1}{a_2}\cos\Phi-r_2a_2^2,$$

where $\Phi=\varphi_1-\varphi_2$.

11.2.2.1 CW-Limit of Nonlinear Opposite Directional Coupler

Let be $\delta = 0$. Here the NLODC of normalized length l will be considered [17]. From (11.6) the two integrals of motion result

$$a_1^2 - a_2^2 = c_0^2, \tag{11.7}$$

$$4\sqrt{a_1^2 - c_0^2}\cos\Phi = (r_1 + r_2)a_1^3 - 2r_2c_0^2a_1, \tag{11.8}$$

where constant c_0 is defined by boundary condition $a_2(l) = 0$. Using these expressions one can reduce the (11.6) to equation for a_1 that can be solved. Finally, amplitudes of the directed waves are

$$\begin{aligned} a_1^2(\zeta) &= c_0^2\frac{\mathrm{dn}[2(\zeta - l)/m, m] + 1}{2\mathrm{dn}[2(\zeta - l)/m, m]}, \\ a_2^2(\zeta) &= c_0^2\frac{\mathrm{dn}[2(\zeta - l)/m, m] - 1}{2\mathrm{dn}[2(\zeta - l)/m, m]}. \end{aligned} \tag{11.9}$$

The parameter c_0 is defined now by transcendental equation

$$a_0^2 = c_0^2\frac{\mathrm{dn}[2l/m,\ m] + 1}{2\mathrm{dn}[2l/m,\ m]}. \tag{11.10}$$

Reflection coefficient of the NLODC is

$$\begin{aligned} \Re &= 1 - a_1^2(l)/a_0^2 = 1 - \frac{c_0^2}{a_0^2} \\ &= 1 - \frac{2\mathrm{dn}[2l/m,\ m]}{1 + \mathrm{dn}[2l/m,\ m]} = \frac{1 - \mathrm{dn}[2l/m,\ m]}{1 + \mathrm{dn}[2l/m,\ m]}. \end{aligned} \tag{11.11}$$

The elliptic function dn(z, m) is periodically variable from unit to some positive value that is less unit. Hence, there are value of the a_0^2, such that reflection coefficient is zero. From (11.9) and (11.10) one can find the dependence output power $a_1^2(l)$ versus input power a_0^2. Example of this dependence is represented by plot in Fig. 11.2. There are some interval of a_0^2, where one value of the input power corresponds two values of the output power. (In really, there are two stable values and one unstable value.) This phenomenon is referred as bistability. The bistability is famous phenomenon in nonlinear optics [18].

The nonlinear transmission properties of nonlinear oppositely directional coupler with one waveguide made of positive index material and the other waveguide made of negative index material while only one of the waveguide is nonlinear has been considered in [19, 20]. In these papers the phase mismatch effect was taken into

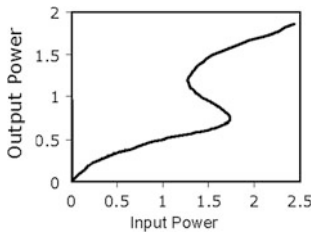

Fig. 11.2 Bistable behavior of the NLODC [17]

account. The effect of nonlinearity and mismatch on the multistable behavior for this coupler was studied.

11.2.3 Gap Solitons in Opposite Directional Coupler

In [21] the solitary wave propagation was considered in frame of the system of (11.4)–(11.5). In the case of $r_2 = 0$ the solitary wave propagation was investigated in [22]. The existence of the steady state solitary waves was found in both cases. The robustness of these solitary waves in relation to small perturbation has been demonstrated. The system of (11.4)–(11.5) does not belong to the class of completely integrable equations. Hence the solution of these equations does not represent true soliton. However, we denote them as gap solitons by analogy with gap solitons in nonlinear periodic structures.

To consider the solitary steady state waves in NLODC we have start from the (11.4)–(11.5) or (11.6). Suppose that solutions of these equation depend only on single variable $\xi = (\zeta + \beta\tau)\sqrt{1-\beta^2}$, with free parameter β. Let be $\sqrt{1+\beta}a_1 = u_1$ and $\sqrt{1-\beta}a_2 = u_2$. System of (11.6) after some transformations takes the following form

$$\frac{\partial}{\partial\xi}u_1 = u_2\sin\Phi, \quad \frac{\partial}{\partial\xi}u_2 = u_1\sin\Phi, \tag{11.12}$$

$$\frac{\partial}{\partial\xi}\Phi = -\frac{2\delta}{\sqrt{1-\beta^2}} + \left(\frac{u_1}{u_2} + \frac{u_2}{u_1}\right)\cos\Phi + \theta_1 u_1^2 + \theta_2 u_2^2, \tag{11.13}$$

where

$$\theta_1 = r_1\left[(1+\beta)\sqrt{(1-\beta)/(1+\beta)}\right]^{-1}, \; \theta_2 = r_2\left[(1-\beta)\sqrt{(1+\beta)/(1-\beta)}\right]^{-1}.$$

Let us consider the case of zero mismatch $\delta = 0$. Solitary wave corresponds with the following boundary condition $a_{1,2} \to 0$ at $\xi \to \pm\infty$. This system of equations

has the following integrals of motions correlated with boundary condition under consideration

$$u_1^2 - u_2^2 = 0, \quad 4\cos\Phi + \varepsilon\theta u_1^2 = 0,$$

where $\theta = \theta_1 + \theta_2$, $\varepsilon = \pm 1$. By the use these relations the analytical solution of the system of (11.12)–(11.13) can be obtained. This solution describes the coupled pair of the forward and backward solitary wave propagating as single wave packet over both waveguides, i.e., gap soliton. Real amplitudes and phases for gap soliton localized at point ξ_0 are represented by following expressions [21]

$$a_1^2(\xi) = \frac{4}{\theta(1+\beta)\cosh 2(\xi - \xi_0)}, \quad a_2^2(\xi) = \frac{4}{\theta(1-\beta)\cosh 2(\xi - \xi_0)},$$
$$\phi_1(\xi) = (1 - 4\theta_1/\theta)\arctan e^{2(\xi-\xi_0)}, \quad \varphi_2(\xi) = (1 - 4\theta_2/\theta)\arctan e^{2(\xi-\xi_0)} - \pi/2. \tag{11.14}$$

The negative value of the parameter β corresponds to solitary wave which propagates in the direction of the axis ξ. The solitary wave characterized by positive value of the parameter β propagates in the opposite direction. Large amplitudes of the solitary waves correspond to large positive values of the parameter β (which determines pulse velocity). When parameter β is negative the gap solitons with smaller values of the parameter β correspond to smaller amplitudes, however the absolute value of velocity determined by the parameter β is larger for less powerful solitary waves.

The gap soliton formation in the NLODC has a threshold character. A small amplitude electromagnetic pulse, introduced into one of the waveguides, is emitted in the opposite direction from the other waveguide. When the amplitude of the input pulse exceeds a certain threshold, then the pair of coupled pulses propagating in both waveguides is formed. Numerical simulation of the gap soliton formation was produced in [23] under condition that $r_2 = 0$, $r_1 = r$.

Gradually increasing incident pulse amplitude $a_1(\zeta = 0)$ it is possible to approach the threshold value of the amplitude a_{th}, when steady state pulse propagating along NLODC is formed (Fig. 11.3).

Using the expressions (11.9)–(11.11) approximately value for a_{th} can be found. It is suggested that soliton is formed on one coupling length, i.e., $l_c = 1$. In this case the coupler will be transparent: $\Re = 0$, that results in $\mathrm{dn}[2/m, m] = 1$. It means that modulus of the elliptical function $\mathrm{dn}(z, m)$ satisfies to equation $m\mathrm{K}(m) = 1$. The transparency of NLODC means that $c_0 = a_{th}$, and one can write for modulus the following formula $m = \left[1 + (ra_{th}^2/4)^2\right]^{-1/2}$. Under assumption that modulus is a small value the complete elliptic integral $\mathrm{K}(m)$ can be estimated as $\pi/2$. Thus the threshold value of the amplitude a_{th} is defined from the following equation $\left[1 + (ra_{th}^2/4)^2\right]^{1/2} = \pi/2$. Finely, we have

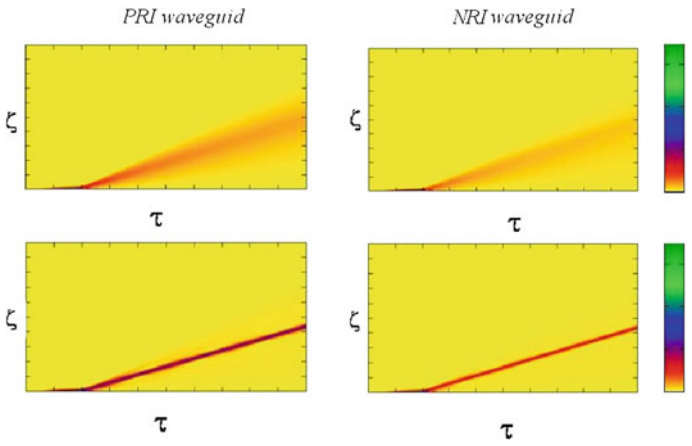

Fig. 11.3 Gap soliton formation in NLODC. *Upper panels* are corresponding for incident pulse amplitude that is less threshold value. *Lower panels* are corresponding for incident pulse amplitude that is over threshold value [23]

$$ra_{th}^2 = 4\sqrt{(\pi/2)^2 - 1} \approx 4847. \tag{11.15}$$

It is important to emphasize that this expression provides the good estimation for numerical results of [23].

11.3 Alternating Nonlinear Optical Waveguide Zigzag Array

The optical waveguide array provides a convenient setup for experimental investigation of periodic nonlinear systems in one dimension [24]. Nonlinear optical waveguide arrays (NOWA) are a natural generalization of nonlinear couplers. NOWA with a positive refractive index have many useful applications and are well studied in the literature (see for example [25–27]). If the sign of the index of refraction of one of waveguides in NOWA is positive and the index of refraction of other neighboring waveguide is negative the alternated NOWA will be obtained [16, 28, 29].

Usually the coupling between nearest neighboring waveguides is taken into account. It is correct approximation for strong localized electromagnetic wave in waveguide. However, the coupling between both nearest neighboring waveguides and the next nearest neighboring ones can be introduced by the use of a zigzag arrangement [30, 31] (Fig. 11.4a). Let ϑ_b is an angle between the lines connecting the centers of neighboring waveguides. In a linear array this angle is π. In a zigzag like array at $\vartheta_b \approx \pi/2$ the coupling between the nearest neighboring waveguides

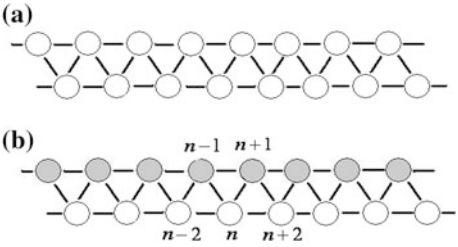

Fig. 11.4 A schematic illustration of zigzag coupled waveguides array (**a**); and zigzag positive-negative coupled waveguides array (**b**) [32]

and the next nearest neighboring ones is approximately the same. Nonlinear optical waveguide zigzag arrays can be considered as generation of NOWA.

11.3.1 Model and the Base Equations

Let us assume that waveguide having numbers n is characterized by positive refractive index (PRI), the nearest neighboring waveguides with numbers $n-1$ and $n+1$ possess negative refractive index (Fig. 11.4b). If the electromagnetic radiation is localized in each waveguide the coupled wave theory can be used. In the case of the array is deformed in the form of zigzag, where the angles between the lines connecting waveguides are equal approximately $\vartheta_b \approx 2\pi/3$, interaction between both the nearest neighboring and the next nearest neighboring waveguides will be important. The configuration of these alternating waveguides will be remarked as alternating nonlinear optical waveguide zigzag arrays (ANOWZA).

The system of equations describing the wave propagation in ANOWZA reads as

$$i\left(\frac{\partial}{\partial\zeta}+\frac{\partial}{\partial\tau}\right)q_n + c_1(q_{n-1}+q_{n+1}) + c_2(q_{n+2}+q_{n-2}) + r_1|q_n|^2 q_n = 0, \quad (11.6)$$

$$i\left(\frac{\partial}{\partial\zeta}-\frac{\partial}{\partial\tau}\right)q_{n+1} - c_1(q_n+q_{n+2}) - c_3(q_{n+3}+q_{n-1}) - r_2|q_{n+1}|^2 q_{n+1} = 0, \quad (11.7)$$

where $q_n(\zeta,\tau)$ is the normalized envelope of the wave localized in nth waveguide. Coupling between neighboring PRI and NRI waveguides is defined by parameter c_1. The $c_2(c_3)$ is coupling constant between neighboring PRI (NRI) waveguides. The phase mismatch is taken equal to zero. The all functions $q_n(\zeta,\tau)$, independent variables ζ, τ and other parameters are expressed in terms of the physical values represented in [32].

11.3.2 Linear Waves in Alternating Waveguide Zigzag Arrays

In [32] the asymmetrical ANOWZA was investigated. In this case NRI waveguides are linear ones ($r_2 = 0$). To find the linear wave spectrum we can employ the presentation of the envelopes in the form of harmonic waves.

$$q_n = A\mathrm{e}^{-i\omega\tau+ik\zeta+in\varphi}, \quad q_{n+1} = B\mathrm{e}^{-i\omega\tau+ik\zeta+i(n+1)\varphi}.$$

Substitution of this expression in the linear version of the (11.6) and (11.7) leads to a system of the algebraic linear equations respecting A and B. This system of linear equations obeys the nonzero solutions if the following condition

$$(\omega + \omega_0)^2 = \gamma_1^2 + (k - k_0)^2,$$

will be held. Here the parameters $\gamma_1 = 2c_1 \cos\varphi$, $\gamma_2 = 2c_2 \cos 2\varphi$, $\gamma_3 = 2c_3 \cos\varphi$, and $2\omega_0 = \gamma_2 + \gamma_3$, $2k_0 = \gamma_2 - \gamma_3$ were introduced. Thus, the linear waves in ANOWZA at $r_1 = 0$ and $r_2 = 0$ are characterized by the dispersion relation

$$\omega(k) = \mp\sqrt{\gamma_1^2 + (k - k_0)^2} - \omega_0. \tag{11.8}$$

This expression shows that (a) the forbidden zone (gap) in spectrum of the linear waves exist $\Delta\omega = 2|\gamma_1|$, (b) spectrum is shifted along both frequency axis and wave numbers axis, (c) the form of spectrum likes the spectrum for linear oppositely-directional coupler [17, 21, 22]. The gapless spectrum appears only when condition $\varphi = \pi/2$ is hold. In this case the radiation propagates along waveguides with the same refractive indexes. It should be noted that energy flux between neighboring waveguides is zero.

11.3.3 Nonlinear Waves in Alternating Waveguide Zigzag Arrays

The intriguing kinds of the nonlinear waves in ANOWZA can be found by the use the following ansatz

$$q_n(\zeta,\tau) = A(\zeta,\tau)\mathrm{e}^{in\varphi}, \quad q_{n+1}(\zeta,\tau) = B(\zeta,\tau)\mathrm{e}^{i(n+1)\varphi},$$

where $A(\zeta,\tau)$ and $B(\zeta,\tau)$ are the envelopes of the quasi-harmonic waves. It allows to do reduction of the (11.6)–(11.7) and to obtain the equations

$$i\left(\frac{\partial}{\partial\zeta}+\frac{\partial}{\partial\tau}\right)A+\gamma_1 B+\gamma_2 A+r_1|A|^2A=0, \tag{11.19}$$

$$i\left(\frac{\partial}{\partial\zeta}-\frac{\partial}{\partial\tau}\right)B-\gamma_1 A-\gamma_3 B-r_2|B|^2B=0. \tag{11.20}$$

These equations have the solutions that describe both steady state wave and spreading waves. The steady state waves correspond to solution of the wave equation depending only one particular variable, for example, $\xi=(\zeta+\beta\tau)\sqrt{1-\beta^2}$. The case of linear NRI waveguides ($r_2=0$) and zero mismatch condition will be discussed now. As above the real variables can be exploited to read the following equations [32]

$$\frac{\partial}{\partial\xi}u_1=u_2\sin\Phi,\quad \frac{\partial}{\partial\xi}u_2=u_1\sin\Phi, \tag{11.21}$$

$$\frac{\partial}{\partial\xi}\Phi=\delta+\left(\frac{u_1}{u_2}+\frac{u_2}{u_1}\right)\cos\Phi+\vartheta u_1^2, \tag{11.22}$$

where $u_1=\sqrt{1+\beta}|A|$, $u_2=\sqrt{1-\beta}|B|$ are new normalized amplitudes and

$$\delta=\left(\frac{\gamma_3}{\gamma_1}\sqrt{\frac{1+\beta}{1-\beta}}+\frac{\gamma_2}{\gamma_1}\sqrt{\frac{1-\beta}{1+\beta}}\right),\quad \vartheta=\frac{r_1}{\gamma_1(1+\beta)}\sqrt{\frac{1-\beta}{1+\beta}}.$$

From (11.21) and (11.22) the integrals of motion follow

$$u_1^2-u_2^2=C_1,\quad 4u_1u_2\cos\Phi+2\delta u_1^2+\vartheta u_1^4=C_2.$$

The boundary conditions $u_1=u_2=0$ at $\xi\to\pm\infty$ result in following value of theses integrals $C_1=C_2=0$.

Taking into account the integrals of motion the (11.21) and (11.22) can be solved. The solutions describing the steady state solitary waves are represented by the following expressions

$$|A|^2=\frac{4\Delta^2}{|\vartheta|(1+\beta)\{\cosh[2(\xi-\xi_c)]+\delta/2\}}, \tag{11.23}$$

$$|B|^2=\frac{4\Delta^2}{|\vartheta|(1-\beta)\{\cosh[2(\xi-\xi_c)]+\delta/2\}}, \tag{11.24}$$

where $\Delta^2=1-\delta^2/4$. The phase difference Φ evolves according to expression

$$\Phi(\xi) = \mathrm{sgn}\vartheta \ \arctan\frac{\Delta e^{2(\xi-\xi_c)}}{1+(\delta/2)e^{2(\xi-\xi_c)}} \pm \frac{\pi}{2}. \tag{11.25}$$

The expression (11.23)–(11.25) describe the exponentially decaying wave fronts. However some times the solitary waves can be decreasing as ξ^{-2}. The solutions found here are correct if $-2<\delta<2$. However, on the boundaries of this interval we have to refine behavior of the solitary waves. When $\delta \to -2$ the solution of the (11.21), (11.22) take the form of the algebraic soliton [32]

$$|A|^2 = \frac{8}{|\vartheta|(1+\beta_1)[1+4(\xi-\xi_c)^2]}, \quad |B|^2 = \frac{8}{|\vartheta|(1-\beta_1)[1+4(\xi-\xi_c)^2]}. \tag{11.26}$$

Here β_1 corresponds with $\delta = -2$. On the other hand, the amplitudes of the solitary waves are equal to zero if $\delta \to +2$.

11.3.4 Robustness of the Solitary Waves in ANOWZA

To investigate of the solitary wave's stability the collision between two solitary waves has been simulated. To produce a collision between two solitary waves we used solutions of the (11.21) and (11.22) with parameters $\beta = 0.4$ and $\beta = -0.4$ as initial conditions for these equations. The pulse with $\beta = 0.4$ was located at $\zeta_c = 50$ and pulse with $\beta = -0.4$ was located at $\zeta_c = 0$. For simplicity the coupling constant γ_1 was set as unite, whereas γ_2 and γ_3 are assumed equal. Parameter γ_2 was varied from 0.001 to 0.2.

It was found that the collision between counter propagating pulses is elastic for the coupling constant γ_2 that is taken from interval [0.001, 0.0075] (Fig. 11.5). Little radiation appears where the coupling constant γ_2 is more then 0.0075. The amplitude of the radiation is increasing and at $\gamma_2 > 0.02$ the reflected wave appears

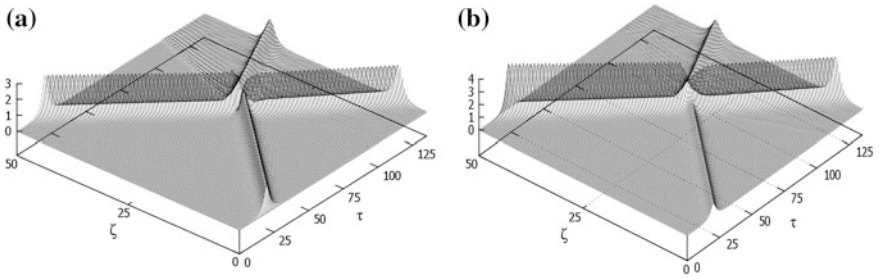

Fig. 11.5 Collision of two steady state pulses in the case of γ_2 = 0.01. *Left panels* are corresponding for PRI waveguides, *right panels* are corresponding for NRI waveguides [32]

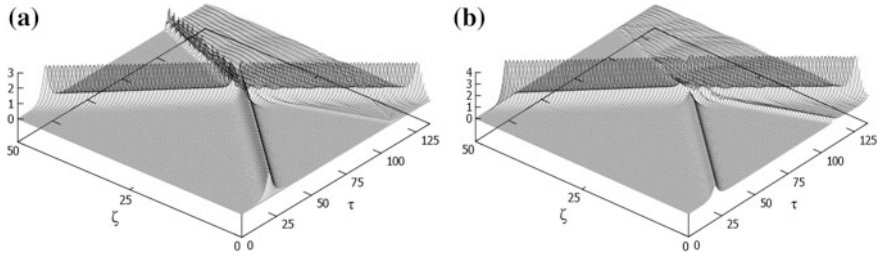

Fig. 11.6 Collision of two steady state pulses in the case of γ_2 = 0.06. *Left panels* are corresponding for PRI waveguides, *right panels* are corresponding for NRI waveguides [32]

in NRI waveguide as a result of the reflection of the incident solitary wave ($\beta = -0.4$) from solitary wave ($\beta = 0.4$) propagated in the opposite direction in ANOWZA (Fig. 11.6).

However, if the coupling constants belong to interval [0.08, 0.135] the steady state solitary waves are akin to elastic interacting waves. There is no radiation after collision, but the velocities of the scattered pulses can be strongly varied with respect of initial values.

The interaction of the incident solitary wave corresponding to $\beta = 0.4$ with quasi-harmonic wave has been considered. Initial incident pulse was located at $\zeta_c = 50$, the quasi-harmonic wave was generated at $\zeta = 0$ and it is characterized by frequency ω_{bg}.

It was found that initial steady state solitary wave is extremely prone to damage if the coupling constants $\gamma_2 = \gamma_3$ are less than 0.05. Thus, the numerical simulation demonstrates robustness of these solitary waves.

11.4 Conclusion

Here the propagation of electromagnetic solitary wave in nonlinear coupler where one of the waveguide is fabricated from a material with a negative refractive index. The zigzag positive-negative coupled waveguide array is generalization of this simple device. These waveguide systems are present the situation in where forward and backward electromagnetic waves interact with each other. Alternate positive and negative refractive indexes result in the gap in linear wave spectrum. That is dissimilarity from a convenient couplers or waveguide array.

In nonlinear coupler and zigzag waveguides array the solitary forward and backward waves can be combined into single solitary wave, which is referred as gap soliton. It should be noted that the term *gap soliton* is often referred to as nonlinear pulses propagating in periodic structures. The waveguide structure considered here, however, is homogeneous. Hence, the existence of a gap soliton, and

the bistability of continuous waves in an oppositely directed coupler represent new effects due to the positive-negative refraction phenomenon.

Recently the new intriguing properties of the twisted alternating waveguide array were predicted in [33]. It was show that forbidden zone in spectrum of linear waves can be controlled by the twist of waveguide array.

Acknowledgements We would like to thank N.M. Litchinitser, I.R. Gabitov, A.S. Desyatnikov and J.G. Caputo for enlightening discussions. AIM thanks the Department of Mathematics of University of Arizona, Laboratoire de Mathematiques, INSA de Rouen and the Nonlinear Physics Center, the Australian National University for the support and hospitality. This work was partially supported by NSF (grant DMS-0509589), ARO-MURI award 50342-PH-MUR and State of Arizona (Proposition 301), and by the Russian Foundation for Basic Research (grants No. 09-02-00701-a, 12-02-00561).

References

1. H. Lamb, On group-velocity. Proc. London Math. Soc. **1**, 473–479 (1904)
2. H.C. Pocklington, Growth of a wave-group when the group velocity is negative. Nature **71**, 607–608 (1905)
3. A. Schuster, *An Introduction to the Theory of Optics* (Edward Arnold, London, 1904)
4. L.I. Mandel'shtam, Group velocity in crystalline arrays. Zh. Eksp. Teor. Fiz. **15**, 475–478 (1945)
5. D.V. Sivukhin, The energy of electromagnetic waves in dispersive media. Opt. Spektrosk. **3** (4), 308–312 (1957)
6. V.E. Pafomov, On transition radiation and the Vavilov-Cherenkov radiation. Sov. Phys. JETP. **9**(6), 1321–11324 (1959)
7. V.G. Veselago, The electrodynamics of substances with simultaneously negative values of ε and μ. Sov. Phys. Usp. **10**(3), 509–526 (1968)
8. D.R. Smith, J.W. Padilla, D.C. Vier, S.C. Nemat-Nasser, S. Schultz, Composite medium with simultaneously negative permeability and permittivity. Phys. Rev. Lett. **84**(18), 4184–4187 (2000)
9. R.A. Shelby, D.R. Smith, S.C. Nemat-Nasser, S. Schultz, Microwave transmission through a two-dimensional, isotropic, left-handed metamaterials. Appl. Phys. Lett. **78**(1), 489–491 (2001)
10. R.A. Shelby, D.R. Smith, S. Schultz, Experimental verification of a negative index of refraction. Science **292**(5514), 77–79 (2001)
11. J. Valentine, Sh Zhang, Th Zentgraf, E. Ulin-Avila, D.A. Genov, G. Bartal, X. Zhang, Three-dimensional optical metamaterial with a negative refractive index. Nature **455**, 376–379 (2008)
12. V.P. Drachev, W. Cai, U. Chettiar, H.K. Yuan, A.K. Sarychev, A.V. Kildishev, G. Klimeck, V.M. Shalaev, Experimental verification of an optical negative-index material. Laser Phys. Lett. **3**(1), 49–55 (2006)
13. V. Veselago, L. Braginsky, V. Shklover, Ch. Hafner, Negative refractive index materials. J. Comput. and Theor. Nanoscience. **3**(2), 189–218 (2006)
14. V.M. Agranovich, YuN Gartstein, Spatial dispersion and negative refraction of light. Phys. Usp. **49**(10), 1029–1044 (2006)
15. N.M. Litchinitser, I.R. Gabitov, A.I. Maimistov, V.M. Shalaev, Negative refractive index metamaterials in optics. Prog. Opt. **51**, 1–68 (2008)

16. A.I. Maimistov, I.R. Gabitov, Nonlinear optical effects in artificial materials. Eur. Phys. J. Special Topics **147**(1), 265–286 (2007)
17. N.M. Litchinitser, I.R. Gabitov, A.I. Maimistov, Optical bistability in a nonlinear optical coupler with a negative index channel. Phys. Rev. Lett. **99**, 113902 (2007)
18. H.M. Gibbs, *Optical Bistability: Controlling Light with Light* (Orlando, San Diego, New York, Academic Press, Inc. 1985)
19. Z. Kudyshev, G. Venugopal, N.M. Litchinitser, Generalized analytical solutions for nonlinear positive-negative index couplers. Phys. Res. Int. **2012**, 945807 (2012) (4 pages)
20. G. Venugopal, Zh Kudyshev, N.M. Litchinitser, Asymmetric positive-negative index nonlinear waveguide couplers. IEEE J. Sel. Top. Quantum Electron. **18**(2), 753–756 (2012)
21. N.M. Litchinitser, I.R. Gabitov, A.I. Maimistov, Solitary waves in nonlinear oppositely directional coupler. Opt. Spectrosc. **104**(2), 253–257 (2008)
22. E.V. Kazantseva, A.I. Maimistov, S.S. Ozhenko, Solitaryelectromagnetic waves propagation in the asymmetric oppositely-directed coupler. Phys.Rev. A. **80**, 043833 (2009) (7 pages)
23. M.S. Ryzhov, A.I. Maimistov, Gap soliton formation in a nonlinear antidirectional coupler. Quantum Electron. **42**(11), 1034–1038 (2012)
24. D.N. Christodoulides, F. Lederer, Y. Silberberg, Discretizing light behavior in linear and nonlinear waveguide lattices. Nature **424**, 817–823 (2003)
25. D.N. Christodoulides, R.I. Joseph, Opt. Letts. **13**(9), 794–796 (1988)
26. C. Schmidt-Hattenberger, U. Trutschel, F. Lederer, Opt. Letts. **16**(5), 294–296 (1991)
27. S. Darmanyan, I. Relke, F. Lederer, Phys. Rev. E **55**(6), 7662–7668 (1997)
28. D.A. Zezyulin, V.V. Konotop, F.K. Abdullaev, Discrete solitons in arrays of positive and negative index waveguides. Optics Letts. **37**(19), 3930–3932 (2012)
29. A.I Maimistov, E.V. Kazantseva, A.S. Desyatnikov, Linear and nonlinear properties of the antidirectional coupler. Lecture Notes in Coherent Optics and Optical Spectroscopy, Kazan State University, Kazan (2102), pp. 21–31 (in Russian)
30. N.K. Efremidis, D.N. Christodoulides, Discrete solitons in nonlinear zigzag optical wave-guide arrays with tailored diffraction properties. Phys. Rev. B **65**, 056607 (2002)
31. G. Wang, J.P. Huang, K.W. Yu, Nontrivial Bloch oscillations in waveguide arrays with second-order coupling. Opt. Letts. **35**(11), 1908–1910 (2010)
32. E.V. Kazantseva, A.I. Maimistov, Nonlinear waves in an array of ziz-zag waveguides with alternating positive and negative refractive index. Quantum Electron. **43**(9), 807–813 (2013)
33. A.S. Desyatnikov, A.I. Maimistov, Y.S. Kivshar, Topological solitons to twisted coupled positive-negative waveguides. In 2nd International Workshop on Nonlinear Photonics, NLP '2013, Sudak, Ukraine, 09–13 Sept 2013

Chapter 12
Characterization of Photonic Crystal Fibers: Selected Methods and Experience

Krzysztof Borzycki and Kay Schuster

Abstract Several techniques for characterization of photonic crystal fibers (PCFs) are reviewed, focusing on measurements of attenuation, optical uniformity, selected polarization parameters, and effects of temperature and mechanical strain applied to the fiber. PCF properties often radically differ from those of conventional fibers used in communications networks, and available lengths are generally short, therefore different approach to characterization is required. Comparisons of alternative methods for selected tests are made, and examples of errors in PCF handling and testing are discussed. Examples of results obtained for silica single-mode PCFs with GeO_2-doped core are also presented, accompanied by geometrical and compositional fiber data.

12.1 Introduction

Photonic crystal fibers, also called "microstructured" or "holey" fibers constitute very diverse class of optical fibers [1, 2], different from conventional single mode and multimode fibers made of solid glass, used in communication networks, industrial control, sensors, etc. In particular, PCF characteristics like:

- chromatic dispersion,
- polarization properties,
- optical nonlinearity,
- mode propagation behavior,
- sensitivity to external factors,

K. Borzycki (✉)
National Institute of Telecommunications (NIT), Szachowa St. 1, 04-894 Warsaw, Poland
e-mail: k.borzycki@itl.waw.pl

K. Schuster
Leibniz Institute of Photonic Technology Jena (IPHT), Albert-Einstein-Str. 9,
07745 Jena, Germany

O. Shulika and I. Sukhoivanov (eds.), *Contemporary Optoelectronics*,
Springer Series in Optical Sciences 199, DOI 10.1007/978-94-017-7315-7_12

can be dramatically modified by changing geometry of core and photonic structure and infiltration of gas or liquid into holes or deposition of metal on their surfaces. This spurred development of PCFs for specific applications [1], including:

- sensing (temperature, gas, strain, magnetic field, …),
- signal processing (wavelength conversion, dispersion compensation, …),
- supercontinuum generation,
- optical fiber lasers,
- tunable and switchable optical devices,
- absorption cells filled with HCN or C_2H_2 gas for frequency standards.

Except for hole-assisted fibers (HAF) [3], PCFs are not used as transmission medium in communications networks. Contrary to early expectations, scattering produced by surface capillary waves limits minimum attenuation of hollow-core PCFs to 0.1–0.2 dB/km, making them no better than existing telecom fibers [4].

Manufacturing of "holey" fibers, dominated by the stack-and-draw method for silica fibers, is far from maturity. In particular, repeatability of product parameters is poor, as the stack-and-draw process is sensitive to variations in temperature,, inflation pressure, moisture absorption, drawing speed, etc. [2, 5, 6]. Correct and uniform hole sizes are particularly difficult to get as glass surface tension closes holes during preform making and fiber drawing. Materials other than silica, like polymers and chalcogenide glasses are also used. There are no standards so far. Usual applications need short lengths of PCF: few meters, not 10–200 km in typical telecom link. As result, PCF characterization has its challenges:

- wide range of fiber parameters,
- working with short samples,
- difficult optical coupling to PCF,
- unstable behavior due to infiltration of humidity, dust, etc. [7].

For sensing applications, measurements of sensitivity of specific PCF parameter to external factor(s) are required, rather than verifying insensitivity to temperature, bending, humidity, etc. of conventional telecom fibers.

The following sections deal with specifics of PCF characterization, drawing primarily on experience with single-mode silica fibers. The list is far from complete: particular applications require characterization of additional properties like optical nonlinearity, group refractive index or effects of ionizing radiation.

12.2 Fiber Geometry

Obtaining of desired PCF properties requires strict control of dimensions. Fiber geometry is checked by examination of cleaved end, using either:

(a) optical microscope (Fig. 12.1),
(b) scanning electron microscope (SEM) (Figs. 12.2 and 12.3).

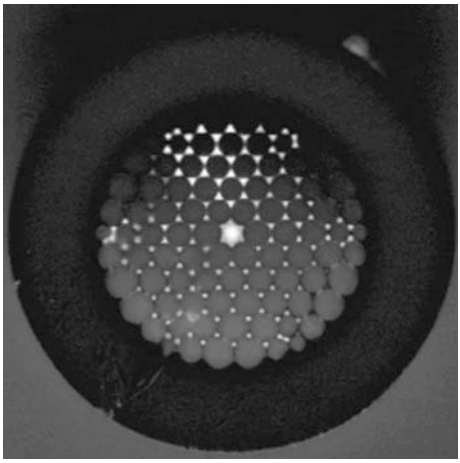

Fig. 12.1 80 μm PCF (IPHT 252b5) seen with optical microscope. *Note* poor resolution

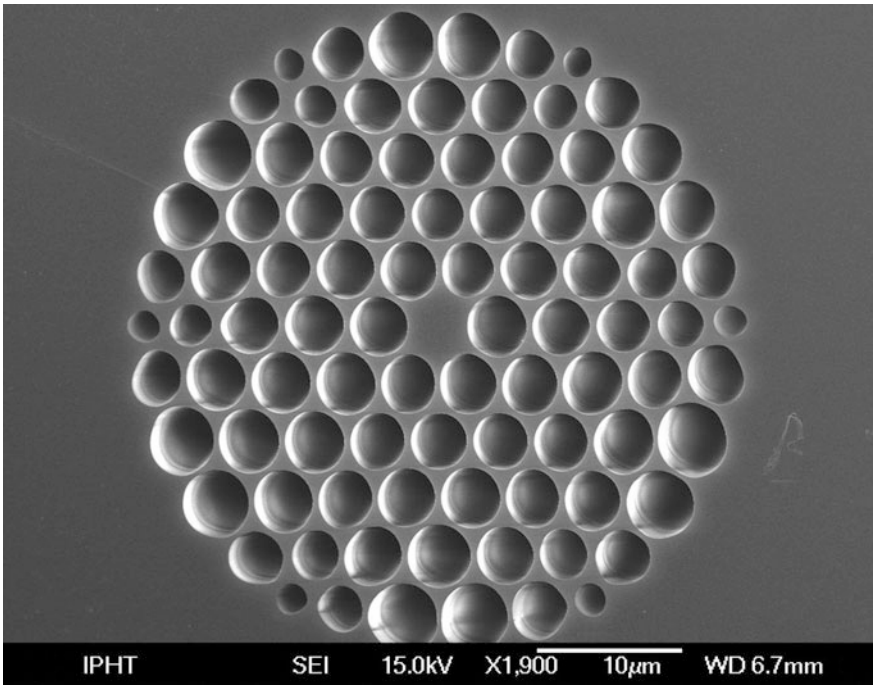

Fig. 12.2 Image of 80 μm PCF (IPHT 252b5) obtained with SEM. Part of cladding not shown. Excellent resolution, but no ability to observe light propagation in the fiber

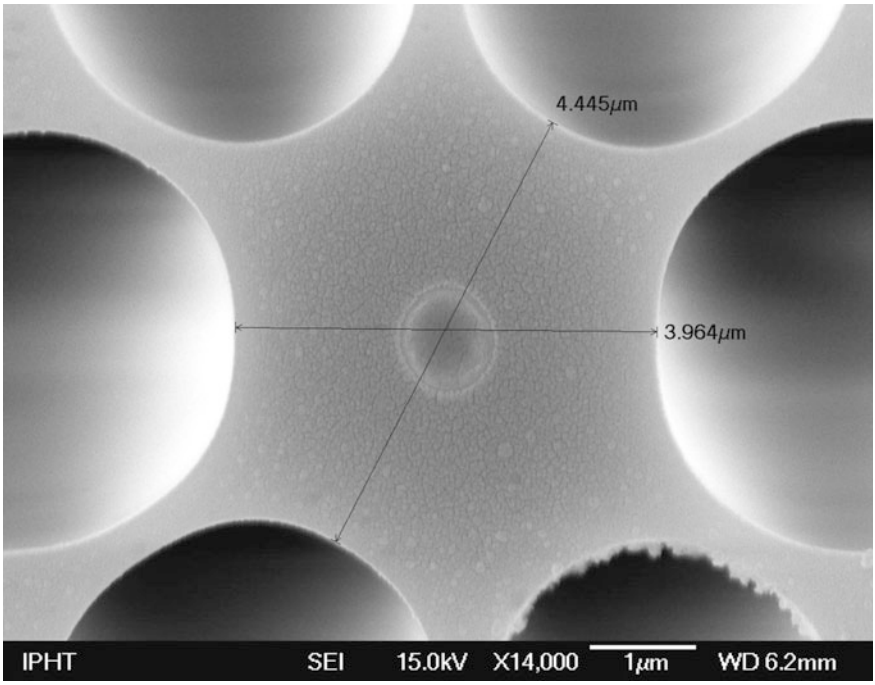

Fig. 12.3 SEM image of central part of PCF (IPHT 252b5). Doped core visible in the center

Method (a) is attractive due to widely available equipment and possibility for cross section control during fiber fabrication. Image is recorded with camera attached to microscope, and analyzed with software, after calibrating equivalent pixel size. Distortion, chromatic aberration and other imperfections of optics can be corrected with image editing software. Microscope resolution (d) is restricted by the Abbe diffraction limit, according to formula:

$$d = \lambda/2NA,$$

where λ is light wavelength and NA numerical aperture of microscope lens. For NA = 0.65 (40× lens) and wavelengths of 0.55 μm (green light) and 0.45 μm (blue light), corresponding resolution limit is 0.42 and 0.35 μm, respectively. Those values are close to hole size in many index-guided PCFs. Even if small holes are visible, their deformations and lack of symmetry of holey structure are often undetectable (Fig. 12.1). The Abbe limit makes observation at infrared wavelengths, e.g. 1.55 μm rather impractical, although suitable cameras are available.

Because of short equivalent wavelength of accelerated electrons, method (b) is free of this limit, showing small details (Figs. 12.2 and 12.3). Other advantages of electron microscope include:

- excellent depth of field due to low NA of electron optics,
- ability to detect some variations in glass composition (Fig. 12.3).

Results depend on cleave quality: good for glass fibers, much worse for microstructured polymer optical fibers (MPOF), made of polymethyl methacrylate (PMMA), cyclic olefin copolymer (TOPAS) or fluoropolymers (CYTOP). MPOFs cannot be cleaved by scribing and breaking under load due to anisotropic properties of drawn fiber, and are cut with blades. Cleave quality depends on temperature of fiber and blade, preferably 70–80 °C for PMMA [8, 9] or 40 °C for TOPAS [9] and cutting speed. To reduce influence of scribing marks and other blemishes, diameters are measured by fitting a circle or oval superimposed on image of fiber cladding or other part of interest.

12.3 Coupling of Light to Fiber Sample

The bulk of fiber characterization is devoted to transmission of light through the sample, which requires coupling the PCF sample to given test setup, usually at both ends. The coupling must meet the following requirements:

(a) PCF excitation approximating steady-state light distribution,
(b) acceptable loss,
(c) stability for duration of a given test (minutes–weeks).

For many tests, requirement (c) is more important than (b), if optical measurements are relative, not absolute. Examples include measurements of polarization mode dispersion (PMD), loss measurements with cutback method or testing sensitivity of fiber to temperature, radiation, etc. Two common arrangements are:

(a) free-space coupling to cleaved PCF with microscope lens,
(b) butt-coupling to intermediate optical fiber (Fig. 12.4),
(c) splicing of PCF to lengths of conventional fiber, usually telecom single-mode fiber (SMF), fitted with connectors at other end (pigtails)—Fig. 12.6.

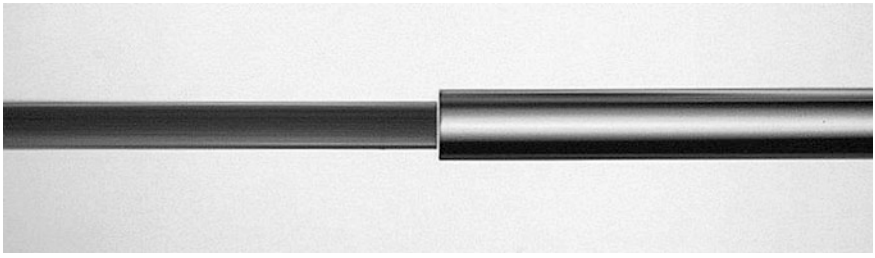

Fig. 12.4 Butt-coupling between 80 µm PCF (IPHT 252b5, *left*) and SMF (*right*). Fibers aligned with 10 µm gap using micropositioner. Because of different core diameters, loss was 5.79 dB at 1558 nm. Loss of fusion splice after pre-forming of the same fibers was about 1 dB

Method (a) is relatively fast, work being limited to cleaving and alignment. Coupling setup can be easily modified, e.g. by changing lens (to match fiber NA) or adding filter. It works with any PCF, including those for which a matching conventional fiber cannot be found. Disadvantages include:

- infiltration of PCF by humidity, dust, etc. through open ends, causing attenuation and scattering of light in the sample [7],
- reflections from lenses,
- slow transfer of sample to another test setup,
- problematic medium-term stability.

Butt-coupling (b) is also fast and simple. The PCF and intermediate fiber leading to other part of test system (light source, interferometer, etc.) are cleaved, aligned for best optical coupling and kept either with small air gap (Figs. 12.4 and 12.5) or put into direct contact. Insertion loss of butt-coupling depends on:

- compatibility of fibers, defined by mode area (single mode-fibers), core diameter (multimode fibers) and mode distribution,
- fiber alignment; preferably to within 10 % of core diameter,
- cleave quality.

As seen in Fig. 12.4, butt-coupling and alignment with micropositioner are particularly useful when working with fibers having different diameters, PCFs with large NA, large mode field, or suspended core. Fusion splicing in such situations is usually complicated and time consuming. Best alignment is achieved by monitoring of coupling loss with optical power meter or other instrument. For fibers of identical cladding diameters, V-groove coupling without index matching fluid can be used. For PCF-PCF coupling, relative rotation of fibers with loss monitoring is often required to align their non-circular cores and photonic structures.

By introducing deliberate perpendicular offset, selective coupling to certain part of PCF photonic structure rather than core is possible. If necessary, increase of gap between fibers can be used for power adjustment.

Fusion splicing (c) is preferable for testing PCFs with instruments for conventional telecom fibers (Fig. 12.6), having interfaces for such fibers terminated with

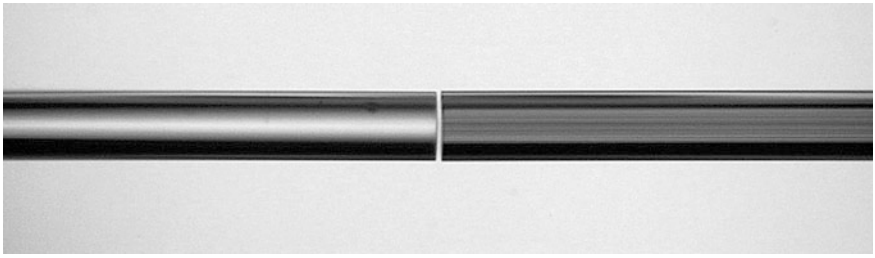

Fig. 12.5 Butt-coupling between 125 μm PCF (IPHT 282b4) and SMF (*left*). Loss of butt-coupling was 2.37 dB at 1558 nm, while loss of fusion splice was 1.25 dB

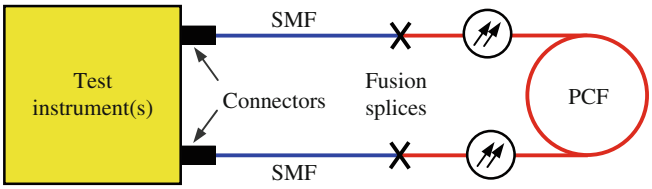

Fig. 12.6 Connection of PCF sample to test instrument with spliced SMF pigtails. Arrangement for measurements with OTDR is presented in Sect. 12.4

connectors—even if their internal components like detectors have free-space coupling (optical spectrum analyzers, power meters). Important is ubiquity of such instruments, mostly made for testing of telecom single mode fiber (SMF) [10], and low-cost fiber pigtails. Range of covered wavelengths is extended with introduction of new fiber systems and test instruments, e.g. operating at 1625 nm (maintenance of fiber networks) or 1490 nm (fiber access networks). CWDM transponders cover 1271–1611 nm span in 20 nm increments, being suitable as light sources.

Fusion splicing was preferred for single-mode silica PCFs intended for signal processing or sensing, working in wavelength bands characteristic for communication systems, usually 1300–1600 nm. Splicing to pigtails ensures:

- stable coupling, resistant to vibration, temperature variations, etc.,
- hermeticity of PCF sample,
- rapid portability of sample between multiple test instruments,
- grip on PCF ends through protection sleeves during mechanical tests [11].

An advantage of fusion splice with respect to butt-coupling is reduction of reflections and loss (Figs. 12.4 and 12.5), because the Fresnel reflection at glass-air interface is greatly reduced for solid-core PCFs; this reduces loss by approx. 0.4 dB. Low reflectivity is important for testing with OTDR or laser sources, which otherwise require optical isolator. Unfortunately, fusion splicing has several disadvantages:

- PCF splicing is complicated and time-consuming,
- procedure must be tailored to each fiber on trial-and-error basis [11, 12],
- fusion splicing of “exotic” PCFs is impossible, or splice loss is high.

Silica PCFs can be spliced on arc fusion splicers for telecom fibers, but splicing procedure is modified substantially [11–18]. Dedicated fusion splicers for PCFs are available, but expensive. Such machines employ either modified arc fusion or hot filament method and are capable of achieving much lower splice loss, with added features important for splicing PCFs and other specialty fibers, like:

- rotation during alignment of fibers (for PCF-PCF splicing),
- extended range of low temperature settings,
- pre-forming of hot fibers: necking, expansion of core, etc.

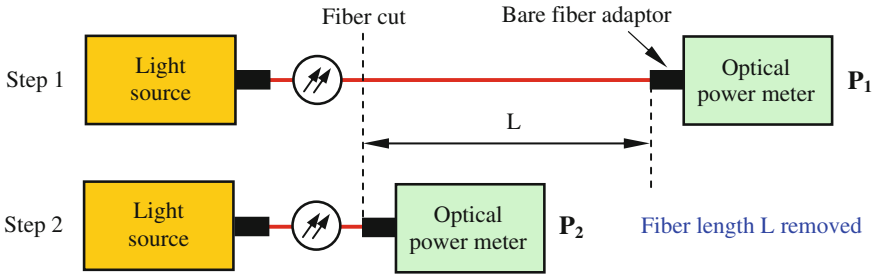

Fig. 12.7 Fiber loss measurement by cutback method

Fusion splicing of polymer fibers is not possible for multiple reasons. Polymers burn and do not flow when hot as the glass does; soft plastic fibers are not compatible with hardware like V-groove holders, fixtures and connectors made for rigid silica fibers, being easily damaged [10]. Coupling of MPOF on fusion splicer micropositioner is difficult, too, because unsupported length of several millimeters of soft plastic fiber sags badly under its own weight.

A solution intermediate between (a) and (b) is fixing cleaved PCF in a connector-style bare fiber adaptor, plugged into instrument having a connector interface with free-space optics inside, not a fiber-fiber contact. Direct contact of cleaved glass PCF with fiber connector can scratch both, and shall be avoided. Suitable instruments include optical power meters (Fig. 12.7), optical spectrum analyzers (OSA), fiber inspection microscopes (useful for checking PCF structure, cleave quality and cleanliness) and several attenuators, but no PMD analyzers or OTDRs.

It is also possible to connect cleaved PCF mounted in adaptor to connector with another (conventional) fiber leading to other part of test setup; risk of scratching is more acceptable here because of low cost of commercial fiber pigtails.

PCF endface shall be checked for cleave quality and cleanliness with microscope. Dust can be removed by contact with sticky tape, but only selected products are suitable [19]. No solvents or index-matching fluids are allowed with PCF, as those penetrate holes, producing high loss.

12.4 Loss, Attenuation and Uniformity

The reference test method for measuring loss of a length of optical fiber is the cutback method [20]; the principle is shown in Fig. 12.7.

Insertion loss IL [dB] and attenuation α [dB/km] of fiber section with length L [km] are calculated from difference between optical powers measured [in dBm] before (P_1) and after the fiber is cut (P_2):

$$IL = P_1 - P_2, \quad \alpha = (P_1 - P_2)/L.$$

Spectral measurements of loss and attenuation can be made with:

- tunable laser source and optical power meter,
- multiple fixed wavelength sources and optical power meter,
- broadband source (LED, tungsten lamp, supercontinuum source) and OSA.

While a robust method for long conventional fibers, cutback works less well with short samples of holey fibers. Variations in coupling to optical power meter or OSA caused primarily by imperfect cleaving easily reach 0.1–0.2 dB. With two connections required, uncertainty in measured loss is doubled: 0.2–0.4 dB. For 50 m long fiber, this produces 4–8 dB/km uncertainty in attenuation measurement.

Situation is worse, when PCF sample is spliced to SMF pigtails (Fig. 12.6), and insertion loss of such assembly measured without cutting fiber. Combined loss of 2 splices and 1 connector is 1.5–5 dB. PCF-SMF splice loss may vary with wavelength, if mode diameters of both fibers change with wavelength in a different way. This causes "baseline problem" in spectral measurements: differences between loss values at specific wavelengths, say OH^- absorption peaks versus surrounding bands are known accurately, but absolute values are not certain (Fig. 12.8).

Alternative test method is the measurement with optical time domain reflectometer (OTDR), widely used for testing conventional fibers [20]. Key advantage of OTDR is elimination of errors produced by variable loss of coupling to fiber under test [21, 22], as it measures difference between intensity of radiation backscattered from different locations in the fiber. OTDR allows selecting a part of fiber trace for loss calculations, and to avoid non-uniform parts of trace, splices, etc. (Fig. 12.9). Attenuation measured with OTDR can be used to correct results of spectral loss measurements, except for spectral dependence of splice loss (Fig. 12.8).

OTDR has a "dead zone": initial length of fiber after location with strong localized loss or reflection of light, where no useful measurements are possible. Additionally, it can measure splice loss and difference between intensity of backscattering in fibers, but correct results are obtained only after measurements from both ends of the optical circuit. For these reasons, it is recommended to splice the PCF sample between two sections of SMF, each at least 100 m long, as in Fig. 12.10, or place suitably long SMF between OTDR and PCF spliced to SMF pigtails.

OTDRs sold for testing of telecom SMFs at 1310, 1550, 1490 and 1625 nm are suitable for single-mode PCFs as well; most useful are high-resolution and short dead zone instruments developed for testing passive optical networks (PON). For characterization of MPOF, 500, 650 and 850 nm OTDRs with 0.1 m or better spatial resolution exist, developed for aerospace applications and testing of conventional polymer fibers [23].

OTDR allows inspecting optical uniformity of fiber. This is important for PCFs, whose manufacturing still lacks consistency. Testing short samples requires short pulses; the lowest setting in telecom OTDRs is 0.2 m [24], good for characterization

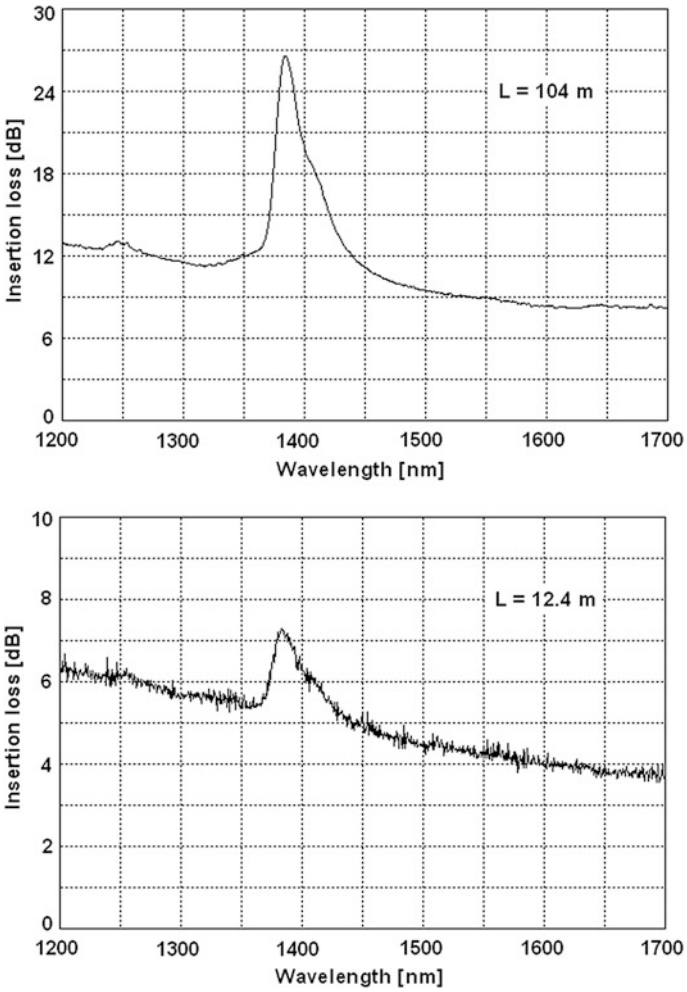

Fig. 12.8 Loss spectra of two lengths of IPHT 282b4 fiber spliced to SMF pigtails [20]. Added attenuation due to OH^- peak at 1385 nm is similar in both measurements: 146 dB/km. Contribution of wavelength-dependent splice loss is visible: PCF loss measured with OTDR was 6.48 dB (104 m)/0.77 dB (12.4 m) at 1550 nm, and 7.21 dB (104 m)/0.86 dB (12.4 m) at 1310 nm

of 5 m sample of PCF, if its attenuation is high enough [22]. Short pulse reduces OTDR dynamic range; but PCFs the authors measured—with cores of un-doped or highly doped silica always produced backscattering stronger than SMF, for which the instruments are specified. Resulting improvement of OTDR dynamic range was up to 11 dB—see examples in Figs. 12.9 and 12.11.

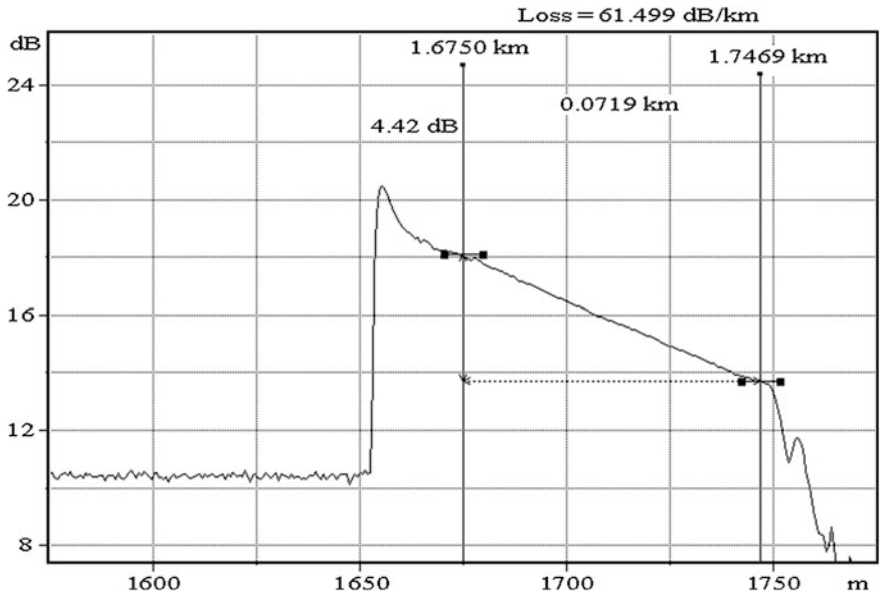

Fig. 12.9 Attenuation measurement of IPHT 282b4 fiber with OTDR. Wavelength: 1550 nm, pulse width: 10 ns (1 m). PCF was preceded by a 1650 m long SMF (lower trace on the *left*) and FC/PC connector. Backscattering in PCF with highly doped core was approx. 80 times stronger than in SMF. This reduced noise in PCF trace and improved OTDR dynamic range by 9.5 dB

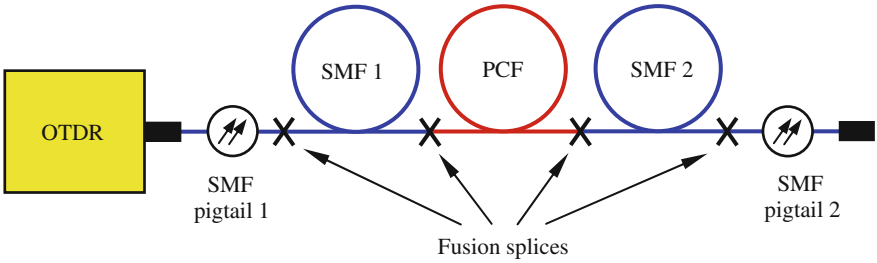

Fig. 12.10 Setup for measurements of single-mode PCF and splices with OTDR

Measurement with OTDR requires certain value of fiber loss to overcome noise from electronics and fiber non-uniformities (T_N), usually 0.02–0.10 dB (p-p). Minimum loss of measured fiber section L_{MIN} [dB] needed to achieve relative error L_{ERR} [%] in 2-point loss measurement (Figs. 12.9 and 12.11) is set by formula [22]:

$$L_{MIN} = 100\frac{T_N}{L_{ERR}}.$$

Consequently, high fiber attenuation enables accurate measurement in proportionally shorter sample. Figure 12.11 shows a good example.

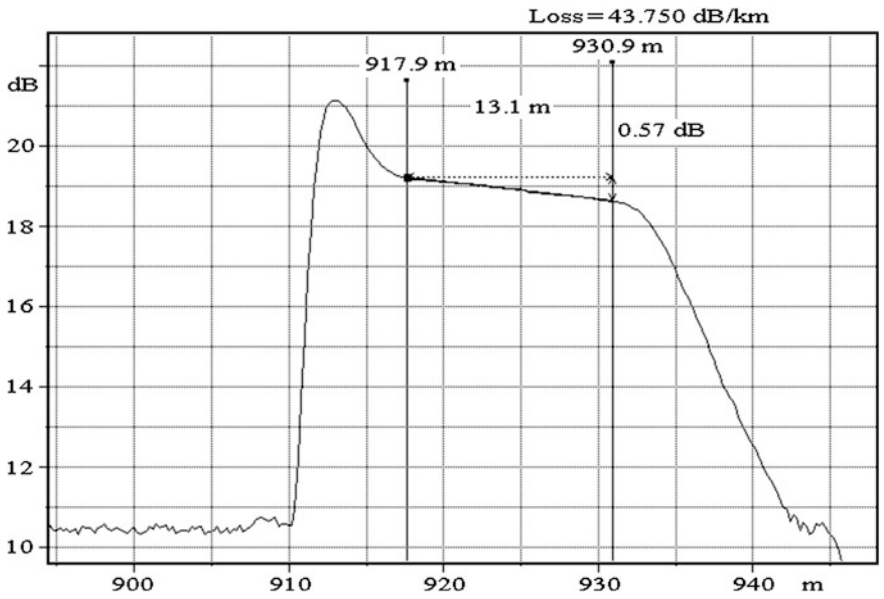

Fig. 12.11 Attenuation measurement of IPHT 252b5 fiber with OTDR. Wavelength: 1310 nm, pulse width: 10 ns (1 m). PCF was preceded by a 910 m SMF and FC/PC connector. Backscattering in PCF was 135 times stronger than in SMF, increasing dynamic range by 11.3 dB

Many PCFs, especially of "suspended core", "hollow core" or similar type have effective refractive index (n_{eff}) much lower than default value, approx. 1.47 for SMF, programmed by manufacturer or set by previous user of the instrument. With lowest values of n_{eff} reported for microstructured fibers approaching 1.02, large errors in measuring fiber length and attenuation coefficient are possible.

12.5 Polarization Parameters

Photonic crystal fibers often lack radial symmetry by design, and even if nominally symmetrical, frequently exhibit deformed holes or core (Fig. 12.3), accompanied by internal strain. Non-symmetry of core and surrounding photonic structure (producing form birefringence) and strain left from drawing process (producing stress birefringence) contribute to birefringence and polarization mode dispersion (PMD) in the fiber. PCF can have birefringence and PMD comparable to PANDA or Bow-Tie fibers, with differing dependence on temperature, twist or strain, useful for making sensors or tunable optical devices [1, 21]. PMD is also an indicator of fiber geometry imperfections. Therefore, modeling and characterization of polarization parameters and their sensitivity to strain, twist, hydrostatic pressure, temperature, etc. are of considerable interest [25–30].

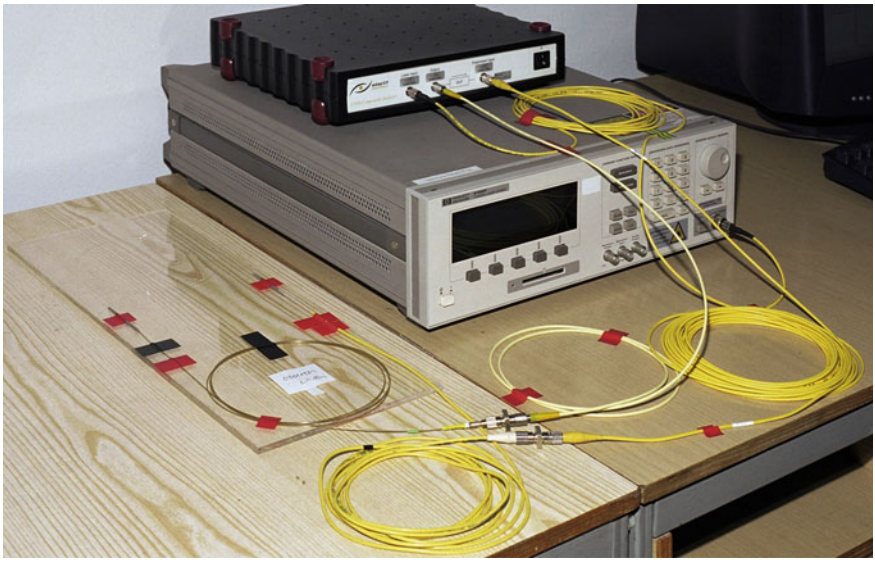

Fig. 12.12 PCF sample (*left*) fixed to PMMA plate for measurements of polarization parameters with tunable laser (*center*) and PMD analyzer (*top*). Fibers were fixed with tapes to prevent movement during test

Commercial PMD analyzers are dedicated to measuring telecom SMF; it is best to splice the sample to SMF pigtails, as shown in Fig. 12.6.

Test setups for polarization parameters are very sensitive to mechanical disturbances to either pigtails or PCF under test, because elastooptic effects in the fibers produce rotation of polarization plane, mixing of polarization modes or other interference, while measurement using tunable laser and Jones Matrix Eigenanalysis (JME) method takes 5–60 min. Fibers shall be laid on stable support and fixed to prevent movement [19], see Fig. 12.12.

During fiber characterization with JME method, differential group delay (DGD) between polarization modes is measured over a certain spectral range. The result may be either a spectrum of DGD (Fig. 12.13) or its average value—the PMD.

Shape of DGD spectrum (Fig. 12.13) provides important information: flat (top graph) is typical for strain-related PMD, rising (bottom graph)—for geometry-related PMD [29]. Irregular DGD spectrum and sub-linear increase of PMD with fiber length indicate propagation of higher order modes, or mixing of polarization modes in long sample, which appeared in the 104 m long section of IPHT 282b4 fiber. For the latter reason, PCF samples shall be short, preferably in the 0.5–20 m range.

Design, modeling and measurements of birefringence in IPHT 252b5 fiber in another laboratory are presented in references [26, 29].

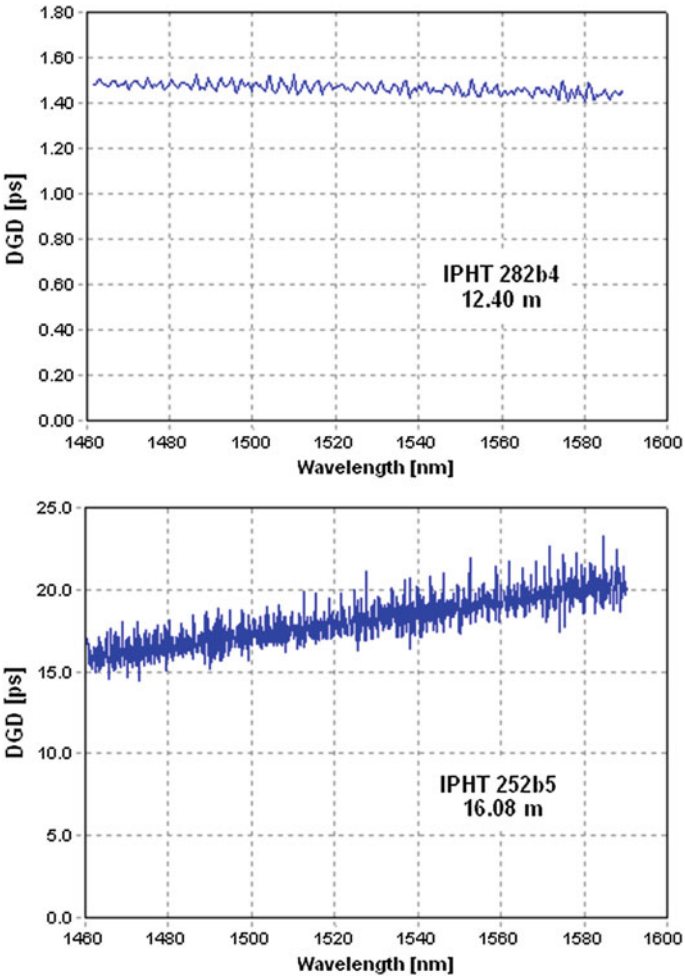

Fig. 12.13 Examples of DGD spectra. PMD in the IPHT 252b5 fiber was high: 1.127 ps/m. *Note* opposite slope of DGD characteristics

12.6 Effects of Temperature

We focus here on measuring temperature dependence of PMD. More details and test results are included in papers [19, 21, 30]. The basic rules for characterization of sensitivity of fiber parameter to certain factor like temperature are:

- stable connections between test instruments and sample,
- elimination of all other external influences,
- optimization of instruments settings to reduce random noise of readings.

As the goal is to establish variations of PMD with temperature, accuracy of absolute calibration of test setup is less important, as long as the expected (frequently small) differences between PMD values at several temperatures can be reliably measured. This rule applies generally to characterization of sensitivity of any fiber parameter to any external factor.

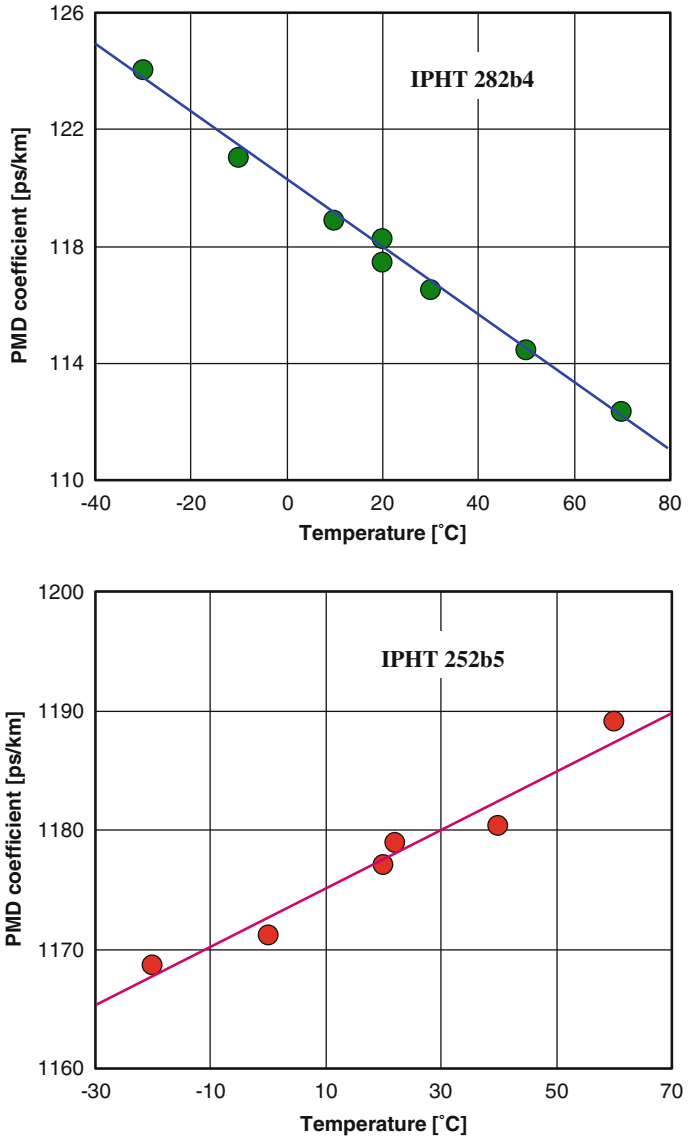

Fig. 12.14 Variations of PMD coefficient with temperature

Unlike bulky equipment or cables, thin, light and exposed fibers respond quickly to varying temperature, so exposure time is dictated by characteristics of climatic chamber (temperature settling time) and duration of PMD measurement, which in case of JME setup may take up to 30 min for high-PMD fiber. The main problem is prevention of fiber shaking by vibrations from cooling system or forced flow of air in the climatic chamber. Besides careful fixing of fibers, temporary stopping of the chamber for duration of measurement may be needed [19].

If an irregular DGD spectrum of PCF shows signs of (even weak) multimode propagation, or mixing of polarization modes, the test cannot be done, because resulting random variations of PMD will mask true temperature dependence [19]. One may try to use a shorter sample, or modify optical coupling to PCF in order to reduce excitation of unwanted modes.

Examples of PMD-temperature characteristics (Fig. 12.14) are presented for the same fibers as in the preceding section, allowing to compare them with DGD spectra in Fig. 12.13.

Temperature coefficients of PMD were:

- 2.13×10^{-4}/K for IPHT 252b5 (λ = 1540–1560 nm),
- 9.7×10^{-4}/K for IPHT 282b4 (λ = 1490–1590 nm). PMD in this fiber is produced by strain resulting from differential shrinking of parts during drawing.

12.7 Effects of Fiber Twist

Strain produced by fiber twisting affects birefringence and PMD of single-mode fiber (both conventional and microstructured) in special way: PMD is first quickly reduced with progressive twist, than begins to linearly rise with further twisting [30]. This complex behavior is explained by (a) rapid reduction of existing fiber birefringence by circular strain, and simultaneously (b) creation of new birefringence proportional to circular strain [18, 31].

In actual testing of highly birefringent fibers, only regime (a) is observed, as fiber breaks, or test is stopped before PMD starts to rise again [18]. This happened also during our experiments, whose results are presented in Fig. 12.15. In both fibers, and several others, PMD reduction was essentially independent of twist direction.

Lower twist sensitivity of IPHT 252b5 fiber is explained by 50 % smaller core diameter and correspondingly lower strain in core area at given twist, as well as almost 10× higher initial PMD coefficient (Table 12.1). According to theory [31], PMD reduction in regime (a) depends on square of twist per unit length of fiber.

PMD in microstructured fiber is modified also by axial strain [28] and bending.

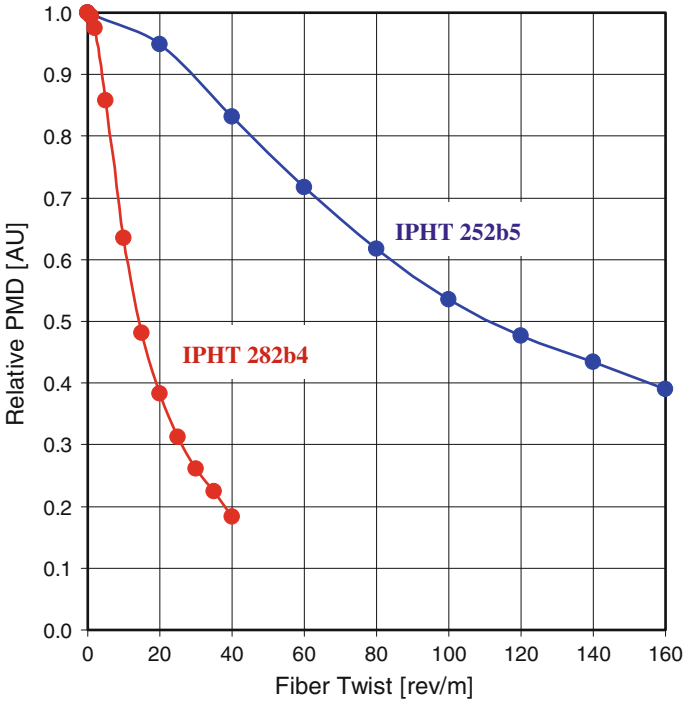

Fig. 12.15 Variations of PMD with fiber twist

Table 12.1 Data of PCFs

Parameter	Unit	IPHT 252b5	IPHT 282b4
Cladding diameter	µm	82.7	124.4
Hole diameter (d)	µm	3.6	0.7
Hole spacing (Λ)	µm	4.2	4.2
Diameter of holey package	µm	42.8	43.0
Diameter of doped core	µm	0.5/2.0/4.1	1.2/3.9/7.3
Attenuation @ 1310 nm	dB/km	43.8	69.3
Attenuation @ 1550 nm	dB/km	58.3	60.2
PMD (1460–1590 nm)	ps/km	1127	117.9

Dimensions measured with optical microscope

12.8 Chromatic Dispersion

Chromatic dispersion (CD) is important for several applications of microstructured fibers, including CD compensation, generation of optical supercontinuum (SC) in fiber optically pumped with picosecond laser pulses, or use as transmission medium

in communication networks. CD characteristics of PCF can be dramatically modified by changing geometry of photonic structure and fiber materials, and needs to be measured over a wide spectral range.

Two methods widely adopted for measuring CD in long (1–100 km) lengths of telecom single mode fibers: phase shift method and pulse delay method [20] are not suitable for characterization of short pieces of fiber due to insufficient resolution. Unfortunately, kilometer-length PCF may be unavailable, have high loss, or insufficient longitudinal uniformity. Most CD test instruments for telecom fibers have spectral range limited to 1310 and 1550 nm bands, while the range of interest for microstructured fibers is wider, often extending down to 800 nm or less [26, 29, 35]. This applies in particular to nonlinear PCFs intended for supercontinuum generation, where fiber CD dictates spectral range of operation.

Chromatic dispersion in short, approx. 1 m long sample of optical fiber can be measured with white-light interferometry. Several variants of this technique are described in literature [32–37]; most of them share the following features:

- broadband light source (tungsten-halogen lamp, LED, SC),
- insertion of sample into Michelson or Mach-Zehnder interferometer,
- finding "equalization wavelength", corresponding to equal delay in both arms of interferometer, for multiple lengths of adjustable arm, using spectrometer/optical spectrum analyzer,
- fitting of test data to analytical function, usually 3- or 5-term Sellmeier function recommended for this purpose by ITU-T [20].

Figure 12.16 shows typical test setup with Mach-Zehnder interferometer. With minor changes to equipment, white-light interferometry is also suitable for

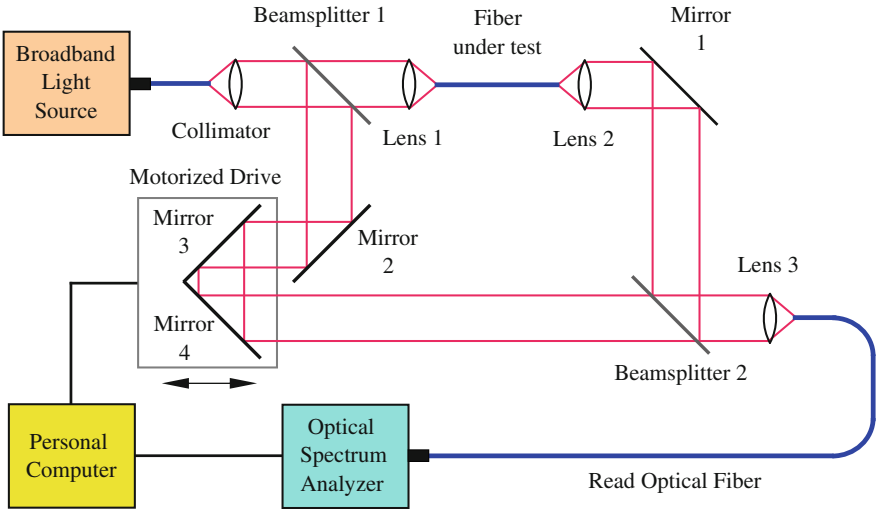

Fig. 12.16 Setup for CD measurements with Mach-Zehnder interferometer [35, 36]. Fiber between light source and collimator shall be single-mode over the spectral range of measurement. The read fiber between interferometer and optical spectrum analyzer (or spectrometer) may be multimode, e.g. 50/125 µm. For broadband measurements, achromatic lenses are required

characterization of conventional optical fibers or bulk materials [33]. This method is also standardized by ITU-T for testing of telecom fibers [20].

Best results are obtained with supercontinuum sources due to their high spectral power density and broad emission spectrum: CD measurements over a spectral span of over 1000 nm were reported [35, 37]. Paper [37] presents CD characterization of nonlinear PCFs developed at IPHT, but different from fibers dealt with in this chapter.

All-fiber setup can be assembled, with moving mirrors replaced by length of stretched single-mode fiber (SMF), and 2 × 2 fiber coupler instead of beamsplitter [32, 34]. It is, however, harder to calibrate as elasto-optic effect in stretched fiber must be taken into account. Propagation delay produced by stretching conventional single-mode fiber (SMF) is only 75–80 % of delay produced by adding the same length of strain-free fiber; exact proportionality factor depends on fiber type and wavelength.

12.9 Fiber Data

Tests presented in preceding sections were done on two silica photonic crystal fibers with core highly doped with germania (GeO_2)—up to 36 % mol, designed as nonlinear optical medium for signal processing, supercontinuum generation, etc. Fibers were designed and made at Institute of Photonic Technology Jena (IPHT), Jena, Germany, using MCVD method for graded-index doping of core rods (Fig. 12.17) and stack-and-draw process for preform assembly [26, 29]. Data of fibers are presented in Table 12.1, and their structures in Fig. 12.18.

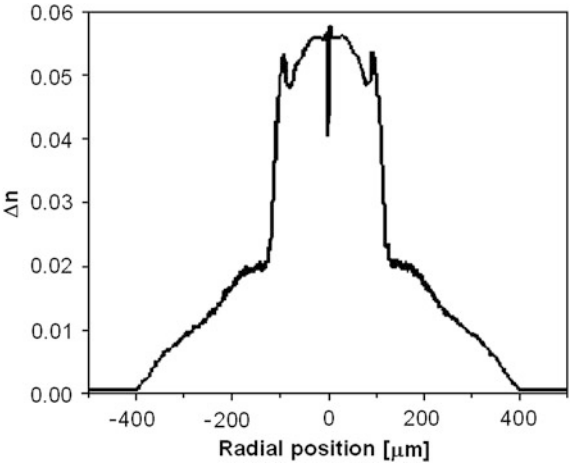

Fig. 12.17 Refractive index profile of doped rod measured at 633 nm; from [29]

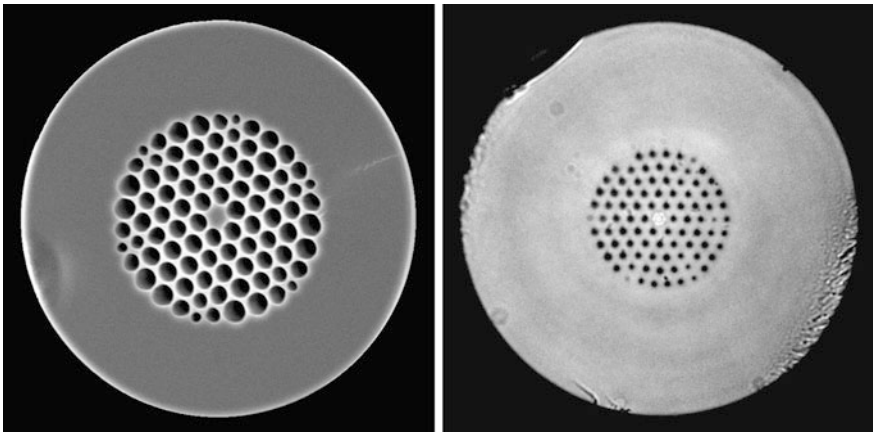

Fig. 12.18 Cross-section of fibers: IPHT 252b5 (*left*) and IPHT 282b4 (*right*, core illuminated). Photonic structures have similar size, but different air filling fraction (d/Λ) and are surrounded by cladding of different thickness

12.10 Conclusions

We have reviewed methods for characterization of selected properties of photonic crystal fibers, with accent on comparing and recommending practical solutions and warning the reader of common errors or difficulties. Results presented in this chapter demonstrate also how a relatively minor differences in dimensions and geometry imperfections of such fibers can dramatically change their parameters and behavior during use. We hope this information will be useful for researchers and manufacturers of such fibers, but we also realize that due to a variety of fiber designs, requirements and test instruments, it cannot be universally applicable.

Acknowledgements Research work at NIT presented in this paper was carried out within COST Action 299 "FIDES" and financially supported by Polish Ministry of Science and Higher Education as special research project COST/39/2007.

References

1. P.S.J. Russell, Photonic-crystal fibers. J. Lightwave Technol. **24**(12), 4729–4749 (2006)
2. R. Buczyński, Photonic crystal fibers. Acta Phys. Pol. A **106**(2), 141–167 (2004)
3. K. Nakajima, K. Hogari, J. Zhou, K. Tajima, I. Sankawa, Hole-assisted fiber design for small bending and splice losses. IEEE Photonics Technol. Lett. **15**(12), 1737–1739 (2003)
4. T.A. Birks, P.J. Roberts, F. Couny, H. Sabert, B.J. Mangan, D.P. Williams, L. Farr, M.W. Mason, A. Tomlinson, J.C. Knight, P.S.J. Russell, The fundamental limits to the attenuation of hollow-core photonic crystal fibres, in *Proceedings of ICTON 2005*, Mo.B2.1 (2005), pp. 107–110

5. D.J. Richardson, F. Poletti, J.Y.Y. Leong, X. Feng, H.E. Heidepreim, H.V. Finazzi, K.E. Frampton, S. Asimakis, R.C. Moore, J.C. Baggett, J.R. Hayes, M.N. Petrovich, M.L. Tse, R. Amezcua, J.H.V. Price, N.G.R. Broderick, P. Petropoulos, T.M. Monro, Advances in microstructured fiber technology, in *Proceedings of 2005 IEEE/LEOS Workshop on Fibres and Optical Passive Components* (2005), pp. 1–9
6. J. Lægsgaard, A.O. Bjarklev, Microstructured optical fibers—fundamentals and applications. J. Am. Ceramic Soc. **89**(1), 2–12 (2006)
7. I. Gris-Sanchez, J.C. Knight, Time-dependent degradation of photonic crystal fiber attenuation around OH absorption wavelengths. J. Lightwave Technol. **30**(23), 3597–3602 (2012)
8. S.H. Law, J.D. Harvey, R.J. Kruhlak, M. Song, E. Wu, G.W. Barton, M.A. van Eijkelenborg, M.C.J. Large, Cleaving of microstructured polymer optical fibres. Opt. Commun. **258**, 193–202 (2006)
9. A. Stefani, K. Nielsen, H.K. Rasmussen, O. Bang, Cleaving of TOPAS and PMMA microstructured polymer optical fibers: core-shift and statistical quality optimization. Opt. Commun. **285**(7), 1825–1833 (2012)
10. ITU-T Recommendation G.652, Characteristics of a single-mode optical fibre and cable (2009)
11. K. Borzycki, K. Schuster, Arc fusion splicing of photonic crystal fibres, in *Photonic Crystal Fibres—Book*, vol. 1 (Intech Publishing, Rijeka, Croatia, 2012), pp. 175–200
12. B. Bourliaguet, C. Pare, F. Emond, A. Croteau, A. Proulx, R. Vallee, Microstructured fiber splicing. Opt. Express **11**(25), 3412–3417 (2003)
13. K. Borzycki, J. Kobelke, K. Schuster, J. Wójcik, Arc fusion splicing of photonic crystal fibers to standard single mode fibers, in *Proceedings of SPIE* (2010), pp. 7714–7738
14. A. Yablon, *Optical Fiber Fusion Splicing* (Springer, Berlin, 2005)
15. L. Xiao, M.S. Demokan, W. Jin, Y. Wang, Ch-L Zhao, Fusion splicing photonic crystal fibers and conventional single-mode fibers: microhole collapse effect. J. Lightwave Technol. **25**(11), 3563–3574 (2007)
16. R. Thapa, K. Knabe, K.L. Corwin, B.R. Washburn, Arc fusion splicing of hollow-core photonic bandgap fibers for gas-filled fiber cells. Opt. Express **14**(21), 9576–9583 (2006)
17. Y. Wang, H. Bartelt, S. Brueckner, J. Kobelke, M. Rothhardt, K. Mörl, W. Ecke, R. Willsch, Splicing Ge-doped photonic crystal fibers using commercial fusion splicer with default discharge parameters. Opt. Express **16**(10), 7258–7263 (2008)
18. T. Hamada, R. Suzuki, K. Takenaga, N. Guan, S. Matsuo, K. Himeno, Arc-fusion splicing techniques for holey fibers. Fujikura Tech. Rev. **35**, 5–9 (2006)
19. K. Borzycki, J. Kobelke, P. Mergo, K. Schuster, Challenges in characterization of photonic crystal fibers, in *Proceedings of SPIE* (2011), pp. 8073B–80107
20. ITU-T Recommendation G.650.1, Definitions and test methods for linear, deterministic attributes of single-mode fibre and cable (2010)
21. K. Borzycki, J. Kobelke, K. Schuster, J. Wójcik, Optical, thermal and mechanical characterization of photonic crystal fibers: results and comparisons, in *Proceedings of SPIE* (2010), pp. 7714–7731
22. K. Borzycki, J. Kobelke, P. Mergo, K. Schuster, Characterization of photonic crystal fibers with OTDR, in *Proceedings of ICTON-2011,* We.B4.5 (2011)
23. v-OTDR Very High Resolution Time Domain Reflectometer. Luciol Instruments SA (2009)
24. LOR-200 High Resolution Time Domain Reflectometer, Luciol Instruments SA (2012)
25. M.A.R. Franco, V.A. Serrao, T.R. Pitarello, A.S. Cerqueira Jr., Hybrid photonic crystal fiber sensing of high hydrostatic pressure, in *Proceedings of SPIE* (2011), p. 775346
26. K. Schuster, J. Kobelke, S. Grimm, A. Schwuchow, J. Kirchhof, H. Bartelt, A. Gebhardt, P. Leproux, V. Couderc, W. Urbanczyk, Microstructured fibers with highly nonlinear materials. Opt. Quant. Electron. **39**, 1057–1069 (2007)
27. T. Martynkien, P. Mergo, W. Urbańczyk, Sensitivity of birefringent microstructured polymer optical fiber to hydrostatic pressure. IEEE Photonics Technol. Lett. **25**(16), 1562–1565 (2013)
28. P. Lesiak, T. Woliński, Simultaneous twist and longitudinal strain effects on polarization mode dispersion in highly birefringent fibers. Opto-Electron. Rev. **13**(2), 183–186 (2005)

29. T. Martynkien, M. Szpulak, G. Statkiewicz-Barabach, J. Olszewski, A. Anuszkiewicz, W. Urbanczyk, K. Schuster, J. Kobelke, Birefringence in microstructure fiber with elliptical GeO_2 highly doped inclusion in the core. Opt. Lett. **33**(23), 2764–2766 (2008)
30. K. Borzycki, K. Schuster, Characterization and fusion splicing of single-mode photonic crystal fibers, in *Proceedings of CAOL-2013* (Sudak, Crimea, Ukraine, 9–13 Sept 2013), pp. 31–34
31. J. Zhou, K. Tajima, K. Nakajima, K. Kurokawa, K. Matsui, C. Fukai, I. Sankawa, PMD Suppression method for photonic crystal fiber, in *Proceedings of OFC/NFOEC*, OTuA6, vol. 2 (2005)
32. L. Thevenaz, J.-P. Pellaux, J.-P. von der Veid, All-fiber interferometer for chromatic dispersion measurements. J. Lightw. Technol. **6**(1), 1–7 (1988)
33. S.A. Diddams, J.-C. Diels, Dispersion measurements with white-light interferometry. J. Opt. Soc. Am. B **13**(6), 1120–1129 (1996)
34. P. Peterka, J. Kanka, P. Honzátko, D. Káčik, Measurement of chromatic dispersion of microstructure optical fibers using interferometric method. Optica Applicata **38**(2), 295–303 (2008)
35. P. Hlubina, M. Kadulova, P. Mergo, Chromatic dispersion measurement of holey fibres using a supercontinuum source and a dispersion balanced interferometer. Opt. Lasers Eng. **51**(4), 421–425 (2013)
36. P. Hlubina, M. Szpulak, D. Ciprian, Measurement of the group dispersion of the fundamental mode of holey fiber by white-light spectral interferometry. Opt. Express **15**(18), 11073–11081 (2007)
37. D. Hoh, R. Spittel, M. Jäger, H. Bartelt, Chromatic dispersion measurement of microstructured optical fibers for nonlinear applications, in *Proceedings of DGaO*, 113, A36 (2012)

Chapter 13
All-Normal-Dispersion Photonic Crystal Fibers Under Prism of Supercontinuum Generation and Pulse Compression

Igor A. Sukhoivanov, Sergii O. Iakushev, Oleksiy V. Shulika, Antonio Diez, Miguel V. Andrés, Igor V. Guryev, José Amparo Andrade Lucio and Oscar G. Ibarra Manzano

Abstract We discuss properties of all-normal-dispersion photonic crystal fibers in context of supercontinuum generation and compression of ultrashort pulses. The application of pump pulses typical for the state of the art Ti:Sapphire lasers allows obtaining quite flat and broad spectra extending more than one octave in this fiber. The influence of initial pump pulse parameters such as pulse energy, duration, and pump wavelength on the SC generation was investigated. It was shown that compression of pulses with such SC spectra allows obtaining a few cycle pulses up to 8.1 fs, if a simple quadratic compressor is used and single cycle pulses up to 2.5 fs, if full phase compensation is provided.

13.1 Introduction

Supercontinuum (SC) generation is very active field of research during the last decade. Light with an initially narrow optical spectrum can undergo an extreme spectral broadening known as supercontinuum generation, when the light is propagating in a nonlinear medium. This phenomenon was at first reported by Alfano and Shapiro in bulk glass using a picosecond laser as the light source [1, 2].

I.A. Sukhoivanov · O.V. Shulika (✉) · J.A. Andrade Lucio · O.G. Ibarra Manzano
Departamento de Ingeniería Electrónica, DICIS, Universidad de Guanajuato, Salamanca, México
e-mail: oshulika@ugto.mx

S.O. Iakushev
Kharkiv National University of Radio Electronics, Kharkiv, Ukraine

A. Diez · M.V. Andrés
University of Valencia, Burjassot Valencia, Spain

I.V. Guryev
Departamento de Estudios Multidisciplinarios, DICIS, Universidad de Guanajuato, Salamanca, México

O. Shulika and I. Sukhoivanov (eds.), *Contemporary Optoelectronics*,
Springer Series in Optical Sciences 199, DOI 10.1007/978-94-017-7315-7_13

Supercontinuum generation was investigated in wide variety of nonlinear media, including solids, organic and inorganic liquids, gases, and various types of waveguide [3]. The nonlinear effects responsible for the spectral broadening require a high light intensity sustained in the medium. This could occur in the bulk glass due to spatial nonlinear effects resulting in self-focusing of the beam. The advent of low loss optical fibers has provided novel efficient nonlinear media. The advantage of optical fibers is that the beam is confined in the transverse plane, so that a high intensity of the light can be sustained over larger propagation distances. This reduces the requirement of high power pump laser for efficient broadband supercontinuum generation.

Supercontinuum generation makes it possible to create light sources with an optical spectrum covering several hundreds of nanometers (more than one octave in frequency domain). The SC spectrum is not only broad, but is also spatially coherent, contrary to light from, e.g., a tungsten lamp, and has higher brightness. Due to its unique properties the supercontinuum has found numerous applications in optical communications, optical coherence tomography, frequency metrology, extremely short pulse generation, dispersion measurements, remote sensing [3, 4].

A huge interest in this field was inspired by application of specially designed photonic crystal fibres (PCFs) which have allowed SC generation in much wider range of source parameters than it has been possible with bulk media or conventional fibers. Particularly it was reported SC generation applying various pump sources such as femtosecond lasers [5], as well as picosecond [6] and nanosecond lasers [7] and even CW sources [8]. Standard optical fibers consist of a cylindrical glass core surrounded by a cladding, with the cladding having a slightly lower index of refraction than the core. The light is confined in the core due to total internal reflection at the interface between core and cladding. Photonic crystal fibers offer a fundamentally different way of guiding the light, namely the photonic band gap effect. A PCF typically consists of silica glass and air-holes comprising a transverse microstructure along the fiber. The most common type of PCF used for SC generation however is the index-guiding PCF, which relies on an effective index difference between the solid silica core and the surrounding silica cladding with air-holes, for a modified total internal reflection guiding mechanism [9]. This allows single-mode guidance over broad wavelength ranges in smaller cores, so that a higher intensity can be obtained, leading to more efficient nonlinear effects [10]. However, the key features of novel fibers important for producing of SC is flexibility in tailoring the dispersion profile, by varying the parameters of the microstructure, e.g., the size of the air-holes and the distance between them.

The relationship between the input pump wavelength and the dispersion profile of the fiber directly governs the various properties of generated SC. At first for SC generation was proposed PCF fibers with a single zero dispersion wavelength shifted to the shorter wavelengths. Then it was applied for SC generation fiber with two ZDWs, and recently was proposed application of all-normal dispersion PCF without any ZDWs. All these dispersion profiles can be obtained in standard PCF with a solid core and hexagonal lattice of air holes by varying geometrical parameters, shown in Fig. 13.1a. The solid core is formed by removal of an air hole in the center introducing a defect associated with a locally elevated refractive index,

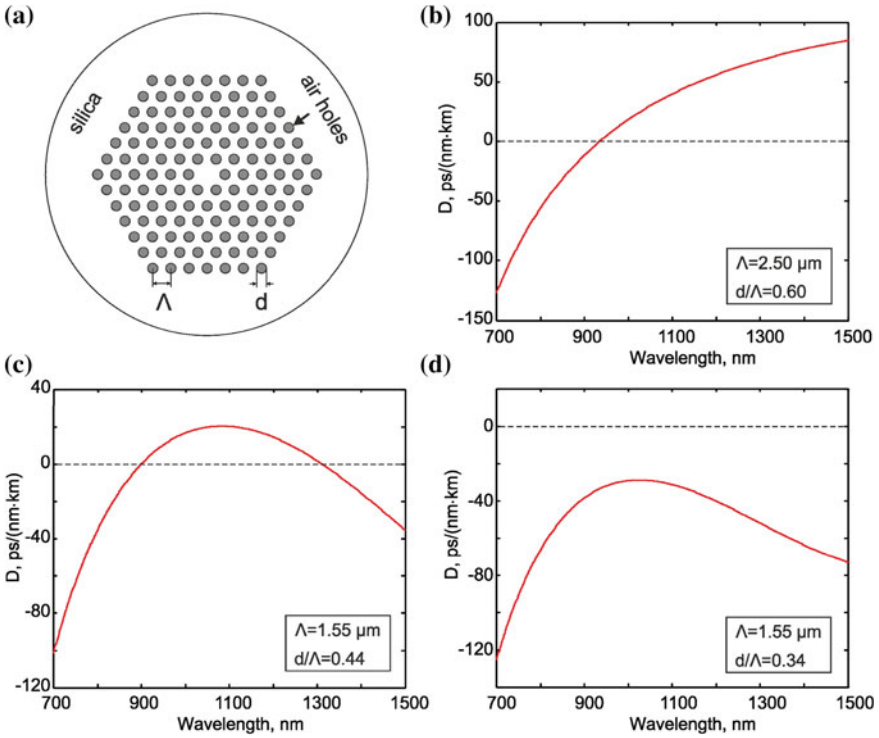

Fig. 13.1 **a** Cross section of the solid core PCF with hexagonal lattice of air holes in the cladding region; **b** dispersion curve of PCF with a single ZDW; **c** dispersion curve of PCF with a two ZDWs; **d** dispersion curve of ANDi PCF without any ZDW. *Insets* show the design parameters of PCFs

and guided wave propagation within this elevated-index region occurs through an equivalent total internal reflection. The examples of dispersion profiles of those fibers are shown in Fig. 13.1.

It was found that the broadest SC spectra are generated when injecting the pump pulse into the anomalous group velocity dispersion (GVD) region near the zero-dispersion wavelength (ZDW) of the fiber [11]. In this case SC generation appears in the anomalous dispersion region of the optical fibers. Owing to that the broadening mechanism here is dominated by soliton dynamics and soliton fission, which is sensitive to the input pulse fluctuations and the pump laser shot noise [12]. This leads to the several problems, such as complex temporal profile, the spectral fine structure, lack of spectral flatness, increment of noise, and low-coherence characteristics [13–15]. Then, it was proposed fibers with two closely spaced ZDWs for SC generation [16]. This resulted in the stable and coherent SC spectrum generation, but having two distinct spectral peaks on the normal dispersion side of each ZDW [16–18], which is undesirable if continuous broadband spectrum is required.

However, recently it was shown that all-normal dispersion photonic crystal fibers (ANDi PCFs) which exhibit convex dispersion profiles lying completely in

the normal dispersion region can be successfully fabricated. Pumping near the flattened top of such ANDi PCF provides generation of highly coherent, flat-top and octave-spanning SC preserving a single pulse in temporal domain [19, 20]. The physical mechanism of SC generation in ANDi PCF is drastically different as compared to that one in anomalous region of the fibers. In normal dispersion region spectral broadening appears preliminary due to the action of self-phase modulation (SPM) and four-wave mixing (FWM) induced by optical wave breaking (OWB) [19, 21]. It was shown that the pumping near the flat top of dispersion curve is highly important providing the maximal spectral broadening and spectral flatness [21], whereas pumping far away from a flat top leads to the degradation of the spectral flatness [19]. Up to now there were proposed a few designs of ANDi PCFs with a flat top of dispersion curve located at near-infrared $\sim$1060 nm wavelength [20, 22] and in the visible range at 650 nm [19]. Practically important is also wavelength 800 nm where Ti:Sapphire lasers and Erbium-doped fiber lasers with second harmonic generation generate. It was shown that at this wavelength one can use ANDi PCF with a flat top at 650 nm [19], however such fiber is difficult in fabrication and usage due to the extremely small geometrical parameters (pitch 0.67 μm, relative hole diameter 0.6).

Recently we have designed ANDi PCF with a flat top located exactly at 800 nm with a larger geometrical parameters (pitch 1.0 μm, relative hole diameter 0.5) and shown that this fiber is attractive for parabolic pulse generation at 800 nm [23]. Moreover our recent theoretical results show that such fiber is also attractive for pulse preserving SC generation in normal dispersion region [24, 25]. Here, we investigate in a detailed way the applicability of this fiber for SC generation with femtosecond pulses delivered by conventional Ti:Sapphire lasers. It is investigated also the compression of pulses with SC spectra obtained at the output of ANDi PCF and the influence of deviations of fiber's geometrical design parameters which can appear during fabrication of the fiber on the SC generation.

13.2 Theory of SC Generation in PCFs

During the optical pulse in a medium the electromagnetic field interacts with the atoms of the medium. This generally means that the pulse experiences loss and dispersion, where the latter effect occurs because the different wavelength components of the pulse travel at different velocities due to the wavelength dependence of the refractive index. These effects are termed the linear response of the medium. If the intensity of the pulse is high enough, the medium also responds in a nonlinear way. Most notably is the Kerr effect when a nonlinear electronic polarization generated in the medium, which itself modifies the propagation properties of the light [26]. The Kerr effect is the effect of an instantaneously occurring nonlinear response, providing that the refractive index of the medium becomes intensity dependent. Time-dependent refractive index change leads to self-phase modulation, when a time-dependent phase shift is induced during pulse propagation according

to the time dependence of the pulse intensity. For very short and broadband pulses Kerr effect leads also to the self-steepening of the pulse, due to the to the intensity dependence of the group velocity. Owing to that the velocity with which the peak of the pulse propagates is reduced and thus leads to an increasing slope of the trailing edge of the pulse. A non-instantaneous nonlinear response is caused by vibrations of the crystal (or glass) lattice. When these vibrations are associated with optical phonons, the effect is called Raman scattering. These nonlinear effects are the basis for the spectral broadening mechanisms in optical fibers.

A propagation equation describing the evolution of the optical pulse envelope in an optical fiber is derived from Maxwell's equations under the assumption of slowly varying envelope approximation [26]. This allows writing the electric field of a pulse linearly polarized along the x-axis and propagating in the fundamental mode of an optical fiber in the following form [26]:

$$\mathbf{E}(x, y, z, t) = 1/2\mathbf{x}\{F(x, y)A(z, t)\exp[i(\beta_0 z - \omega_0 t)] + c.c.\}, \tag{13.1}$$

where $\mathbf{x}$ is the polarization unit vector, $F(x, y)$ describes the transverse field distribution, $A(z, t)$ is the slowly varying pulse envelope, and β_0 is the mode propagation constant $\beta(\omega)$ at the center angular frequency ω_0 of the pulse spectrum. The change in pulse envelope $A(z, t)$ as the pulse propagates along the fiber axis z is described by the generalized nonlinear Schrödinger equation (GNLSE) [4, 11, 26]. We apply here GNLSE for the electric field envelope $A(z, T)$ in a retarded reference time frame $T = t - \beta_1 z$ in the following form:

$$\frac{\partial A(z, T)}{\partial z} = (\hat{D} + \hat{N})A(z, T), \tag{13.2}$$

where $\hat{D}$ is a linear operator, and $\hat{N}$ is a nonlinear operator. Linear operator $\hat{D}$ can be written in the following form [4, 11]:

$$\hat{D} = -\frac{\alpha}{2} + (\beta(\omega) - (\omega - \omega_0)\beta_1 - \beta_0). \tag{13.3}$$

The left-hand side of the operator $\hat{D}$ gives the linear loss in the fiber α, whereas the right-hand side describes dispersion. In (13.3) dispersion is given directly applying the propagation constant $\beta(\omega)$ and the dispersion coefficients β_0, β_1 associated with the Taylor series expansion of the propagation constant $\beta(\omega)$ about the center frequency ω_0.

Nonlinear operator $\hat{N}$ in (13.2) is written by the following way:

$$\hat{N} = i\gamma \frac{1}{A(z, T)}\left(1 + i\tau_{\text{shock}}\frac{\partial}{\partial T}\right) \times \left(A(z, T)\int_{-\infty}^{\infty} R(T')|A(z, T - T')|dT'\right). \tag{13.4}$$

The expression (13.4) includes self-phase modulation (SPM) associated with a nonlinear coefficient γ. The time derivative in the nonlinear operator (13.4) includes the effects of self-steepening and optical shock formation, characterized on a time scale $\tau_{\text{shock}} = 1/\omega_0$. The response function $R(t) = (1 - f_R)\delta(t) + f_R h_R(t)$ includes both the instantaneous electronic and delayed Raman contributions, with $f_R = 0.18$ representing the fractional contribution of the delayed Raman response. For the Raman response function of the silica fiber, $h_R(t)$, the analytical expression is used [27]:

$$h_R(t) = \frac{\tau_1^2 + \tau_2^2}{\tau_1 \tau_2^2} \exp\left(-\frac{t}{\tau_2}\right) \sin\left(\frac{t}{\tau_1}\right), \tag{13.5}$$

where the parameters $\tau_1 = 12.2$ fs and $\tau_2 = 32$ fs are two adjustable parameters and chosen such that to provide a good fit to the actual Raman-gain spectrum [27]. The inverse time scale $1/\tau_1$ gives the phonon frequency and $1/\tau_2$ determines the bandwidth of the Lorentzian line. Nonlinear coefficient γ is defined as following:

$$\gamma = \frac{\omega_0 n_2(\omega_0)}{c A_{\text{eff}}(\omega_0)}, \tag{13.6}$$

where $n_2 = 2.9 \times 10^{-20}$ m^2/W is the nonlinear refractive index of the silica glass, c is the vacuum speed of light, A_{eff} is the effective mode field area of the fiber. GNLSE (13.1) is well described SC generation in PCFs [4, 11]. Here it is solved numerically by means of method proposed in [4], which implies finding the solution in the frequency domain while making use of a change of variables to shift into the so-called interaction picture.

13.3 Design and Fabrication of ANDi PCF

The optimal supercontinuum generation in all-normal dispersion fiber requires pumping near the flattened top of dispersion curve. Up to now there were proposed a few designs of ANDi PCFs with a flat top of dispersion curve located at near-infrared $\sim$1060 nm wavelength [20, 22] and in the visible range at 650 nm [19]. Here, we have designed ANDi PCF with a flat-top located at 800 nm, suitable for pumping with Ti:Sapphire lasers. The dispersion profile and mode field diameter (MFD) of the PCF were calculated with the analytical method described in [28, 29]. They are shown in Fig. 13.2. The designed ANDi PCF has the fused silica solid core and hexagonal lattice of air holes in the cladding region, with pitch $\Lambda = 1$ μm and a relative hole size $d/\Lambda = 0.5$. The solid core is formed by removal of an air hole in the center introducing a defect, the diameter of the core here is 1.5 μm. Dispersion and nonlinear coefficient of this fiber at 800 nm are following: $D = -40$ ps/(nm km), $\gamma = 1131/(\text{W km})$.

Fabrication of the designed ANDi PCF was made by stack-and-draw method. This technique provides high versatility, allowing complex lattices to be assembled

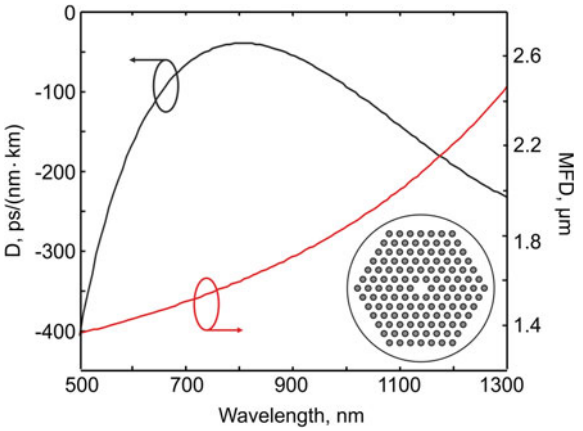

Fig. 13.2 Calculated dispersion profile and MFD of the designed ANDi PCF, *inset* shows cross section of a PCF

from individual stackable units [30–32]. Solid, empty or doped glass regions can be incorporated, without involving chemical processes. The fiber is fabricated typically in a few steps. The first step implies drawing capillaries, when the circular silica tubes and rods of several centimeters external diameter are drawn on the fiber-drawing tower in order to reduce its diameter to about 1.0 mm. The ratio of inner diameter to outer diameter of the capillaries must be chosen to closely match the air-filling fraction (d/Λ) of the final structure. Next step is building a necessary stack form the capillaries typically 10 mm in diameter in order to obtain the desired hexagonally air–silica structure. The core is formed by replacing the capillaries near the center with solid silica rods. When the stack is complete, it is inserted into a tube and then drawing into typically meter-long preforms with a few millimeters diameter. In the final step, the resulting preform is drawn down to the typical fiber dimensions (a few hundred microns) using a fiber-drawing tower.

Figure 13.3 shows microphotography of the cross-section and the core of the fabricated ANDi PCF. The shown PCF sample has following parameters: pitch

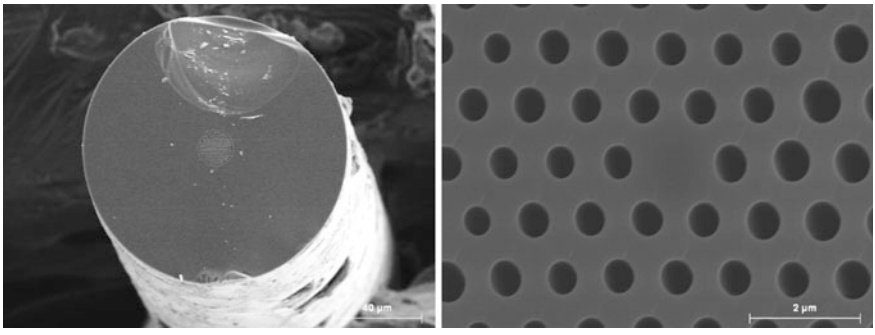

Fig. 13.3 Microphotography of the cross-section and the core of the fabricated ANDi PCF

$\Lambda = 1$ μm and hole's diameter $d = 0.53$ μm. That is the hole's diameter is a little bit larger than nominal value, this is happened due to the fabrication errors occurred during the fabrication process. This small deviation form a nominal value does not lead to the sufficient changes of fiber characteristics.

13.4 Supercontinuum Generation in ANDi PCF

At first we investigate supercontinuum generation in the designed ANDi PCF. For pumping has been choosing initial unchirped Gaussian pulses similar to that one produced by conventional Ti:Sapphire lasers with pulse duration (FWHM) 50–100 fs and pulse energy 5–10 nJ (repetition rate 80 MHz). Figure 13.4 shows simulation results of pulse temporal and spectral profile evolution in ANDi PCF over the fiber's length.

From Fig. 13.4 we can see that in temporal domain the main feature is preserving of a single pulse without splitting, only temporal broadening is occurred. In spectral domain we can see supercontinuum generation process. One can see that at first (<1 cm) pulse spreading is appeared due to the self-phase modulation and typical multi-peak spectral structure is formed. But further spectral shape becomes smother at the center of the spectrum and also lateral spectral bands are developed due to the four-wave mixing induced by optical wave breaking (OWB) [19, 21]. This resulted in quite smooth and broad spectrum already at 10 cm, after that distance pulse shape and width do not change sufficiently.

Figure 13.5 shows the simulation results of SC generation in the designed ANDi PCF using 10 cm fiber's piece.

Figure 13.5a shows pulses in temporal domain for different variations of initial pulse energies and durations. One can see that in temporal domain pulse shape at

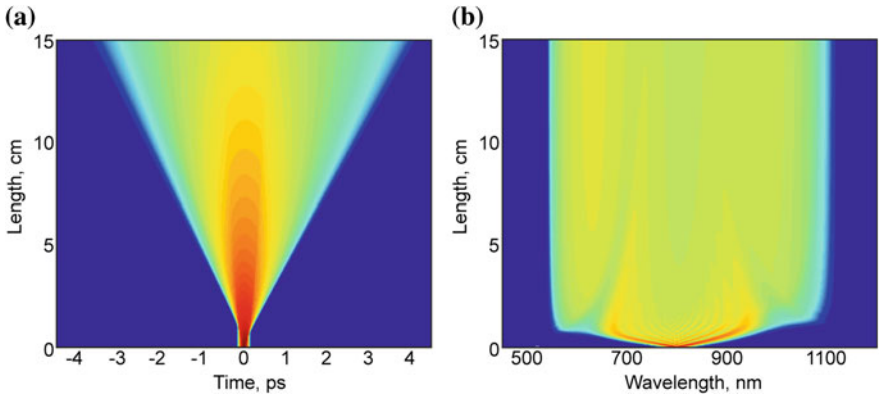

Fig. 13.4 Pulse evolution over the fiber's length in a logarithmic scale: **a** temporal pulse intensity evolution; **b** spectral pulse intensity evolution

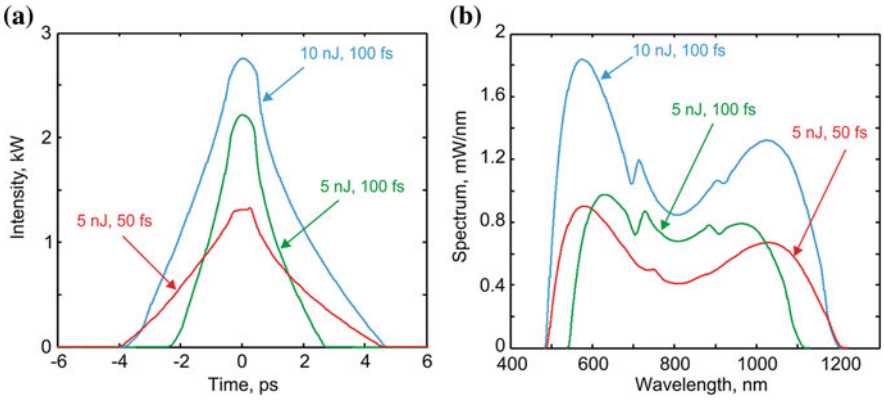

Fig. 13.5 Supercontinuum generation in ANDi PCF of 10 cm length for different pulse energies and durations. **a** Pulse profiles in temporal domain; **b** corresponding pulse spectra

the output of ANDi PCF is not already a Gaussian one and pulse duration increases up to a few picoseconds. Figure 13.5b shows the corresponding spectra of those pulses. One can see that the best flatness of the SC spectrum is achieved for smaller pulse energy −5 nJ and larger pulse duration −100 fs. However, spectral width in this case is smaller ∼572 nm. If we increase initial pulse energy up to 10 nJ, spectral width is increased up to 710 nm corresponding to ∼1.3 octave. Spectral width is also increased up to 711 nm, if we use initial pulses with smaller duration −50 fs. Thus, increasing of initial pulse energy or application of shorter initial pulses allows obtaining wider spectral width. However, the price for that is worse spectral flatness. Additional spectral broadening is accompanied by the depletion of central part of the spectrum such that a dip appears at the pumping wavelength. Spectral splitting is appeared as a result of complex dynamic of pulse evolution in the ANDi PCF involving nonlinear effects of self-steepening, frequency dependence of the nonlinear coefficient, in combination with the SPM and an optical wave breaking induced FWM process [21]. Here we can see that spectral splitting is appeared, when initial pulse with higher energy or shorter duration is used. This corresponds to the higher peak power of initial pulse which is responsible for the strength of nonlinear effects during pulse propagation in the fiber. Therefore, one has to find some compromise between spectral flatness and maximal spectral width by varying initial pump pulse.

Another important issue is spectral changes appeared when the pump wavelength is shifted from the top of dispersion curve of ANDi PCF, here it is 800 nm. The tuning range of typical Ti:Sapphire lasers is 700–900 nm, therefore we investigated what is happened if pumping is made within this tuning range. Figure 13.6 shows SC spectra generated at different pump wavelengths.

From Fig. 13.6 we can see that pumping far away from the top of dispersion curve leads to the strong asymmetry of the SC. At 700 nm red part of the spectrum is amplified, whereas the blue spectral part is depleted. The opposite picture appears

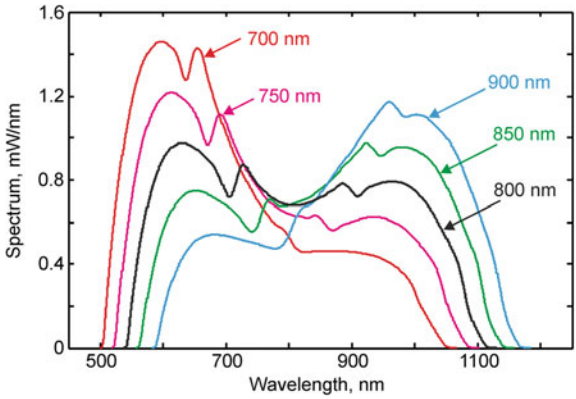

Fig. 13.6 Supercontinuum spectra generated in ANDi PCF of 10 cm length for different pump wavelengths. In all cases initial pulse energy is 5 nJ, pulse duration is 100 fs

at 900 nm. One can see that sufficient spectral asymmetry still exists for 750 and 850 nm pumping. Thus, we suppose that the optimal pump wavelength range for obtaining of SC spectra with a good flatness in the designed ANDi PCF is $\sim 760\ \text{nm} < \lambda_p < 840\ \text{nm}$.

Similar spectral distortions were observed experimentally, when the pumping wavelength was shifted to shorter wavelength on ~ 200 nm as compared to the top of dispersion curve [19]. Here we can see actually that spectral asymmetry appears when pump wavelength shifts to the both side from the top of dispersion curve. Moreover, the strong spectral asymmetry appears here faster already for ± 100 nm shift. We suppose this is related to the stronger curvature of dispersion curve of the designed ANDi PCF at 800 nm, whereas fiber *NL-1050-NEG-1* [22] used in [19] has wider flattened top at 1060 nm.

13.5 Pulse Compression

Because of SC generation in ANDi PCF is accompanied by preserving of a single pulse with a smooth profile in temporal domain, it is attractive for subsequent pulse compression. Previously it was reported compression of pulses with SC spectra generated in ANDi PCF up to 26 fs [20], 5.0 fs [33], 3.64 fs [34]. The most attractive is the possibility to generate a few-cycle pulses because such pulses are highly important in time-resolved studies of fundamental processes in physics, chemistry and biology [35]. Previous studies [33, 34] used commercially available fiber with a flat top located at 1060 nm [22] as well as special oscillators which produce already very short pulses for fiber's pump (15 fs in [33] and 6 fs in [34]). Here we examine the applicability of specially designed ANDi PCF with a flat top at 800 nm in combination with conventional Ti:Sapphire lasers for pulse compression. The chirp of pulses produced at the output of ANDi PCF is already quite close to a linear one [21], thus one can expect that applications of even a simple

compression technique allow obtaining good compression results. Therefore, at first we investigate application of a simple quadratic compressor for compression of only a linear chirp, this can be done for example by gratings or prism pairs. Figure 13.7a shows simulation results of pulse compression for pulses obtained at the output of ANDi PCF shown in Fig. 13.5a. The amount of group delay dispersion of compressor in each case was chosen such that to obtain the highest peak power of the compressed pulse, this usually corresponds to the shortest pulse duration as well. From Fig. 13.7a we can see that in all case compressed pulse durations are ~ 8 fs, which corresponds to the ~ 3 cycles of optical filed of the pulse at 800 nm. The highest peak power corresponds naturally to the pulse with larger initial energy (10 nJ, 100 fs). The unexpected feature is that application of shorter initial pulse (5 nJ, 50 fs) or larger energy pulse (10 nJ, 100 fs) does not give a shorter compressed pulse as compared to the pulse with small energy and large duration (5 nJ, 100 fs). From Fig. 13.3b we can see that increasing of initial pulse energy or decreasing of pulse duration provides larger spectral bandwidth, thus one could expect shorter compressed pulse duration in these cases. We suppose that this is not observed in Fig. 13.7a because of a larger amount of nonlinear chirp acquired by pulse in the fiber owing to the stronger impact of nonlinear effects when initial pulse duration is shorter or pulse energy is larger. The visible results of nonideal compression are excessive oscillated pulse tails in Fig. 13.7a.

Nonlinear chirp remains uncompressed, if quadratic compressor is used. However, more sophisticated compression techniques can be also applied, which are able compensate also nonlinear chirp [34, 36, 37] and providing shorter pulses up to the transform-limited one. Therefore, we investigate here also the case of full phase compensation. Figure 13.7b shows simulation results of pulse compression for pulses obtained at the output of ANDi PCF when full phase compensation is applied. We can see that now the potential of wider spectral bandwidth is fully exploited and shorter pulses are obtained from initial pulses with higher energy

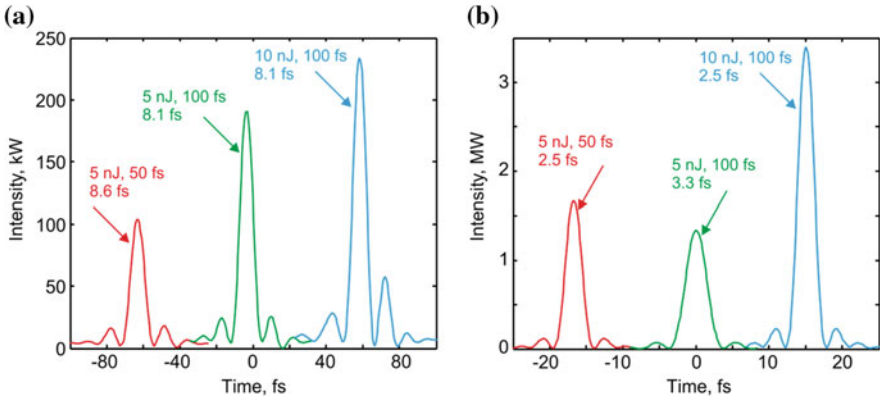

Fig. 13.7 Compression of pulses obtained at the output of ANDi PCF shown in Fig. 13.5a. **a** Compensation of only a linear chirp; **b** full phase compensation

(10 nJ, 100 fs) and with shorter duration (5 nJ, 50 fs). In these cases pulse duration is as short as 2.5 fs which corresponds to the one cycle of optical filed of the pulse at 800 nm. Thus, application of specially designed ANDi PCF with a flat at 800 nm together with conventional Ti:Sapphire laser allows obtaining of a few cycle pulses, if a simple quadratic compressor is used and a single-cycle pulses, if full phase compensation is provided.

To conclude, we have investigated numerically supercontinuum generation in the specially designed all-normal dispersive photonic crystal fiber with a flat top at 800 nm. It was shown that pumping at 800 nm by pulse with energy 5 nJ and duration 100 fs provides a good compromise between spectral width and flatness. Application of pump pulses with larger energy or shorter pulse duration provides wider spectrum, but spectral flatness becomes worth due to the appearance of a dip in the central part. The shifting of the pump wavelength from the 800 nm leads to the appearance of strong spectral asymmetry. In order to maintain good spectral flatness one have to pump within ±40 nm wavelength range around the top of dispersion curve. It was shown that compression of pulses with SC spectra generated in the designed ANDi PCF allows obtaining a few cycle pulses up to 8.1 fs, if a simple quadratic compressor is used and single cycle pulses up to 2.5 fs, if full phase compensation is provided.

Acknowledgements This work was supported by Universidad de Guanajuato under projects DAIP-633/2015, DAIP-609/2015, and DAIP-430/2014, by FoMix (CONACyT & CONCyTEG) under project GTO-2012-C04-195229, and in part by the Ministerio de Economía y Competitividad under project TEC-2013-46643-C2-1-R, and the Generalitat Valenciana under project PROMETEO II/2014/072.

References

1. R.R. Alfano, S.L. Shapiro, Emission in the region 4000 to 7000 Å via four-photon coupling in glass. Phys. Rev. Lett. **24**(11), 584–587 (1970)
2. R.R. Alfano, S.L. Shapiro, Observation of self-phase modulation and small-scale filaments in crystals and glasses. Phys. Rev. Lett. **24**(11), 592–594 (1970)
3. R.R. Alfano, *The Supercontinuum Laser Source*, 2nd edn. (Springer, Berlin, 2006)
4. J.M. Dudley, J.R. Taylor, *Supercontinuum Generation in Optical Fibers* (Cambridge 2010)
5. J.K. Ranka, R.S. Windeler, A.J. Stentz, Visible continuum generation in air-silica microstructure optical fibers with anomalous dispersion at 800 nm. Opt. Lett. **25**(1), 25–27 (2000)
6. S. Coen, A.H.L. Chau, R. Leonhardt, J.D. Harvey, J.C. Knight, W.J. Wadsworth, P. Russell, St. J. White-light supercontinuum generation with 60-ps pump pulses in a photonic crystal fiber. Opt. Lett. **26**(17), 1356–1358 (2001)
7. L. Provino, J.M. Dudley, H. Maillotte, N. Grossard, R.S. Windeler, B.J. Eggleton, Compact broadband continuum source based on microchip laser pumped microstructured fibre. Electron. Lett. **37**(9), 558–560 (2001)
8. A.K. Abeeluck, C. Headley, C.G. Jørgensen, High-power supercontinuum generation in highly nonlinear, dispersion-shifted fibers by use of a continuous-wave Raman fiber laser. Opt. Lett. **29**(18), 2163–2165 (2004)

9. A. Bjarklev, J. Broeng, A.S. Bjarklev, *Photonic Crystal Fibres* (Kluwer Academic Publishers, 2003)
10. W.H. Reeves, D.V. Skryabin, F. Biancalana, J.C. Knight, P.J. Russell, F.G. Omenetto, A. Efimov, A.J. Taylor, Transformation and control of ultra-short pulses in dispersion-engineered photonic crystal fibres. Nature **424**, 511–515 (2003)
11. J.M. Dudley, G. Genty, S. Coen, Supercontinuum generation in photonic crystal fiber. Rev. Mod. Phys. **78**(4), 1135–1184 (2006)
12. J. Herrmann, U. Griebner, N. Zhavoronkov, A. Husakou, D. Nickel, J. Knight, W. Wadsworth, P.S.J. Russell, G. Korn, Experimental evidence for supercontinuum generation by fission of higher-order solitons in photonic crystal fibers. Phys. Rev. Lett. **88**(17), 173901 (2002)
13. X. Gu, L. Xu, M. Kimmel, E. Zeek, P. O'Shea, A.P. Shreenath, R. Trebino, R.S. Windeler, Frequency-resolved optical gating and single-shot spectral measurements reveal fine structure in microstructure-fiber continuum. Opt. Lett. **27**(13), 1174–1176 (2002)
14. K.L. Corwin, N.R. Newbury, J.M. Dudley, S. Coen, S.A. Diddams, K. Weber, R.S. Windeler, Fundamental noise limitations to supercontinuum generation in microstructure fiber. Phys. Rev. Lett. **90**(11), 113904 (2003)
15. N.R. Newbury, B.R. Washburn, K.L. Corwin, Noise amplification during supercontinuum generation in microstructure fiber. Opt. Lett. **28**(11), 944–946 (2003)
16. K.M. Hilligsøe, T. Andersen, H. Paulsen, C. Nielsen, K. Mølmer, S. Keiding, R. Kristiansen, K. Hansen, J. Larsen, Supercontinuum generation in a photonic crystal fiber with two zero dispersion wavelengths. Opt. Express **12**(6), 1045–1054 (2004)
17. M. Frosz, P. Falk, O. Bang, The role of the second zero-dispersion wavelength in generation of supercontinua and bright-bright soliton-pairs across the zero-dispersion wavelength. Opt. Express **13**(16), 6181–6192 (2005)
18. M.-L.V. Tse, P. Horak, F. Poletti, N.G. Broderick, J.H. Price, J.R. Hayes, D.J. Richardson, Supercontinuum generation at 1.06 μm in holey fibers with dispersion flattened profiles. Opt. Express **14**(10), 4445–4451 (2006)
19. A.M. Heidt, A. Hartung, G.W. Bosman, P. Krok, E.G. Rohwer, H. Schwoerer, H. Bartelt, Coherent octave spanning near-infrared and visible supercontinuum generation in all-normal dispersion photonic crystal fibers. Opt. Express **19**(4), 3775–3787 (2011)
20. L.E. Hooper, P.J. Mosley, A.C. Muir, W.J. Wadsworth, J.C. Knight, Coherent supercontinuum generation in photonic crystal fiber with all-normal group velocity dispersion. Opt. Express **19**(6), 4902–4907 (2011)
21. A.M. Heidt, Pulse preserving flat-top supercontinuum generation in all-normal dispersion photonic crystal fibers. J. Opt. Soc. Am. B **27**(3), 550–559 (2010)
22. Nonlinear Photonic Crystal Fiber NL-1050-NEG-1. http://www.nktphotonics.com
23. I.A. Sukhoivanov, S.O. Iakushev, O.V. Shulika, A. Díez, M. Andrés, Femtosecond parabolic pulse shaping in normally dispersive optical fibers. Opt. Express **21**(15), 17769–17785 (2013)
24. S.O. Iakushev, O.V. Shulika, I.A. Sukhoivanov, Sub-10-fs pulses produced from compression of supercontinuum generated in all-normal dispersion photonic crystal fiber, in *Technical Digest of conference on Frontiers in Optics 2012/Laser Science XXVIII*, October 14–18, Rochester, NY, FW3A.41 (2012)
25. I.A. Sukhoivanov, J.A. Andrade Lucio, O.V. Shulika, S.O. Iakushev, A.B. García, G. Ramos-Ortiz, I.V. Guryev, O.G. IbarraManzano, A.G. Perez, (2013) All-normal dispersion photonic crystal fiber for parabolic pulses and supercontinuum generation. Proc. SPIE **8847**, 88470H-1–88470H-8 (2013)
26. G.P. Agrawal, *Nonlinear Fiber Optics*, 4th edn. (Academic Press, Boston, 2007)
27. K.J. Blow, D. Wood, Theoretical description of transient stimulated scattering in optical fibers. IEEE J. Quantum Electron. **25**(12), 2665–2673 (1989)
28. M. Koshiba, K. Saitoh, Applicability of classical optical fiber theories to holey fibers. Opt. Lett. **29**(15), 1739–1741 (2004)
29. K. Saitoh, M. Koshiba, Empirical relations for simple design of photonic crystal fibers. Opt. Express **13**(1), 267–274 (2005)

30. J.C. Knight, T.A. Birks, P.J. Russell, D.M. Atkin, All-silica single-mode optical fiber with photonic crystal cladding. Opt. Lett. **21**(19), 1547–1549 (1996)
31. P. Russell, Photonic crystal fibers. Science **299**, 358–362 (2003)
32. J.C. Knight, Photonic crystal fibres. Nature **424**, 847–851 (2003)
33. A.M. Heidt, J. Rothhardt, A. Hartung, H. Bartelt, E.G. Rohwer, J. Limpert, A. Tünnermann, High quality sub-two cycle pulses from compression of supercontinuum generated in all-normal dispersion photonic crystal fiber. Opt. Express **19**(15), 13873–13879 (2011)
34. S. Demmler, J. Rothhardt, A.M. Heidt, A. Hartung, E.G. Rohwer, H. Bartelt, J. Limpert, A. Tünnermann, Generation of high quality, 1.3 cycle pulses by active phase control of an octave spanning supercontinuum. Opt. Express **19**(21), 20151–20158 (2011)
35. F.X. Kärtner, *Few-Cycle Laser Pulse Generation and Its Applications* (Springer, Berlin, 2004)
36. Y. Liu, H. Tu, S.A. Boppart, Wave-breaking-extended fiber supercontinuum generation for high compression ratio transform-limited pulse compression. Opt. Lett. **37**(12), 2172–2174 (2012)
37. B. Schenkel, J. Biegert, U. Keller, C. Vozzi, M. Nisoli, G. Sansone, S. Stagira, S. De Silvestri, O. Svelto, Generation of 3.8-fs pulses from adaptive compression of a cascaded hollow fiber supercontinuum. Opt. Lett. **28**(20), 1987–1989 (2003)

Index

O. Shulika and I. Sukhoivanov (eds.), *Contemporary Optoelectronics*,
Springer Series in Optical Sciences 199, DOI 10.1007/978-94-017-7315-7